TURBULENT DRAG REDUCTION USING SURFACE PLASMA

Timothy N. Jukes, MEng.

THESIS SUBMITTED TO THE UNIVERSITY OF NOTTINGHAM

FOR THE DEGREE OF DOCTOR OF PHILOSOPHY

January 2007

Abstract

An experimental investigation has been undertaken in a wind tunnel to study the induced airflow and drag reduction capability of AC glow discharge plasma actuators.

Plasma is the fourth state of matter whereby a medium, such as air, is ionized creating a system of electrons, ions and neutral particles. Surface glow discharge plasma actuators have recently become a topic for flow control due to their ability to exert a body force near the wall of an aerodynamic object which can create or alter a flow. The exact nature of this force is not well understood, although the current state of knowledge is that the phenomenon results from the presence of charged plasma particles in a highly non-uniform electric field. Such actuators are lightweight, fully electronic (needing no moving parts or complicated ducting), have high bandwidth and high energy density. The manufacture of plasma actuators is relatively cheap and they can be easily retrofitted to existing surfaces.

The first part of this study aims at characterising the airflow induced by surface plasma actuators in initially static air. Ambient air temperature and velocity profiles are presented around a variety of actuators in order to understand the nature of the induced flow for various parameters such as applied voltage, frequency, actuator geometry and material. It is found that the plasma actuator creates a laminar wall jet along the surface of the material on which it is placed.

The second part of the study aims at using plasma actuators to reduce skin-friction drag in a fully developed turbulent boundary layer. Actuators are

designed to induce spanwise forcing near the wall, oscillating in time. Thermal anemometry measurements within the boundary layer are presented. These show that the surface plasma can cause a skin-friction drag reduction of up to 45% due to the creation of streamwise vortices which interact with, and disrupt the near-wall turbulence production cycle.

Acknowledgements

I am indebted to my supervisor, Prof. Kwing-So Choi, for his support, helpful suggestions and encouragement during the course of this study. I would also like to extend my thanks to Dr. Graham Johnson and Dr. Simon Scott from BAE SYSTEMS, UK, for useful advice, the loan of the plasma equipment and for co-funding the project. Thanks are given to the EPSRC for project funding and for the loan of the thermal camera. Also, thanks are extended to Dr. Takehiko Segawa and Dr. Hiro Yoshida from the National Institute of Advanced Industrial Science and Technology, Japan, for their useful discussions and providing the ceramic samples.

Thanks must go to my colleagues Dr. Faycal Bahri, Yang Xu, Peng Xu and Yong-Duck Kang for their support and suggestions over the years. I would especially like to thank Tracey for her patience and support, especially whilst writing this thesis, and to Mum and Dad.

And finally, this thesis is dedicated to the memory of Richard Allen.

Contents

Nomenclature

A	calibration constant
a	hot-wire heating ratio (R_w/R_a); electrode spacing
$\mathbf{B}$	magnetic induction tensor
B	calibration constant
B_0	magnetic field strength at wall
C	capacitance; calibration constant
c	chord length
c_f	skin-friction coefficient
$\mathbf{D}$	electric induction tensor
D	VITA detector function; calibration constant
d	distance between electrodes; hot-wire diameter
$\mathbf{E}$	electric field tensor
E	voltage
E_B	breakdown voltage
e	electron change
F	calibration constant
f	oscillation frequency
f_b	body force
f_c	cut-off frequency
Gr	Grasshof number ($g\beta(T - T_\infty)l^3/\nu$)
g	gravitational acceleration
$\mathbf{H}$	magnetic field strength tensor
H	shape factor (δ^*/θ)
h	channel half-height; heat transfer coefficient
I	current
$\boldsymbol{j}$	current density tensor
k	thermal conductivity; VITA detector threshold; Boltzmann constant
l	reference length
m_e	electron mass
m_i	ion mass
n	number of molecules

P	power
p	pressure
PED	Pulse Envelope Duration
PEF	Pulse Envelope Frequency
PRF	Pulse Repetition Frequency
Q	Flow rate
q	charge
R	molar gas constant
R_a	resistance of wire at ambient temperature, T_a
R_c	cable resistance
R_l	lead resistance
$R_x(\tau)$	autocorrelation function
R_w	resistance of heated wire at temperature, T_w
Re_δ	Reynolds number of wall jet ($U_{max}\delta_{½}/\nu$)
Re_θ	momentum thickness Reynolds number ($U_\infty\theta/\nu$)
Re_τ	friction velocity Reynolds number ($u^*\delta/\nu$)
r	radial distance
St	Stuart number ($J_0B_0\delta/\rho u^{*2}$)
s	electrode spacing
T	temperature; oscillation period
$T_{a,}\, T_\infty$	ambient temperature
T_e	electron temperature
T_{ens}	VITA ensembling window length
T_I	integral time scale
T_i	ion temperature
T_w	temperature of heated wire
T_{win}	window length
$\tan\delta$	dielectric loss tangent
t	time
t_{AC}	plasma repetition period ($2/PRF$)
U	mean streamwise velocity
U_∞	free-stream velocity
U_{max}	maximum wall-jet velocity
U_{eff}	effective velocity

u^*	friction velocity
u'	streamwise turbulence intensity
V	mean wall-normal velocity
v'	wall-normal turbulence intensity
v_c	particle collision frequency
W	mean spanwise velocity; radiation power
W^+	non-dimensional wall speed ($\pi.\Delta z^+/T^+$)
$W_{eq}{}^+$	equivalent non-dimensional wall speed ($St.T^+/(2\pi.Re_\tau)$)
w'	spanwise turbulence intensity
x	streamwise direction
y	wall-normal direction
z	spanwise direction
Δz^+	non-dimensional wall-oscillation amplitude
α	phase angle; coefficient of resistivity; spectral absoptance; thermal diffusivity
β	thermal expansion coefficient; yaw angle
Δ	change in a quantity
Δ	thermal boundary layer thickness
Δ^+	non-dimensional penetration depth ($au^*/\pi\nu$)
δ	boundary layer thickness
δ^*	displacement thickness
$\delta_{½}$	wall-jet half-width
ε	dielectric constant; spectral emissivity
ε_0	permittivity of free space
θ	momentum thickness; pitch angle
λ	wavelength
λ_D	Debye length
μ	dynamic viscosity
ν	kinematic viscosity (μ/ρ)
ρ	density; spectral reflectance
ρ_c	charge density
$\rho_x(\tau)$	autocorrelation coefficient function
τ	shear stress; spectral transmittance; time delay
τ_w	mean wall shear stress (skin-friction)

φ	electric potential
ω	vorticity; angular velocity

Subscripts and Superscripts

+	indicates viscous scaling, also referred to as inner-scaling. Viscous time, length and velocity scales are $t^+ = tu^{*2}/\nu$, $l^+ = lu^*/\nu$, $u^+ = U/u^*$
*	indicates wall-jet scaling with local maximum velocity, U_{max}, and jet half-width, $\delta_{½}$. Time, length and velocity scales are $t^* = tU_{max}/\delta_{½}$, $l^* = l/\delta_{½}$, $U^* = U/U_{max}$
$'$	rms value
#1, #2	wires 1 and 2
0	value at 0°C; value at $y = 0$
∞	free-stream condition
w	value at wall
$\langle u \rangle$	ensemble-averaged quantity (in this case streamwise velocity)
$\bar{u}$	time-averaged quantity
$\hat{u}$	pulse-averaged quantity

List of Tables

List of Figures

Chapter

Introduction

1.1. Nature of the Problem

Drag is generally a result of three components; form or pressure drag resulting from the difference in pressure between the wake of an object and the upstream, wave drag associated with the formation of shock waves (supersonic flow) or surface waves (hydrodynamic vehicles) and skin-friction drag resulting from the action of fluid shear at the interface between a solid and fluid. Pressure and wave drag can be reduced by careful design of the body shape (i.e. streamlining), such that flow separation is postponed or eliminated and shock wave effects are minimized. Skin-friction drag is traditionally minimised by improving the surface finish of the aerodynamic body. However, in many applications, we have reached the limits of the amount of drag that can be reduced by careful streamlining and using smooth surfaces. For example, on a commercial airliner around 50% of the drag is still associated with turbulent skin-friction, yet the surface roughness is as economically smooth as possible. Huge benefit in direct fuel costs and reduced pollution could be achieved if skin-friction is reduced, even by only a small percentage. In 2005, U.S. passenger and cargo airlines consumed more than 19.9 billion gallons of jet fuel, costing more than $33 billion. The average cost of a gallon of jet fuel has more than doubled, from 75 cents per gallon in 2001 to $1.98 in the first half of 2006. At current consumption rates, every penny increase in the price of a gallon of jet fuel results in an additional $199 million

in annual operating expenses for the industry (http://www.airlines.org/econ/, last accessed 27/07/06). In an age where both air traffic and the price of oil is rapidly increasing, we must find ways to use fuel more efficiently. It is clear that skin-friction drag must be reduced further and this will require innovative techniques.

Spanwise oscillation by a moving wall or Lorentz force has shown very promising results for reducing skin-friction drag, where reductions of up to 45% have been reported. While there has been success with these techniques in the laboratory, there are many problems with scaling to real applications. Spanwise wall oscillation is simply not feasible for application on an aircraft due to the high oscillation frequencies required (O[100kHz]). Similarly, the low conductivity of seawater makes the Lorentz forcing inefficient for use on a ship or submarine.

Plasma aerodynamics has recently become a topic for flow control due to technological advancements that allow weakly-ionized plasma to be generated over large surfaces. Such surface plasma actuators show a curious effect of creating a force on the ambient gas that can be used to either drive a flow or alter an existing flow to achieve global effects such as; delaying airfoil stall, delaying/promoting transition and moving/eliminating shock waves. Plasma offers many advantages over conventional actuators: it has high bandwidth, is purely electrical (requires no moving parts) and can be of low power.

In this thesis the properties of surface plasma actuators will be experimentally studied and used to create a spanwise oscillation at the wall of a turbulent boundary layer in order to see if a skin-friction drag reduction can be achieved with the benefits as outlined above.

1.2. Outline of Thesis

Chapter 2 provides a literature review of turbulent boundary layers in general, followed by a discussion of drag reduction techniques with particular emphasis on spanwise wall oscillation and spanwise Lorentz forcing. Plasma actuators used in subsonic airflow will then be discussed, with emphasis on their construction and the possible mechanism of how they create a flow of gas. In Chapter 3, the experimental arrangement and test procedures are discussed.

Chapters 4 through 7 are concerned with the characteristics of the induced airflow by a surface plasma actuator in initially static air. Hot-wire and cold-wire anemometry, flow visualisation and thermal imagery are used to study a range of actuators with different excitation parameters, geometry and dielectric properties. Chapter 7 finishes with a description of a novel way to produce wall normal jets with plasma actuators.

Chapters 8 through 10 are concerned with plasma actuators at the wall of a turbulent boundary layer arranged such that an oscillatory spanwise forcing is produced. Single hot-wire, crossed hot-wire and cold-wire anemometry is used to study turbulence statistics. An extensive study is presented in Ch. 9 for one actuator configuration, including conditional sampling of the near wall turbulent events. Parametric effects of electrode sheet geometry and forcing parameters are given in Ch. 10.

Finally, Chapter 11 summarises and concludes the thesis and gives recommendations for future work.

Chapter 2

Literature Review

2.1. Introduction

This chapter summarises some of the key research conducted over the last 100 years into the turbulent boundary layer, drag reduction and plasma aerodynamics. The cited papers are not intended as an exhaustive list; such a task would be extremely arduous due to the sheer magnitude of papers written on the subjects. Readers requiring a deeper understanding will find many additional references within the cited papers.

A semi-historical review of turbulent boundary layer theory is given in Sec. 2.2. Particular emphasis is placed on coherent structures and the turbulent energy production cycle; a modification of this cycle can lead to a reduction of drag.

Several drag reduction methods are reviewed in Sec. 2.3. Mechanical spanwise-wall oscillation and spanwise Lorentz forcing is highlighted since it is this technique that is attempted in this thesis. However, the spanwise oscillatory force will be produced using surface plasma in this study. As far as the author is aware, this technique has never been implemented before.

The chapter concludes with a review of plasma and plasma actuators designed for the use of aerodynamic flow control in Sec. 2.4. The classification of plasma is extremely diverse and we focus attention on atmospheric RF glow discharge plasmas for subsonic applications.

2.2. Turbulent Boundary Layers

The theory of boundary layers began with Ludwig Prantdl's groundbreaking paper in 1905 (Prantdl, 1905). In this paper, he showed that flows over solid surfaces could be separated into two regions; an outer region, where the effects of viscosity were negligible, and an inner region, whereby viscosity dominates. The thin viscous layer, or "transition layer" as Prantdl called it (Tani, 1977), soon became known as the "boundary layer" which is still a major research topic today.

The turbulent boundary layer produces significantly higher skin-friction drag than its laminar counterpart. In most practical situations, for example flow over aircraft, ships and automobiles, the flow will inherently be turbulent due to the high Reynolds number. This has promoted much research into understanding the fluid motion so that the drag force can be reduced and energy and fuel savings can be made.

In the early days, the turbulent boundary layer was viewed as comprising random turbulent motions across a range of scales and the only approach was to adopt a statistical view (for example see Schlichting 1979, and Murlis *et al.* 1982). Recent developments are focussed towards understanding the motions within the boundary layer structure – which are surprisingly found to be structured in both space and time. The boundary layer is said to be composed of 'coherent structures' which, adopting the definition of Robinson (1991a):

"A three-dimensional region of the flow over which at least one fundamental flow variable (velocity component, density, temperature, etc.) exhibits significant correlation with itself or another flow variable over a range of space and/or time that is significantly larger than the smallest scales of the flow."

The importance of coherent structures in all turbulent flows has been discussed by Hussain (1986). The understanding of coherent structures is of paramount importance in the manipulation of the turbulent boundary layer to reduce skin-friction drag as it is thought that these structures are responsible for the entire communication of information throughout the boundary layer. Indeed if turbulence production, and hence skin-friction, is to be reduced, it is these structures which must be targeted for elimination.

2.2.1. Near Wall Region

We shall start our discussion of the turbulent boundary layer structure with the pioneering work of Kline *et al.* (1967), where flow visualisation was primarily used to study the boundary layer structure. Such early studies had particular emphasis on the viscous sublayer – the region next to the wall extending to $y^+ = yu^*/\nu \approx 10$, which was previously assumed to be a region of laminar flow. Here, y is the wall normal distance, u^* is the friction velocity, and ν is the kinematic viscosity of the fluid. However, their flow visualisation clearly showed a structure in this region, shown in Fig. 2.2.1. The images showed hydrogen bubble markers to collect into longitudinal streaks of low speed (u-component) fluid which waver and oscillate within the viscous sublayer.

These ‘low-speed streaks’, formed by streamwise vorticity, occur from very close to the wall ($y^+ < 1$) to around $y^+ = 50$, and are a universal feature of turbulent boundary layers - occurring for a range of pressure gradients and Reynolds number. Although these low-speed streaks occurred at random positions and random times in the flow, the average spanwise steak spacing was $z^+ = zu^*/\nu \approx 100$; roughly 10 times the thickness of the viscous sublayer. They extended for a streamwise distance of up to $x^+ = xu^*/\nu \approx 1000$.

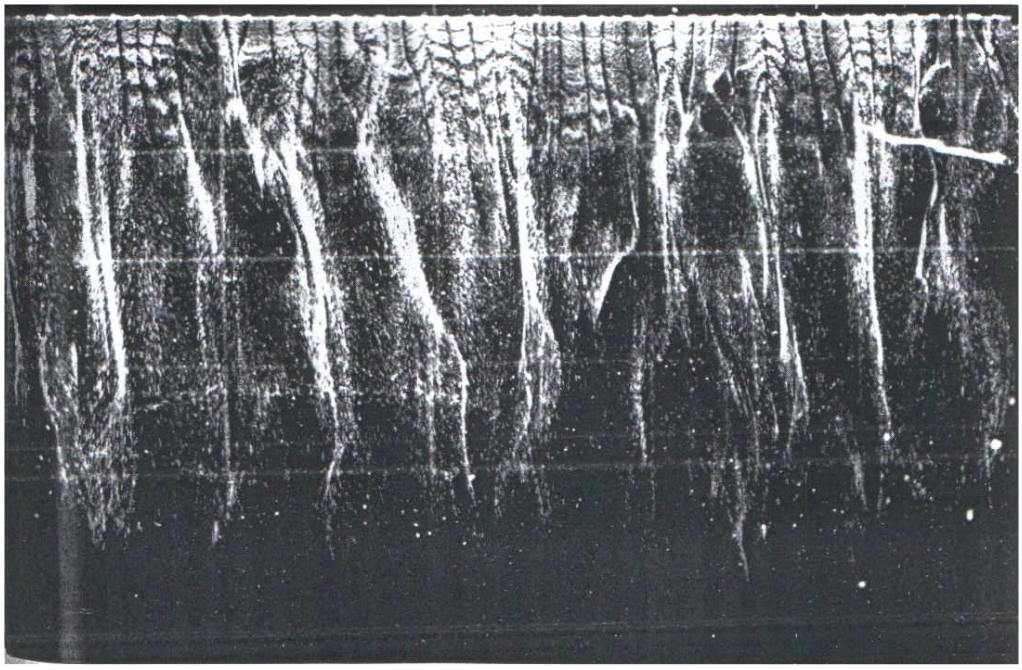

Figure 2.2.1. Photograph of structure of a flat plate turbulent boundary layer at $y^+ = 4.5$. Flow is from top to bottom and visualised by the hydrogen bubble technique. Note the collection of bubbles into streaks of low-speed fluid. From Kline *et al.* (1967).

Perhaps more importantly, Kline *et al.* (1967) observed that these 'low-speed streaks' slowly lifted from the surface and began to oscillate at around $y^+ \approx 8$-12. This oscillation amplified as it moved outward and at $10 < y^+ < 30$, 'ejected' low-speed fluid away from the wall and out into the faster flowing region of the boundary layer. Since turbulence kinetic energy in a turbulent boundary layer is continuously dissipated to heat through viscous action, a continuous supply of new turbulence must be given within the flow if the quasi-steady-state character is to be maintained. The source of the energy is the flow outside of the boundary layer, but little was known about the mechanism of energy transfer. Klebanoff (1954), had already shown that the majority of turbulence energy production occurs just outside of the viscous sublayer. The flow visualisation study of Kline *et al.* (1967), now gave a possible reason as to why this could be. This violent 'ejection' process seemed to play an important process of transferring momentum, energy and vorticity between inner and outer regions of the boundary layer. The authors propose a model of how the streaks are created and eject (Fig. 2.2.2) and state:

> *"... We view the formation of wall-layer streaks as the result of vortex stretching due to large fluctuations acting on the flow near a smooth wall in the presence of strong mean strain. We believe that the production of turbulence near the wall in such a flow arises primarily from a local, short-duration, intermittent dynamic instability of the instantaneous velocity profile near the wall. This instability acts not to alter the mean flow field but rather maintain it."*

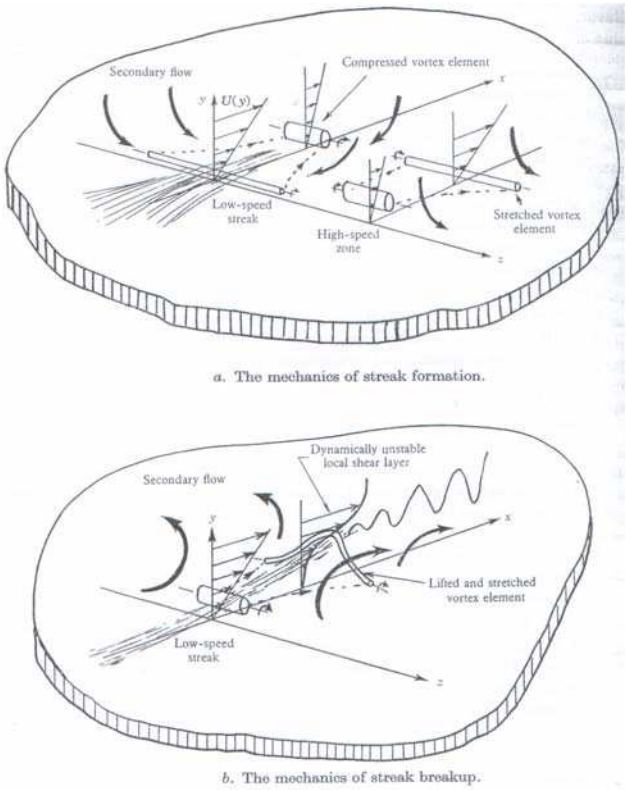

Figure 2.2.2. a) Proposed mechanism of low-speed streak creation from stretched/compressed vortex lines due to the inherent three-dimensionality of the outer boundary layer turbulence. b) Mechanism of streak lift up and ejection of low speed fluid into the outer regions of the boundary layer. From Kline *et al.* (1967).

Corino and Brodkey (1969) observed that the actual ejections were only a part of a 'chain of events', or 'bursting cycle', suggesting that it was this process that was the most important feature of the wall region and played a key role in the generation and maintenance of turbulence throughout the whole boundary layer. Kim *et al.* (1971), described the process. The first stage was the relatively slow lifting of a low-speed streak away from the wall. However, at some critical distance away from the wall, the streak appeared to rise much more quickly and 'low-speed-streak-lifting' occurred. During this process, low speed fluid was carried away from the wall with it and a local inflectional zone

occurred in the velocity profile. This then lead to the second stage, whereby a rapid growth of an oscillatory disturbance occurred just downstream of the inflexional zone. This oscillation terminated in a much more chaotic motion – 'breakup'; the third stage of the process. Following 'breakup', the low-speed streak returned to the wall, although the process was observed to spontaneously start again in due course. They observed that essentially all of the turbulence production occurred during this 'bursting process', or 'burst', in the zone $0 < y^+ < 100$.

Offen and Kline (1975) proposed that the 'bursting cycle' was a closed chain of events. They observed that a downwash of high momentum fluid, or 'sweep', acted to impress an adverse pressure gradient above a low-speed streak. This process would start the 'bursting cycle' by lifting the streak away from the wall, which was then followed by oscillation and 'ejection' of the low-momentum fluid away from the wall. However, following 'ejection', which ultimately destroys the streak, they observed an inrush of high-momentum fluid to be splashed against the wall to replace the ejected low-momentum fluid (i.e. another 'sweep' event), such that a 'sweep' event is actually the remainder of a previous 'ejection' event. This 'sweep' formed new low-speed streaks at the location between the old streaks, thus closing the chain of turbulence energy producing events.

Following advances in digital technology, the turbulent boundary layer began to be analysed with more and more sophisticated techniques, marking the start of the conditional sampling era (Robinson, 1991a). Wallace *et al.* (1972), classified the turbulent motions into four classes which contribute to the Reynolds stress, $-\rho\overline{uv}$, as shown in Table 2.2.1. Two of these types of

motion are associated with positive Reynolds stress producing events that were clearly observed in the flow visualisation studies described above. These are the movement of low-speed fluid away from the wall ('ejections', $u < 0$, $v > 0$; quadrant 2), and the movement of high speed fluid towards the wall ('sweeps', $u > 0$, $v < 0$; quadrant 4). The other motions give negative contributions of the Reynolds stress and are events involved with the deflection of low u-velocity regions back to the wall (wallward interaction, $u < 0$, $v < 0$; quadrant 3) and the reflection of high u-velocity sweeps away from the wall (outward interaction, $u > 0$, $v > 0$; quadrant 1). The numbering convention of each quadrant was defined by Lu and Willmarth (1973).

Using an X-wire, Wallace *et al.* (1972) were able to show that at $y^+ \approx 15$, the contribution to the Reynolds stress by sweeps and ejections were nearly equal, and each contribute around 70% of the total Reynolds stress (i.e. 140% total). The wallward and outward interaction made up a negative contribution of about 20% each, thus balancing the stress production. The sweep events contributed more to the Reynolds stress nearer the wall ($y^+ < 15$; $u > 0$, $v < 0$,

Sign of u	Sign of v	Sign of uv	Type of motion	Quadrant
−	+	−	Ejection	Q2
+	−	−	Sweep	Q4
+	+	+	Interaction (outward)	Q1
−	−	+	Interaction (wallward)	Q3

Table 2.2.1. The four classes of motion within the turbulent boundary layer which contribute to the Reynolds stress, $-\rho\overline{uv}$. From Wallace *et al.* (1972).

Q4), and further away from the wall the ejections dominated ($y^+ > 15$; $u < 0$, $v > 0$, Q2). It was also observed that the sweep and ejection motions correlate over a significantly longer time than the interaction motions, and the flow appeared laminar-like between the events, suggesting that the turbulent boundary layer does have a true 'structure' within it and there is little turbulence other than the events themselves.

Willmarth and Lu (1972) and Lu and Willmarth (1973), extended the *uv*-quadrant analysis to concentrate on only strong events by ignoring regions of small $\overline{uv}$. They also observed that the largest contributions to $\overline{uv}$ come from Q2 events (ejections, 77%), and the second largest contribution was from Q4 events (sweeps, 55%). These ratios were nearly constant across the entire boundary layer except very close to the wall ($y/\delta < 0.05$, δ is the boundary layer thickness) and near the boundary layer edge ($y/\delta > 0.7$). The frequency of which ejections and sweeps occur were found to be around the same, with $TU_\infty/\delta^* \approx 30$, where T is the time between events, U_∞ is the free-stream velocity and δ^* is the displacement thickness. The durations of ejections and sweeps, τ, were also observed to be about the same, with $\tau U_\infty/\delta^* \approx 0.5$.

Blackwelder and Kaplan (1976), were among the first people to use the conditional sampling technique of Variable-Interval Time Averaging (VITA), to look at the structure of sweep events (see Bruun 1995). The VITA technique ensemble-averages signals based on a whether a turbulent event of rapidly changing quantity (e.g. velocity) is detected, such as a sweep or ejection passing through a probe. Using rakes of hotwires oriented in the wall-normal direction, Blackwelder and Kaplan (1976), were able to track a typical sweep event. The velocity profile during the sweep is plotted together with the

mean velocity profile in Fig. 2.2.3a. They observed that before the sweep was detected (-3.1ms < τ < 0ms, τ = 0 corresponds to the time of detection) there was an inflectional velocity profile, as also observed by Kline *et al.* (1967). After detection they observed a region of high speed fluid moving from the outer region and splashing onto the wall. Note also that after the burst has passed the instantaneous velocity profile was nearly identical to the time averaged profile (τ > 30ms). Figure 2.2.3b shows the magnitude of the burst event throughout the boundary layer. Blackwelder and Kaplan (1976), observed that the signals were highly correlated in the wall normal direction, which suggested that the events affect a large region of the boundary layer. Their data also showed that the structures were skewed at an angle of around 20-30° to the streamwise direction.

In summary, the near wall region of a turbulent boundary layer is organized into streaks of low speed fluid, which are persistent and relatively quiescent for most of the time. The majority of the turbulent production in the entire boundary layer occurs in the buffer layer during violent, intermittent 'ejections' of low-speed fluid away from the wall and during inrushes of high-speed fluid towards the wall ('sweeps'). This 'bursting cycle' is quasi-cyclic and self-generating. The recent Direct Numerical Simulation (DNS) study of Orlandi and Jimenez (1994) showed that it is the transport of high momentum fluid towards the wall ('sweeps') that is responsible for the high skin-friction in the turbulent boundary layer.

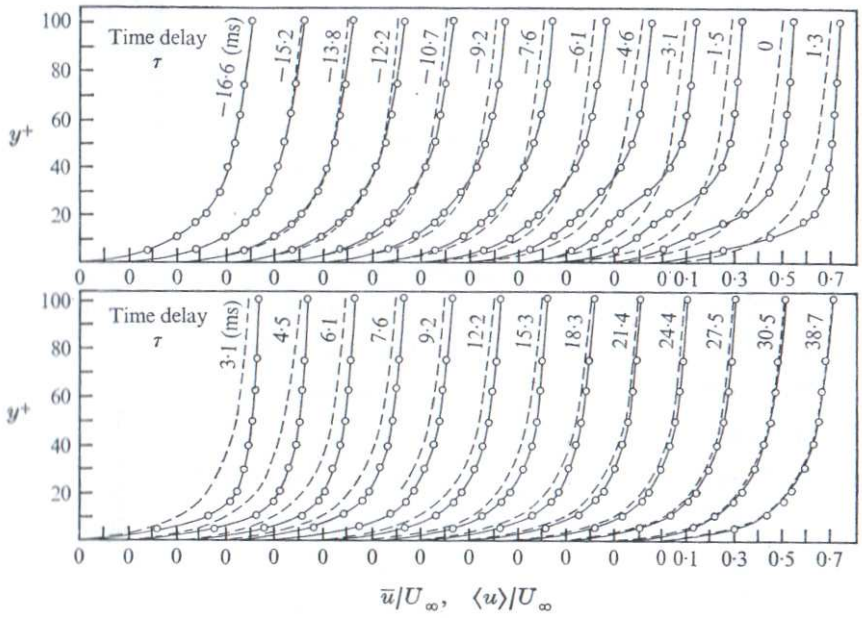

a)

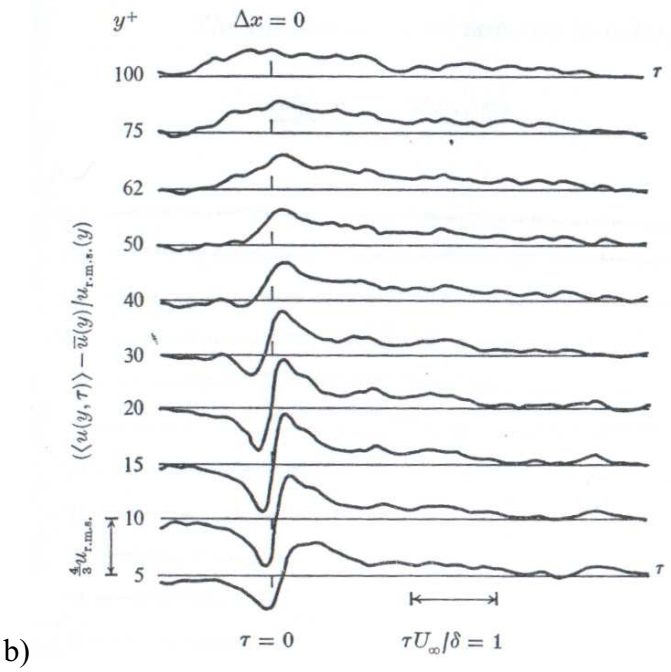

b)

Figure 2.2.3. a) Conditionally averaged 'burst' event and mean velocity profiles at various time delays, τ, relative to the point of detection ($\tau = 0$). b). Conditionally averaged hotwire signal at several wall normal locations. From Blackwelder and Kaplan (1976).

2.2.2. Outer Region

The outer region of the turbulent boundary layer is usually defined as the region $y/\delta > 0.15$, whereby the action of viscosity becomes less and less dominant (Panton, 2001). This region is not smooth, like the time averaged boundary layer profile, but consists of three-dimensional bulges that are of the same scale as the boundary layer thickness in both x and z. Deep irrotational valleys occur on the edges of these bulges, through which free-stream velocity is entrained into the turbulent region.

The outer layer exhibits a sharp interface between the turbulent interior and the non-turbulent exterior (Corrsin 1943, Corrsin and Kistler 1954). Conditional sampling techniques have been employed to study the intermittency and structure of the outer layer (Favre *et al*. 1965, and Kovasznay *et al*., 1970), which showed that these bulges are elongated in the streamwise direction. Flow visualisation studies by Falco (1977) showed 'typical eddies' or 'Falco eddies' on the upstream sides of the turbulent bulges, which moved towards the wall and are possibly responsible for the 'sweep' type motions near the wall (Fig. 2.2.4).

The debate is still open as to how the inner region interacts with the outer region and *vice versa*. There is, however, evidence of direct mass transfer through 'ejections' emanating from the wall (see Sec. 2.2.1). Also, indirect interactions occur through the growth of vortical structures from the wall to the outer regions. The effect of the outer boundary layer on the inner turbulent production process is not well understood. Panton (2001) stated that as the large outer flow eddy structure move along the wall, they impose pressure fluctuations on the inner region, hence influencing the near wall events.

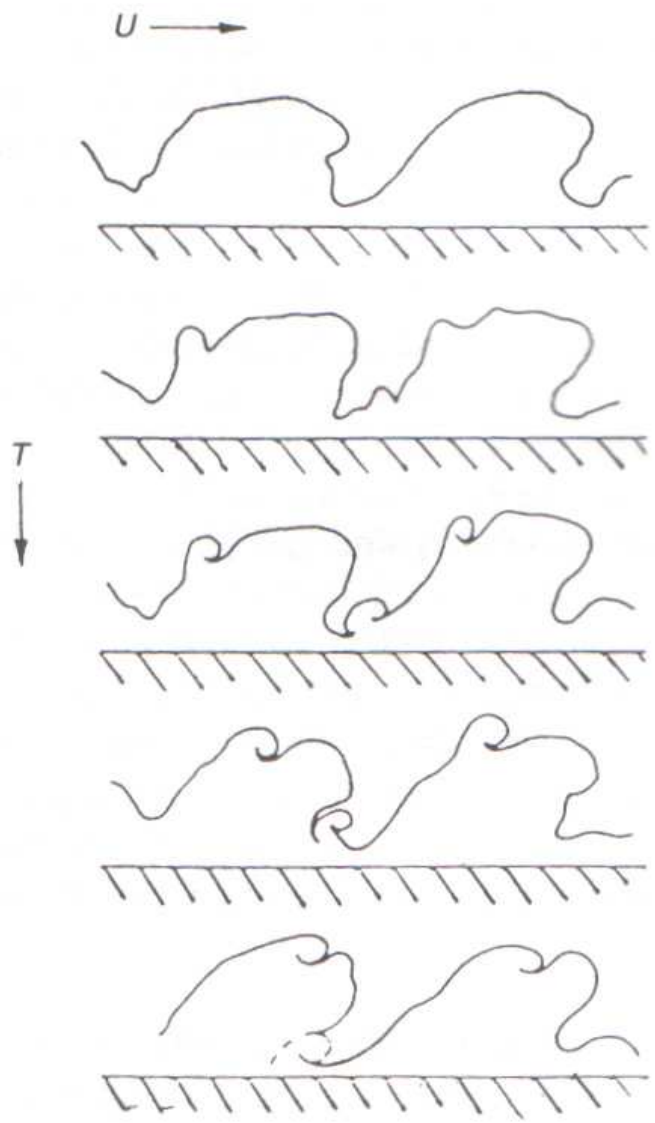

Figure 2.2.4. The outer boundary layer structure showing a sharp interface between rotational turbulent flow within the boundary layer and irrotational free-stream flow. 'Typical (Falco) eddies' are formed on the back interfaces of the turbulent bulges. From Falco (1977).

2.2.3. Hairpin Vortices

The previous sections have shown that the turbulent boundary layer consists of a number of different types of coherent motions. Kline and Robinson (1989a and 1989b), attempted to organise coherent motions into classes. They tentatively proposed the following hierarchy of importance with respect to the creation of turbulent Reynolds stress and turbulent kinetic energy.

Most important and most active;

- Vortices – Vortex elements and vortical structures

Play an important role;

- Ejections of low-speed fluid away from the wall
- Sweeps of high-speed fluid towards the wall
- Strong near wall shear layers

Plays some role;

- Large δ-scale bulges in the outer region of the boundary layer
- Shear-layer "backs" of large-scale outer-region motions
- Near-wall "pockets", visible in the laboratory as regions swept clear of marked near-wall fluid
- Low-speed streaks in the viscous sublayer.

Of the most important are vortical structures. It should be noted that any vortex element, except those located in the wall normal direction, has the potential to "pump" fluid away and towards the wall across the mean velocity gradient. It should therefore be of little surprise that vortex motions are so important in the production of turbulence kinetic energy.

In the early studies of the near wall structure and turbulence generation cycle, there was evidence to suggest that bursts and ejections may be part of structures that span the whole boundary layer region (Willmarth and Lu, 1972, and Lu and Willmarth, 1973, Blackwelder and Kaplan, 1976). Kovasznay (1970), postulated that there are a whole series of burst events of differing scales, whereby frequent small-scale bursts occur near the wall which grow or coalesce into large ones. This process was suggested to continue until the largest scale bursts reach the outer edge of the boundary layer, and are thus responsible for the 'bulges' (see Sherman (1990)). The existence of a dominant vortex structure throughout the whole boundary layer has received much attention over the years and investigations have been conducted into its form and regeneration mechanism.

Theodorsen (1952), proposed that turbulence is characterised by a definite three-dimensional flow pattern, and the motions it induces are responsible for the transfer of momentum and heat. Such structures were shown to be horseshoe or ring shaped in appearance, as depicted in Fig. 2.2.5, and were thought to cause almost all the dissipation in the turbulent boundary layer. This large-scale structure was proposed to be similar everywhere in wall-bounded turbulent flow and to have a different scale at different wall-normal distances.

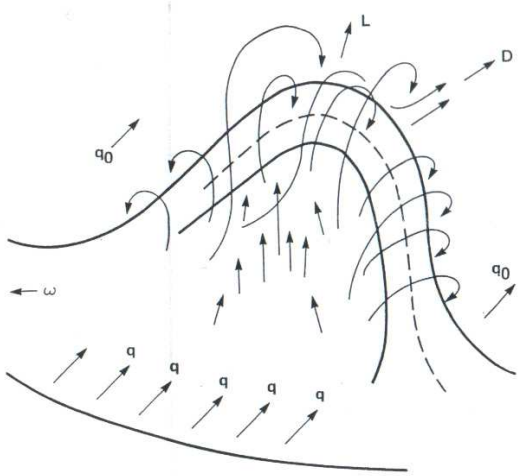

Figure 2.2.5. Primary structure of wall-bound turbulence. From Theodorsen (1952).

Head and Bandyopadhyay (1981), were among the first to observe these hairpin structures in experiment and confirmed that nearly the entire boundary layer consisted of hairpin vortices, or stretched hairpin loops. It was certainly a surprise to them to see that something as complicated as the turbulent boundary layer had only one kind of dominant motion repeated over a range of scales. Using smoke flow visualisation and a laser sheet inclined to the wall, they were able to observe that the hairpin loops were straight over a large proportion of their length and were inclined, on average, at an angle of 45° to the wall into the flow. More recently using Particle Image Velocimetry (PIV), Liu *et al.* (1991) observed shear layers growing from the wall at 45° that ended with a region of spanwise vorticity - the heads of the hairpins. The cross-stream dimensions of the loops appeared to scale with the wall variables, u^* and ν. However, the length of the hairpins appeared to be limited only by the boundary layer thickness, δ. Thus the aspect ratio increased with the Reynolds number, as depicted in Fig. 2.2.6.

Robinson (1991a and 1991b), divided the hairpin structures into three parts; legs, neck and head as shown in Fig. 2.2.7. He emphasised that these are not necessarily symmetrical structures. In fact they are more common as asymmetric structures which are shaped like canes (also Moin and Kim, 1985). Robinson also suggested a link between the quasi-streamwise vortices and hairpin vortices (Fig. 2.2.8). Could it be that the counter-rotating legs of the hairpin vortices are actually responsible for the low speed streaks by the uplift of fluid between the legs? The topic is still subject to debate.

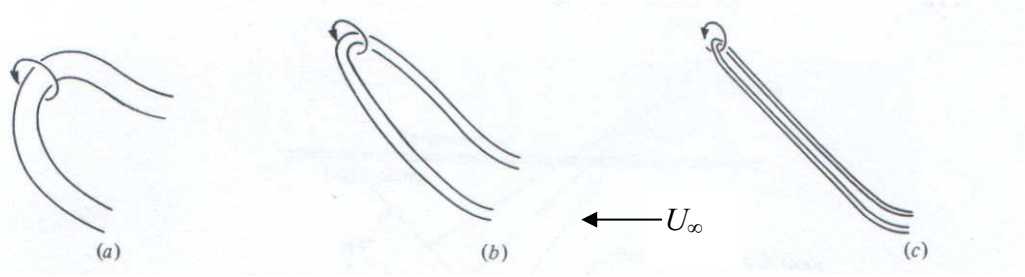

Figure 2.2.6. Effect of Reynolds number on hairpin structures in the outer boundary layer. a) Very low Re. b) Moderate Re. c) High Re. From Head and Bandyopadhyay (1981).

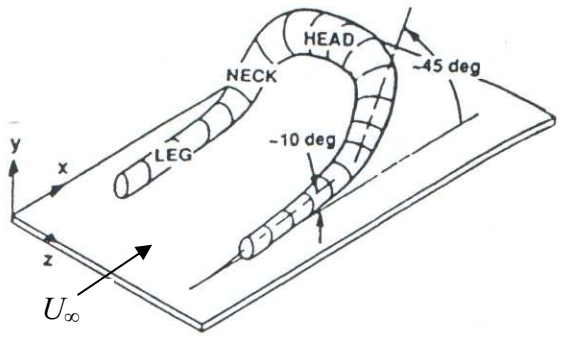

Figure 2.2.7. Parts of a horseshoe vortex as defined by Robinson (1991b).

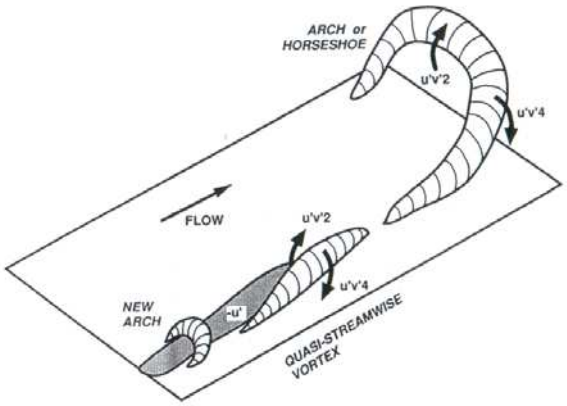

Figure 2.2.8. Conceptual model of relationships between ejection/sweep and quasi-streamwise vortices in the near wall, and relationship between ejection/sweep and arch-shaped vortices in the outer region. From Robinson (1991b).

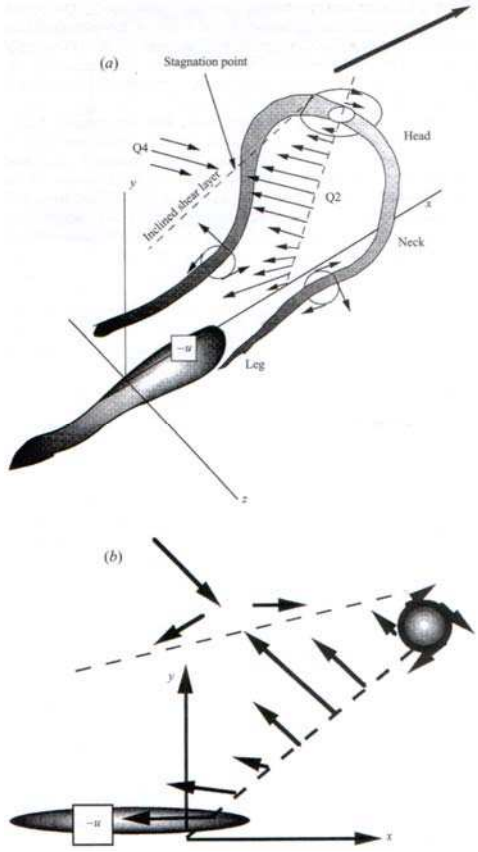

Figure 2.2.9. a) Schematic of a single hairpin vortex with the corresponding Q2 pumping in the neck region and the formation of a low-speed-streak between the legs. b) Signature of a hairpin in the *x*-*y* plane. From Adrian *et al.* (2000).

The characteristics of hairpins and their appearance in the *x-y* plane are presented in Fig. 2.2.9 according to Adrian *et al.*, (2000). The vortex head was said to have a Q2 event (ejection) located beneath it and at around 45° to the wall, associated with the induced motion pumping fluid away from the wall due to the vortex neck. The legs of the vortex become quasi-streamwise near the wall with counter-rotation such that near-wall fluid between the legs is lifted away from the wall. There is also a stagnation zone marking the shear layer caused by the interaction of the Q2 event (ejection) with a Q4 event (sweep) above the structure. Using PIV, Adrian *et al.* (2000) observed that the hairpin structures were the single most readily observable flow pattern in a turbulent boundary layer from $y^+ \approx 50$ right to the boundary layer edge. The angle that the neck and head make with the wall was observed to be a strong position of height, with the hairpins near the wall typically at 25-45° to it, and close to the boundary layer edge they are nearly vertical.

Head and Bandyopadhyay (1981), observed hairpin vortices to agglomerate into regular packets. Adrian *et al.* (2000), used PIV to show that these 'packets' often occur with more than 10 individual hairpins, all moving with a similar convection velocity so that they may be as long as 2δ in the streamwise direction. In fact, they observed at least one hairpin vortex packet in 85% of their PIV images. It also appeared that many hairpin packets, each with their own convection velocity, seemed to coexist within other packets of different size and convection velocity. There appeared to be small, young packets lying close to the wall which exist within larger, older packets as depicted in Fig. 2.2.10.

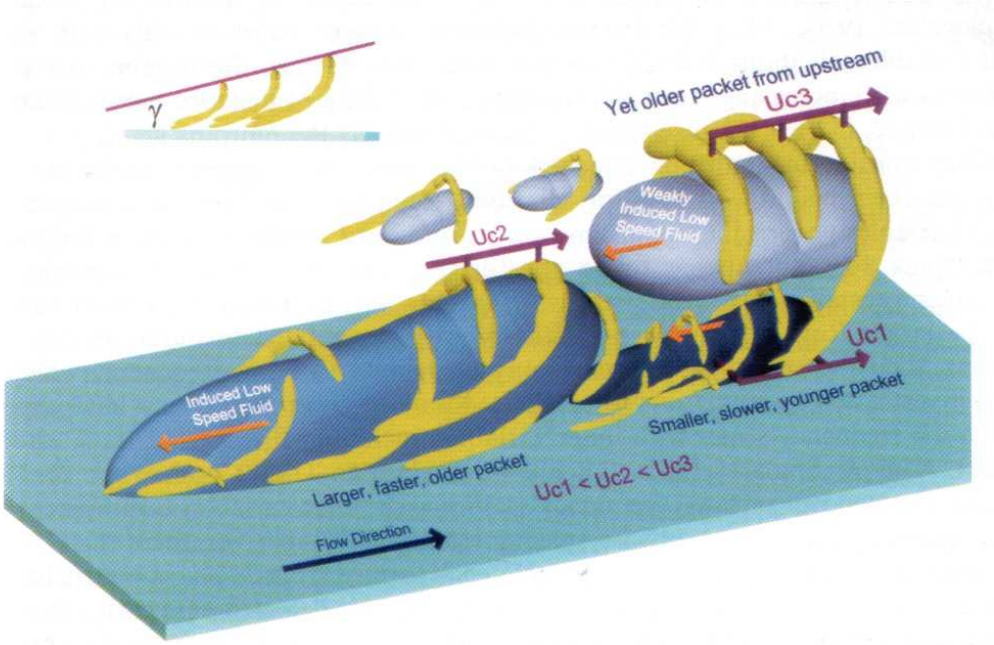

Figure 2.2.10. Conceptual scenario of nested packets of hairpins or cane-type vortices growing up from the wall. These packets align in the streamwise direction and coherently add together to create large zones of nearly uniform streamwise momentum. Large-scale motions in the wake region ultimately limit their growth. Smaller packets move more slowly because they induce faster upstream propagation. Caption and Figure from Adrian *et al.* (2000).

The concept of hairpin ‘packets’ can account for much of the observed behaviour in a turbulent boundary layer. A single hairpin characteristically extends for a streamwise distance of $x^+ = 100$ (Zhou *et al*. 1999), but low-speed-streaks often extend to $x^+ = 1000$ (Kline *et al.* 1967). The occurrence of many sets of Q2 pumping from packets of hairpins would certainly enable low speed streaks to reach this length. The presence of many hairpins in a packet may also account for the meandering streaks since the hairpins will inherently have some spanwise variation in their individual locations. They also explain the multiple ejections observed by many authors, for example Corino and Brodkey (1969), whereby the passage of each individual hairpin in a packet produces its own Q2 event. The hairpin packet concept can also explain the oscillation observed before breakup in a ‘burst’ sequence. The oscillation may not be a temporal oscillation but a spatial oscillation caused by a series of Q2 events produced by each hairpin in the packet as it moves along the wall.

2.2.4. Turbulence Regeneration Cycle

The turbulent boundary layer is a self-sustaining phenomenon, such that new turbulence is constantly being created to counteract that dissipated as heat through viscous action. Many conceptual models have been produced to describe how the turbulence regenerates itself, based on the sweep-ejection cycle discussed in Sec. 2.2.1. These models can be categorised into parent-offspring or instability based mechanisms (Schoppa and Hussain 2002). Here, we shall focus only on selected parent-offspring mechanisms for brevity.

Zhou *et al.* (1999), used DNS to study the development of a hairpin vortex and observed that a single hairpin does indeed have the ability to develop into a 'hairpin packet' provided it is sufficiently strong, as illustrated in Fig. 2.2.11. Thus, a hairpin vortex can naturally form a coherent packet, tent-like in appearance, with several hairpins upstream and downstream of the original hairpin. These self-sustaining properties make the hairpin vortex a fundamental flow structure in the turbulent boundary layer.

Choi (1989, 2001) presents a slightly different conceptual model to describe the self-generating turbulence events in the sweep-ejection cycle, as illustrated in Fig. 2.2.12. In the first stage of the model, a spanwise vortex filament is deformed by a near-wall burst event upstream of it. This causes the vortex to deform in the downstream direction, which is deformed further by the vortex filaments own self induction mechanism and due to the high shear near the wall (Stage 2). As the development proceeds further, hairpin vortices are created, and move away from the wall as an ejection motion. However, as neighbouring hairpin vortices 'eject', their legs come in close proximity and form a counter rotating pair with action so as to induce another sweep event,

which leads to high skin friction and provides the perturbation to the next (upstream) vortex filament. Thus the chain of turbulence producing events is complete and the sweep leads to an ejection which leads to a sweep and so on.

More recently, Kim (2005), gives a summary of the self sustaining turbulence process in the turbulent boundary layer, as depicted in Fig. 2.2.13. He emphasises that a common feature of drag reducing flows, regardless of how drag was reduced, is near-wall streamwise vortices with reduced strength and increased spacing, thus indicating their importance in the turbulence generation process.

There is still much to learn about the turbulent boundary layer and the nature of turbulence itself. Although hairpin vortices seem dominant, there are many other vortex motions within the boundary layer which may also play key roles in the production of turbulence. With the rapid advancement in computational facilities and memory storage, DNS studies are becoming more and more complex and higher Reynolds number flows are now able to be solved (for example at $Re_\tau = 590$ by Moser *et al*. 1999). It remains to be seen whether we will ever fully understand the turbulent boundary layer and if and how the low-Reynolds number observations described above will translate to flight conditions (Andreopoulos *et al.* 1984).

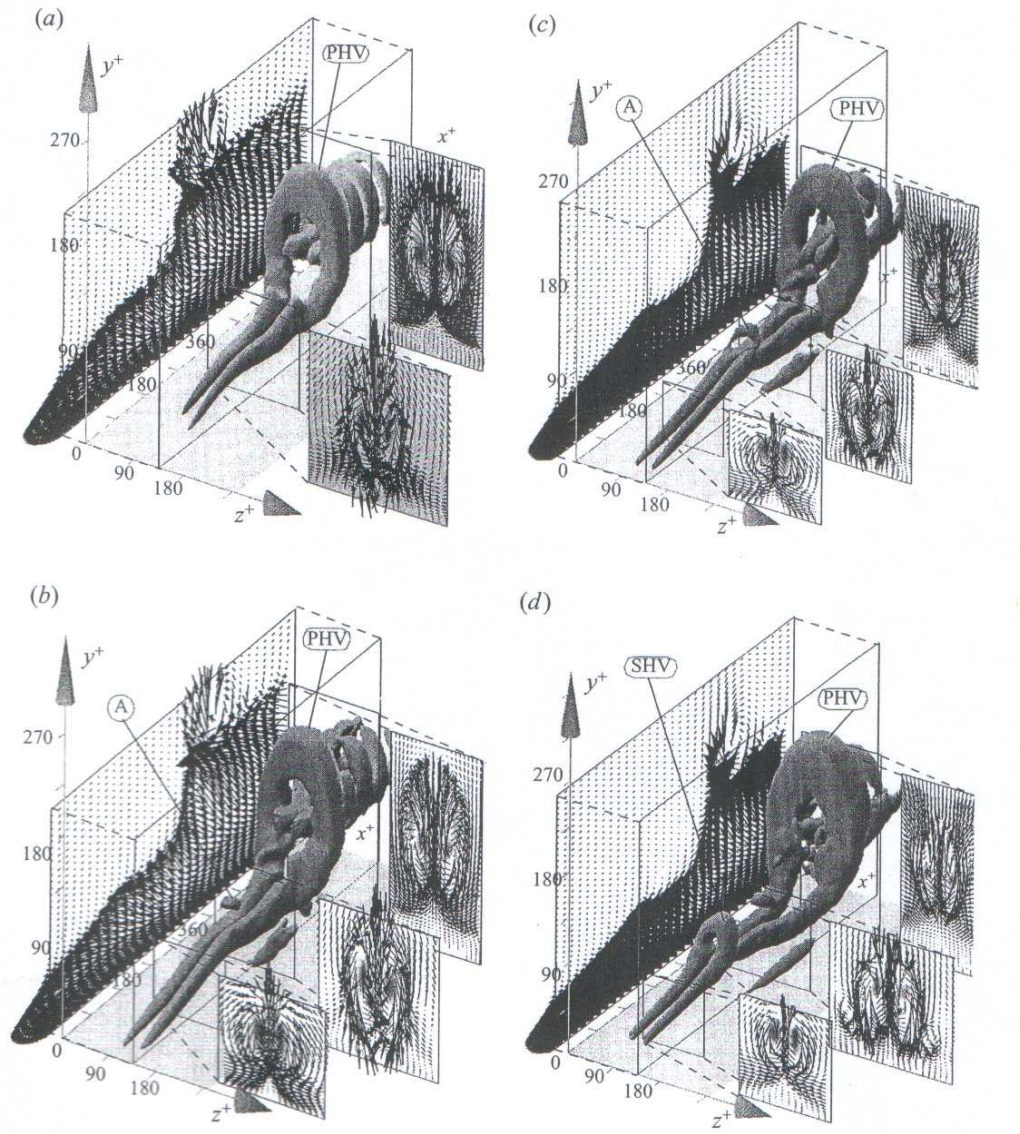

Figure 2.2.11. The generation of a secondary hairpin vortex, SHV, upstream of the Ω-shaped head of the primary hairpin vortex, PHV. Secondary vortex initiates from location marked A in b) and c). Also note formation of a downstream hairpin vortex, starting from streamwise vortices ahead of the head of the PHV. a) $t^+ = 63$, b) $t^+ = 72$, c) $t^+ = 81$, d) $t^+ = 117$. From Zhou *et al.* (1999).

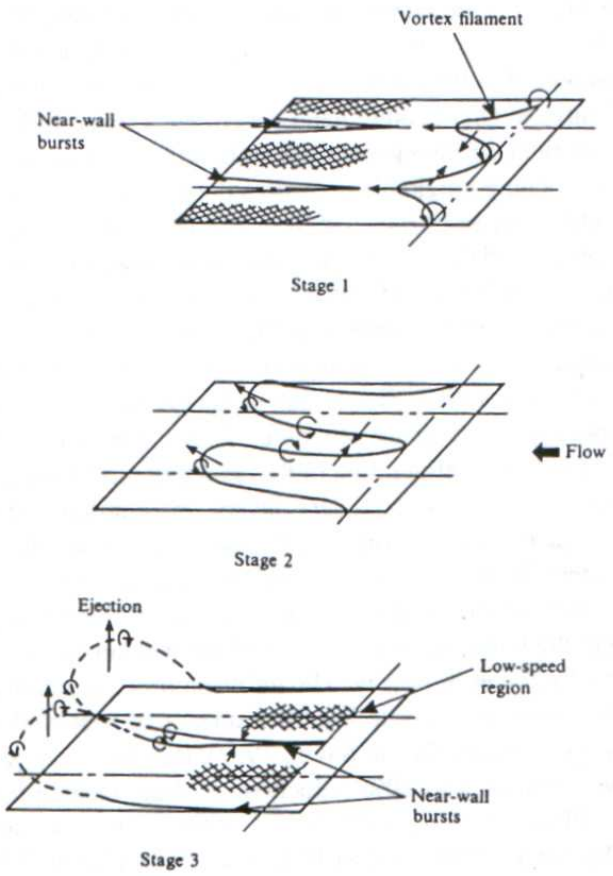

Figure 2.2.12. Conceptual model for the sequence of burst events from Choi (1989, 2001).

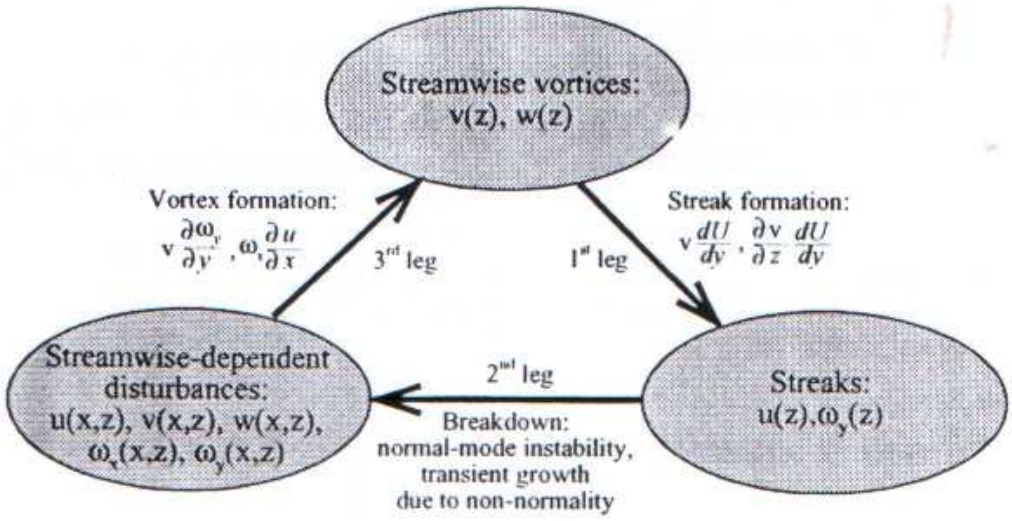

Figure 2.2.13. Schematic illustration of a self-sustaining process of near-wall turbulence structures. From Kim (2005).

2.3. Skin-Friction Drag Reduction

Through better understanding of the turbulent boundary layer, many strategies have been formulated to reduce skin-friction drag. The general approach is to provide some perturbation that will alter the sweep-ejection process described in Sec. 2.2. This has the aim of reducing the strength of the 'sweep' events, which are responsible for the majority of the skin-friction drag (Orlandi and Jiménez, 1994). The exact strategy and mechanism differs somewhat between techniques and there is much debate over the precise mechanism for a given technique. In this section we shall briefly review a few successful approaches of reducing skin-friction drag and move on to a detailed discussion of drag reduction by creating a spanwise oscillation at the wall. Overviews of drag reduction, including techniques for reducing pressure drag (i.e. streamlining) and postponing transition, can be found in Gad-el-Hak (2000), and Sellin and Moses (1989).

2.3.1. Overview

One of the most successful techniques of achieving skin-friction drag reduction is polymer or surfactant addition. These techniques involve adding tiny quantities of long chain polymers, or string-like surfactants, to liquids. Drag reductions of 70% have been achieved, which enables an increased flow rate or decreased pressure drop in turbulent pipe flow (Berman, 1978). In fact, polymer additives are used today in the Trans-Alaskan-Pipeline. The exact drag reduction mechanism has been discussed by Virk (1975), whereby the long chain-like molecules are believed to interfere with the turbulent bursting process by molecular extension. The additives appear to kill turbulence near

the wall, such that the laminar sublayer becomes thicker and the peak in turbulence intensity moves to higher y^+.

Another successful technique, riblets, has been used on the hull of the *Stars and Stripes*, which won the Americas cup yacht race in 1987. Riblets are passive devices which consist of longitudinal grooves placed on the wall with depth, h, and spacing, s, of around the same order as the thickness as the viscous sublayer (h^+ and $s^+ \approx 15$ is optimal, Choi, 2001). Research on riblets began in the late 1970s by Walsh (see Walsh 1990). Many profiles of riblets have been studied and it is V-shaped grooves that are the most practical to manufacture. The concept seems to have been inspired by the skin of fast swimming sharks, which have rough dermal denticals with ridges that align with the flow direction. Drag reductions of around 8% have been observed using riblets, although their alignment must be within 30° of the mean flow direction in order to observe an effect. Choi (1987), deduced that the riblets act as small fences to restrict the movement of vortices near the wall. This weakens the induction velocity between adjacent quasi-streamwise vortices. Consequently, the near-wall bursts take place prematurely but at higher frequency which leads to a reduction in skin friction and turbulent intensity. The viscous sublayer also becomes thicker.

Another idea that has come from nature is the use of compliant coatings, which was inspired by dolphin's skin (Kramer, 1961). Compliant coatings are deformable substances applied over a rigid wall. If the material properties are chosen such that the surface deformation is small and the material natural frequency, f_o, is of the order of the average period between sweep events ($50 < 1/f_o^+ < 150$), then drag reductions of around 10% can be achieved (Choi *et al.*,

1997). The surface movement of the compliant coating due to near wall turbulent structures are believed to be such that act to damp and weaken the strength of the upwash during ejections. The burst frequency and intensity is also reduced and the viscous sublayer is observed to thicken.

One of the more recent and exciting developments is the use of Micro-Electro-Mechanical-Systems (MEMS) technology for active turbulence control. This enables micron-sized sensors, actuators and electronics to be fabricated on a common substrate using conventional integrated circuit-board manufacturing techniques. Manufacture is becoming increasingly inexpensive due to the recent explosion in computer technology. Such 'smart skin technology' for boundary layer drag reduction is still a long way off for practical use (see Warsop, 2004), but the concept has recently received much attention. For example, Rathnasingham and Breuer (2003) demonstrated the 'smart skin' concept using an array of three, millimetre-scale, wall-mounted shear stress detectors, with three wall-based actuators placed downstream. The actuators were designed to induce a 'synthetic' streak which acts to counteract the near wall streaks. A linear active control scheme was applied to trigger the actuators once a large scale turbulent motion is detected. Streamwise velocity fluctuations were reduced by up to 30% and a drag reduction of 7% was achieved.

Other techniques for turbulent drag reduction include micro-bubbles (Merkle and Deutsch, 1989), Large-Eddy-Break-Up devices (LEBUs) (Badyopadhyay, 1986), and blowing / suction control (Antonia *et al*., 1995). The above list is by no means exhaustive and more strategies are formulated every year. One

thing is for sure is that as our understanding of the turbulent boundary layer grows, we shall endeavour to find more ways to control it.

2.3.2. Spanwise Wall Oscillation

The idea of inducing a spanwise perturbation into a turbulent boundary layer stems from the observation that skin-friction and turbulence production is suppressed in a 3D boundary layer when subjected to a sudden spanwise pressure gradient, for example on a swept wing (Bradshaw and Pontikos, 1985). It appears that the spanwise pressure gradient induced in this configuration imposes a fundamental modification to the flow structures responsible for the bursting process. However, as the flow travels downstream it will eventually return to its originally state.

It was first discovered by Jung *et al.* (1992), that this drag reduction can be maintained indefinitely by applying an oscillatory spanwise motion. DNS was used in a planar channel with fully developed turbulent flow before the start of spanwise forcing ($Re_\tau = hu^*/\nu = 200$, where h is the channel half height). An oscillatory spanwise motion was induced by either superimposing a spanwise crossflow with specified flow rate (equivalent to a spanwise pressure gradient), or by inducing a prescribed velocity at the wall. They observed sustained drag reduction for oscillation periods of $25 \leq T^+ \leq 200$, with a maximum drag reduction of 40% at the optimal oscillation period $T^+ = 100$ and spanwise flow rate (per unit width) equal to $0.8Q_x\sin\omega t$. Here, Q_x is the unperturbed flow rate in the streamwise direction (per unit width) and $T^+ = Tu^{*2}/\nu$, where T is the oscillation period and u^* is the friction velocity of the unperturbed flow. Very similar results were observed when the wall was oscillated with velocity $W_0 = 0.8(Q_x/2h)\sin\omega t$. The level of drag reduction

with time is shown in Figure 2.3.1, where at optimal conditions the maximum level of drag reduction is achieved after only five oscillation periods. The oscillations caused a 40% reduction in the Reynolds shear stress, $-\rho\overline{uv}$, with no significant increase in $-\rho\overline{vw}$. Turbulence intensities dropped significantly (*u'*, *v'* and *w'* by 14%, 30% and 35%, respectively) and the peak in each quantity shifted away from the wall. The DNS study also showed that the wall oscillation causes a decrease in the number and intensity of turbulence structures, as can be seen in the iso-contour plot of vorticity magnitude in Figure 2.3.2.

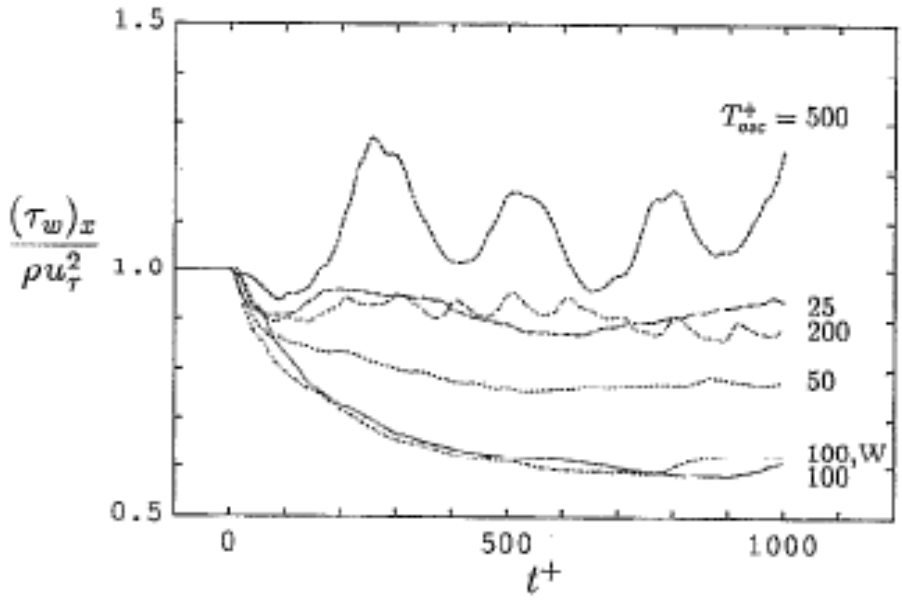

Figure 2.3.1. Time evolution of the streamwise wall shear stress after the start of oscillation at various frequencies. W denotes wall oscillation, all others from imposed spanwise flow. From Jung *et al.* (1992).

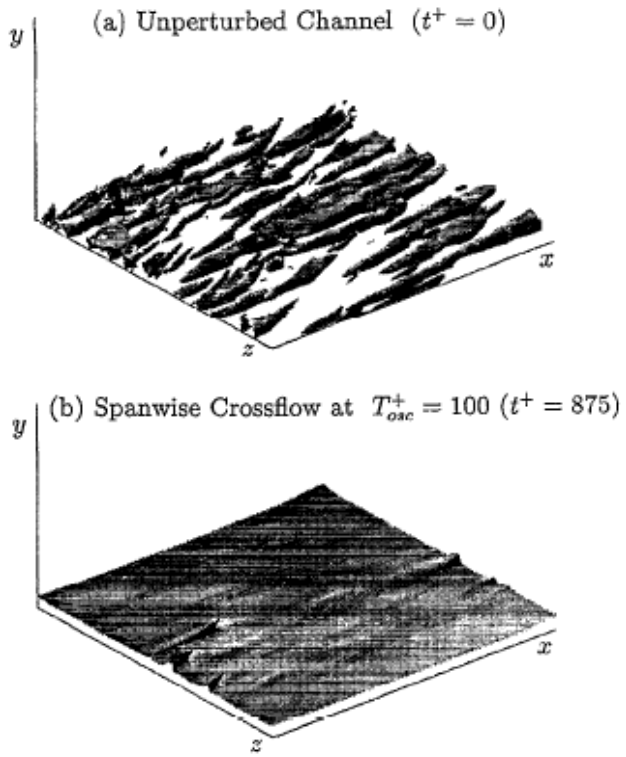

Figure 2.3.2. Turbulence structure in the unperturbed channel compared to a channel with cross-flow oscillations at $T^+ = 100$. The turbulence structures are represented by contour surfaces of constant vorticity magnitude; $|\omega| = 1.1u^{*2}/\nu$. From Jung *et al.* (1992).

The DNS results of Jung *et al.* (1992) were soon confirmed experimentally by Laadhari *et al*. (1994) in a fully developed turbulent boundary layer over a flat plate ($Re_\tau = \delta u^*/\nu \approx 440$). A moving plate was installed in part of the wall which was oscillated sinusoidally with amplitude, $\Delta z^+ = 160$, oscillation period, $T^+ = 100$, and wall speed, $W_0 = 0.45U_\infty \sin \omega t$. The results showed that the mean streamwise velocity, U, was reduced for $y^+ < 30$, and a reduction in dU/dy occurred for $y^+ < 8$. This suggested that there was a skin-friction drag reduction although the exact amount was not quoted. Contrary to Jung *et al*. (1992), they observe that the relative reductions in u' (45%) and $-\overline{uv}$ (50%) to be larger than in v' (34%) and w' (16%). The turbulence statistics are shown

in Figure 2.3.3, whereby all turbulent intensities are observed to be considerably reduced for $y^+ < 200$. Laadhari *et al*. (1994) suggest that the reason for the drag reduction was because the quasi-streamwise vortices near the wall become displaced relative to the low and high speed streaks by the wall oscillation. This caused the quasi-streamwise vortices near the wall to pump high speed fluid into low speed streaks and low speed fluid into high speed ones, instead of the other way round. Thus, the intensity of the streaks was weakened and the sweep-ejection cycle was disrupted, which lead to the reduction in drag.

The global energy balance of spanwise wall oscillation was studied in a DNS experiment by Baron and Quadrio (1996), where a non-zero transverse velocity was imposing at the wall at the same Reynolds number as Jung *et al*. (1992). The power saved was defined as $(-dp/dx|_c + dp/dx|_m)U_{bulk}$, where dp/dx is the streamwise pressure gradient, U_{bulk} is the bulk mean velocity, and the subscripts c and m indicate canonical and manipulated respectively. The power saved is compared to the power spent, defined as $\int \tau_{wz}.w_{wall}$, where τ_{wz} is the spanwise shear stress, and w_{wall} is the spanwise wall velocity. For a fixed oscillation frequency of $T^+ = 100$, the skin friction was reduced by 40% for amplitudes larger than $0.75Q_x/2h$, consistent with the study of Jung *et al*. (1992). However, a net energy saving was only found for low amplitude oscillations ($< 0.5Q_x/2h$), with a net energy saving of around 10%, as illustrated in Fig. 2.3.4.

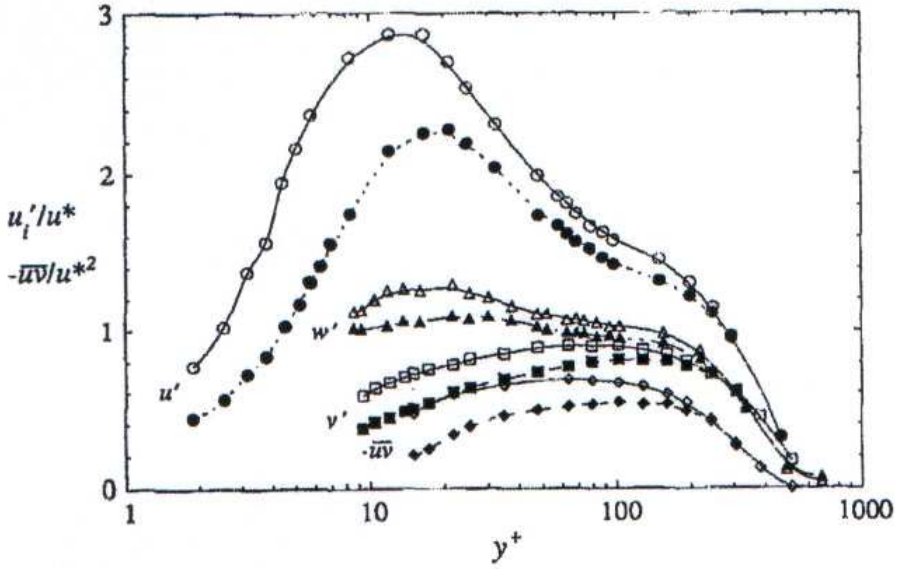

Figure 2.3.3. RMS profiles of the three fluctuating velocity components and Reynolds stress for spanwise wall oscillation with $T^+ = 100$, $\Delta z^+ = 160$ (closed symbols), compared to unperturbed boundary layer (open symbols). From Laadhari *et al*. (1994).

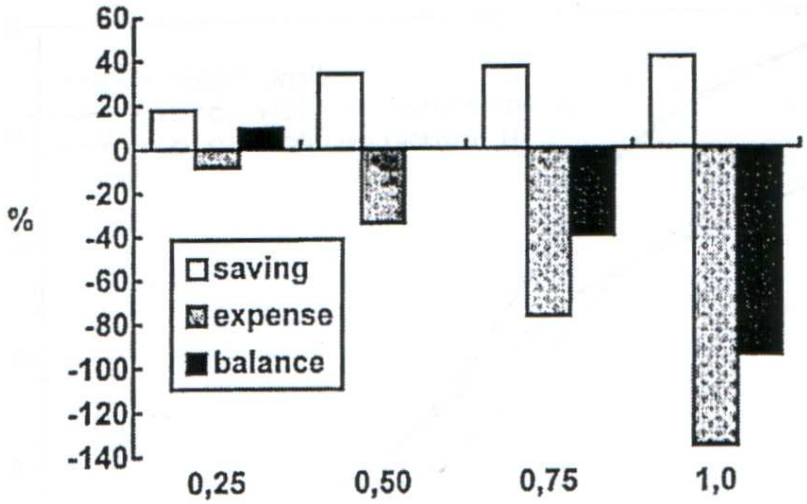

Figure 2.3.4. Energy balance using spanwise wall oscillation at different oscillation amplitudes, $T^+ = 100$. Friction power saved in white ($(-dp/dx|_c + dp/dx|_m)U_{bulk}$). Power spent on oscillating wall shown in grey ($\int \tau_{wz}.w_{wall}\, dS$). Net power saved shown in black. From Baron and Quadrio (1996).

There have been numerous studies conducted at the University of Nottingham using spanwise wall oscillation by Choi (Choi *et al.*, 1998, Choi and Graham, 1998, Choi and Clayton, 2001, Choi, 2002, 2005, Karniadakis and Choi, 2003). It is these experiments that are the inspiration and knowledge base for this thesis.

Choi *et al.* (1998), used hot-wire anemometry and flow visualisation in an experimental investigation of wall oscillation in a low speed wind tunnel (δ = 60mm, $R_\theta = 1.2\text{x}10^3$, U_∞ = 2.5m/s). The boundary layer was tripped at the test section inlet such that a fully developed boundary layer was present. A 500mm long oscillating plate was located 2m downstream of the trip and set flush with the surrounding surface. A crankshaft mechanism was then used to oscillate the plate sinusoidally at various amplitudes and frequencies.

Using hotwire measurements 10mm downstream of the oscillating plate ($x^+ \approx$ 70), Choi *et al.* (1998), showed that the spanwise oscillation reduced the mean-velocity gradient in the near wall region, thus indicating a reduction in shear stress, $\tau_w = \mu du/dy|_{wall}$,. This is clearly illustrated in the outer scaled near wall velocity profiles of Fig. 2.3.5a. The inner scaled near wall velocity profile in Fig. 2.3.5b, shows that the viscous sublayer becomes thicker and for some oscillation parameters extends beyond $y^+ = 10$. The streamwise turbulence intensity was observed to be reduced in the inner region ($y^+ \leq 100$), and the skewness and kurtosis were increased. However, the turbulence statistics remained unaltered in the outer regions, suggesting that the spanwise oscillation effect is only 'felt' in the near wall region. The maximum level of drag reduction was reached after only 5 boundary layer thicknesses from the leading edge of the oscillating plate, as shown in Fig. 2.3.6. This seems to

plateau towards the end of the plate before returning slowly to canonical levels some distance downstream.

Choi *et al*. (1998), also showed that the level of skin-friction reduction is a function of oscillation frequency, f, and the amplitude of the oscillation, Δz, as depicted in Fig. 2.3.7. It was therefore suggested that the level of drag reduction is actually a function of wall speed. A good collapse of the data occurred when plotting the level of drag reduction with the non-dimensional wall speed $W^+ = \Delta z.\omega/2u^*$, where ω is the angular velocity, such that $\Delta z.\omega/2$ is the maximum amplitude of the wall velocity. In the 1998 study, there was not enough data to give an optimum value.

Using flow-visualisation and infrared spectrometry, Choi *et al*. (1998) observed that the oscillation caused the low-speed streaks to merge together and alternately realign into the $\pm z$ direction. This caused the average low-speed streak spacing to increase by as much as 45%, whereas the duration of the streaks increased by a factor of 4. It was proposed that the oscillating wall promoted a laminar Stokes layer in the near wall region. The oscillatory Stokes layer created streamwise vortex sheets of alternating sign ($\pm\Omega_x$), and as these vortex sheets are tilted into the alternating spanwise directions by the wall movement ($\mp z$), a net spanwise vorticity was created near the edge of the Stokes layer ($-\Omega_z$). This net spanwise vorticity acted to reduce the near wall velocity gradient whilst increasing the velocity in the logarithmic region, as depicted in Fig. 2.3.8.

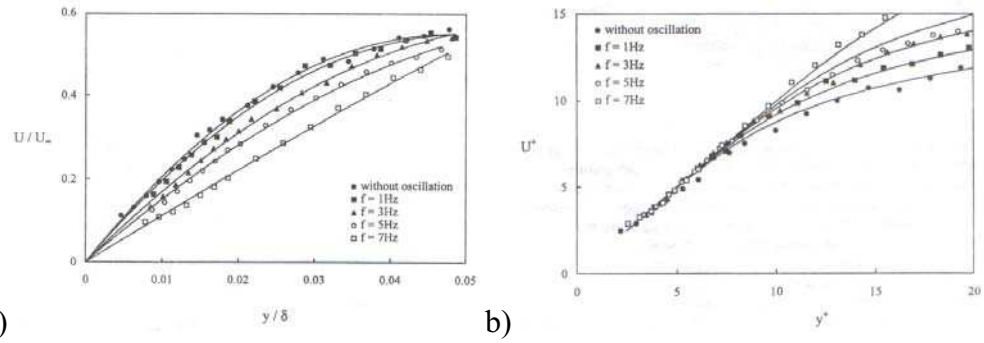

a) b)

Figure 2.3.5. Near wall velocity profile 10mm downstream of the trailing edge of an oscillating plate at different oscillation frequencies (Δz = 70mm). a) Outer scaled profile and b) inner scaled profile. From Choi *et al.* (1998).

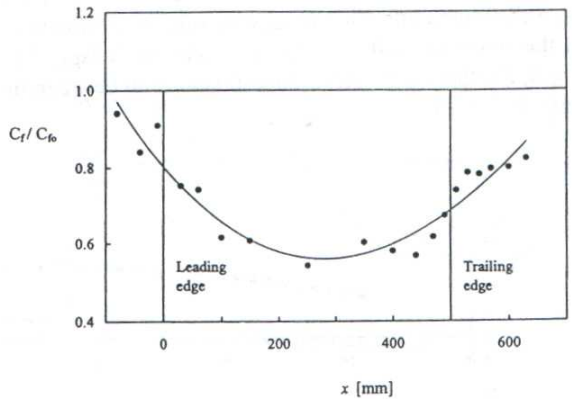

Figure 2.3.6. Variation of skin-friction reduction along the oscillating plate. (f = 5Hz, Δz = 70mm). From Choi *et al.* (1998).

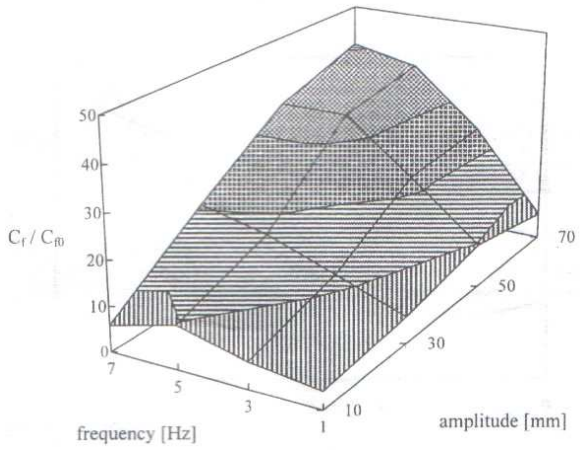

Figure 2.3.7. Variation of skin-friction reduction with oscillation frequency and amplitude. From Choi *et al.* (1998).

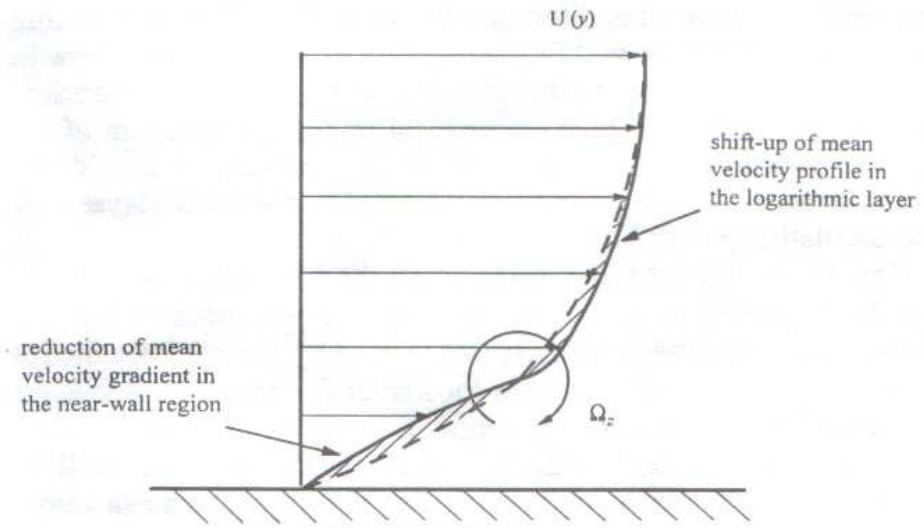

Figure 2.3.8. Conceptual model for a turbulent boundary layer over an oscillating wall showing a net spanwise vorticity, Ω_z, created by a periodic stokes layer. From Choi *et al.* (1998).

Choi and Clayton (2001), pointed out that the creation of a net spanwise vorticity located at the edge of the viscous sublayer not only reduced the mean velocity gradient near the wall (Fig. 2.3.8), but also impeded the stretching of the quasi-streamwise vortices, thus reducing their intensity. As a result, the downwash of high-momentum fluid associated with these vortices (sweep) were of reduced intensity, thus leading to a reduction of skin-friction drag. In fact, the VITA burst signature duration was reduced by as much as one third, as shown in Fig. 2.3.9, which suggested that the sweep events were much weaker. Such modifications to the sweep events were observed to at least $y^+ = 20$.

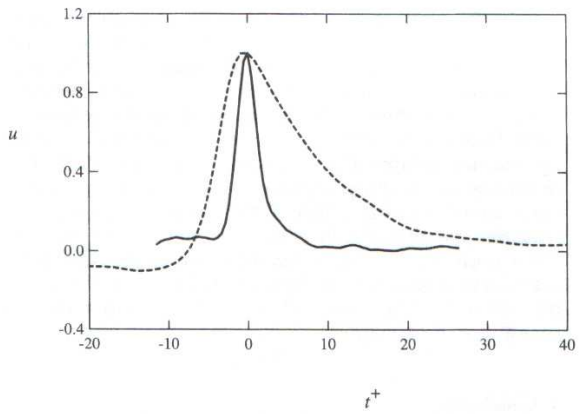

Figure 2.3.9. Variable Interval Time Averaged (VITA) near-wall burst signature at y^+ = 1.5. — with spanwise wall oscillation, --- without wall oscillation. From Choi and Clayton (2001).

Further investigation was carried out in the same facility by Choi (2002) using sub-miniature cross wire probes in order to study the spanwise velocity profile near the wall. The measurements showed that the spanwise velocity profile in the near wall region was nearly identical to the theoretical laminar Stokes flow over an oscillating plate, and extended to approximately y^+ = 30 as shown in Fig. 2.3.10. This confirmed their earlier beliefs as to the drag reduction mechanism. They presented evidence of the production of net spanwise vorticity by the Stokes layer by measuring the velocity increase, Δu^+, such that $\Omega_z^+ = -\partial \Delta u^+/\partial y$, (The vorticity contribution due to $|\partial \Delta v^+/\partial x|$ is ignored since $|\partial \Delta u^+/\partial y| >> |\partial \Delta v^+/\partial x|$). The results are shown in Fig. 2.3.11, where a net vorticity was created at $y^+ \approx 10$ (the sign conventions from Choi *et al*. (1998) and Choi (2002) are different, but in both cases the net vorticity is as in Fig. 2.3.8).

There was now enough data to re-examine whether it was the non-dimensional wall speed, $W^+ = \Delta z.\omega/2u^*$, that is the important parameter for drag reduction using spanwise wall oscillation. Figure 2.3.12 shows the data of Jung *et al.*

(1992), Laadhari *et al.* (1994) and Choi *et al.* (1998) which confirmed that the amount of drag reduction did indeed depend on W^+, with an optimum value of $W^+ \approx 15$. The results of Choi showed a maximum of 45% drag reduction, when the plate was oscillated with $W^+ = 15$, $\Delta z^+ = 400$ and $T^+ = 80$.

The University of Nottingham group have also tested the spanwise oscillation using a 'real-world' application of rotating the wall of a fully developed turbulent pipe flow at $Re_d \approx 3x10^4$ (Choi and Graham (1998)). A maximum drag reduction of 25% occurred by exciting the wall with a nondimensional wall speed of $W^+ \approx 15$ ($T^+ \approx$ 50-100), consistent with the flat plate oscillation and DNS results discussed previously. The lower drag reduction was attributed to the higher Reynolds number, differences in outer boundary layer structures in pipe flow, and the centrifugal force.

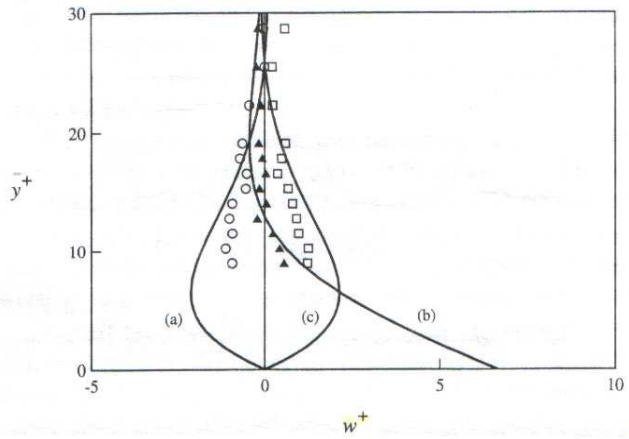

Figure 2.3.10. Phase averaged spanwise velocity profile over the oscillating wall. The theoretical spanwise velocity profile within the Stokes layer is given by $w/W_0 = e^{-\varphi}cos(\omega t-\varphi)$, where $\varphi=y\sqrt{(\omega/2\nu)}$ is the phase lag, ω is the angular velocity and W_0 the velocity amplitude of the oscillation (Schlichting, 1979). Solid lines are from Stokes' theory, and symbols are from experimental data. a) $\theta = -\pi$, b) $\theta = -\pi/2$, and c) $\theta = 0$. From Choi (2002).

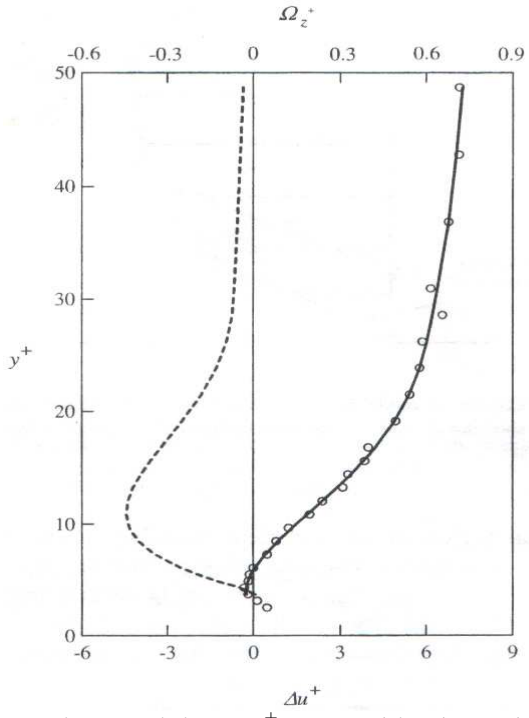

Figure 2.3.11. Spanwise vorticity, Ω_z^+, created in the turbulent boundary layer due to wall oscillation, ---; mean velocity increase, Δu^+, —. From Choi (2002).

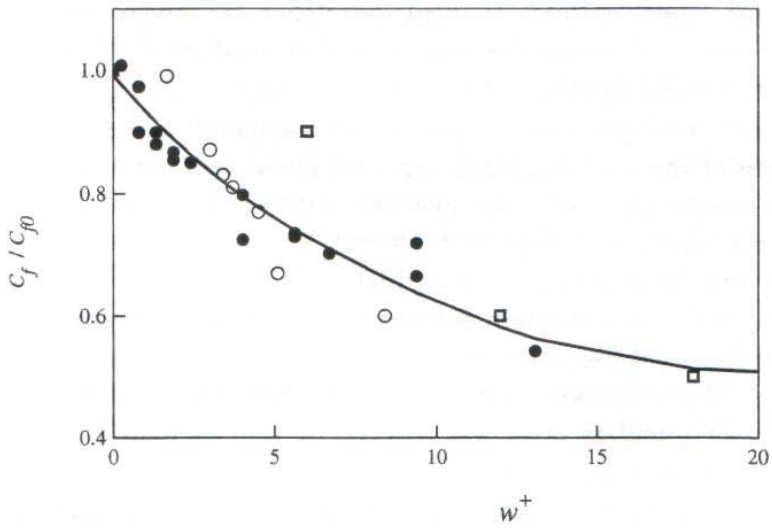

Figure 2.3.12. Turbulent skin-friction drag reduction by spanwise wall oscillation as a function of nondimensional wall velocity. From Choi (2002). ● Choi *et al*. (1998); ○ Laadhari *et al*. (1994); □ Jung *et al*. (1992).

Further investigation of the drag reduction mechanism was performed by Dhanak and Si (1999), who present DNS data using a 2D model of the *y-z* plane across the wall region of the turbulent boundary layer. The Navier-Stokes equations were solved locally with the assumption that the spatial variation of a quasi-streamwise vortex along its length is less than that in the *y-z* plane. They focused on the effect of spanwise wall oscillation on a single pair of counter-rotating streamwise vortices near the wall. An oscillation period of $T^+ = 100$ was used with different vortex strengths and sizes and it was observed that the spanwise cross flow caused by the wall oscillation deforms and leads to a mutual annihilation of the vortices. Figure 2.3.13a shows the evolution of the vortices in the un-manipulated flow. The vortices rolled-up and moved away from the wall forming a low speed region below the structures, and finally underwent a mutual viscous annihilation at some distance from the wall. Note that two more vortices were formed between the primary vortices at the wall, which rotated in the opposite direction. Figure 2.3.13b shows the case with wall oscillation. The wall motion induced the vortex initially on the right hand side of the figure to move underneath the other vortex and caused them to cancel very rapidly. Consequently, the vortices and associated Reynolds stresses had nearly disappeared by $t^+ = 10$. Note that the vortices in the un-manipulated case were present to at least $t^+ = 30$. A net (phase averaged) drag reduction of around 10% was found in their study, but their model was only valid for short time scales ($t^+ \leq 40$), only one structural scale, and 2D flow assumptions were made. By comparison, Jung *et al.* (1992) showed that the flow did not reach a statistically steady state, with 40% drag reduction, until $t^+ \approx 500$ (or five oscillation periods, see Fig. 2.3.1).

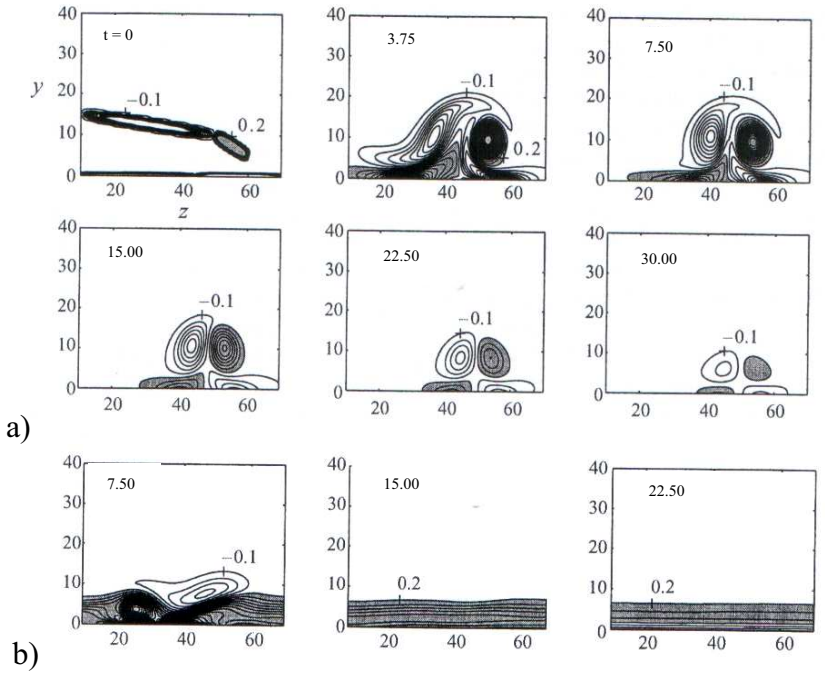

Figure 2.3.13. Evolution of quasi-streamwise vortices with and without spanwise wall oscillation. Contours of streamwise vorticity are shown, a) in the absence of wall oscillation, and b) with wall oscillation of period $T^+ = 100$, and amplitude $W_o^+ = 12$. Reproduced from Dhanak and Si (1999).

Further DNS experiments were performed by Choi *et al*. (2002), to extract a simple equation for the drag reduction rate, $D_r = (\tau_{no\ osc} - \tau_{osc})/\tau_{no\ osc}$. Like Choi (2002), they concluded that the drag reduction was based on the interaction between the Stokes layer and the near-wall turbulence. More specifically, Choi *et al*. (2002), state that the amount of drag reduction was not only based on how far from the wall the oscillations extend (or, the penetration depth, as previously discussed by Choi *et al.* 1998), but also on the acceleration produced near the wall. A new parameter, $V_c^+ = a_5^+ y_d^+ / A^+ Re_\tau^{0.2}$, was proposed and the drag reduction rate of many studies collapsed reasonably well according to $D_r = 1000 V_c^{+2} + 50 V_c^+$, as shown in Fig. 2.3.14. Here, a_5^+ is a

measure of the acceleration of the Stokes layer at $y^+ = 5$, y_d^+ is the influential range of the Stokes layer and A^+ is the oscillation velocity amplitude of the wall. However, this scaling did not correlate with the data of Jung *et al*. (1992) for $T^+ = 200$ and $T^+ = 500$.

More recently, Quadrio and Ricco (2004) addressed the issue of the different scaling parameters used by the different authors (i.e. T^+ and W^+), the different quoted maximum drag reductions and the net energy saving achievable using spanwise oscillation. They performed a DNS experiment by oscillating the top and bottom walls of a channel sinusoidally, in phase, with velocity $W = W_m \sin(2\pi t/T)$. The Reynolds number was $Re_\tau = 200$, such that results could be directly compared with Jung *et al*. (1992), Baron and Quadrio (1996) and Choi *et al*. (2002). A large computational domain was used ($L_x = 21h$) and the computational experiments ran for a long time ($t^+ \approx 9000$) to ensure high accuracy solutions. The oscillation period, T, and the maximum velocity, W, were varied independently and Fig. 2.3.15 shows the percentage drag reduction versus T^+ and W^+. The highest computed drag reduction was 44.7% for $T^+ = 100$ and $W^+ = 27$, confirming the experimental results of Choi (2002). The highest computed net energy balance was 7.3% and occurs at approximately the optimum oscillation period but with reduced oscillation speed, due to increased viscous losses as the oscillation speed was increased. This was similar to the 10% net saving observed by Baron and Quadrio (1996). Contrary to Choi (2002), Quadrio and Ricco (2004) observed that the drag reduction depends on both the nondimensional oscillation period, T^+, *and* the nondimensional wall speed, W^+. The following parameter, S^+, was proposed to scale the drag reduction results by combining a wall normal length

scale, l^+, related to the distance at which the wall oscillation affects the turbulent structures (from the Stokes solution), and the local spanwise acceleration, $a_m{}^+$.

$$S^+ = \frac{a_m{}^+ l^+}{W_m{}^+} = 2\sqrt{\frac{\pi}{T^+}} \ln\left(\frac{W_m{}^+}{W_{th}{}^+}\right) \exp\left(-\bar{y}^+ \sqrt{\frac{\pi}{T^+}}\right) \qquad (2.3.1)$$

Where, $W_{th}{}^+$ is the threshold velocity necessary for the oscillation to affect the structures and $\bar{y}^+$ is a distance related to the local maximum acceleration. Based on physical arguments they selected $W_{th}{}^+ = 1.2$ and $\bar{y}^+ = 6.3$ and a good collapse of the data was observed as shown in Fig. 2.3.16. It was found that the correlation holds, provided that the oscillation period was shorter than the typical time scale of the survivability of the near-wall structures. If the oscillation period was greater than this, the flow has time to readjust to its natural state between the oscillation and the assumption made for the parameters were no longer valid.

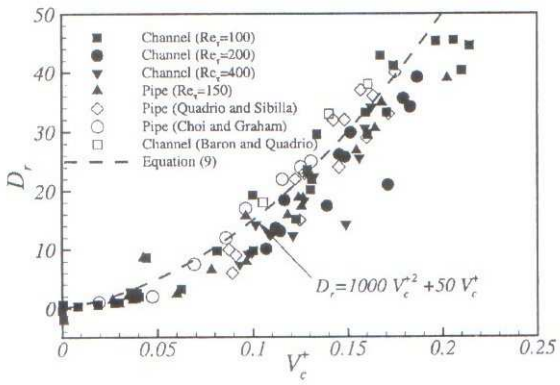

Figure 2.3.14. Drag Reduction rate as a function of $V_c^+ = a_5^+ y_d^+ / A^+ Re_\tau^{0.2}$. From Choi *et al*. (2002).

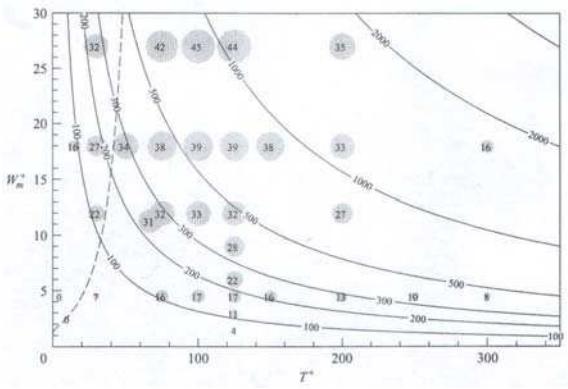

Figure 2.3.15. Plot of percentage drag reduction against T^+ and W_m^+. Size of circles is proportional to the drag reduction with computed amount given within. Hyperbolae are lines of constant maximum displacement, $D_m = W_m T/\pi$. From Quadrio and Ricco (2004).

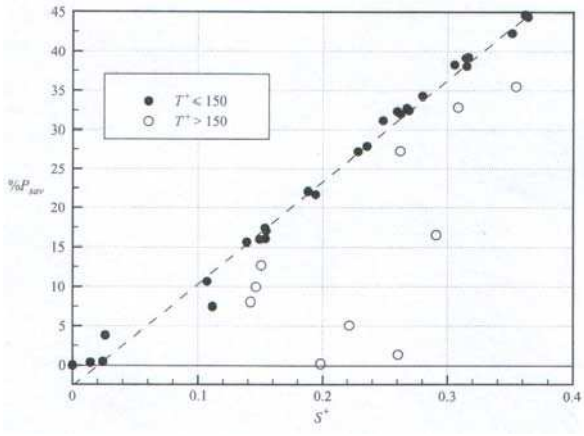

Figure 2.3.16. Drag reduction versus S^+. From Quadrio and Ricco (2004).

2.3.2. Lorentz Force Spanwise Oscillation

The mechanical spanwise oscillation described above is clearly effective in reducing skin-friction; with a maximum of 45% drag reduction quoted by most authors. However, the oscillation method is not very practical, except perhaps in pipes. To oscillate a surface of an aircraft or ship is simply not feasible and has many issues with reliability and corrosion, not to mention the added weight of mechanical parts needed to oscillate the surface. Researchers have subsequently tried to mimic the wall oscillation without the need for moving parts. The most popular method is Lorentz force oscillation (also known as Electro-Magnetic Turbulence Control, EMTC). This utilises the force generated by the combination of an electric field and a magnetic field, within a conductive medium (e.g. salt water), to achieve flow control. EMTC is not just limited to spanwise oscillation configurations. In fact the idea has been used for, amongst other things, wall normal blowing and suction (Rossi and Thibault, 2002), streamwise forcing (Crawford and Karniadakis, 1997), and pulsation (O'Sullivan, 1998). For brevity, we shall only discuss the results of spanwise Lorentz forcing to look for similarities with the mechanical oscillation case.

Berger *et al*., (2000), found that the important parameters for drag reduction using spanwise oscillating Lorentz forcing are the penetration depth, Δ^+, the oscillation period, T^+, and the Stuart number, $St = J_0 B_0 \delta / \rho u^{*2}$. The penetration depth is a measure of how far the Lorentz force protrudes into the flow, $\Delta^+ = a^+/\pi = au^*/\pi\nu$, where a is the electrode spacing (see Fig. 2.3.17 for a typical Lorentz forcing actuator). In order to have the greatest effect on the near wall structure, Berger *et al*. (2000), found that Δ^+ should be set to match the

location of the quasi-streamwise vortex cores ($y^+ \approx$ 15-25), and is similar to the required depth of the Stokes layer for mechanical wall oscillation (Choi, 2002). The oscillation period has the same definition as for mechanical wall oscillation, $T^+ = Tu^{*2}/\nu$, and the Stuart number represents the ratio of the electromagnetic force to the initial force of the fluid. Here, J_0 is the current density at the electrode surface, B_0 is the magnetic field strength, and δ is the undisturbed boundary layer thickness.

Various combinations of parameters were studied using DNS by Berger *et al*. (2000), who found that by applying a spanwise Lorentz force, drag reductions of around 40% could be achieved. Optimal drag reduction occurred when $\Delta^+ \approx$ 10, $T^+ \approx$ 50-100 and $(St.T^+/Re_\tau\pi) \approx$ 20. They stated that the Lorentz force caused a shear force to be applied to the near-wall quasi-streamwise vortices, such that the vortices of the same sign as the shear survived, while the vortices of opposite sign were suppressed. By oscillating the shear, it was possible to suppress vortices of both sign, which ultimately disrupted the turbulence production cycle and lead to a drag reduction. They also found that the shear force had to be great enough to overcome the natural dynamics of the near-wall quasi-streamwise vortices and had to be applied in the region where the vortices are located. The annihilation of streamwise vorticity near the manipulated surface is clearly visible in Figure 2.3.18.

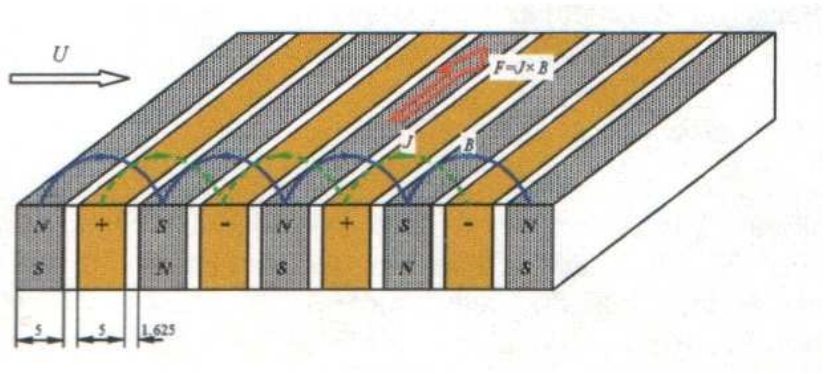

Figure 2.3.17. Details of the EMTC actuator modelled by Berger *et al*. (2000) and used experimentally by Pang *et al*. (2004). From Pang *et al*. (2004).

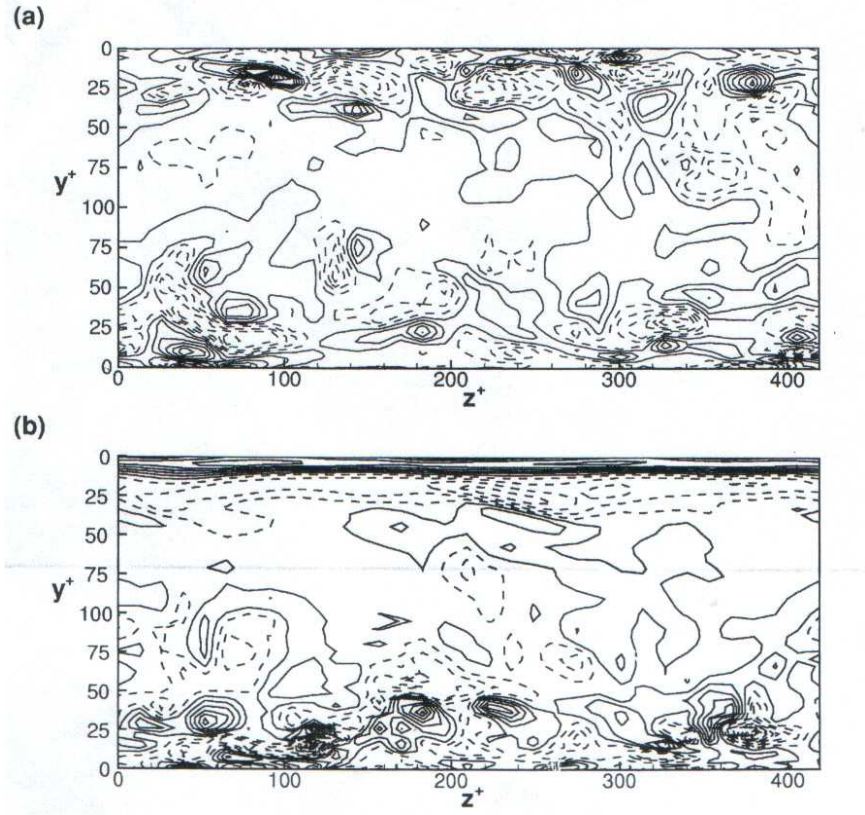

Figure 2.3.18. Contour of streamwise vorticity, ω_x, a) without control and b) with Lorentz forcing applied to top wall only with $\Delta^+ = 10$, $T^+ = 100$, $St = 20\pi$, $Re_\tau = 100$ ($St.T^+/Re_\tau\pi = 20$). Dashed lines correspond to negative vorticity. Note that the streamwise vortices have been nearly completely annihilated on the Lorentz forcing surface. From Berger *et al*. (2000).

Recently, Pang *et al*. (2004), and Pang and Choi (2004), performed an experimental study in a water channel using an array of permanent magnets and electrodes to create a spanwise Lorentz forcing in a turbulent boundary layer. The oscillation was achieved by switching the polarity of the electric field, and copper sulphate, $CuSO_4$, was injected near the wall to make the fluid conductive. The schematic of the test surface is shown in Fig. 2.3.17. Figure 2.3.19 shows the drag reduction achieved through variation of St and T^+, with fixed $\Delta^+ = 12.4$. This penetration depth was similar to the optimal depth from Berger *et al*. (2000). It was observed that a band of maximum drag reduction occurs at approximately $St.T^+ = 21000$, with a maximum drag reduction of 40%. This prompted Pang and Choi (2004) to define an "equivalent spanwise-wall velocity", $W_{eq}^+ = StT^+/(2\pi Re_\tau)$, in order to compare these results with that of mechanical wall-oscillation. The dependency of drag reduction with W_{eq}^+ is plotted in Fig. 2.3.20, where maximum drag reduction was found at $W_{eq}^+ \approx 10$-15, consistent with the mechanical wall oscillation case ($W^+ = 15$, Choi, 2002). This suggested that there was a similar drag reduction mechanism in both cases. Certainly, the statistical and VITA trends in Pang *et al*. (2004) are very similar to the mechanical wall oscillation study of Choi (2002).

Breuer *et al*. (2004), presented results for a similar electrode-magnet array as Pang *et al*. (2004). Using PIV in initially stationary saltwater they observed a sinusiodally varying spanwise velocity with thickness of several millimetres (Fig. 2.3.21). Using a floating element drag balance, a drag reduction of 10% was observed when the actuators were used in a turbulent boundary layer. However, this was averaged over the entire floating plate, which included corner flows and a region where the flow is adjusting to the Lorentz forcing.

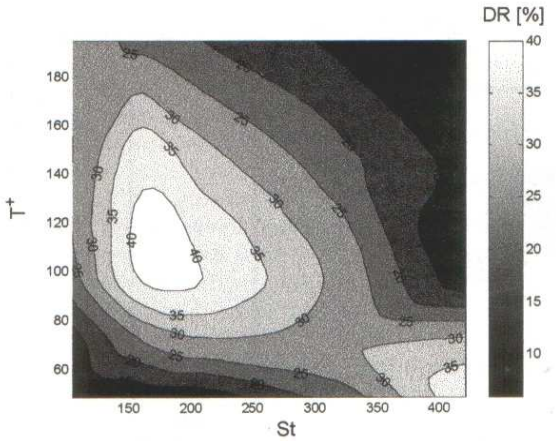

Figure 2.3.19. Contour plot of skin-friction drag reduction (DR [%]) using Lorentz force oscillation at different *St* and T^+. From Pang *et al*. (2004).

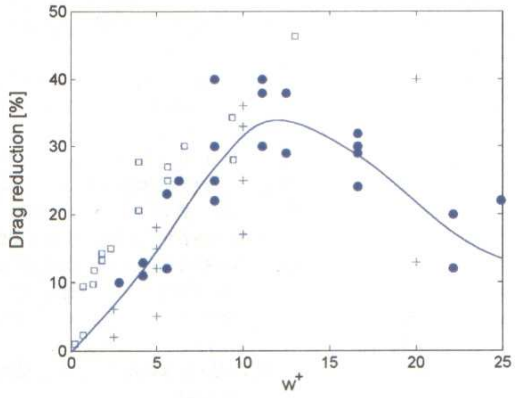

Figure 2.3.20. Skin-friction drag reduction against $W_{eq}^{+} = StT^{+}/(2\pi Re_{\tau})$ using Lorentz force oscillation. (●) EMTC experimental results of Pang *et al*. (2004), (+) EMTC DNS results of Berger *et al*. (2000), (□) mechanical wall oscillation experimental results of Choi (2002). Reproduced from Pang *et al*. (2004).

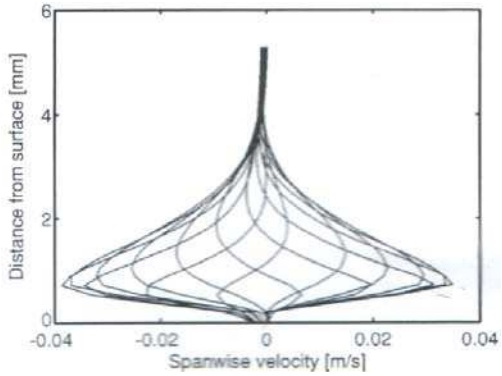

Figure 2.3.21. Velocity profiles due to oscillatory Lorentz forcing in initially static saltwater. From Breuer *et al*. (2004).

It would appear that there are many parallels between the spanwise mechanical wall oscillation and spanwise Lortenz (EMTC) forcing techniques. In both cases, the maximum attainable drag reduction was around 45%, which occurred when the period, $T^+ \approx 100$, and the wall speed, $W^+ \approx 15$. Note, however, that the definition of wall speed differs between the two cases ($W_{mech}{}^+ = (\Delta z^+/2).\omega^+ = \pi\Delta z^+/T^+$, $W_{eq}{}^+ = StT^+/(2\pi Re_\tau)$). The required penetration depth and thickness of the Stokes layer were the same in both cases (i.e. at $y^+ \approx$ 10-15). This would tend to suggests that drag can be significantly reduced by the oscillatory spanwise-displacement of near wall structures, regardless of the physical means of creating the oscillation.

However, neither of the above spanwise oscillation techniques is very practical. As mentioned, mechanical wall oscillation is far from feasible on aircraft, especially given the huge oscillation frequencies required at flight speeds ($f = O$[100kHz]). Lorentz forcing, apart from the being restricted to liquid applications, has very poor efficiency. Berger *et al*. (2000) and Breuer *et al*. (2004), showed that the electrical-to-mechanical efficiency is of order 10^{-4}, due to the low field strength of the permanent magnets and the low conductivity of saltwater. Also, the technique would require large, heavy magnets where the extra weight and corrosion issues may outweigh the gains.

Given the success of the two techniques, spanwise oscillation will be attempted in this thesis by creating an oscillating force using surface plasma. Plasma is fast acting such that bandwidth issues are not expected to be encountered, and the devices require no moving parts, complicated ducting or heavy magnets. RF glow discharge plasma actuators for subsonic airflow applications will be discussed in the next section.

2.4. Plasma Aerodynamics

2.4.1. Introduction

Plasma is defined as the fourth state of matter, of which nearly 99% of the universe is composed. Plasma is created when sufficient energy is added to a gas so that it becomes ionized. The result is a quasi-neutral particle system containing free electrons, ions and, depending on the degree of ionization, neutral particles. The energy required to ionize the gas may be thermal or electrical. In the case of 'hot' plasmas, the thermal energy of the gas is so great that electrons are no longer bound to their atomic core, such as in stars where the temperature is several million degrees K. Alternatively, and as a requirement for terrestrial applications, strong electric fields or ionizing radiation, such as X-rays, are used to strip the electrons from the atoms to create plasma (Kunhardt, 2000). In either case, once generated, the plasma can be manipulated by electric or magnetic fields.

Plasma has been used in microelectronic device fabrication, ozone generation and in gas laser excitation for some time and it is used everyday to light offices all over the world in fluorescent tubes (Roth, 1995 and 2001a). More recently, plasma has found application in high definition plasma screen televisions and in manoeuvring orbiting satellites. It has even been used as an anemometer by Reid (1962), and by Corke and Post (2005).

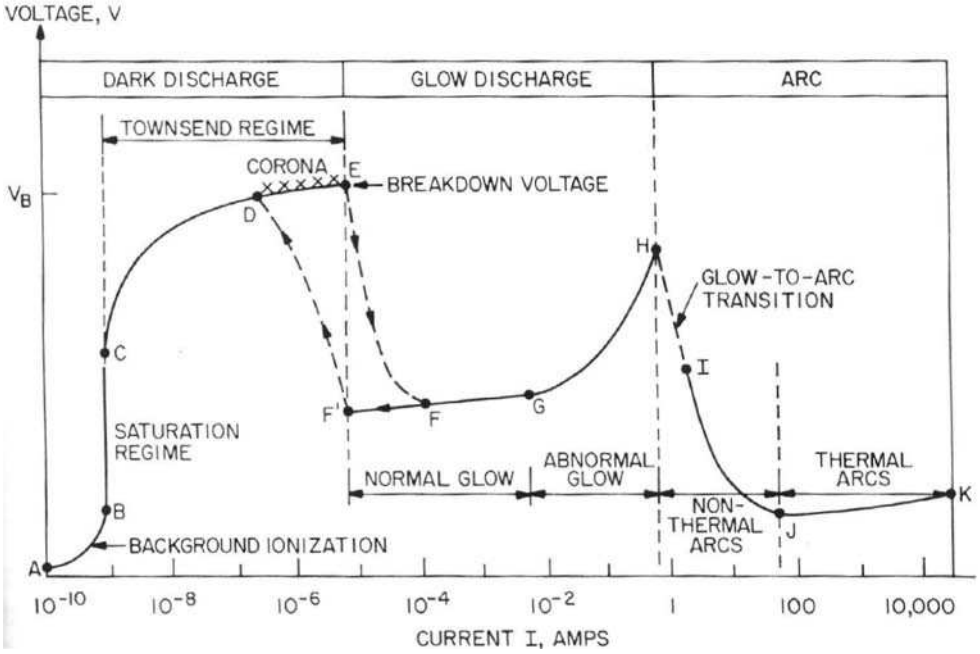

Figure 2.4.1. Voltage-Current characteristics of a DC low pressure electrical discharge tube. From Roth, (1995).

Most of our understanding of plasma comes from studying electrical discharge tubes, with groundbreaking works by Faraday and Maxwell in the late 19th Century. In such configurations, plasma is maintained by applying a high DC voltage between parallel plates in a partially evacuated chamber. Roth (1995), provided a detailed explanation of the formation of plasma between the electrodes and presented the above Voltage-Current characteristics as the potential difference is steadily increased (Fig. 2.4.1).

As the voltage is initially increased (A-B), current is drawn due to the naturally occurring ions and electrons present in the gas which flow due to the electric field until they are removed from the volume (saturation B-C). As the voltage is increased further, electrons acquire enough energy from the electric field to be emitted from the cathode and ionise some of the neutral background gas through particle collisions. This process creates additional ions and electrons and the current increases exponentially (C-D). At a critical voltage,

V_B (E), electrical breakdown occurs and a transition is made to the glow regime, whereby the amount of excitation to the background gas is visible to the eye (F-H). In air, this appears as a light purple glow. The exact breakdown voltage for a particular gas depends on the product of the gas pressure, *P*, and the distance between electrodes, *d*. For air, the critical *P.d* value (Stoletow point) is 5.7 x 10^{-3} Torr-m and the minimum breakdown voltage, $E_{B,min}$, is 360V. As the voltage is increased still further (H-K), destructive and unpredictable arcs occur between the two plates. The normal glow regime is a stable structure and is the region of interest in this study (F-G).

For plasma to be useful in aerospace applications, the device must operate at atmospheric pressure (as a maximum), with air as the ambient gas. Roth (1995, 2001a, 2001b), showed how the glow discharge can be maintained at these conditions with a device dubbed the 'One Atmosphere Uniform Glow Discharge Plasma' (OAUGDP). This plasma was maintained by a radio frequency (RF) AC voltage, so that the distance between electrodes did not have to be unfeasibly small or the voltage unfeasibly high (d = 0.077mm for DC glow discharge in atmospheric pressure air at $E_{B,min}$ = 360V). Such plasma has a low degree of ionisation and hence a large amount of neutral particles exist within it.

Roth (1995, 2001a) and Roth *et al*. (1995) stated that stable glow discharge plasma can be maintained in ambient air if the driving voltage switches polarity at such a high frequency that the electrons have enough time to travel from one electrode to the other (due to their low mass), but the heavier ions do not. Thus, plasma is 'artificially' held between the plates yet has all the

characteristics of the classic DC glow discharge. This 'ion trapping' frequency for a pair of parallel plates was given as:

$$\frac{eE_{rms}}{\pi\, m_i v_{ci} d^2} \leq v_0 \leq \frac{eE_{rms}}{\pi\, m_e v_{ce} d^2} \quad , \qquad (2.4.1)$$

where e is the charge of an electron, E_{rms} is the applied voltage, m_i is the mass of an ion, m_e is mass of an electron, v_{ci} is the ion collision frequency, v_{ce} is the electron collision frequency, v_0 is the AC driving frequency and d is the plate separation. Roth *et al*. (1995), said that if the driving frequency is below the above range, both ions and electrons will have enough time to reach the other electrode during an AC cycle and no plasma will form. They also said that if the driving frequency is above the range, both electrons and ions will effectively be trapped between the plates and unstable filamentary breakdown occurs. The ion-trapping regime was shown to require a driving frequency of several kHz at a voltage of several kV for a gap distance of several mm in atmospheric air (Roth *et al*. 1995).

Figure 2.4.2 illustrates a typical plasma reactor, where plasma is formed between parallel plates (from Roth, 2001a). Yokoyama *et al*., (1990) showed that the glow discharge at atmospheric pressure can be stabilised by using a high-frequency source or by inserting a dielectric plate between the electrodes. Fast rise-time voltage pulses were also said to improve the uniformity of the discharge (Pashaie *et al*., 1994). In addition, short duration square-wave pulses have been used to exploit the charge build up on the dielectric during each half of the AC cycle, so that a secondary discharge occurs (driven by the electric field of the surface charge) without consuming energy from the applied circuit (Liu and Neiger 2001).

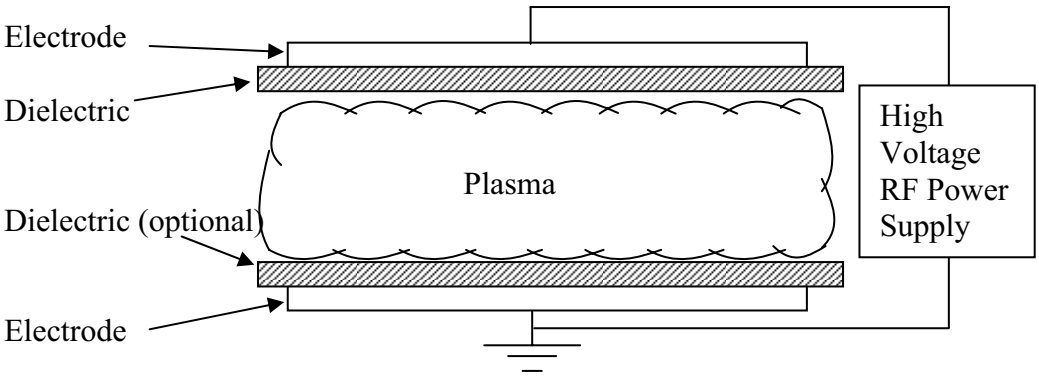

Figure 2.4.2. Parallel plate OAUGDP geometry. Adapted from Roth (2001a).

Roth's OAUGDP was said to be homogeneous and spatially stable (Roth, 2001a). Massines *at al*. (1998), found that truly uniform glow discharge at atmospheric pressure was indeed possible if the gas is relatively free from impurities. There is, however, much evidence from plasma reactors used in ozone generation that the plasma does not form as a diffuse glow, but actually consists of a number of tiny individual breakdown channels (radius ≈ 0.1mm, duration ≈ 10ns). These channels are known as microdischarges, and the corresponding plasma is known as a Dielectric-Barrier Discharge (DBD), or silent discharge. Kogelshatz *et al*. (1997), provided a review of the subject. Note that DBD reactors are very efficient at producing ozone and may have an additional advantage for aerospace applications since when attached to aircraft, vast quantities of ozone will be created in the upper atmosphere. This may potentially add ozone back to the depleted ozone layer.

Dielectric-Barrier Discharges can be created in a range of geometries, as illustrated in Fig. 2.4.3. For industrial ozone generation the coaxial geometry is popular, which are typically operated between 500Hz and 500kHz with amplitudes of 10kV and a gap spacing of a few mm (Kogelshatz *et al*. 1997). The parallel plate geometry can be effectively uncoiled, as in Fig. 2.4.3c. It is

this geometry that is of interest to the aerodynamicist since this enables plasma to be formed at the surface of a body. Such devices are known as surface plasma actuators.

Enloe *et al*. (2004a and 2004b) explained the operation of surface plasma actuators. With reference to Fig. 2.4.4, they state;

> *"Figure* 2.4.4a *illustrates the half-cycle of the discharge for which the exposed electrode is more negative than the surface of the dielectric and the insulated electrode, thus taking the role of the cathode in the discharge. In this case, assuming the potential difference is high enough, the exposed electrode can emit electrons. Because the discharge terminates on a dielectric surface, however, the build-up of surface charge opposes the applied voltage, and the discharge shuts off unless the magnitude of the applied voltage in continually increased… The behaviour of the discharge is similar on the opposite half cycle: a positive slope in the applied voltage is necessary to maintain the discharge. In this half-cycle, the charge available to the discharge is limited to that deposited during the previous half-cycle on the dielectric surface"*

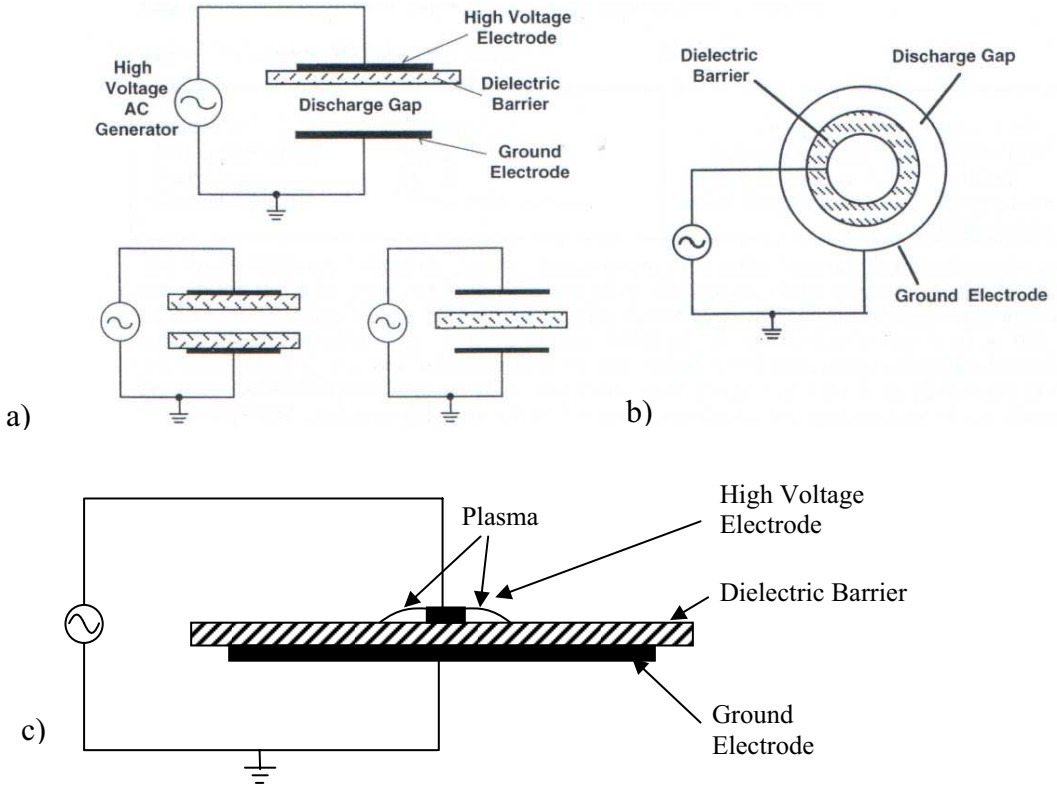

Figure 2.4.3. Schematic of common dielectric-barrier discharge configurations. a) parallel plate reactors and b) coaxial reactors from Kogelshatz *et al*. (1997). c) Surface discharge reactor adapted from Gibalov and Pietsch (2000).

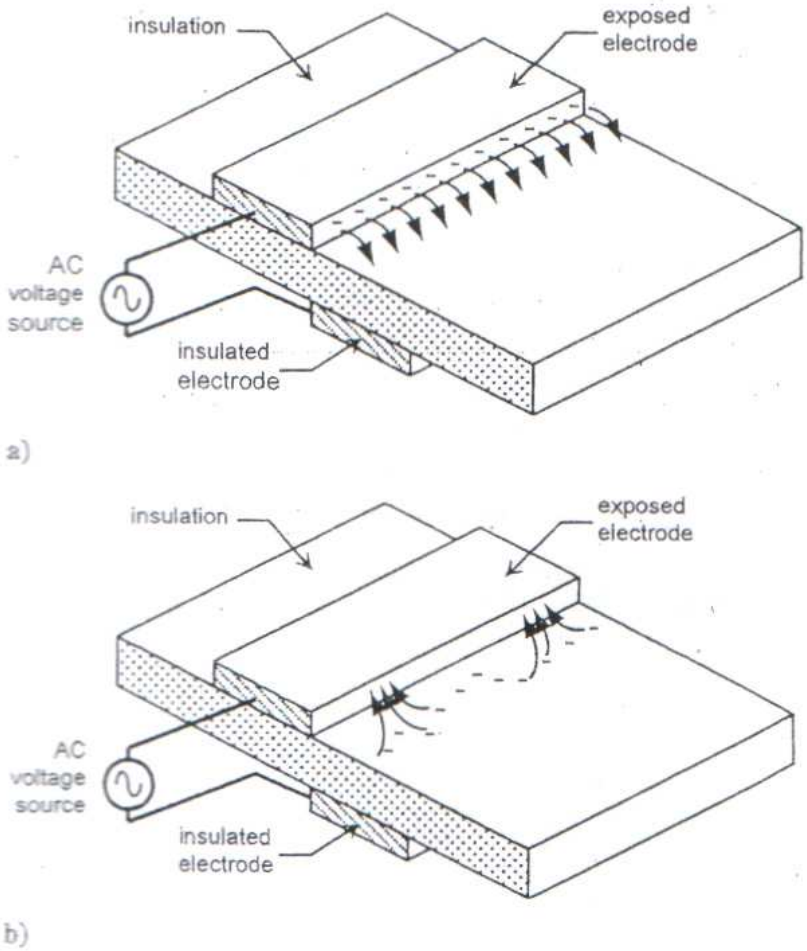

Figure 2.4.4. Illustration of the self limiting nature of the dielectric barrier discharge. Electrons are emitted from the exposed electrode during the negative part of the AC cycle (a). These are subsequently deposited on the dielectric surface and build up charge which opposes the potential at the exposed electrode, causing the discharge to extinguish as soon as the exposed electrode potential stops rising. In the positive half-cycle (b), the electrons are removed from the dielectric and travel back to the exposed electrode. From Enloe *et al*. (2004b).

Gibalov and Pietsch (2000), studied the structure of the dielectric barrier discharge in parallel plate and surface discharge geometries. For the surface discharge case, distinct channels appeared on the surface with widths of the order of 1mm, as illustrated in Fig. 2.4.5. Since there is no defined discharge gap, the filaments spread out over the surface of the dielectric and charge transfer takes place in a very thin layer. They noted that an increasing applied voltage caused an increase in the discharge area on the dielectric surface. Also, the length of the discharge region decreased with an increase in dielectric constant of the material. However, the number of charge carriers accumulating on the dielectric surface increased with dielectric constant.

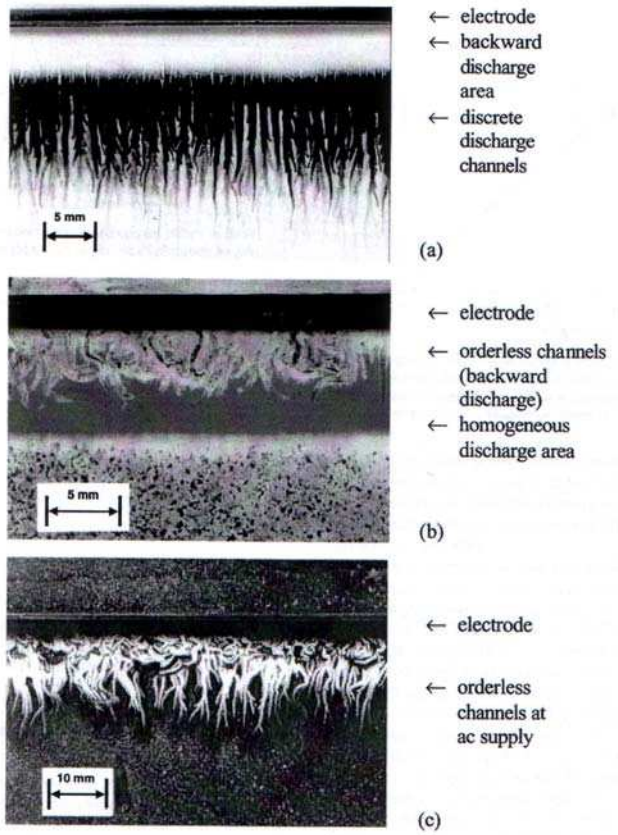

Figure 2.4.5. Discharge patterns on the dielectric surface of a surface discharge plasma actuator (dust figures). a) a positive voltage pulse of 20kV at the surface electrode; b) a negative voltage pulse of 20kV; and c) an AC voltage of 10kV. From Gibalov and Pietsch (2000).

The filamentary nature of surface plasma actuators was also confirmed by Wilkinson (2003) and Enloe *et al*. (2004a and 2004b). As shown in Fig. 2.4.6, the plasma structure appeared as discrete "fountains" when the upper electrode was the instantaneous anode. When the upper electrode was the instantaneous cathode, the plasma structure showed closed loops and bridges across peaks of the plasma structure. Thus, the plasma is both spatially and temporally non-uniform. However, the cathode plasma formation appeared to be more energetic; an observation also noted by Johnson and Scott (2001).

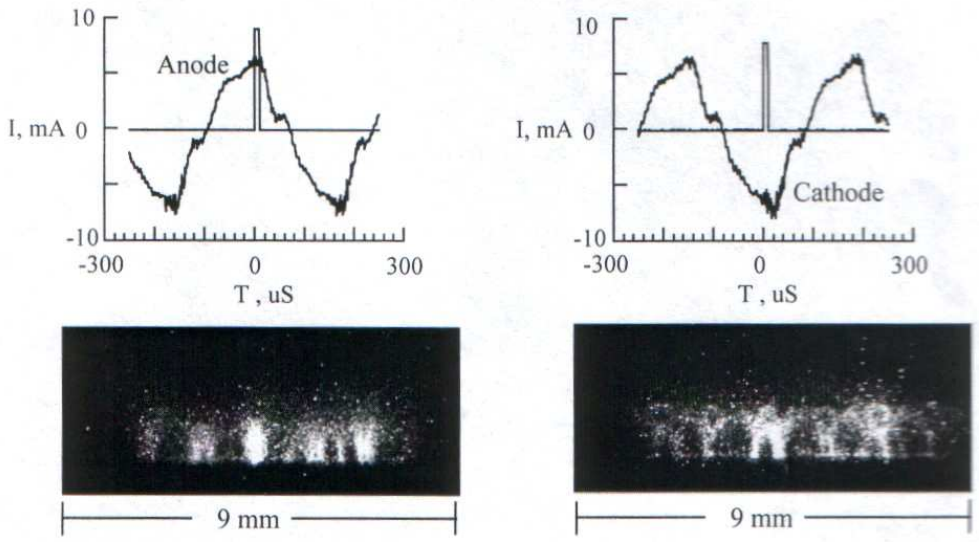

Figure 2.4.6. CCD phase averaged photographs of the plasma along the edge of an electrode, running horizontally along the bottom of the picture. Timing is shown with respect to plasma current above each image. Plasma excitation is at 8.5kV$_{pp}$ at 3kHz. From Wilkinson (2003).

2.4.2. Plasma Forcing

What is truly remarkable about surface plasma actuators is their ability to produce a force on the surrounding gas, and hence create or alter a flow. This gives the aerodynamicists the ability to tailor a force near the surface of a body in order to achieve global gains such as flow separation control or drag reduction. The exact cause of this forcing has been a subject of investigation for some time and is still a hot topic for debate within the research community to this day.

Robinson (1962), provided a history of the phenomena of the 'electric wind', which dates back to the 16th Century. Such research focused upon the movement of gas induced by the repulsion of ions from a high voltage corona discharge (c.f. Fig. 2.4.1). DC coronas, or ion winds, have been used to reduce viscous drag (Malik *et al*. 1983, El-Khabiry and Colver 1997) and have been used to explain the force that occurs on asymmetric capacitors operated at high DC voltages (~30kV). This so-called 'Biefild-Brown' effect has been demonstrated in devices called 'lifters', whereby the force exceeds the devices weight causing the devices to float magically in the air (Bahder and Fazi 2003). Plasmas have also received much attention for supersonic and hypersonic applications. A short review of such applications was provided by Fomin *et al*. (2004).

However, the surface glow discharge plasma actuator is fundamentally different from DC corona discharges. Here we explore two views of how surface plasma actuators produce a force within the ambient gas.

Roth and his colleagues at the University of Knoxville, Tennessee, have performed much work on the use of plasma actuators for aerodynamic flow

control (Roth, 2001a, 2001b, Roth and Sherman, 2000, Roth *et al*., 1998, 2001, 2004, 2005, Sherman, 1998). Terming the device as an Electro-Hydro-Dynamic (EHD) actuator, Roth stated that a "paraelectric" body force can act on the charges within the plasma if a non-uniform electric field is present. With reference to Fig. 2.4.7, Roth said:

> *"... electric field lines terminate on free charges, or on charged conductors, and these electric field lines act like rubber bands in tension to pull polarised charges of opposite sign together. If an electric field gradient is present, as in a tilted-plate configuration* (Fig. 2.4.7), *the polarised electric field within the plasma causes the charges, the plasma, and (as a result of Lorentzian momentum transfer) the background gas to move towards regions with shorter electric field lines and stronger electric fields, i.e. the plasma will move towards increasing electric field gradients, and drag the neutral gas along with it"*

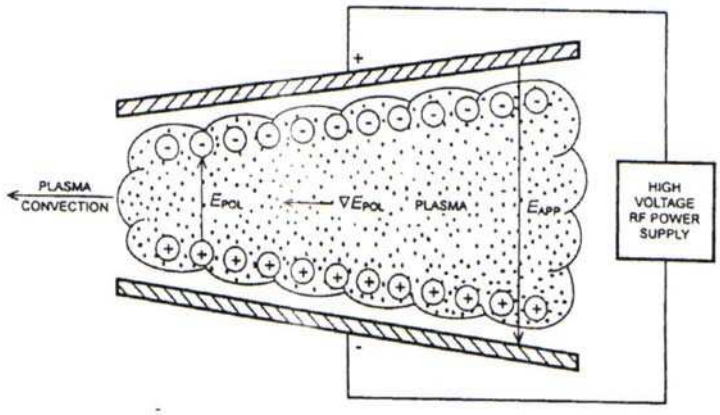

Figure 2.4.7. Paraelectrically unstable plasma between two tilted planar electrodes with plasma motion to the left. From Roth, 2001b.

Roth stated that the electrostatic body force per unit volume of plasma, $\mathbf{f}_b$, with net charge density, ρ_c, is given by:

$$\mathbf{f}_b = \rho_c \mathbf{E} \ , \tag{2.4.2}$$

where **E** is the electric field. The net charge density if related to the electric field through a Poisson equation:

$$\nabla \bullet \mathbf{E} = \frac{\rho_c}{\varepsilon_0} \ , \tag{2.4.3}$$

where ε_0 is the permittivity of free space. Thus:

$$\mathbf{f}_b = \varepsilon_0 \mathbf{E} \nabla \bullet \mathbf{E} = \frac{1}{2}\varepsilon_0 \nabla \bullet \mathbf{E}^2 => \frac{d}{dx}\left(\frac{1}{2}\varepsilon_0 E^2\right), \tag{2.4.4}$$

where the one-dimensional formulation has been derived and the bracketed term was dubbed the 'electrostatic pressure'. Neglecting viscous forces and centrifugal forces, Roth assumed that the electrostatic pressure and gas pressure to be in equilibrium. This then allowed estimation of the neutral gas velocity, v_0, by equating the electrostatic pressure to the stagnation pressure, p_s:

$$p_s = \frac{1}{2}\rho {v_0}^2 = \frac{1}{2}\varepsilon_0 E^2 \, . \tag{2.4.5}$$

Thus, inputting typical values for air with an actuator with electric field of 10^6 (i.e. 1kV across 1mm):

$$v_0 = E\sqrt{\frac{\varepsilon_0}{\rho}} \approx 10^6 \sqrt{\frac{8.854x10^{-12}}{1.3}} = 2.6\,\text{m/s}. \tag{2.4.6}$$

Therefore, Roth showed that the plasma actuator induced a flow of ambient gas with velocity magnitude proportional to the electric field. The ambient gas was expected to flow into regions of increasing electric field gradient.

Roth *et al*. (1998), presented evidence of the surface plasmas ability to drive a flow of ambient gas. Actuators were designed which produced plasma on both sides of the electrode (symmetric configuration) and on one side only (asymmetric configuration). These configurations subsequently produced bi-lateral or uni-lateral EHD forcing respectively as illustrated in Fig. 2.4.8. Figures 2.4.9 and 2.4.10 present flow visualisation and Pitot tube measurements of the plasma induced flow caused by an asymmetric plasma actuator in still air. Roth *et al*. (1998), explain the phenomena as;

> *"In* Fig. 2.4.9b, *the flow is drawn downward by a low pressure above the low electric field gradient region of the plasma, entrained in the ion-driven plasma flow toward the region of high electric field gradient, and forced outward by the region of high (plasma stagnation) pressure along the surface of the panel. The flow is rapidly accelerated away from the region of high gas pressure and high electric field gradient (primarily to the left of the electrode due to asymmetry but to a lesser degree to the right as well)."*

Bulk heating was discounted as the mechanism of inducing the flow because the flow direction is counter to that expected from buoyant flow: plasma actuators create flow along the surface laterally, not rising upward (Sherman 1998). In a later paper (Roth, 2004), it was shown through Pitot tube measurements that the plasma-induced flow profile was similar to a Glauert laminar wall jet (Glauert 1956). A maximum velocity of 3m/s was measured at around 1mm from the dielectric surface when a series of 12 asymmetric actuators were activated simultaneously with E_{RMS} = 5kV at 6kHz.

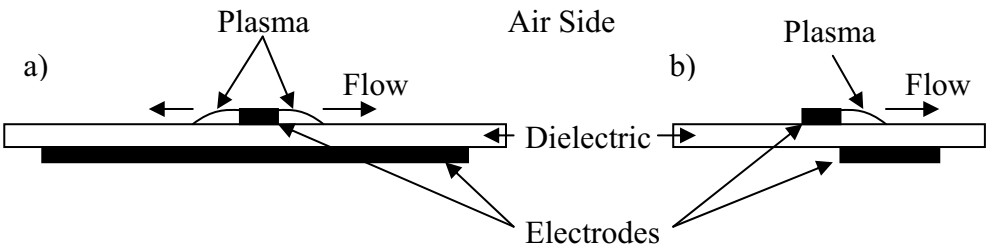

Figure 2.4.8. Schematic of a) symmetric and b) asymmetric electrode sheets with direction of induced plasma forcing.

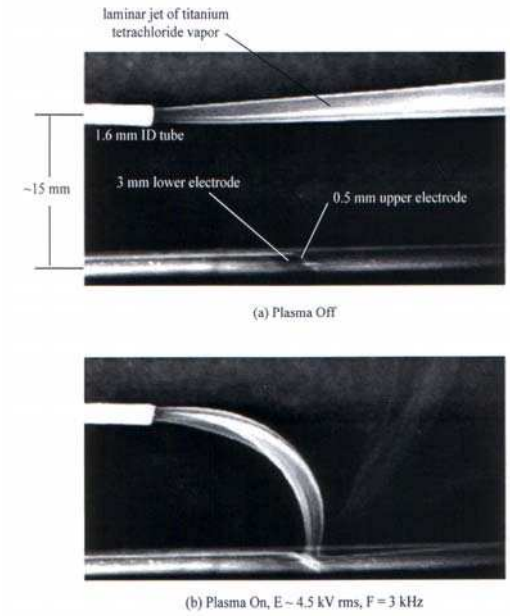

Figure 2.4.9. Demonstration of plasma forcing in still air for an asymmetric electrode. Lower electrode is offset to the left such that EHD forcing is to the left. From Roth *et al.* (1998).

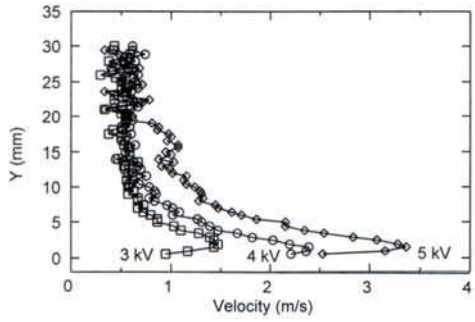

Figure 2.4.10. Magnitude of plasma induced flow velocity in still air for an asymmetric electrode. Excitation at 3kHz at various applied voltages. Measurements take with a pitot tube 28mm downstream of the electrode. From Roth *et al*. (1998).

Corke and his colleagues at the University of Notre Dame, Indiana, have also conducted much research into the use of surface plasma actuators for flow control (see Corke and Post 2005). In a recent paper addressing the operation of the plasma actuator, it was stated that the actuator's behaviour is primarily governed by the build-up of charge on the dielectric surface (Orlov and Corke 2005), not the bulk motion of plasma as Roth suggested (Roth 2001b). The plasma was said to be net neutral (i.e. equal number of negative and positive charges), and the charges respond to the external electric field (i.e. electrons move to the positive electrode and positive ions move to the negative electrode). This motion was thought to set up an electric field within the bulk of the plasma which cancels the external field. However, they stated that regions of charge imbalance exist at the electrode surface and at the dielectric surface because of the solid boundaries. Since these regions exist within an external electric field (see Fig. 2.4.11), a force is produced. The direction of the force was said to be the same during each half AC cycle since at a particular location, the sign of the charges *and* the sign of the electric field change.

Orlov and Corke (2005), used Maxwell's equations in differential form to analyse the phenomenon:

$$\begin{aligned} \nabla \times \mathbf{H} &= \mathbf{j} + \frac{\partial \mathbf{D}}{\partial t} \\ \nabla \times \mathbf{E} &= -\frac{\partial \mathbf{B}}{\partial t} \\ \nabla \bullet \mathbf{D} &= \rho_c \\ \nabla \bullet \mathbf{B} &= 0 \end{aligned} \qquad , \qquad (2.4.7)$$

where **H** is the magnetic field strength, **j** is the electric current, **D** is the electric induction, **E** is the electric field strength, **B** is the magnetic induction,

and ρ_c is the charge density. They assumed that enough time has past for the charge to redistribute themselves (a few nanoseconds), so that the plasma is quasi-steady state. Thus, **j**, **H**, **B**, and their time derivatives are all equal to 0 and there was only one applicable Maxwell equation for the electric induction, **D**:

$$\nabla \bullet \mathbf{D} = \rho_c \ . \tag{2.4.8}$$

D is related to the electric field, **E**, through the dielectric coefficient, ε:

$$\mathbf{D} = \varepsilon \mathbf{E} \ , \tag{2.4.9}$$

and the electric field strength, **E**, is related to the electric potential, φ, by:

$$\mathbf{E} = -\nabla \varphi \ . \tag{2.4.10}$$

Thus, Eq. (2.4.8) becomes:

$$\nabla \bullet (\varepsilon \nabla \varphi) = -\frac{\rho_c}{\varepsilon_0} \ . \tag{2.4.11}$$

Orlov and Corke (2005) then substituted for the Debye length, λ_D, which is a characteristic length for electrostatic shielding in plasma (c.f. Fig. 2.4.11):

$$\lambda_D{}^2 = -\frac{\varepsilon_0}{\rho_c}\varphi = \left(\frac{e^2 n_0}{\varepsilon_0} \left(\frac{1}{kT_i} + \frac{1}{kT_e} \right) \right)^{-1} \ , \tag{2.4.12}$$

where e is the charge of an electron, n_0 is the number of molecules which were separated into ions and electrons by the electric field, k is Boltzmann's constant, and $T_{i,e}$ are temperatures of ion and electron species. Substituting into (2.4.11):

$$\nabla \bullet (\varepsilon \nabla \varphi) = \frac{1}{\lambda_D{}^2}\varphi \ . \tag{2.4.13}$$

Finally, by solving (2.4.13) for the electric potential, Orlov and Corke (2005) stated that the body force per unit volume of plasma is given by the Lorentz equation:

$$\mathbf{f}_b = \rho_c \mathbf{E} = -\left(\frac{\varepsilon_0}{\lambda_D{}^2}\right)\varphi\mathbf{E} \ . \qquad (2.4.14)$$

Here, $\mathbf{f}_b$, is the body force vector per unit volume of plasma. Thus, Orlov and Corke (2005) found that the force is proportional to the electric field multiplied by the electric potential, in contrast to Roth (see Eq. (2.4.4)). Note that in order to calculate this force, one requires knowledge of the volume of the plasma, which varies with time throughout the AC cycle. This body force was added to the 2D Navier-Stokes momentum equations in a simplified model by Shyy *et al*. (2002), and more recently by Suzen *at al*. (2005).

In the experimental work of Corke, the actuator was observed to draw ambient fluid towards the wall above the actuator, and then accelerate it away from the greatest electric field potential to produce a jet which is initially parallel to the wall, as illustrated in Fig. 2.4.12 (Corke *et al*., 2002). Enloe *et al*. (2004a), showed that the length of the lower electrode has no effect on the amount of plasma formation (and hence body force), provided that it was longer than that naturally occupied by the plasma. Thus, when designing electrodes, one must take care not to inadvertently limit the plasma formation by constructing a lower electrode that is too short; nor waste space by providing a lower electrode that is too big. For a $12kV_{P\text{-}P}$ input, Enloe *et al*. (2004a), found that the limit of plasma formation was around 12mm. With regards to the exposed electrode, the width appeared to have no effect on the discharge phenomenon. However, there was a dramatic effect in changing its height, where the momentum coupling increased as the height of the exposed electrode decreased. Thus, the exposed electrode should be made as thin as possible.

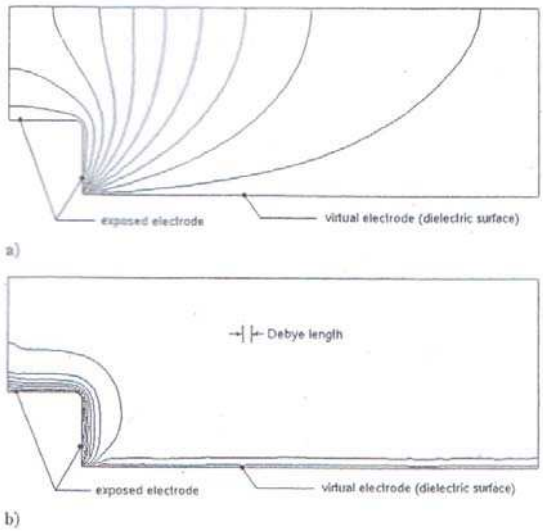

Figure 2.4.11. Electric potential for the plasma actuator geometry calculated numerically a) without and b) with plasma. From Enloe *et al*. (2004a).

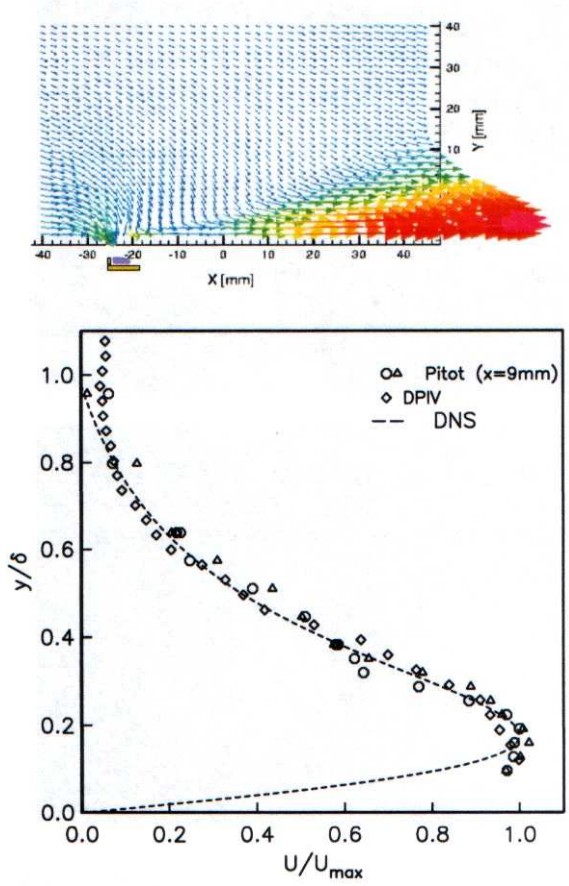

Figure 2.4.12. Measured velocity vectors (top) and time-averaged *U* component (bottom) of the flow field induced by an asymmetric plasma actuator. Measurements taken using PIV, a pitot tube and though DNS modelling of Eq. (2.4.4). From Corke *et al*. (2002).

In both of the above models it can be seen that the body force is directed towards increasing electric field gradient (i.e. towards the electrode), whereas the induced airflow has been observed to be away from the electrode. Enloe *et al*. (2004b) showed it is the negative-going part of the discharge cycle which couples more momentum into the air. In this part of the cycle, electrons are emitted away from the electrode towards the dielectric while ions are expected to be moving towards the electrode. It was suspected that it is the ions that transfer the most momentum to the neutral gas due to their increased mass compared to electrons (Roth, 2001a), yet their motion seems contradictory to the experimental observations.

Enloe *et al*. (2005), attempted to harmonise these conflicting observations. A laser beam was directed across the region around the plasma and the deflection was measured, which was proportional to the air density. This technique allowed the air density to be measured at time scales similar to the plasma formation (100kHz bandwidth), and data could be taken within 1mm of the electrode surface. Their observations showed that the air density builds up (2% above ambient) near the edge of the exposed electrode when the plasma is on because particles are taken from downstream of the plasma region by the action of the body force. This gas was subsequently released away from the electrode once the plasma quenches. After the release of gas, air was sucked in from above the actuator to replace it. This process of pressurisation and release was repeated twice per AC cycle and is consistent with flow measurements and visualisation.

The functional relationship between plasma frequency and voltage with induced velocity has been addressed by many authors. Roth (2004) found that

the maximum jet velocity increased linearly with the RF driving frequency and voltage. Johnson and Scott (2001) also showed that the induced-flow velocity was linearly proportional to the driving frequency (Fig. 2.4.13), and the peak velocity rises linearly with the duration of a plasma pulse (Fig. 2.4.14). Contrary to Roth (2004), the PIV measurements of Corke and Post (2005) showed that the maximum velocity produced by an asymmetric electrode arrangement varies as $E^{7/2}$, as illustrated in Fig. 2.4.15. Orlov and Corke (2005) simulated the plasma by a lumped circuit model and found that the dissipated power in the plasma is also proportional to $E^{7/2}$. The exact reasons for these relationships are not well understood.

There is still much uncertainty as to how the plasma creates the observed airflow, and much has changed over the duration of this study (started Sept 2002). It should be noted that the majority of the papers referenced in this section have been published during the last 5 years and in fact, Roth's conclusion that the induced flow is a Glauert wall jet (Roth, 2004), post-dates the conclusions in Chapter 4.

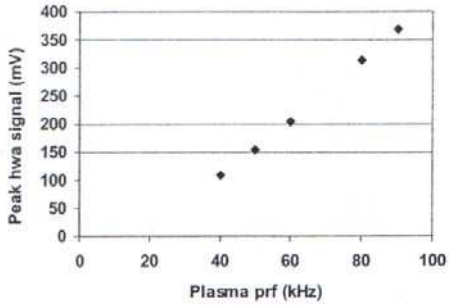

Figure 2.4.13. Effect of the excitation frequency on the induced flow around a single symmetric electrode in initially static air. Measurements were taken with a hotwire at y = 1mm, z = 3.5mm, (400mV output ≈ 0.8m/s). From Johnson and Scott (2001).

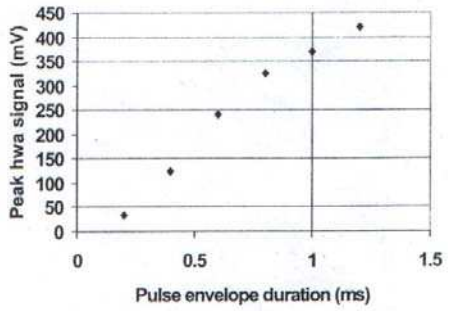

Figure 2.4.14. Effect of the plasma pulse duration on the induced flow around a single symmetric electrode in initially static air. From Johnson and Scott (2001).

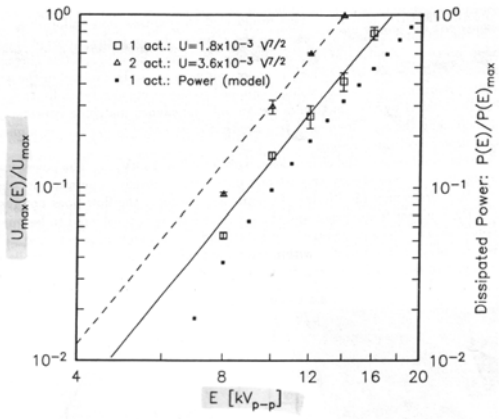

Figure 2.4.15. Dependence of plasma actuator maximum induced velocity (open Symbols) and dependence of plasma dissipated power based on lumped capacitance model (closed symbols) as a function of AC voltage. Power calculations from Orlov and Corke (2005). From Corke and Post (2005).

2.4.3. Plasma Actuators for Aerodynamic Flow Control

The first attempt at manipulating subsonic flows using surface glow discharge plasma actuators was performed by Roth *et al.* (1998) and Sherman (1998). Here they noted that the boundary layer viscous dissipation for a long range commercial transport is estimated to be roughly 5000W/m^2, whereas the surface plasma operates at around 320W/m^2 or less, suggesting that net energy savings could be possible if the plasma can be demonstrated to significantly reduce drag.

Roth *et al.* (1998) and Sherman (1998), used either streamwise or spanwise arrays of symmetric or asymmetric surface plasma actuators in laminar, transitional and turbulent boundary layers. The plasma acted as an efficient turbulent trip for the laminar case and thus caused a large increase in drag. For the streamwise symmetric electrodes, the plasma induced large counter-rotating streamwise vortices that also increased the drag. The streamwise vortex formation around a single streamwise-oriented symmetric actuator is shown in Fig. 2.4.16. The resulting velocity profile downstream of an array of such actuators is shown in Fig. 2.4.17, where the vortices increased the flow near the wall (increasing the skin friction), while retarding it further out. A significant thrust force, however, was produced by using asymmetric actuators oriented in the spanwise direction, such that the plasma forcing is directed with the free-stream flow (co-flow). Drag was increased by directing the asymmetric actuator force upstream (counter-flow), suggesting that the actuator acts as a gas flow accelerator, adding or subtracting a reactive thrust to the test plate. Though their study did not use optimal actuators or

geometrical arrangements, it did demonstrate that surface plasma actuators could produce significant effects on airflow.

The plasma effect was lost at high Reynolds numbers which lead Roth to suggest 'peristaltic' plasma actuators to try to increase the plasma-induced gas velocity (Roth *et al*. 2004). This approach used several actuators which were activated at slightly different times using a polyphase power supply, which enabled a travelling wave of plasma to be produced. This technique was also used by Corke and Matlis (2000) to excite axisymmetric jets.

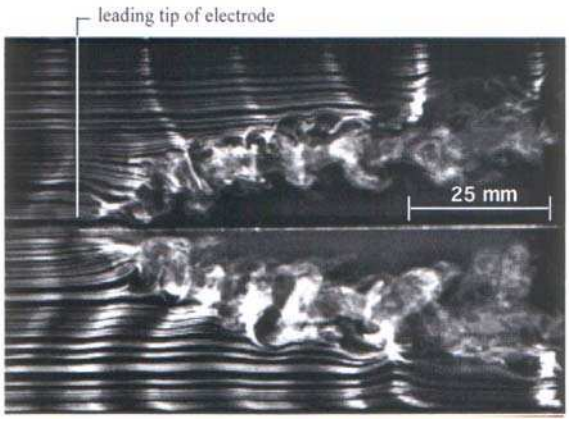

Figure 2.4.16. Horizontal smoke wire flow visualisation of a single streamwise electrode with symmetric plasma formation. Note formation of counter-rotating vortices. From Roth *et al.* (1998).

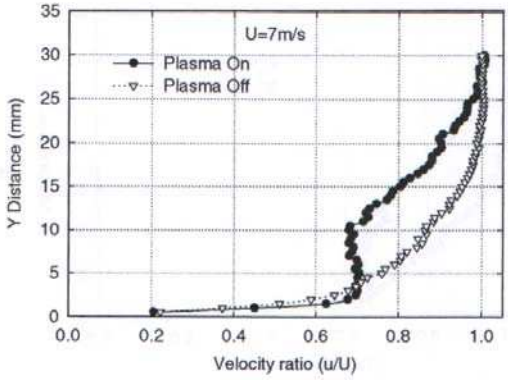

Figure 2.4.17. Wall normal velocity profile 28mm downstream of symmetric streamwise electrodes. Plasma excited at 3kHz, 5.1 kV. From Roth *et al.* (1998).

BAE SYSTEMS became interested in plasma technology for aerodynamic applications at around the same time as Roth (Johnson and Scott, 2001, Scott *et al*., 2002a, 2002b). Based on studies in the former Soviet Union, their interest was in initiating plasma at the nose of a blunt body for supersonic flows, and generating large surface area discharges for subsonic flow. These studies are the motivation for this thesis.

Tests of plasma actuators in initially static air showed that the plasma actuators could produce maximum induced velocities on the order of 1m/s. It was postulated that the plasma could be used to manipulate regions where the flow is very sensitive, thus creating global changes to the flow structure. Initial tests on an unswept 2D wing showed the plasma to be an efficient laminar-turbulent trip, which delayed stall by up to 2°. It was noted that to prevent stall, only one electrode at the correct location would be necessary. Power requirements were expected to be only 100W/m. Attempts were also made to control the leading-edge vortices shed by a swept wing (Fig. 2.4.18). Small, but significant changes were observed in lift (2.5%), roll (2%) and yaw (4.5%) forces. However, the electrode needed to be placed at the separation point within sub-millimetre accuracy to achieve the desired effect.

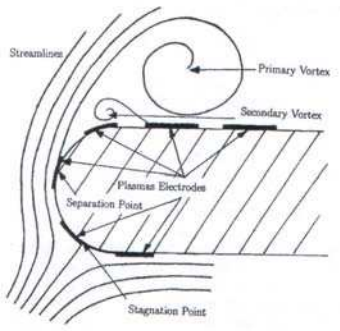

Figure 2.4.18. Schematic of plasma electrodes used to control leading edge vortices on a swept wing. From Johnson and Scott (2001).

Corke has undertaken many studies on surface plasma actuators for wing flow-control devices (Corke *et al*. 2002, Post 2001, Post and Corke 2003, 2004, Corke *et al*. 2004, Corke and Post 2005). Asymmetric actuators were constructed from copper foil tape separated by layers of Kapton film (typically 0.1mm thick). Sinusoidal excitation was used with amplitude 7-12k$V_{p\text{-}p}$ at typically 3-10kHz. These actuators were then placed at various positions on the suction surface of airfoils and actuated such that the plasma-induced flow was with the mean flow direction (i.e. spanwise orientation), thus adding momentum to the near wall region. The amount of lift increased (Corke *et al*. 2002), and stall was delayed by up to 8° by placing an actuator at the airfoil leading edge at a Reynolds number, based on cord length, c, of Re_c = 158,000 (Fig. 2.4.19, Post and Corke 2003).

Plasma actuators have also been used to control the dynamic stall on oscillating airfoils simulating helicopter rotors (Post and Corke 2004). Such actuators have been used in a 'steady' manner, whereby the plasma is continuously activated, and in an 'unsteady' manner, where the plasma formation is switched on and off at low frequency. The 'unsteady' mode can be used to excited fluid instabilities and is obviously beneficial for reducing the energy input since the plasma is on for only a fraction of the time (Corke *et al*. 2004).

This research lead Corke to hypothesise a completely 'electric wing', whereby the leading edge slat and trailing edge flap could be replaced by plasma actuators which are activated as and when required (i.e. at take-off and landing), without detrimental effects when not in operation (Corke *et al*. 2004, Corke and Post 2005). This would greatly reduce the weight of the wing as the

mechanical apparatus for moving slats/flaps would be redundant. This application is not just limited to separation control of wings, but has also been demonstrated for turbine blades (Huang *et al*. 2003, Hultgren and Ashpis 2003), and to effect the vortex shedding from circular cylinders (Asghar and Jumper 2003). Streamwise plasma actuators at the leading edge of an airfoil ('plasma vortex generators') have been suggested (Post and Corke 2003), and MEMS scale plasma actuators have even been attempted by Lorber *et al*. (2000).

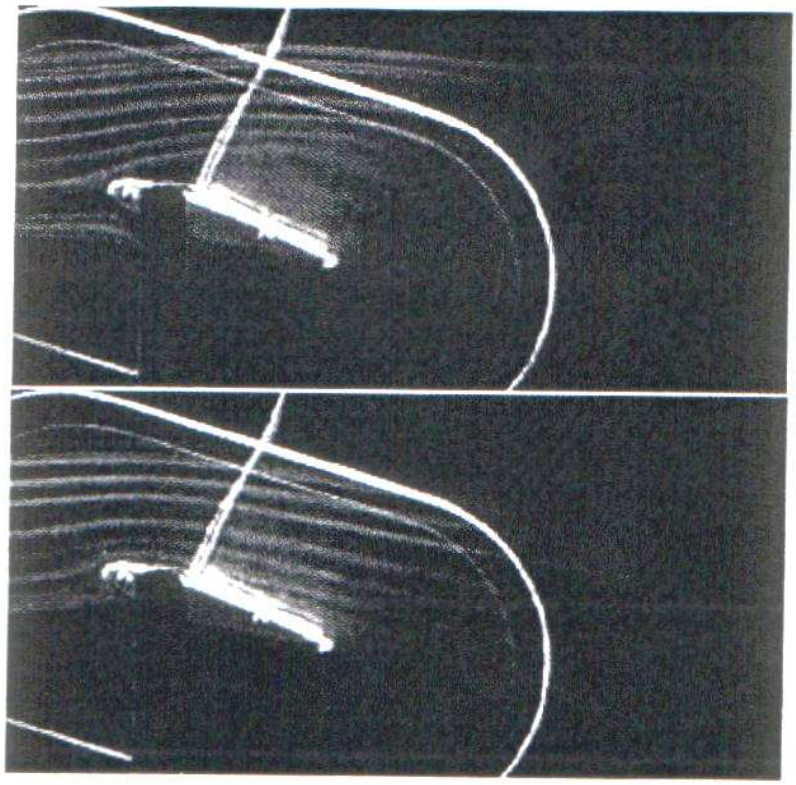

Figure 2.4.19. Visualised flow around a NACA 0015 airfoil at 16° angle of attack. Flow direction from left to right. Top picture without plasma. Bottom picture with plasma formed at $x/c = 0$ promoting co-flow forcing over the suction surface. Flow reattachment is clearly visible with plasma. From Corke *et al*. (2004).

Wilkinson (2003) used plasma to generate an oscillatory flow over a surface with the intention of using it to produce a spanwise oscillation within a boundary layer to reduce skin-friction drag. Using asymmetric electrodes with a frequency modulated input single, plasma was created on either side of the exposed electrodes which oscillated with time. Uncompensated hot-wire anemometry and Pitot tubes were used to measure the induced flow in initially static air. However, due to the frequency modulation there were regions within the oscillation cycle where both sides of the electrodes form plasma (one side increasing in strength whilst the other side was diminishing). This created a bi-directional forcing which drives a mean flow between the electrodes, as shown in Fig. 2.4.20. This approach was deemed unsuitable for generating spanwise oscillation and the approach was not testing in a turbulent boundary layer.

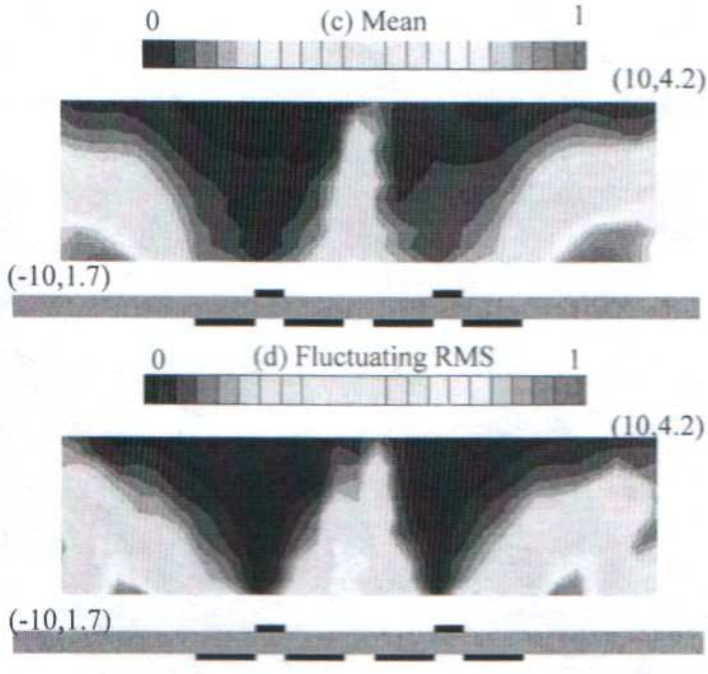

Figure 2.4.20. Contour plot of mean and fluctuating velocity magnitude around a pair of plasma electrodes, each with oscillatory plasma formation on either side of the electrode. Plasma excitation is at $8.5kV_{pp}$ at 3kHz, with a modulation frequency of 20Hz. From Wilkinson (2003).

Chapter 3

Experimental Facility and Technique

3.1. Introduction

This chapter outlines the experimental facility used in this study. Details of the wind tunnel are given, along with details of the diagnostic tools and the data acquisition system. The plasma generation system is explained and key parameters of the plasma excitation are defined. Basic data processing techniques are given although detailed experimental procedure and data analysis techniques will be presented as and when required in later chapters.

3.2. Wind Tunnel

The wind tunnel used in this study was a closed-return wind tunnel, with an octagonal cross section as depicted in Fig. 3.2.1. It was powered by a 7.5kW motor and fan. A maximum flow velocity of 10m/s was attainable in the test section, but only due to the fan speed being limited by the fan controller.

The test section was 3m long and has cross-sectional dimensions of 508 x 508 mm. The test section walls diverged slightly such that the streamwise pressure gradient was nearly zero. Upstream of the tests section was a 7:1 area ratio contraction preceded by a series of mesh screens and honeycomb to enhance flow uniformity and reduce turbulence. Free stream turbulence intensity in the test section, u'/U_∞, was 0.4% at U_∞ = 1.7m/s.

The turbulent boundary layer in the latter part of this study was developed over a 3m long smooth flat plate, set in the upper part of the test section as

depicted in Fig. 3.2.2. This boundary layer plate was constructed from polished MDF board, 20mm thick. The leading edge consisted of a symmetric super-ellipse with semi-major axis of 75mm. The trailing edge consisted of an adjustable flap which terminated at a sharp point. The angle of this flap was adjusted such that leading edge separation was avoided. The boundary layer was tripped into a turbulent state using an array of 3mm diameter by 10mm high rods. These were placed 100mm downstream of the leading edge and covered a streamwise distance of 60mm. Note that the lower surface of the test plate is the test surface in this study (i.e. gravity acts in $+y$ direction).

Measurements of the boundary layer were typically taken 2.3m downstream of the leading edge. With a free stream speed, U_∞, of 1.7m/s the boundary layer thickness, δ, was approximately 70mm. The corresponding Reynolds number based on the streamwise distance, x, was $Re_x = U_\infty x/\nu \approx 2.6\text{x}10^5$ and the Reynolds number based on momentum thickness, θ, was $Re_\theta = U_\infty \theta/\nu \approx 1000$.

During flow measurements the free stream speed, U_∞, and the ambient temperature, T_∞, were simultaneously recorded so that the boundary layer profiles could be corrected for changes in these conditions. The free-stream flow velocity was measured using a fixed Dantec 55P15 hot-wire probe placed 100mm away from the wind tunnel wall to avoid the boundary layer. Ambient temperature was measured using an in-house manufactured temperature device, which contained a LM35 precision integrated-circuit temperature sensor previously calibrated to a platinum resistance thermometer.

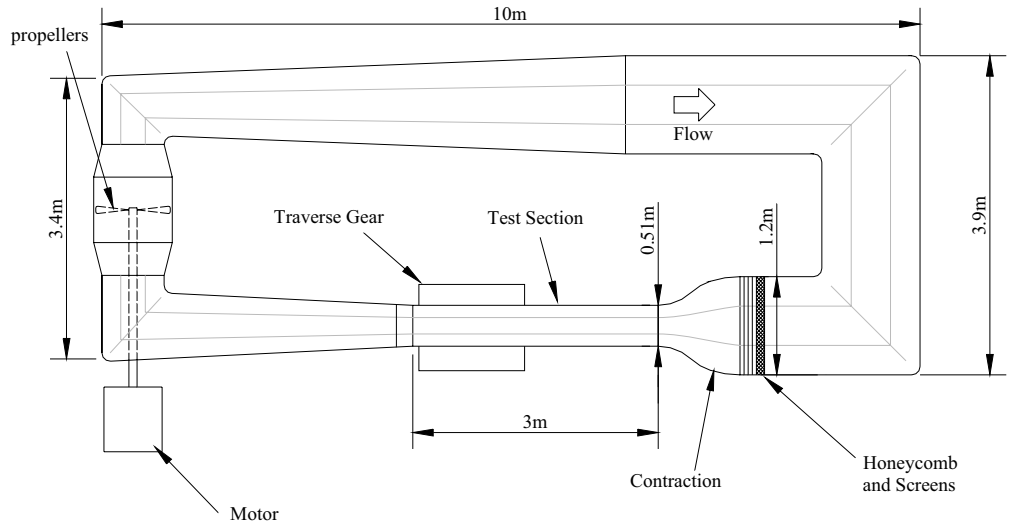

Figure 3.2.1. Schematic of the octagonal cross section closed return wind tunnel.

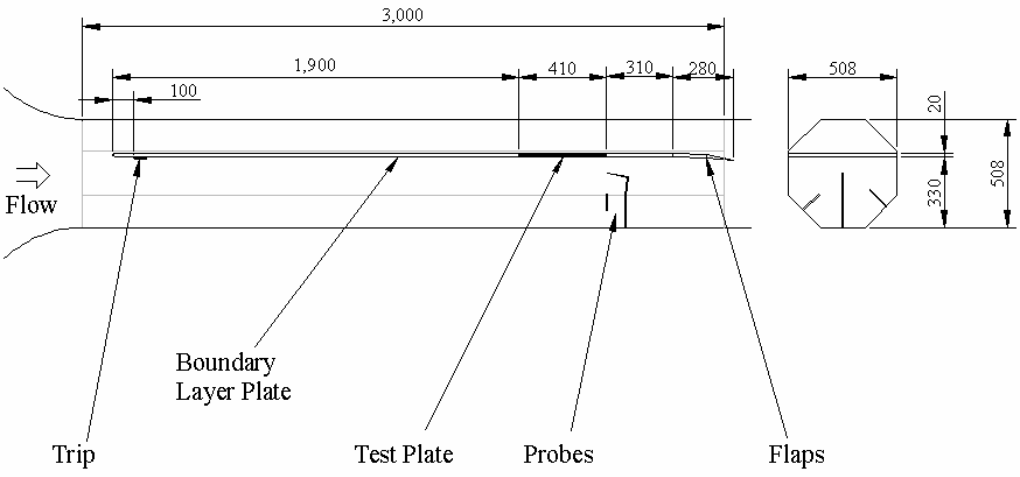

Figure 3.2.2. Cross section of test section. All dimensions in mm

3.3. Thermal Anemometry System

Flow diagnostics were achieved using hot- and cold-wire anemometry. The thermal anemometry system consists of a Dantec 56B10 frame, incorporating a Dantec 56N22 Mean Value Unit, with numerous plug-in units. For velocity measurements, Dantec 56C01 Constant Temperature Anemometers (CTA) and Dantec 56C17 CTA bridge units were used together with Dantec 56N20 signal conditioners. For temperature measurements, Dantec 56C20 temperature bridges were used. All anemometry bridges were placed within a copper-walled sealed enclosure to minimise radiated electronic noise entering the system, typically due to the plasma.

The velocity measurement system was such that a hot-wire probe was connected to the 56C01 CTA unit so that it forms one arm of a Wheatstone bridge. The bridge was servo-controlled, with programmable gain and bandwidth. As the heat loss from the sensor was changed by increased/decreased convection due to an increased/decreased flow velocity, the resulting temperature change of the sensor caused an imbalance of the bridge. This imbalance was corrected by the servo-amplifier so that the probe resistance (and hence temperature), remained constant. The bridge voltage, and thus flow velocity, was monitored via a BNC connection at the rear of the 56B10 frame.

Prior to data acquisition, the hot-wire voltage signal was fed through the 56N20 signal conditioner unit. This enables the signal to be passed through a 2^{nd} order low-pass Butterworth filter, a 1^{st} order high-pass filter, and a gain amplifier. In the experiments, the signal was low-pass filtered at half the

sampling frequency (anti-aliasing filter) and amplified with a gain of 5 to minimise the signal-to-noise ratio (SNR). The high-pass filter was not used.

It was found that the plasma radiated high frequency noise (> 50kHz) into the anemometer signal after the signal conditioner unit. An additional 25kHz passive filter was subsequently usel in the signal line prior to data acquisition. This proved successful in eliminating these high frequency electrical noise components.

A Dantec 55P16 single-normal probe was used to study the plasma actuators in initially static air and a Dantec 55P15 boundary layer probe was used to study the effect of the plasma actuators in the boundary layer. Both of these probes used a 1.25mm long platinum-plated tungsten wire, 5μm in diameter. The 55P16 had straight prongs which allowed the wire to be oriented parallel to the wall with the probe support normal to the wall. This probe type also included the probe support in a low-cost, semi-disposable unit which was advantageous for use near the plasma as many probes were destroyed by electrical arcing. The 55P15 boundary layer probe had bent prongs that allowed the wire to be placed close to the wall while the probe support is some distance away, thus minimising the aerodynamic interference from the probe body. The boundary layer probes were mounted in a modified L-shaped probe holder (Dantec 55H22) which had been bent such that the probe stem makes an angle of around 5° to the test plate surface to ensure the wire could be traversed to the wall. The two probes are depicted in Fig. 3.3.1a and b.

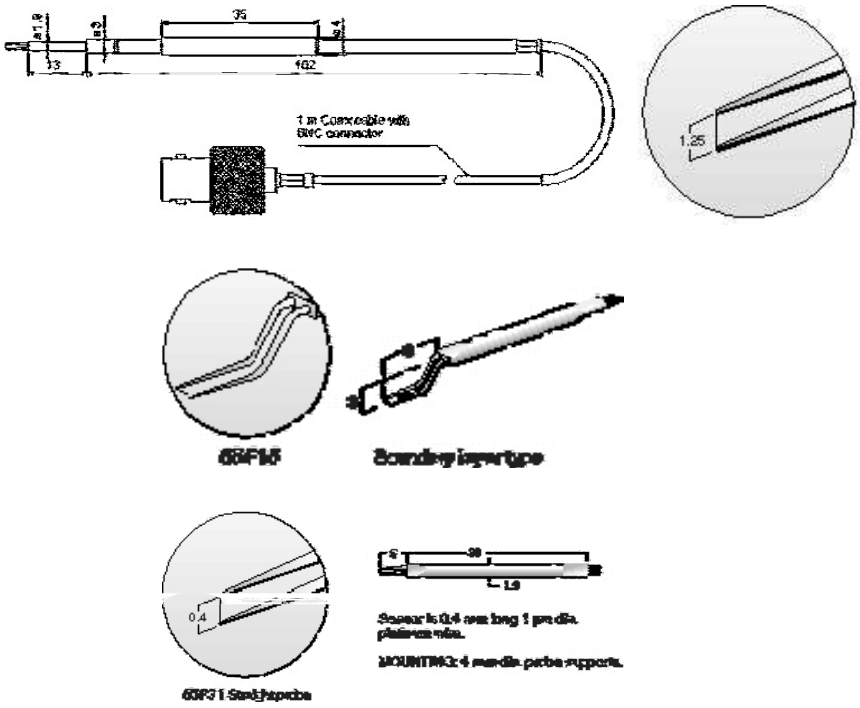

a)

b)

c)

Figure 3.3.1. Probe types used during experiments. a) 55P16 single-normal probe used for velocity measurements in initially static air. b) 55P15 single-normal probe used for velocity measurements in a turbulent boundary layer. c) 55P31 cold wire probe used for air temperature measurements. Reproduced from Dantec Dynamics.

Both probes types were used at a heating ratio:

$$a = \frac{R_w}{R_a} = 1.8 \ , \qquad (3.3.1)$$

where R_w is the hot resistance of the wire and R_a is the resistance of the wire at ambient temperature. This set the probe at a high operating temperature which enabled high sensitivity of the probe to velocity whilst minimising sensitivity to ambient temperature changes and preventing oxidization of the wire. Bruun (1995), stated that to avoid oxidization on tungsten wires, the maximum

temperature should be below 350°C. Assuming ambient temperature is approximately 20°C, the mean wire temperature can be evaluated using:

$$R_w = R_{20}[1 + \alpha_{20}(T_w - T_{20})] \ , \qquad (3.3.2)$$

where R_{20} is the probe resistance at 20°C and α_{20} is the temperature coefficient of resistivity at 20°C. Using typical values of R_{20} = 3Ω and a_{20} = 0.0036°C^{-1}, Eq. (3.3.2) gives the mean wire temperature, T_w = 240°C. The maximum temperature along the wire length, $T_{w,max}$, for a 5μm diameter wire with length 1.25mm at a = 1.8, can be approximated by (Bruun, 1995):

$$\frac{(T_{w,\max} - T_{20})}{(T_w - T_{20})} = 1.3 \ , \qquad (3.3.3)$$

yielding $T_{w,max}$ = 310 °C, which is below the oxidization temperature. The overheat ratio for the probes was set as outlined by the Dantec manuals, taking care to take the probe prong and cable resistances into account.

A cold wire probe was used to take air temperature measurements around the plasma actuators in initially static air and in the turbulent boundary layer. This was a Dantec 55P31 resistance thermometer probe with 0.4mm long platinum wire, 1μm in diameter, as shown in Fig. 3.3.1c. The probe was used in constant current (CC) mode, and controlled by the 56C20 temperature bridge. A small current was applied to the wire (0.2mA) which maintained the wire very close to ambient temperature. Any change in the fluid temperature changed the resistance of the wire and thus the voltage applied to maintain this current changed in direct proportion. Such probes typically have a cut-off frequency of around 2kHz. The sensitivity of the probe to temperature was checked within the temperature bridge by applying a 1% change in current,

simulating a 1% change in probe resistance (and hence temperature). The exact sensitivity can be calculated from:

$$V/°C = TCR \frac{R_0}{R_0 + R_l + R_c} \Delta V \quad , \qquad (3.3.4)$$

where, ΔV is the voltage change experience when the 1% unbalance is applied, TCR is the temperature coefficient of resistivity in %/°C, R_o is the probe resistance at ambient temperature, R_l is the probe lead resistance and R_c is the cable resistance. The calculated sensitivity of the probe was typically -0.48 V/°C and a check was performed by observing the voltage change due to ambient temperature drift over a 24 hour period, as shown in Fig. 3.3.2. The calibrated sensitivity was within 7% of the calculated value, although the calculated value was considered more accurate due to the inaccuracy of the temperature sensor used in the calibration (±0.5°C).

For further details about the operation of thermal anemometers the reader is referred to Bruun (1995).

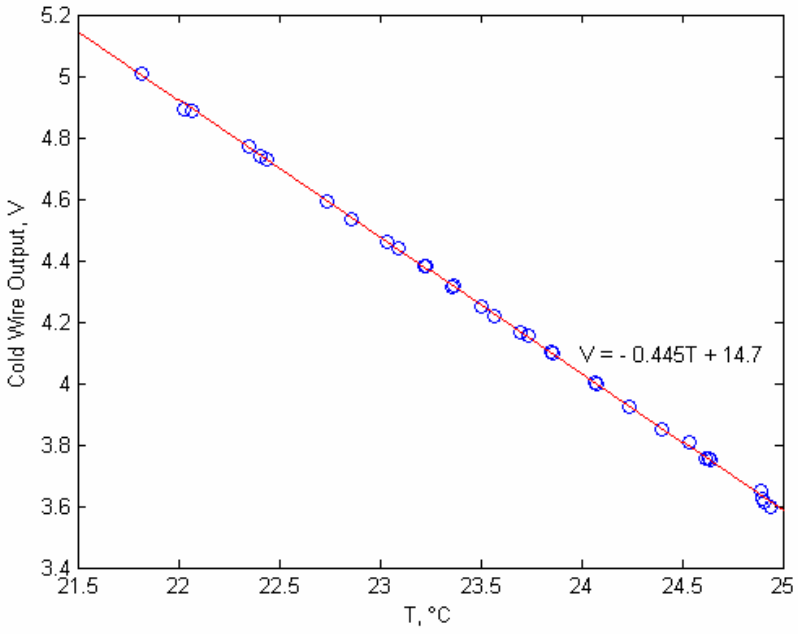

Figure 3.3.2. Calibration of the cold wire probe.

3.4. Hot Wire Probe Calibration

The anemometer units were optimised for each hot-wire probe prior to use in the experiments. The procedure involved applying a square wave to the bridge and observing the anemometer output. This is equivalent to a step change in flow velocity and thus measures the response time of the probe to an instantaneous velocity change. The optimum response to a square wave was obtained by adjusting the anemometer unit gain, filter and high-frequency balance until a response signal similar to Fig. 3.4.1a was obtained (Bruun, 1995). Following the procedure outlined in the Dantec instruction manuals, the typical response curve shown in Fig. 3.4.1b was achieved which shows that the cut-off frequency, f_c, of the probes was about 50 kHz.

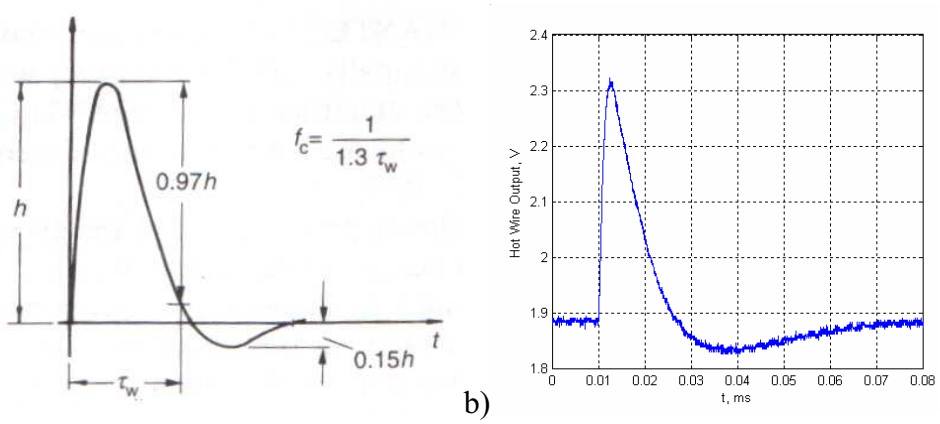

a) b)

Figure 3.4.1. Optimisation of hot-wire for a square wave test. a) Optimal response from Bruun (1995). b) Boundary layer probe response to a square wave at U_∞ = 3m/s, a = 1.8, after anemometer optimisation. The cut-off frequency, f_c, is 51 kHz.

Calibration of the hot-wire probes were performed against a Dantec 54N60 FlowMaster. This was a velocity sensor with calibration traceable to Dantec Measurement Technology, Denmark, in the range 0-30m/s. The sensor had an accuracy of ±0.02m/s and corrected itself for ambient temperature using a thermistor. The general procedure involved placing the hot-wire sensor close to the FlowMaster in the wind tunnel and varying the flow speed over the entire range expected during a particular experiment. The hot-wire signal and FlowMaster velocity were simultaneously sampled and averaged over a period of 10s, thus giving a relationship between hot-wire voltage and flow velocity. The wind tunnel speed was ramped up and down to check for hysteresis and 17 calibration points were usually taken. Care was taken to ensure that the wind tunnel flow speed was steady prior to each data acquisition.

However, the hot-wire probes also responded to changes in the temperature of the ambient fluid. Calibrations were consequently taken before and after experiments to observe the effect of this temperature change on the hot-wire response. The experimental results were then corrected for ambient temperature drift by linearly interpolating calibration curves at different temperatures.

Difficulties were encountered when calibrating the hot-wire probes at low speed (U_∞ < 0.5m/s). This was due to a problem with the wind tunnel shaft coupling between the motor and fan. The coupling had become worn and severe vibrations were introduced into the shaft at low speed, which meant that the minimum stable flow speed obtainable in the test section was 0.5m/s. Since the hot-wires were used to measure air velocity in initially static air and near the wall of a turbulent boundary layer, it was necessary to calibrate the

probes below this speed (to U = 0m/s in the initially static air testing and to U = 0.25m/s for the boundary layer testing).

It is well known that the hot-wire characteristics change at low-velocities because of the increasing influence of free convection on the free stream flow, due to the buoyant plume driven by the elevated temperature of the wire. Specifically, it is found that the hotwire characteristics deviate significantly from King's Law at low speed (King, 1914), defined as:

$$E^2 = A + BU^n \ , \qquad (3.4.1)$$

where, E is the anemometer voltage, U is the flow velocity, A and B are constants to be found from the calibration procedure, and the exponent, n = 0.5. Collis and Williams (1959), appear to be one of the first to study the hot-wire response at low speed and find that the square root relationship of King becomes invalid for wire Reynolds numbers less that about 44. This marks the onset of eddy-shedding from the wire. It was suggested that for $0.02 < \mathrm{Re} < 44$ a velocity exponent, n, of 0.45 should be used instead. However, there is a further deviation from this exponent law for $\mathrm{Re} \lesssim 0.1$ (U < 0.3m/s for these probes), whereby the buoyancy driven flow becomes comparable in magnitude to the forced convection (free-stream) flow, thus necessitating careful calibration at very low speeds.

Many methods have been suggested for calibrating hot-wire probes at low velocities which can be generalised into two techniques. Firstly, the fluid is moved past the probe and the velocity measured with a pre-calibrated device. This can be inaccurate at low speeds, especially if a pitot-tube is used. Dantec manufactures calibration jets (54H10 and 55D90), in which compressed air is forced through a nozzle and the flow speed derived from the pressure drop

across the nozzle. However, such facilities perform poorly below 0.5m/s due to inaccuracies in the pressure measurement. In order to overcome these problems, Almquist and Legath (1965), and Manca *et al*. (1988), used fully developed laminar pipe flow of air, for which the Blasius velocity profile is accurately known for a prescribed flow rate. Calibration was then performed by varying the flow rate with the probe at the pipe centreline.

The second technique involves moving the probe through quiescent fluid at a known velocity. For example, Aydin and Leutheusser (1980) and Tsanis (1987) use plane Couette flow of air forming between a moving sled and the ground. Dring and Gebhart (1969) moved a container of fluid past a fixed probe and Tewari and Jaluria (1990) used a probe on a sled moving in quiescent air. Problems are frequently encountered with probe vibration using such techniques and it is difficult to ensure that the fluid is quiescent, especially if the medium is a gas.

Bradshaw (1971), suggested calibrating the hot-wire probe in the settling chamber of the wind tunnel and it is this method that was adopted for the plasma-induced flow measurements in initially static air (55P16 probes). The technique is relatively straightforward and does not require moving the system to another laboratory (which would introduce much uncertainty into the calibration due to temperature differences, electrical connections, etc.). Due to the change in wind tunnel area across the contraction section, the flow speed in the settling chamber was approximately $1/6^{th}$ that in the test section. Thus, flow speeds of below 0.1m/s could be achieved in the settling chamber before the problems with the fan coupling were encountered ($U_{test\ section} < 0.5$m/s). A hole was drilled into the settling chamber wall and the 55P16 probe was

inserted together with the FlowMaster, such that the devices had a separation of 10mm. Both probes were placed 200mm from the settling chamber wall to avoid the boundary layer there. Calibration was actually performed at two different locations in the settling chamber. Care was taken to rotate the hot wire perpendicular to the flow direction and the two calibrations were used to check the consistency of orientation. After calibration, the probe and connecting wires were moved into the test section for experiments.

This technique does, however, have disadvantages since the probe is not calibrated *in-situ*. Differences in conditions between the settling chamber and test section may introduce calibration errors (e.g. temperature differences, probe orientation). For the plasma-induced flow measurements in initially static air, these problems were minimised since there was no free-stream flow. It was, however, necessary to take a point on the calibration curve for which the wind tunnel is turned off (i.e. $U_\infty = 0$). It is important to note that this should not be interpreted as "zero-flow" velocity as the buoyant plume, driven by the heated wire, still exists. Here, this point is to be interpreted as "the voltage for which there is no external flow".

A 4th order polynomial curve fit was applied to the calibration data points in the form:

$$U = AE^4 + BE^3 + CE^2 + DE + F \ , \qquad (3.4.2)$$

where A, B, C, D and F are constant to be determined. Bruun (1995) stated that this method gives comparable accuracy to eq. (3.4.1) which is solved for A, B and n using least square fitting. However, the 4th order polynomial curve fit is much easier to implement on a computer.

For the hot-wire measurements in the turbulent boundary layer (55P15 probes), many problems were encountered using this calibration technique due to differences between the flow in the settling chamber and that in the test section. These differences generally caused the measured flow velocity to be higher than the true value. Investigations showed that the settling chamber temperature was 0.1°C above that in the test section, which was partially responsible for the observed behaviour. More importantly, there appeared to be some non-uniformity in the settling chamber flow. Figure 3.4.2 shows the effect of rotating the probe in the air-flow in the test section and each hole in the settling chamber. The probes sensitivity to yaw in the test section is parabolic, as expected. However, in the settling chamber there is a peak velocity detected for angles to either side of the axis of the wind tunnel. This suggests that there is some non-uniformity of the flow, which is expected to be caused by the honeycomb or from the 90° bend upstream of the settling chamber (c.f. Fig. 3.2.1). Note that this non-uniformity is exemplified by the L-shaped probe holder because the wire is located 65mm from the axis of rotation. Further problems were encountered because the wind tunnel had to be run to the maximum speed ($U_{\infty,\ test\ section} \approx 10$m/s) in order to obtain the same free-stream speed in the settling chamber as used during boundary layer testing ($U_\infty \approx 1.7$m/s). This caused additional heating and significant temperature changes during the calibration ($\Delta T \approx 0.3$°C).

For these reasons it was decided to calibrate the boundary layer probes in situ in the test section and extrapolate the low-speed region ($U_\infty < 0.5$m/s). The characteristics of the probe in this low-speed region were known from the settling chamber calibration. Thus, it is reasonable to plot this low-speed trend

onto the test section calibration. It should be noted that the measured velocity during boundary layer testing was never below 0.25m/s because of the "wall-effect" on the probe (Bruun, 1995). Thus extrapolation was only necessary for the 0.25 – 0.5m/s range. Figure 3.4.3 shows several curve fitting methods for a typical 'simulated' test section calibration. Here, a calibration performed in the settling chamber has been curve-fitted on data where U_∞ > 0.5m/s (i.e. as is possible in the test section), so that the extrapolated fit can be compared to the true curve. It is observed that the curve suggested by Collis and Williams (1959) performs poorly in the low-speed region. However, it does appear that the 4th order polynomial fit can be extrapolated provided the voltage at zero free-stream velocity is included in the fit. This results in a curve fit within 0.015m/s of the true polynomial fit (6% error at U_∞ = 0.25m/s), which is comparable to the accuracy of the FlowMaster itself. This technique was used for the calibration of the boundary layer type probes (55P15, Chaps. 4-7), whereas the settling chamber calibration technique was used to measure plasma-induced airflow in initially static air (55P16, Chaps 8-10).

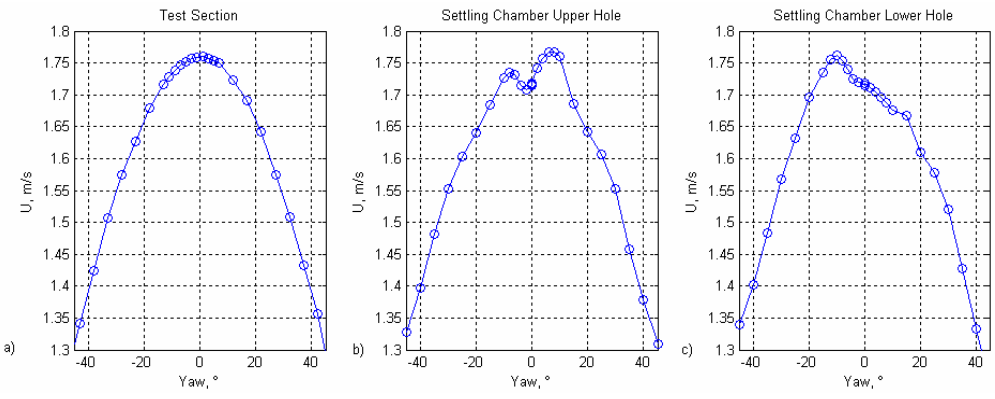

Figure 3.4.2. Effect of probe orientation for a local free stream flow speed of 1.7 m/s in a) the test section, b) the settling chamber upper hole, c) the settling chamber lower hole. The two settling chamber holes were vertically separated by 50mm and the wire extended around 65mm from the axis of rotation.

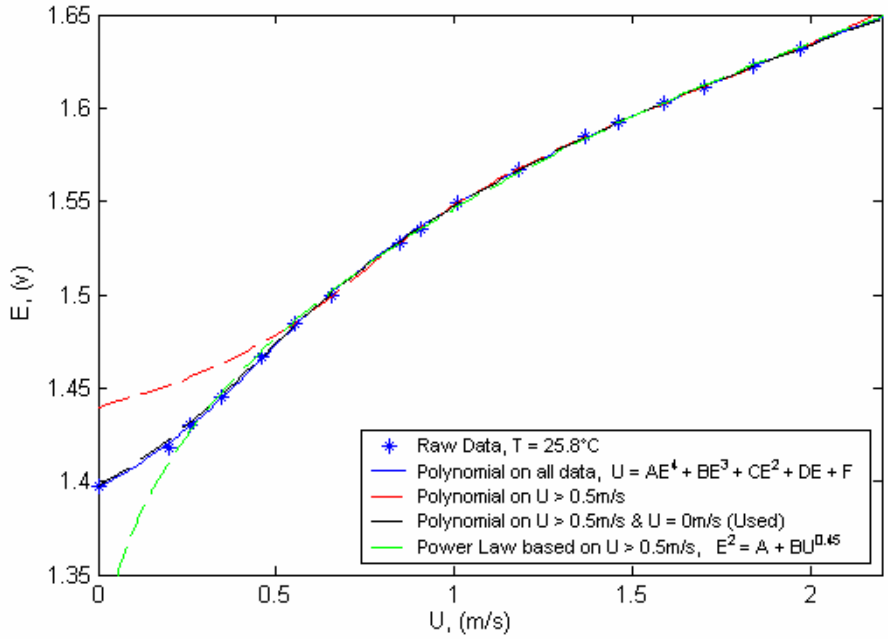

Figure 3.4.3. Different curve fits applied to a calibration curve in the settling chamber of the wind tunnel. 4th order polynomial fitting using $U > 0.5$ m/s and U = 0m/s was within 0.015 m/s of the curve using all the data points, suggesting extrapolation into the low-speed region can be performed with accuracy comparable to that of the FlowMaster.

For the turbulent boundary layer investigation, the probe used to measure the boundary layer and the free-stream reference probe were calibrated simultaneously. It was, however, discovered that there was also some non-uniform flow in the test section. Figure 3.4.4 shows the variation in streamwise velocity measured with a traversable hot-wire probe with reference to a fixed probe at y = 155mm, z = -100mm. It can be seen that there is a spanwise variation in mean velocity across the test section, with magnitude of around 0.03m/s. The low speed region for y < 80mm marks the edge of the boundary layer. Figure 3.4.5 shows the variation in temperature across the test section, measured with a traversable cold wire probe referenced to a

temperature sensor at y = 30mm, z = -90mm. This shows a reasonably linear variation of temperature with height through the test section, and a maximum difference of 0.15°C. To ensure that the FlowMaster, boundary layer hot wire, free-stream hot wire and temperature sensor were all located in near identical flow conditions during calibration, they were located as depicted in Figs. 3.4.4 and 3.4.5. Note that the boundary layer tests were performed near the tunnel centreline ($z \approx 0$) for $y < 120$mm.

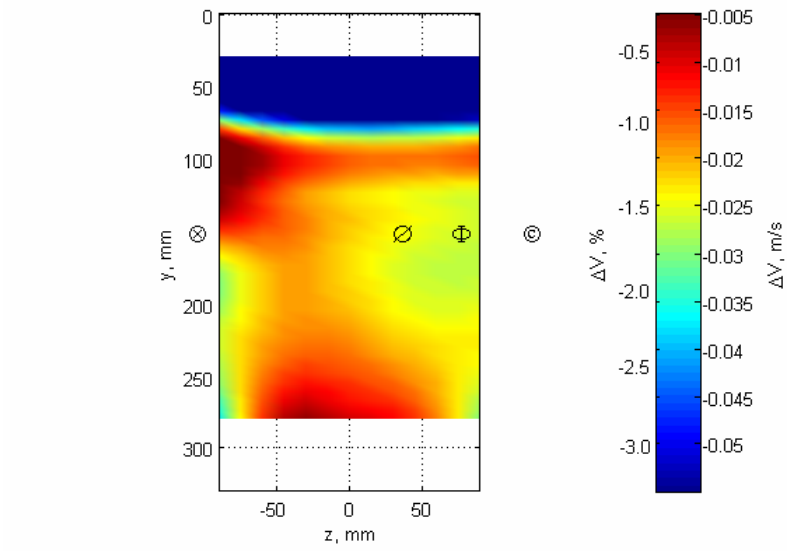

Figure 3.4.4. Variation in free-stream velocity across the test section. z = 0 corresponds to the test section centreline and y = 0 corresponds to the boundary layer plate. The velocity difference was referenced to the velocity at y = 155mm, z = -100mm. Temperature sensor location, ⊗; boundary layer probe, Ø; FlowMaster probe, Φ; and free stream probe, ©.

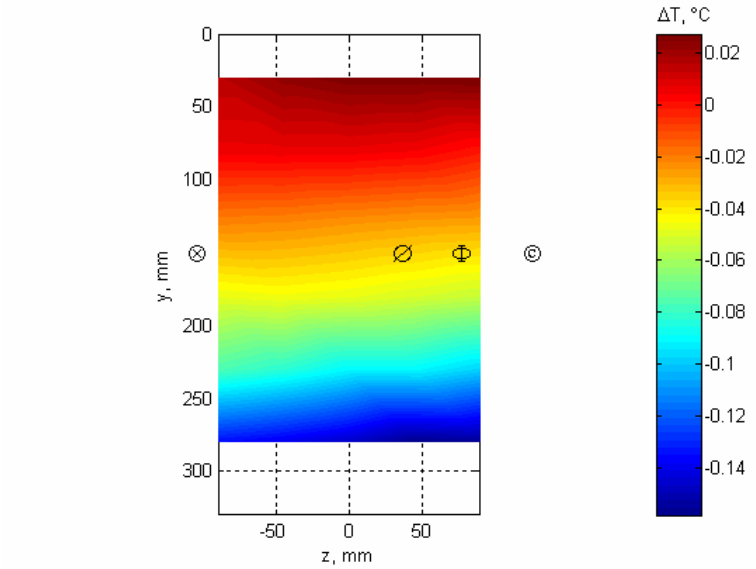

Figure 3.4.5. Variation in temperature across the test section. Temperature difference was referenced to z = -90mm, y = 30mm. Ambient temperature drift has been accounted for. Temperature sensor location, ⊗; boundary layer probe, Ø; FlowMaster probe, Φ; and free stream probe, ©.

3.5. Traverse System

A three-axis traverse system was used to position the probes. This consisted of 3 stepper motor controlled slides (for independent movement in the streamwise direction, x, the wall-normal direction, y, and the transverse direction, z), mounted on a square section aluminium frame. Positioning was achieved via a PC and Digiplan CD25 stepper motor controllers. The stepper motors and controllers gave positioning resolution of 2.5μm in the x and z direction and 1.25μm in the y direction. The traverse unit was aligned parallel to the boundary layer plate to within ±0.5mm over a 300 x 300mm area. Where possible, the traverse was moved in only one direction to avoid problems of backlash, although this was very small due to the use of ball screw assemblies on the slides.

3.6. Data Acquisition System

The flow diagnostic probes were sampled on a data acquisition system consisting of an IOTech 488/8SA Analogue-Digital Converter (ADC) and a laboratory PC. The system allowed simultaneous sample and hold for up to 8 channels. The ADC provided 16-bit resolution at a sampling rate up to 100kHz, and had programmable input ranges of ±1, ±2, ±5, and ±10V. QBasic programs were written on the PC to control the ADC and traverse system. Limitations of data transfer rates between the ADC and PC restricted the data acquisition to 32768 samples above a sampling frequency of 2kHz. At lower sampling frequencies, the data acquisition could continue indefinitely. For the experiments in initially static air, the maximum possible sampling rate of 5kHz was used, since it was necessary to sample for at least 3s. This was adequate to accurately reproduce the velocity signal.

The autocorrelation function, $R_x(\tau)$, gives the dependence of a time-history record at one time, t, to the value at another time, $t + \tau$, and is defined as (Bruun, 1995):

$$R_x(\tau) = \lim_{T\to\infty} \frac{1}{T} \int_0^T x(t)x(t+\tau)dt \ , \qquad (3.6.1)$$

where, $x(t)$ is a time history of a flow quantity. The autocorrelation coefficient function, $\rho_x(\tau)$, is obtained by normalising $R_x(\tau)$ with the maximum value, which occurs at $\tau = 0$:

$$\rho_x(\tau) = \frac{R_x(\tau)}{R_x(0)} \ . \qquad (3.6.2)$$

The corresponding integral time-scale, T_I, is:

$$T_I = \int_0^\infty \rho_x(\tau)d\tau \ . \qquad (3.6.3)$$

The integral time scale is a measure of the time separation over which the signals $x(t)$ and $x(t + \tau)$ are correlated. Taking $x(t)$ as the time history of streamwise velocity fluctuations, u', at $y^+ = 15$ in the turbulent boundary layer (i.e. position of maximum turbulent intensity), it was found that $T_I \approx 45$ms. This is illustrated in Fig. 3.6.1 (note $U_\infty = 1.8$m/s). Thus, the largest coherent structure at this position in the boundary layer took around 45ms to pass the stationary probe. This indicates that the optimum time between independent samples, $2T_I$, is 90ms. Thus, a sample rate of 11Hz would have been optimum if mean velocity and turbulence statistics were to be measured, only. However, this sample rate yields little information about the nature of the turbulence within the coherent structures, so a higher sampling frequency was used.

The power spectrum at various positions in the boundary layer at $U_\infty = 1.8$m/s is shown in Fig. 3.6.2, where $3\text{x}10^6$ data points have been recorded at a sampling frequency of 1kHz. It was observed that the boundary layer turbulence had an upper frequency limit of around 400Hz. Thus a sampling frequency of 1kHz was adequate to capture all scales of the turbulence, and all measurements within the turbulent boundary layer were taken at this acquisition rate.

Using the method outlined by Bruun (1995), it can be shown that 950 independent samples are required to produce mean u-component velocity values to an accuracy of ±1% with 99% confidence at $y^+ = 15$ (where $u'/U_\infty \approx$ 12%). Using the optimum time between independent samples, ($2T_I = 90$ms, from above), shows that a sample length of around 86s is required. To give further evidence, Fig. 3.6.3 shows the variation of the running average

velocity with sampling time at y^+ = 15. This shows that the statistical mean is within 1% of the true value after 80s of sampling.

At each measurement position in the boundary layer studies, the hot-wire probe was sampled for 80s at 1kHz such that the turbulence statistics were converged to ±1% (99% confidence), and all scales of turbulence were adequately captured. The length of samples was also adequate to capture many turbulence events (e.g. sweeps / ejections), so that conditional sampling could be performed, as described later in Ch. 9.

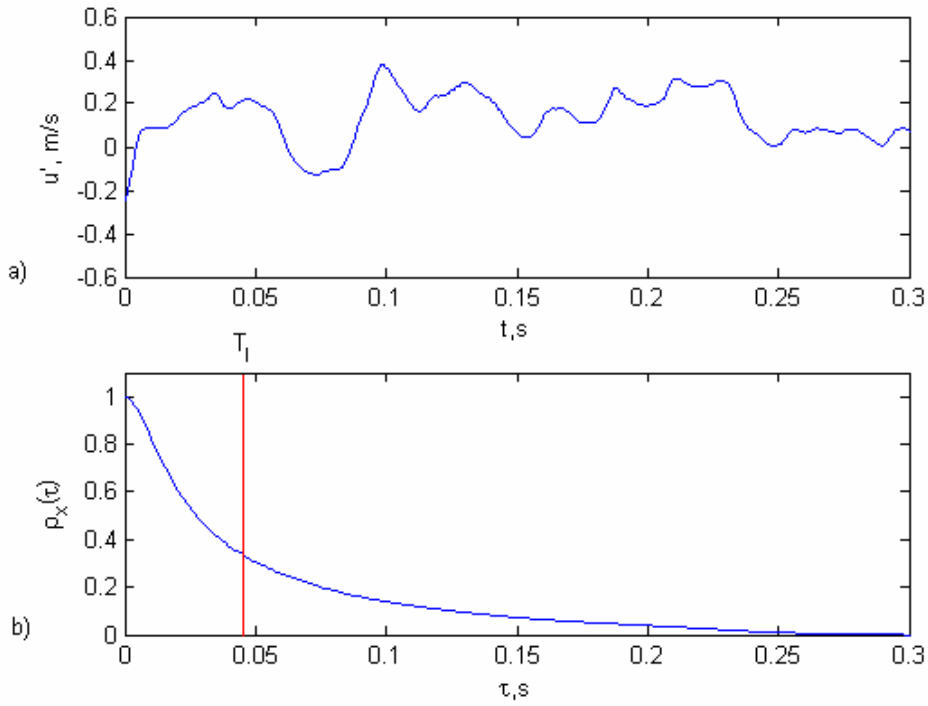

Figure 3.6.1. a) Velocity fluctuation signal at y^+ = 15 in the turbulent boundary layer and b), autocorrelation function, $\rho_x(\tau)$, showing the integral time scale, T_I. U_∞ = 1.8m/s.

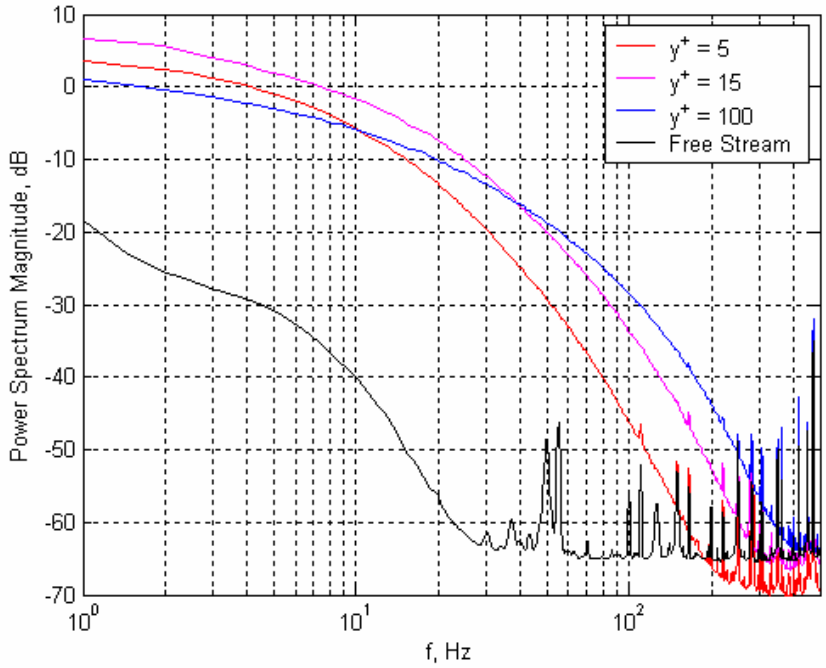

Figure 3.6.2. Power Spectral Magnitude at various positions in the turbulent boundary layer. The hot-wire signal was sampled for 3000s at 1kHz ($3x10^6$ data points).

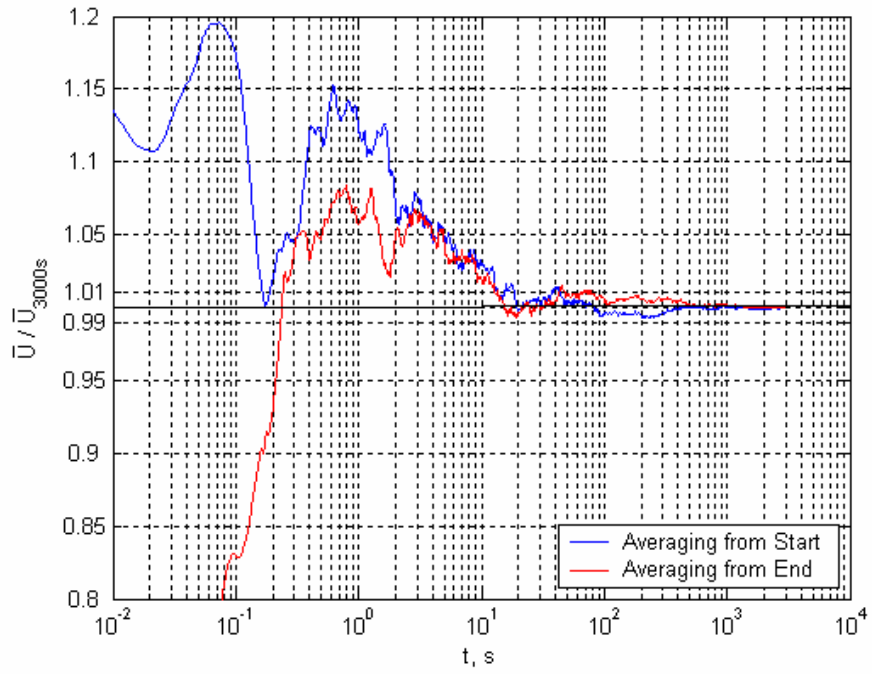

Figure 3.6.3. Running average of data sampled for 3000s at 1 kHz at $y^+ = 15$. The average is within 1% of the true value after 80s of data collection.

3.7. Plasma Generation System

3.7.1. Plasma Power Supply

The power supply used to generate plasma was kindly loaned to us from BAE SYSTEMS. This was an in-house manufactured power supply based on Russian technology from the Cold War era.

The power supply was dual channel (referred to as channel X and Y), with bipolar output on each. The maximum output was ±4kV at 90kHz. Power was taken from a 3-phase wall outlet, via a 3-phase variac, into the plasma power supply. The variac was used to control the output voltage delivered to the load (i.e. the plasma actuator). Two TTi TGP110 10MHz Pulse generators controlled the frequency and timing of the plasma (referred to as Signal Generator A and B).

The power-supply output was in the form of positive and negative high-voltage square-wave pulses of controllable duration (charge time) and frequency (Pulse Repetition Frequency, *PRF*), as illustrated in Fig. 3.7.1. These parameters controlled the plasma formation and were set via TTL signals from Signal Generator B. The charge time was typically set to slightly exceed the time it takes the load to reach the full voltage (≈ 7μs) and the *PRF* was typically set to several tens of kHz. Note that the *PRF* is equal to the frequency between alternating polarity pulses (as set on the signal generator). The AC cycle actually occurs at a frequency of *PRF*/2. This convention will be used throughout.

The high voltage pulse train was split into short duration pulses (Pulse Envelope Duration, *PED* ≈ 1ms), so that the heat build-up in the plasma

actuator was minimised. These short duration pulses occurred at a frequency of several tens of Hz (Pulse Envelope Frequency, *PEF*). The *PEF* also controls the frequency of output channel switching between X and Y, so that two sets of electrode can be activated at different times and, for example, oscillatory forcing can be created. The *PED* and *PEF* were both controlled by TTL signals from Signal Generator A, which acted as a trigger input to Signal Generator B (c.f. Fig. 3.8.1). The total time of plasma forcing was set within the computer, which provided a trigger input to Signal Generator A.

The high voltage pulse train was transferred to the load using BNC cable with PET connectors. These lead to a safety box within the wind tunnel that splits the BNC cable to two safety sockets. Wires were then soldered to the load using low melting point solder, wrapped together and then attached to the safety box using 4mm jacks.

The power supply contained internal voltage probes and the current supplied to the electrode sheet was monitored using an in-house manufactured current shunt. The signal generators, current shunt signal and voltage probe signals were recorded using a Tektronix TDS2024 4ch 200MHz digital storage oscilloscope. These signals were stored and then processed on an IBM compatible PC via the RS232 port.

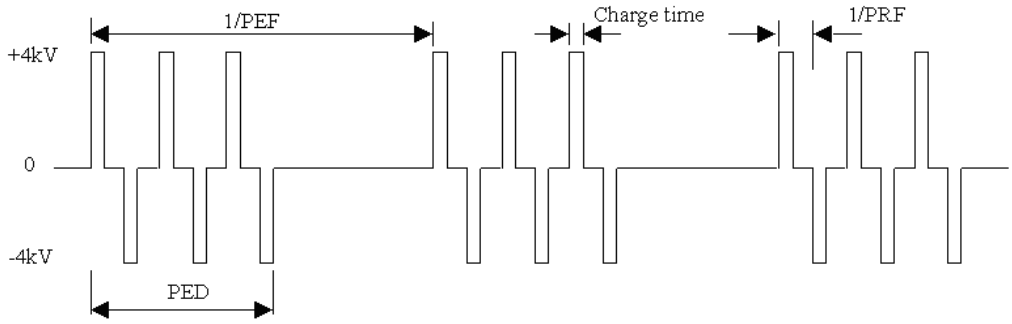

Figure. 3.7.1. Schematic of plasma excitation parameters. The Pulse Repetition Frequency, *PRF*, and charge time control the formation of plasma and were set using Signal Generator B. Plasma formation was typically split into short duration bursts with the Pulse Envelope Duration, *PED*, and Pulse Envelope Frequency, *PEF*, set by Signal Generator A. The *PEF* also defined the frequency of channel switching between output X and Y. Typical excitation parameters were E_{max} = 3.6kV, *PRF* = 50kHz, Charge Time = 7μs, *PEF* = 50Hz, *PED* = 1ms.

3.7.2. Plasma Electrode Sheets

The design of the plasma electrode sheets was based on an uncoiled parallel plate plasma reactor as described in Ch. 2. These consisted of two electrodes separated by a dielectric layer, as illustrated in Fig. 3.7.2. The upper electrode was exposed to the working gas, in this case atmospheric pressure air, whereas the lower electrode was totally encapsulated by the dielectric and the test plate. The high voltage pulse train was delivered to the electrodes, which caused localised ionization around the exposed electrode, thus creating glow discharge plasma which spread out over the surface. This appeared as a diffuse purple glow, extending for approximately 3mm to either side of the exposed electrode. Various electrode sheets have been used in this study and the effect of plasma excitation parameters, electrode sheet thickness, electrode geometry, and dielectric material are presented in Chaps. 4-6. A detailed description of the electrode sheet construction and operating principles is given in Ch. 4 and the *AIAA J.* paper in the Appendix.

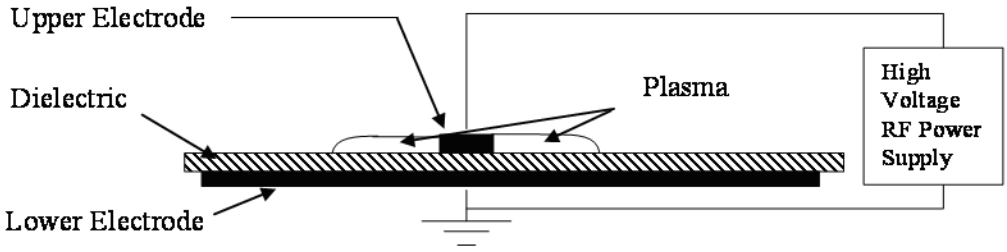

Figure. 3.7.2. Plasma electrode sheet cross section schematic. Upper and lower electrodes are typically 17μm thick copper, photochemically etched to the required design. The dielectric is typically 250μm thick Mylar.

3.7.3. Test Plate

The plasma electrode sheets were attached to an aluminium test plate, as shown in Fig. 3.7.3. The assembly was then mounted into the wooden boundary layer plate within the wind tunnel test section. The test plate had dimensions of 410 x 310mm (≈ 6 x 4δ at U_∞ = 1.7m/s) and was inserted 1.9m downstream of the boundary layer test plate leading edge. Care was taken to ensure that the test plate was flush with the boundary layer plate, and any roughness was smoothed by using pressure sensitive tape. Discontinuities were of the order of 0.2mm ($y^+ \approx 1$).

The test plate consisted of a sandwich structure of 12mm thick aluminium, 12mm thick perspex then 5mm thick aluminium. The electrode sheets were attached to the 12mm thick aluminium which acted as a heat sink to draw away any heat in the dielectric generated by the plasma. The perspex provided electrical insulation as a safety feature in case the plasma arced to the aluminium. The rear 5mm-thick aluminium layer supported the test plate within the wind tunnel. Electrode sheets were attached to the aluminium plate using double sided tape, adhesive spray or silicone gel, depending on the application.

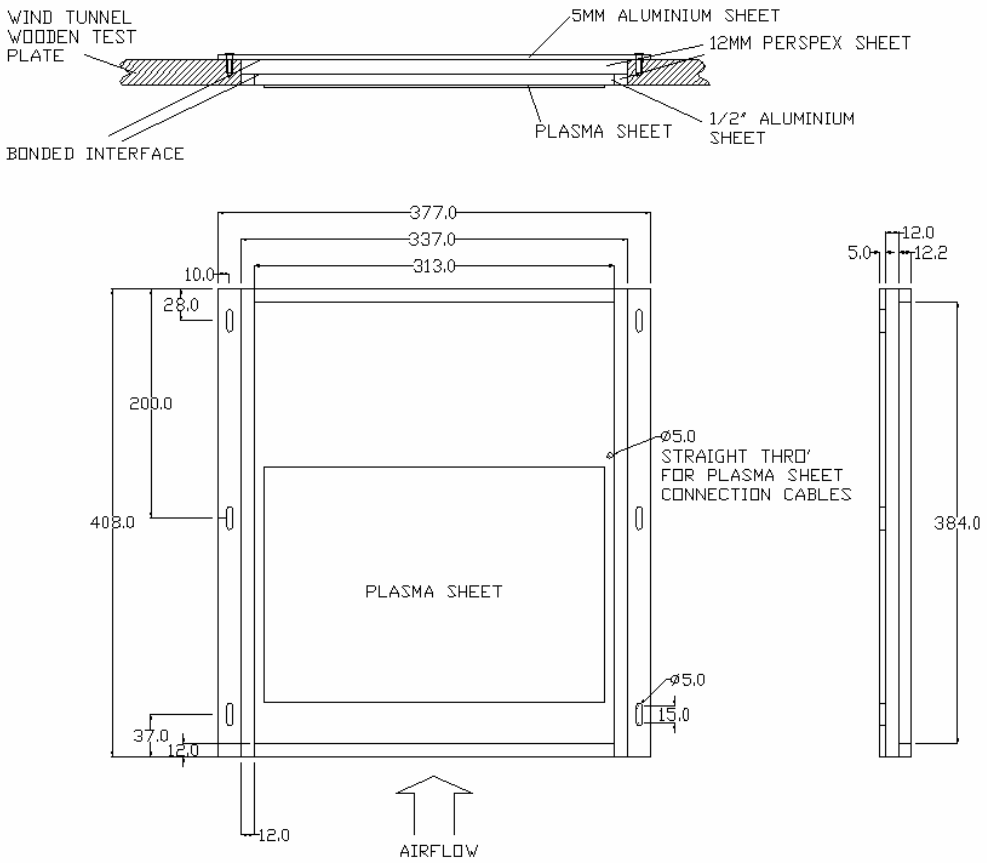

Figure 3.7.3. Detail of test plate. Plasma electrode sheets were bonded to the aluminium surface of the test plate to aid heat transfer away from the sheet. The test plate was flush mounted into the boundary layer plate (Fig 3.2.2), 1.9m from the leading edge.

3.7.4. Health and Safety

Due to the high voltage required to produce plasma, several modifications were made to the wind tunnel in order to minimise the risk to the operator. Cut-off switches were located at the wind tunnel entrance and the wind tunnel centre. When pressed these switched off the 3-phase plasma power supply which was key operated, and had to be reset each time. An interlock device was located on the test section access hatch. This disconnected the 3-phase supply whenever it was open so that the electrode sheet could not be live while the operator was working inside the test section. An earthing stick was also used to discharge any remaining charge on the plasma sheet after each experiment.

Ozone production was monitored using a Gastec pump with Dräger ozone tubes (67 33 181 0.05/b). After approximately 400s of plasma formation, the ozone levels were found to be 0.25ppm inside the wind tunnel and < 0.05ppm outside. Ozone has a short-term exposure limit (15 minutes duration), that is 0.2ppm. Consequently, the wind tunnel was flushed of ozone after each experiment.

3.8. Experimental Procedure

A schematic of the entire experimental configuration is presented in Fig. 3.8.1. The general experimental procedure was as follows. Firstly the thermal anemometer would be setup (i.e. overheat ratio, filter, gain, etc.) and calibrated with the procedure of Sec. 3.4. Then the anemometer would be traversed to the required location (typically $y = 0$, $z = 0$). Next, the plasma parameters (E_{max}, *PRF*, Charge Time, *PEF* and *PED*), would be set on the variac, Signal Generators B and Signal Generators A, respectively. These plasma parameters would then be verified and monitored using the oscilloscope.

QBasic programs were written on the laboratory computer that would automate the experiments. They typically activated and moved the traverse, issued a command to the ADC to start data acquisition, triggered signal generator A to start / stop plasma formation and then repeated until the desired number of measurement locations was complete.

The ambient temperature sensor and free-stream hot wire (not shown in Fig. 3.8.1), were simultaneously sampled with the traversable hot wire so that the measurements could be corrected for ambient temperature and free-stream velocity drift. Also, signal generator A was simultaneously sampled so that the hot-wire signal could be synchronised to the plasma formation during data processing.

Care was taken to avoid ground loops in the experimental setup, and the plasma system and anemometer / ADC system operated on separate power lines and were kept physically as far apart as possible.

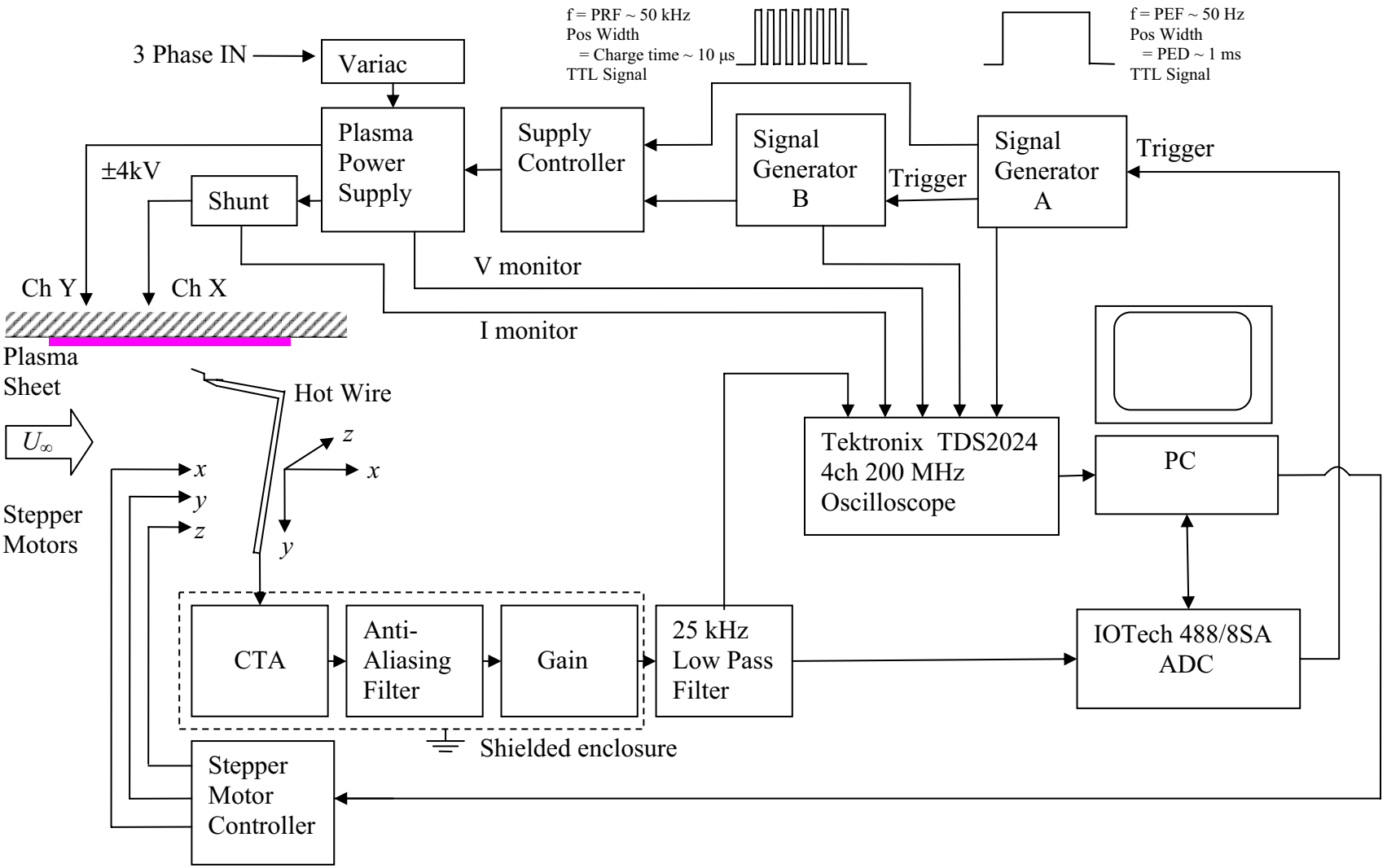

Figure 3.8.1. Schematic of experimental configuration including plasma generation system, thermal anemometry system, traverse system and data acquisition system. Most connections are made using BNC cables.

Chapter 4

Induced Flow from Single Plasma Actuators

4.1. Introduction

The following chapter presents experimental results concerning the induced air flow by a single symmetric and a single asymmetric plasma actuator in initially static air. It is worth noting here that the asymmetric configuration was produced from one of the spanwise oscillation sheets used in boundary layer testing of Chaps. 8 and 9. The work in this chapter was published in the *AIAA Journal* in April 2006. Section 4.3 is a modified copy of the published work and the full paper can be seen in the Appendix.

The paper discusses previous works using surface plasma actuators and explains the experimental techniques used in this study. These techniques are identical to those used later in Ch 5. The results show that the plasma imparts momentum into the air, such that a laminar wall jet is produced that travels away from the exposed electrode. It is shown that the flow is unlikely to be buoyancy driven and only occurs when the plasma forms, suggesting that the flow is caused by the result of the force produced on the plasma charges by the applied electric field. Functional relationships between induced velocity and plasma parameters are given, and it is concluded that the induced velocity is roughly proportional to the applied power.

The paper focuses upon the transient development of the wall-jet type flow. It is found that there is an initiation stage, whereby the plasma creates a start-up vortex that travels away from the electrode. This behaviour does not seem to

have been reported in the literature before. Such vortices were clearly visible using flow visualisation techniques and were tracked using the cold-wire probe. It was found that the vortex dominated the flow field for the first 0.4s. After this time, the plasma created a pulsed quasi-steady wall-jet flow. The steady-state velocity profile was nearly identical to the theoretical laminar wall jet profile given by Glauert (1956). The induced velocity could not be increased above 2.5m/s, but it was concluded that the magnitude of the induced flow would be sufficient for the boundary layer experiments in Chaps. 9 and 10.

In addition to the published work, the flow field induced by firing the plasma continuously (non-pulsed mode) is presented in Sec. 4.4. The chapter is concluded by considering the experimental errors associated with these hotwire measurements in Sec. 4.5. The effect of dielectric thickness and dielectric materials on the induced flow field are studied later in Ch. 5.

4.2. Experimental Procedure

The single symmetric and single asymmetric plasma actuators studied in this chapter are drawn schematically in Fig. 4.2.1. The symmetric actuator consisted of a photo-chemically etched 90mm long, 200μm wide, and 17μm thick copper electrode with 17μm thick solid copper backing. This produced equal plasma formation on both sides of the exposed electrode. The asymmetric actuator consisted of an 85mm long, 1mm wide, 17μm thick upper electrode with a lower electrode 9mm wide, flush with the edge of the exposed electrode. Here, plasma was formed only on the side of the electrode under

which the lower electrode was placed. In both cases the dielectric was 250μm thick Mylar sheet (dielectric constant = 3.1 at 1MHz).

The coordinate system and hot/cold-wire probe orientation is shown in Fig. 4.2.2. Probe positioning relative to the electrode was achieved using a CCD camera with a zoom lens, giving positional accuracy better than 200μm. The typical experimental setup in the wind tunnel is shown in Fig. 4.2.3.

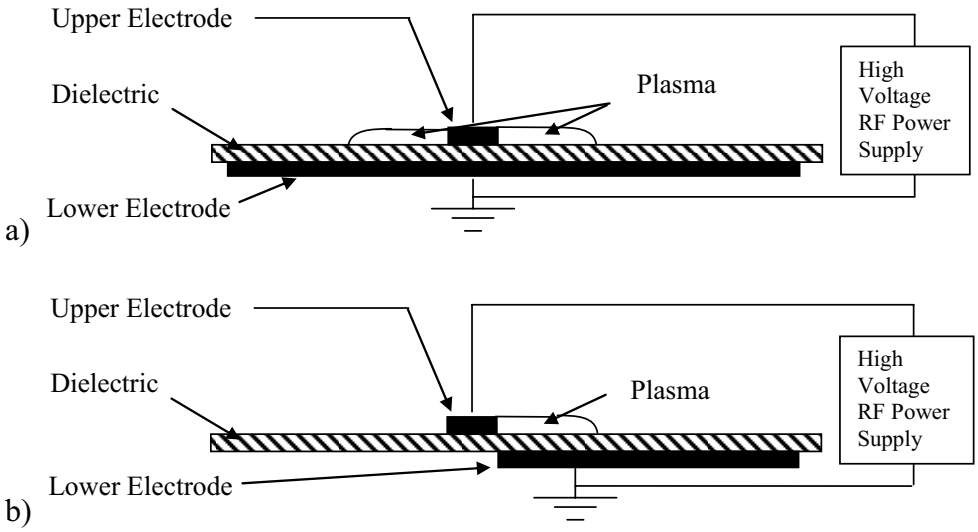

Figure 4.2.1. Plasma electrode sheet cross section schematic. a) Symmetric electrode configuration and b) asymmetric electrode configuration. Not shown to scale.

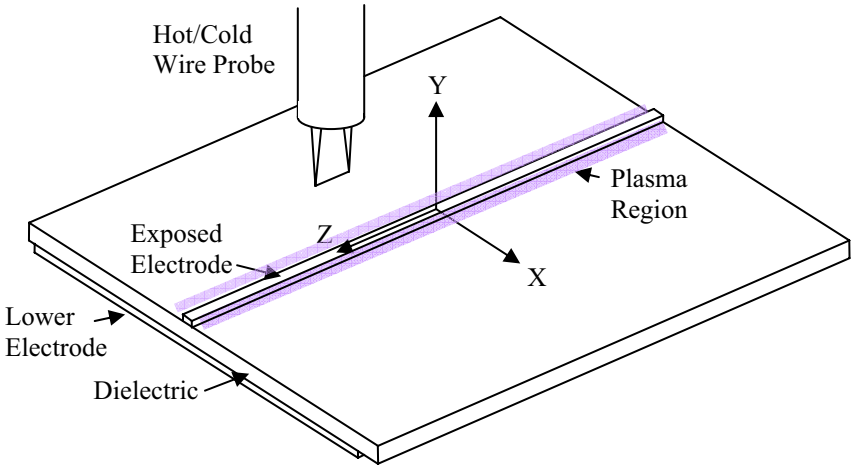

Figure 4.2.2. Coordinate system and probe orientation.

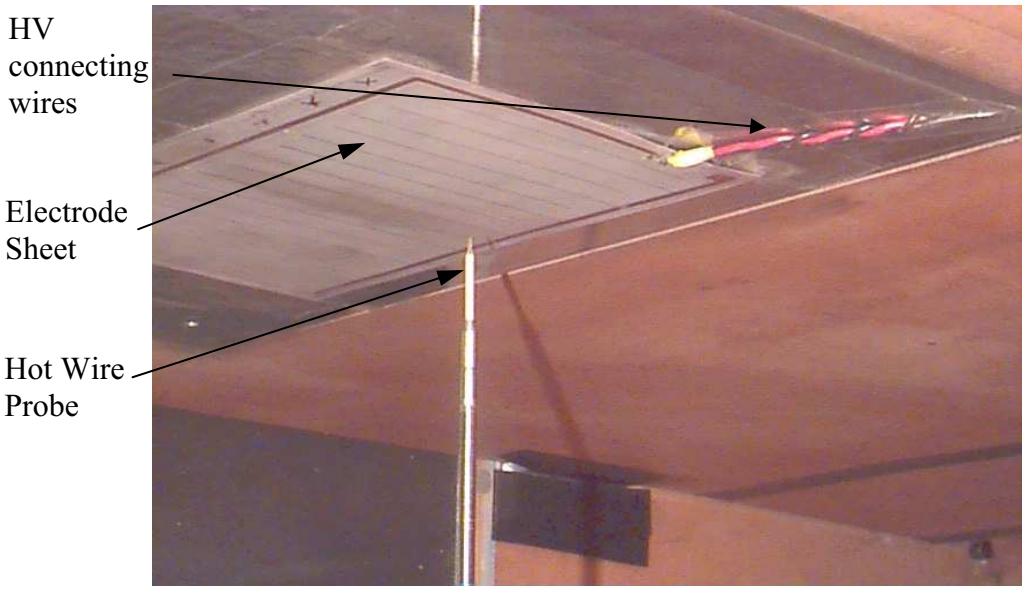

Figure 4.2.3. Photograph of electrode sheet and hot wire in the wind tunnel.

Dantec 55P16 hot-wire probes and 55P31 cold-wire probes (c.f. Fig. 3.3.1) were traversed in a 2-D grid pattern around the plasma electrodes. Measurements were taken with the hot-wire probe at 2mm intervals from the electrode centreline in the streamwise direction, x (-12mm $\leq x \leq$ 12mm, $x = 0$ is the electrode centreline), and at 0.25mm intervals in the wall-normal direction, y (0.25mm $\leq y \leq$ 4mm, $y = 0$ is the electrode surface). Data collection for the cold-wire probe was taken at 1mm intervals in the wall-normal direction and was extended to a wall-normal distance of 11mm (1mm $\leq y \leq$ 11mm).

The probe signal was sampled for a total of 3s at a frequency of 5kHz at each grid position. During this time there was around 0.5s of pre-plasma data (i.e. signal in quiescent air), then the plasma was activated for 1.4s in short duration pulses (*PED* ≈ 1ms, *PEF* ≈ 50Hz, c.f. Fig 3.7.1), followed by 1.1s of post plasma data. The probe signal and signal generator A were simultaneously sampled so that the timing of the hot-wire signal could be phase-locked to the timing of the plasma. Ambient temperature measurements were taken periodically to allow compensation for temperature drift during the experiments. A typical hot-wire and signal generator signal is given in Fig. 4.2.4. Four of such acquisitions were made at each grid position and it took around 4 hours to complete the measurements of the entire 2-D grid.

The average velocity was calculated at each grid location over the entire 1.4s of plasma forcing ($\overline{U}\,(x,y)$), and subsequently averaged over the four independent events. The transient development of the plasma was also studied ($U(x,y,t)$), where average velocity was calculated every 10 samples (2ms) to reduce noise. This noise reduction technique was especially important during

each pulse envelope because high frequency electrical noise was coupled into the signal due to the plasma.

The flow field induced by the plasma actuator typically took around 0.4s to establish a quasi-steady state; with characteristics repeated every plasma pulse. Consequently, the plasma signal was ensemble-averaged between plasma pulses (i.e. at the *PEF*), and ensemble averaged over the remaining plasma-on time and over the four acquisitions. This yields a characteristic transient velocity profile between plasma events, hereafter referred to as the ensemble-averaged velocity, $\langle U \rangle(x,y,t)$.

In addition, the development of the flow was studied by averaging the velocity between each pulse envelope, called the pulse-averaged velocity, $\hat{U}(x,y,t)$. This gives information on the flow field development without the complication of the induced flow from each individual plasma event (which occurs on a faster time scale). The data processing procedures are illustrated in Fig. 4.2.5.

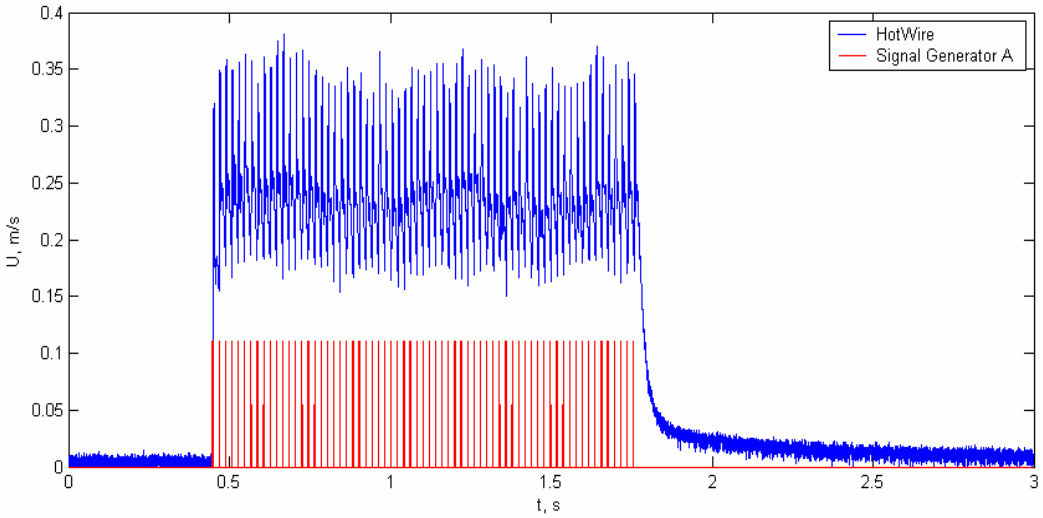

Figure 4.2.4. Hotwire (-) and signal generator A (-) signal at x = 4mm, y = 1mm from a symmetric plasma electrode with 250µm thick Mylar dielectric. E_{max} = 3.6kV, *PRF* = 50kHz, Charge Time = 7µs, *PEF* = 50Hz, *PED* = 1ms.

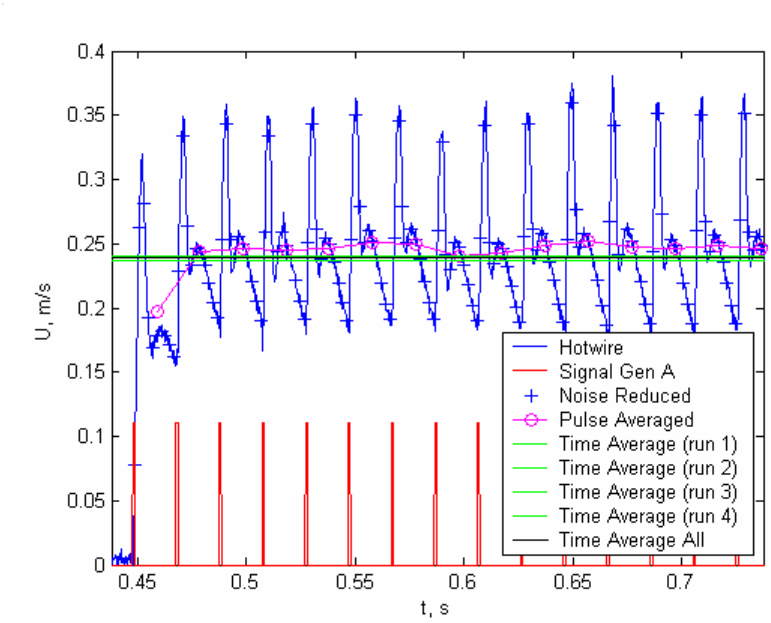

a)

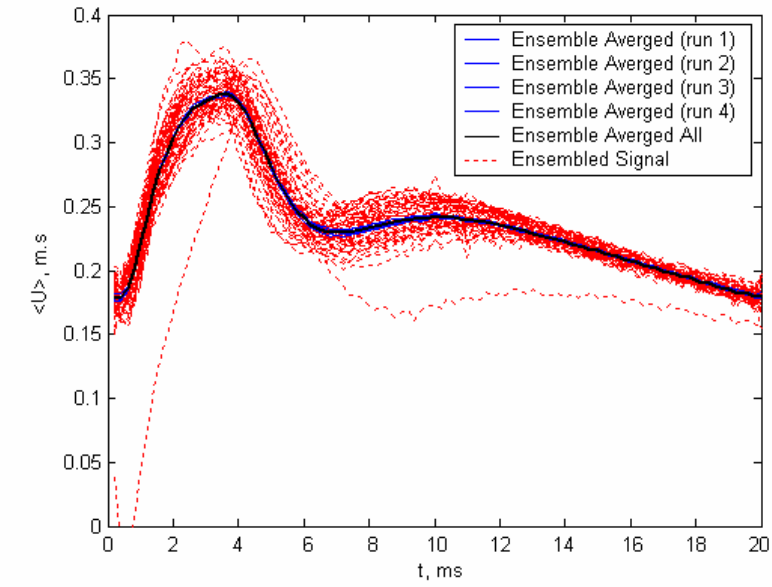

b)

Figure 4.2.5. Data processing at x = 4mm, y = 1mm, E_{max} = 3.6kV, PRF = 50kHz, Charge Time = 7µs, PEF = 50Hz, PED = 1ms. a) Raw hot-wire velocity signal (-), raw signal generator signal showing position of plasma events (-), noise-reduced velocity $U(x,y,t)$ (+), pulse-averaged velocity $\hat{U}(x,y,t)$ (o), and time-averaged velocity $\overline{U}(x,y)$ (-,-). b) Example of the ensemble-averaging process between plasma pulses (- -) and the ensemble averaged velocity $\langle U \rangle(x,y,t)$ (-,-).

4.3. Results

4.3.1. Plasma Characteristics

Typical voltage and current waveforms during a single plasma cycle are shown in Fig. 4.3.1. Note, the current shown is that delivered to the plasma sheet and contains the current flowing in the plasma and that charging the capacitance of the dielectric (Liu and Neiger 2001). Gibalov and Pietsch (2000) have performed a detailed study of the surface discharge development and Enloe *et al.* (2004b) presents details of the self-limiting nature of a dielectric barrier discharge (DBD). Plasma is formed when the upper (exposed) electrode is at high enough negative potential relative to the dielectric surface for electrons to be emitted. These subsequently ionize the surrounding air and build up charge on the dielectric. A secondary discharge is initiated at the end of the pulse without simultaneously consuming energy from the electrical circuit (Liu and Neiger 2001). In Fig. 4.3.1, discharge is initiated once the potential exceeds 2kV and continues until the applied voltage has reached the maximum value (4.1kV on positive pulses, -3.7kV on

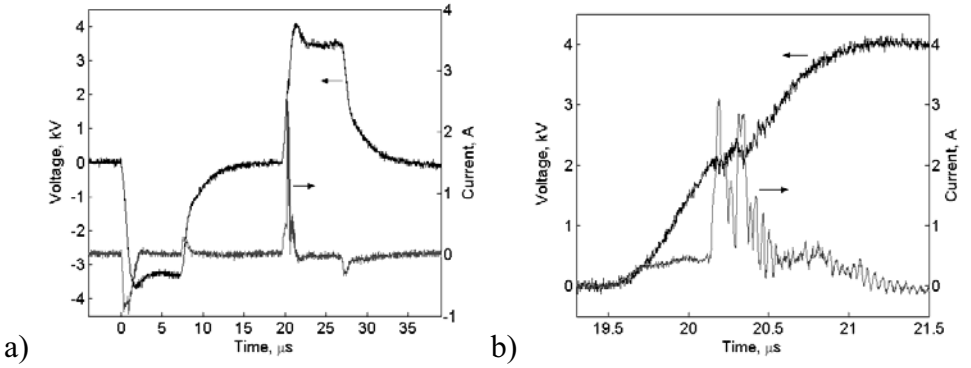

Figure 4.3.1. Voltage and current waveforms: a) during a full ac cycle and b) detail of positive pulse. *PRF* = 50kHz, charge time = 7μs, E_{max} = 4.1kV.

negative pulses). At the maximum, the applied voltage ceases to increase and the surface charge build-up will oppose the electrode potential. This inhibits further electron emission and the plasma quenches. Once the applied voltage is turned off, there is a momentary reverse flow of current due to the resulting electric field of the surface charge. This process also applies to positive going pulses, except that the charge available is limited to that deposited on the dielectric on the previous half cycle. The positive going waveforms have a more irregular current pulse (Fig. 4.3.1b), consistent with the behavior of a DBD (Enloe *et al.* 2004b). On integrating voltage and current waveforms it is found that 1.1mJ (25μJ/cm) are deposited into the plasma for positive pulses and 1.6mJ (30μJ/cm) for the negative pulses. Measurements in initially static air (Enloe *et al.* 2004b), showed that it was the negative going waveforms that produced the greater force. It is thought that collisions between the ions and background gas are the mechanism for coupling momentum into the airflow (Roth 2001).

4.3.2. Preliminary Hot-wire Study

There are many issues relating to the use of the hot-wire probe for measuring the airflow around a high voltage electrical source, such as plasma. Firstly, the formation of plasma may cause electrical interference in the anemometry system. Despite efforts to reduce the electrical noise by signal filtering and shielding, the anemometer signal during a plasma pulse could include interference. The presented results are based only on data taken after each plasma envelope and are therefore devoid of this electromagnetic (EM) noise. Figure 4.3.2 shows the hot-wire voltage signal at nearly identical radial distances vertically above (Fig. 4.3.2a) and to the side (Fig. 4.3.2b) of the

electrode. The hot-wire signals are markedly different, suggesting they are attributed to a flow phenomenon, not electrical noise. In addition, the hot wire has been placed at the side of the electrode with a small piece of Mylar between the plasma and probe in order to block the induced flow. The probe signal is shown in Fig. 4.3.2c. The hot-wire voltage change is small (< 3mV), confirming the signal of Fig. 4.3.2b is from an induced flow.

Experiments with (broken) hot-wire probes show that flashover will occur between the high voltage electrodes and the anemometer at a radial distance of ~3mm. In one instance, a working probe was traversed within 3mm of the electrode and arcing occurred, vaporizing the sensor wire and part of the prongs. Damage was caused to the anemometry system. Hence, no data can be taken in a region less than 3mm around the electrode. This is approximately 20 viscous units of the boundary layer in the current experimental facility.

Preliminary results show that there is some effect on the hot-wire measurements due to the presence of the wall. An apparent velocity is observed in still air at wall normal distances less than 1.25mm (250 wire diameters), because the wall drawing heat from the hot-wire and the anemometer compensating by increasing the wire temperature / voltage. Other studies show the wall-effect generally occurs at distances less than 50 wire diameters (Wills 1962) and for $y^+ < 3$ in a turbulent boundary layer (Hutchins and Choi 2002). Although the wall effect error will decrease when airflow is present, the results presented should be treated with some caution, particularly for the data close to the wall.

The hot-wire will also respond to the rise in ambient air temperature due to the plasma heating the flow. An overheat ratio of 1.8 has been used to minimize

the probes sensitivity to temperature changes. The wall-effect would tend to cause the measured velocity to be higher than the true velocity, whereas an increase in ambient fluid temperature will tend to cause the measured velocity to be lower.

a)

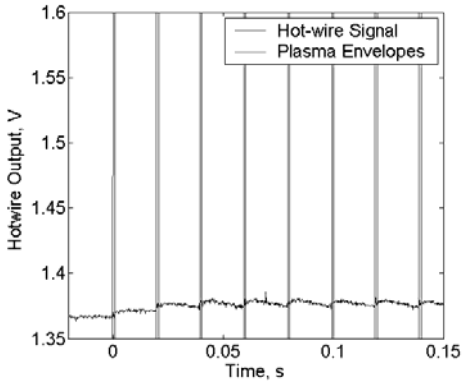

b)

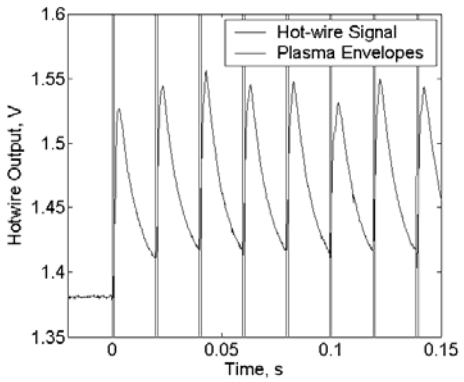

c)

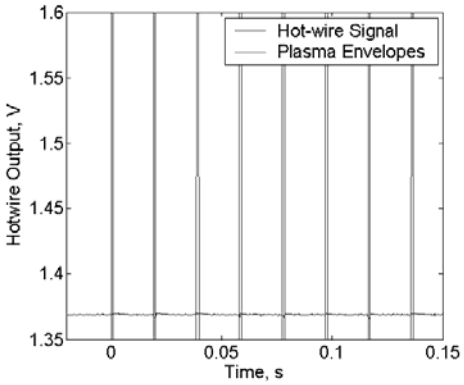

Figure 4.3.2. Hot-wire signals around the symmetric electrode. a) x = 0mm, y = 4mm, r = 4mm, b) x = 4mm, y = 0.5mm, r = 4.03mm and c) x = 4mm, y = 0.5mm, r = 4.03mm with 250μm thick Mylar placed between the electrode and probe. Plasma envelopes of 1ms duration occur at a frequency of 50Hz (i.e. every 20ms). PRF = 50kHz, charge time = 7μs, E_{max} = 4.1kV.

4.3.3. Parametric Testing

The hot-wire velocity data yields information on two time scales. There is an effect of the plasma on the flow field after each individual plasma pulse and a cumulative effect of each subsequent plasma pulse. The phase averaged velocity profile after a plasma pulse is obtained by ensemble averaging the hot-wire signal between pulses after the flow field is established. Figure 4.3.3 shows a typical hot-wire signal at y = 1mm, x = 8mm. It can be seen that some time is necessary before the airflow exhibits similar behavior between each subsequent plasma envelope (~0.4s or 20 pulses within the entire measurement area, although this is shorter at closer distances to the electrode). The quasi-steady fluctuation in velocity is then repeated each cycle until the end of the total plasma on period (t = 1.3s).

A parametric study was undertaken on the effects of the *PRF*, *PEF* and *PED* on the flow field. All parameters were varied independently from a base case of *PRF* = 50kHz, charge time = 7μs, E_{max} = 4.1kV, *PED* = 1ms, *PEF* = 50Hz. The power supply is limited to a *PRF* of 90kHz and a duty cycle of 50% (= *PED*(s).*PEF*(Hz)), though the duty cycle was not increased above 25% for fear of thermal failure of the electrode sheet.

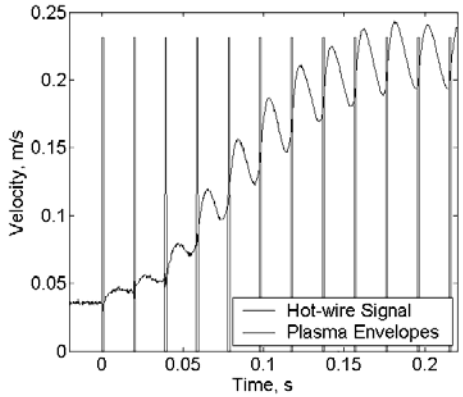

Figure 4.3.3. Hot-Wire signal at y = 1mm, x = 8mm. *PRF* = 50kHz, charge time = 7μs, E_{max} = 4.1kV, *PED* = 1ms, *PEF* = 50Hz. Symmetric actuator.

The maximum phase averaged velocity is shown as a function of *PRF*, *PEF* and *PED* in Figs. 4.3.4-6, respectively. This is defined as the maximum phase averaged velocity observed between plasma envelopes at $x = \pm 4$mm, $y =$ 0.5mm. It is found that for all tests, this is the location of the peak velocity for which there is data. The differences in the peak velocity observed on either side of the electrode for the symmetric case in Figs. 4.3.4-6, may have resulted from probe positional error and asymmetry in the formation of plasma due to surface irregularities.

The induced airflow is observed to vary slightly non-linearly with the *PRF* for both the symmetric and asymmetric electrode sheets. For the symmetric electrode sheet a maximum of 1.4m/s was observed at a *PRF* of 85kHz. This is a 280% increase of the velocity induced with a *PRF* of 50kHz. For the asymmetric case, the induced velocity is nearly 90% higher than for the symmetric case, with a maximum flow of 1.95m/s being observed at a *PRF* of 80kHz. Below excitation frequencies of 3kHz for both cases, no plasma could be detected and the hot-wire signals were too small to distinguish from background noise.

A small linear increase in the velocity was achieved by increasing the *PEF* (i.e. reducing the time between envelopes). For the symmetric case, a maximum velocity of 0.9m/s was obtained at a pulse envelope frequency of 250Hz (25% duty cycle). This is a 180% increase to the velocity generated with a pulse envelope frequency of 50Hz (5% duty cycle). For the asymmetric case, a maximum of 1.2m/s was observed and again, the induced airflow velocity is around 90% higher than the symmetric case.

A significant linear increase in induced velocity can be achieved by increasing the *PED*. A maximum velocity of 2.1 m/s was achieved by increasing the *PED* to 5ms (25% duty cycle) with the symmetric sheet, whereas a maximum of 2.4m/s was obtained with the asymmetric sheet. However, both electrode sheets exhibit a saturation effect for *PED* > 4ms, whereby increasing the *PED* further does not increase the induced airflow; thus indicating the timescale of momentum coupling between the plasma and air.

The variation of maximum phase averaged velocity with applied voltage is shown in Fig. 4.3.7. The hot-wire was placed at x = 4mm, y = 0.5mm with plasma parameters such that a substantial jet velocity is generated at the maximum applied voltage. It is evident that a minimum voltage of 2kV is required for plasma to be generated and a flow to be established. Below this voltage, no plasma can be seen with the naked eye and no spikes were evident in the current waveform. Above this threshold, the generated flow velocity increases rapidly with applied voltage, limited only by the power supply. Previous studies have shown that the plasma induced flow velocity is proportional to 7/2 power of voltage ($U_{max} \propto E^{7/2}$, Enloe *et al.* 2004a), and our results for the symmetric electrode sheet suggest a similar trend. However, for the asymmetric case, the variation in induced velocity appears to vary as E^2.

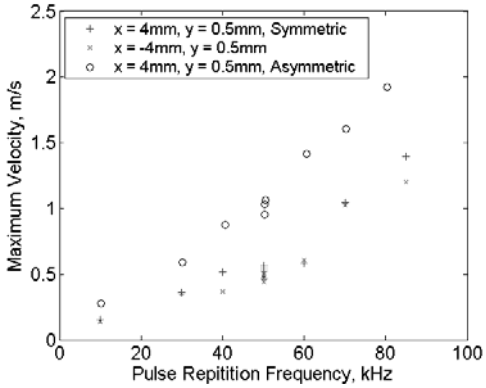

Figure 4.3.4. Variation of maximum phase-averaged velocity with *PRF* at $x = \pm 4$mm, $y = 0.5$mm. Charge time = 7μs, E_{max} = 4.1kV, *PED* = 1ms, *PEF* = 50Hz.

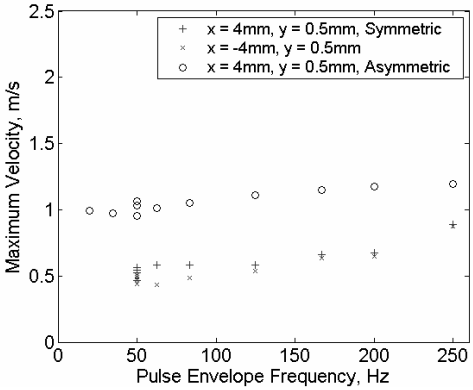

Figure 4.3.5. Variation of maximum phase-averaged velocity with *PEF* at $x = \pm 4$mm, $y = 0.5$mm. *PRF* = 50kHz, charge time = 7μs, E_{max} = 4.1kV, *PED* = 1ms.

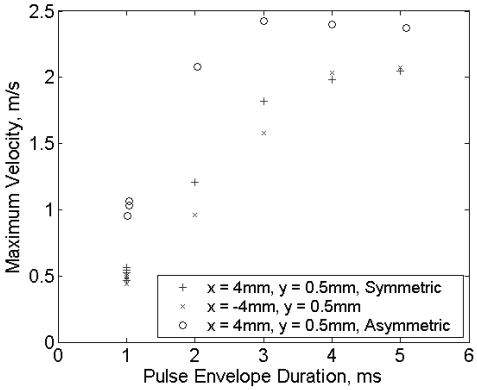

Figure 4.3.6. Variation of maximum phase-averaged velocity with *PED* at $x = \pm 4$mm, $y = 0.5$mm. *PRF* = 50kHz, charge time = 7μs, E_{max} = 4.1kV, *PEF* = 50Hz.

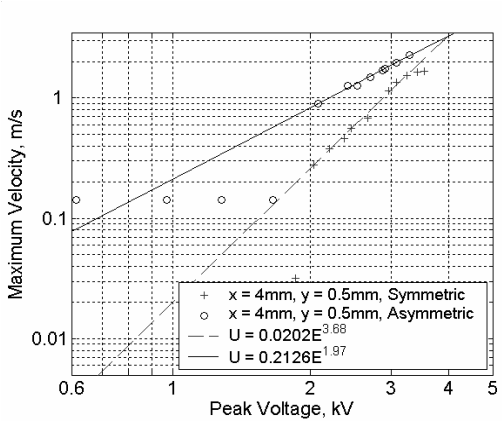

Figure 4.3.7. Variation of maximum phase-averaged velocity with applied voltage at x = 4mm, y = 0.5mm. *PRF* = 60kHz, Charge time = 7μs, *PEF* = 100Hz, *PED* = 2ms.

The power input into the plasma, P, is calculated as;

$$P = \frac{PRF}{2} \cdot PED \cdot PEF \int_0^{t_{AC}} (EI)\ dt \qquad (4.3.1)$$

where, t_{AC} is the time to complete one AC cycle (i.e. 2/*PRF*). The voltage and current waveforms are obtained from averages of multiple cycles to eliminate random noise. The maximum observed velocity is plotted against power in Fig. 4.3.8 for the symmetric electrode sheet. Similar results are observed for the asymmetric case. A reasonable collapse of data is observed through variation of the *PRF*, *PED* and E_{max}, suggesting the induced velocity is proportional to the power delivered to the electrode sheet. It should be noted that the power calculated here is not equivalent to the power consumed by the plasma and contains contributions of dielectric heating and electric losses. It appears to be more efficient to increase the jet velocity by increasing the *PRF*, and it is evident that limited gains can be made by increase of the *PEF*. The effect of reducing the charge time has also been studied. The induced velocity is not affected by a reduction in this parameter, although the charge time was

not reduced below 5μs. Improvements to the power supply and interconnecting cables may reduce the rise and fall time of the voltage signal, thus enabling higher oscillation frequencies, and hence flow velocities, to be generated.

The fluid power produced by the plasma has been evaluated from the ensemble averaged velocity distribution at $x = \pm 4$mm. Fluid power of the order of 10^{-4} W is created by the plasma and the mechanical efficiency of the device is of the order 10^{-2} %, similar to the results of Enloe *et al*. 2004a. This is, however, based on the electrical power dissipated in the whole system, not just the plasma. The actual efficiency of the plasma itself is expected to be significantly greater than this.

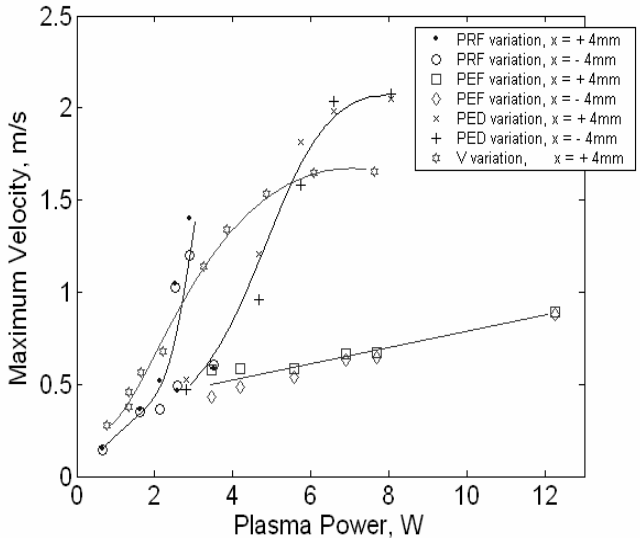

Figure 4.3.8. Variation in maximum phase-averaged velocity with plasma power, through varying individual plasma excitation parameters. Symmetric sheet, $y = 0.5$mm.

4.3.4. Velocity Profile

A contour plot of the phase averaged velocity profile of the symmetric base case at t = 5ms and 15ms are shown in Fig. 4.3.9 (t = 0 corresponds to the initiation of the 1ms duration plasma envelope). For these results, the plasma was created with PRF = 50kHz, charge time = 7μs, E_{max} = 4.1kV, and split into envelopes of PED = 1ms, PEF = 50Hz. This pulse train was activated for a total of 1.3s. The position of the electrode is given below each plot and the blackened area represents the region for which no data was taken because of the danger of arcing between the electrode and the probe. These data have been spatially and temporally corrected for the cold wire temperature measurements of Section 4.3.5. Firstly, it should be noted that the induced airflow is nearly symmetric around the electrode centerline. This is to be

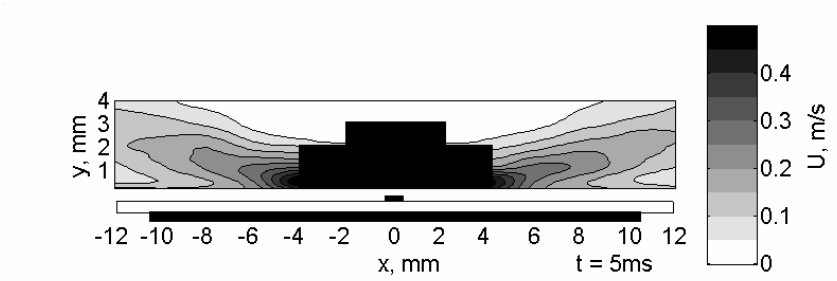

a)

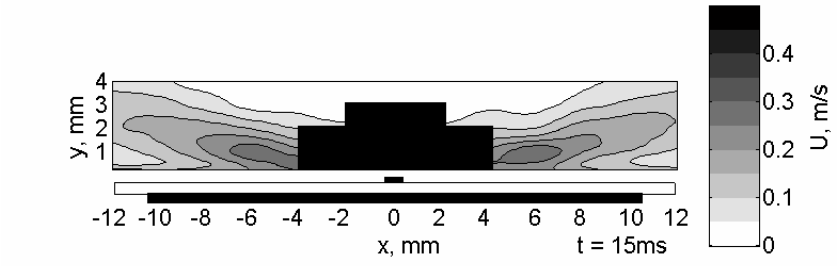

b)

Figure 4.3.9. Phase-averaged velocity contours around a single symmetric electrode. Electrode sheet shown below each plot is not to scale. Blackened area represents area where no hot-wire data is taken due to the high risk of flashover. a) t = 5ms and b) t = 15ms.

expected from the electrode geometry. A decelerating, broadening velocity profile is observed traveling in either direction away from the plasma. A peak velocity, U_{max}, of 0.51 ± 0.05m/s is observed at the closest lateral location (x = 4mm) and 0.5mm from the electrode surface. Though this induced velocity is lower than the maximum that occurred during parametric testing (2.1 m/s), the presented results are representative of all the tests above.

The peak velocity is observed within the measurement area, 5ms after the start of the plasma envelope (Fig. 4.3.9a). After this time a steady decrease in velocity is observed throughout the measurement area, though the general characteristics of the profile remain the same (Fig. 4.3.9b). The contour plots suggest a velocity that is even higher closer to the electrode. However, measurement limitations due to high voltage flashover inhibit data collection in this region. Figure 4.3.10 shows the velocity profiles on either side of the electrode. The plotted curves are polynomial fits to the data points. The nondimensional profiles have been plotted in Fig. 4.3.11, normalizing with the maximum velocity across the profile, U_{max}, and the jet half-width, $\delta_{½}$, defined as the distance to the point where the jet velocity has dropped to $U_{max}/2$. Also plotted are the theoretical profiles of the turbulent and laminar wall-jet, studied by Glauert (1656). The plasma-induced airflow appears to be similar to a laminar wall jet, also reported by Roth (2004). The Reynolds number of the flow, based on U_{max} and $\delta_{½}$, is Re_{δ} = 40. Chun and Schwarz (1967) show the critical Reynolds number of a laminar wall-jet is $Re_{\delta crit}$ = 57. This profile is typical for all times between plasma envelopes. Discrepancies occur in the outer regions of the wall-jet ($y^{*} = y/\delta_{½} > 1.2$). These errors occur due to a wall normal component of velocity in the outer region (-v), due to the entrainment

action of the flow. The profile also deviates from the theoretical laminar-wall jet profile in the inner region ($y^* < 0.4$). This is a result of the near-wall effect, as discussed in Sec. 4.3.2.

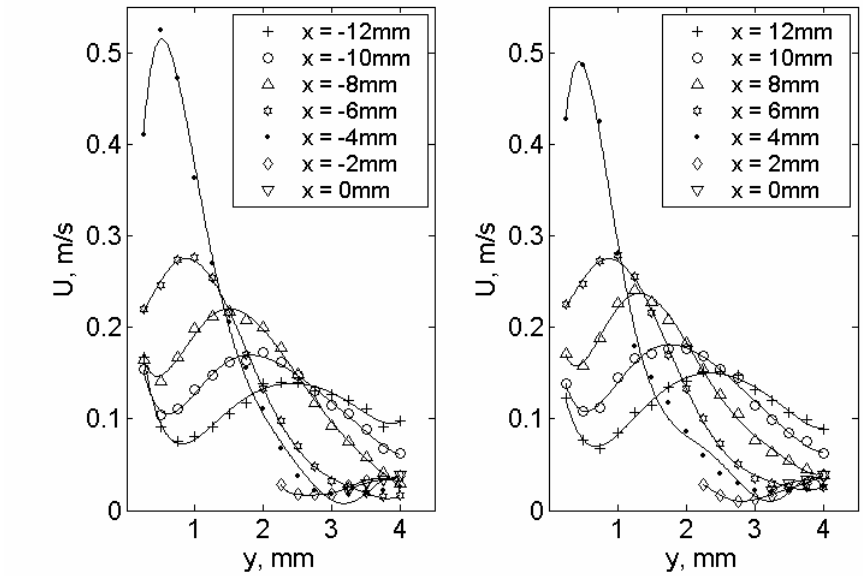

Figure 4.3.10. Velocity profiles on either side of the symmetric electrode. Curves are polynomial fits to the data points. t = 5ms.

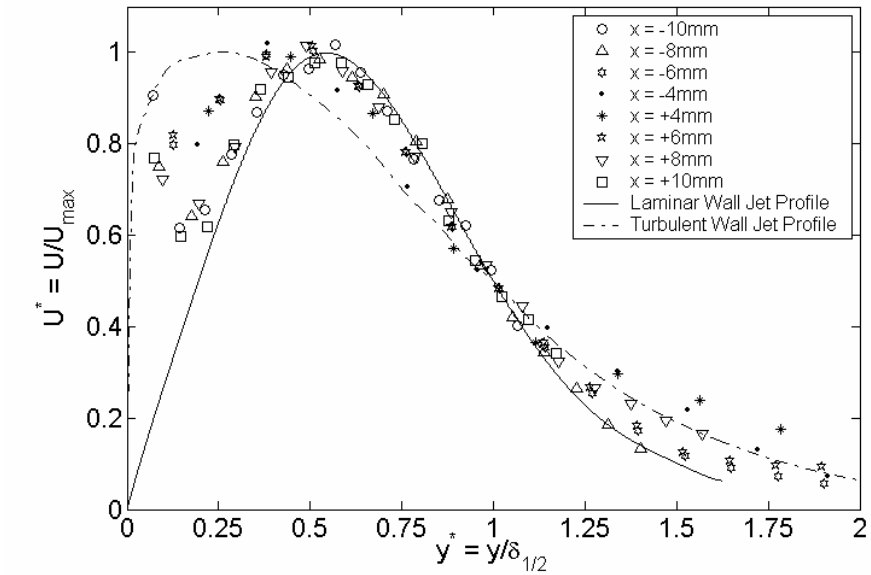

Figure 4.3.11. Non-dimensional velocity profile. Normalized with the maximum velocity, U_{max}, and jet half-width, $\delta_{½}$. The theoretical profiles of the laminar and turbulent wall-jet are plotted from Glauert[25]. t = 5ms.

The pulse averaged velocity profile, taken as the time-averaged velocity between plasma pulses, is shown as a contour plot at t = 0.05s and t = 1.01s in Fig. 4.3.12. The pulse averaged velocity profile is constant with time after t = 0.4s and takes the form of Fig. 4.3.12b. Also plotted in Fig. 4.3.12c is a contour plot of the asymmetric electrode configuration at t = 1.01s. The flow characteristics around the asymmetric electrode sheet are similar to the symmetric case; except the flow is clearly uni-directional and the induced flow velocity is higher. The velocity profile and similarity to a laminar wall jet are as above and we consequently focus on the symmetric case.

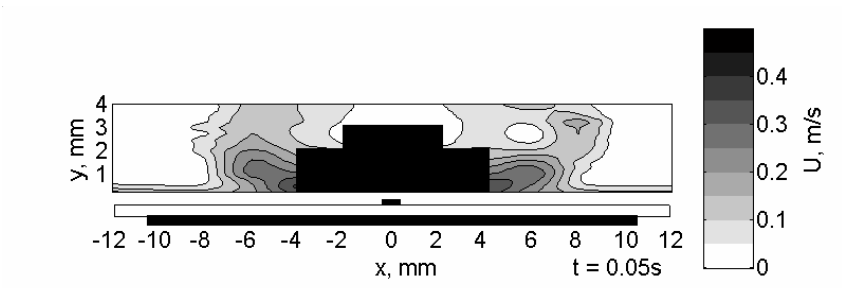

a)

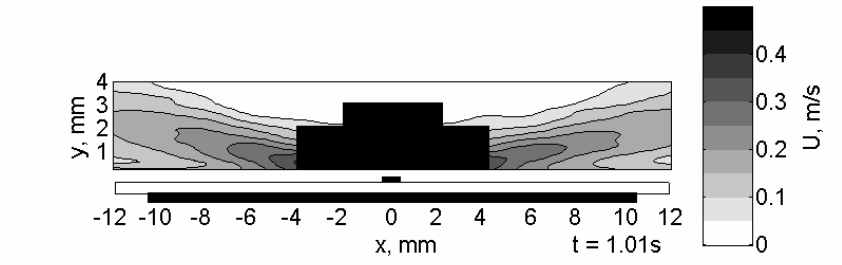

b)

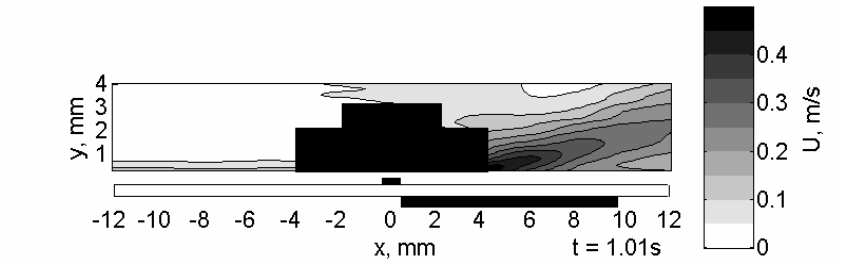

c)

Figure 4.3.12. Pulse-averaged velocity contours around a single electrode. Electrode sheet shown below each plot is not to scale. a) symmetric electrode, t = 0.05s and b) t = 1.01s. c) asymmetric electrode, t = 1.01s.

Figure 4.3.13 shows flow visualization images of the symmetric electrode using a smoke wire at similar times to Fig. 4.3.12. The quasi-steady flow can be seen in Fig. 4.3.13b, whereby a series of wall jets are produced in either direction. The individual jets are created during each plasma pulse and agglomerate at some distance downstream. Note that the airflow is primarily in the negative y direction above the electrode and in the $\pm x$ direction for $y <$ 2.5mm. The hotwire error associated with this non-parallel flow is less than 11% for $y < 2.5$mm.

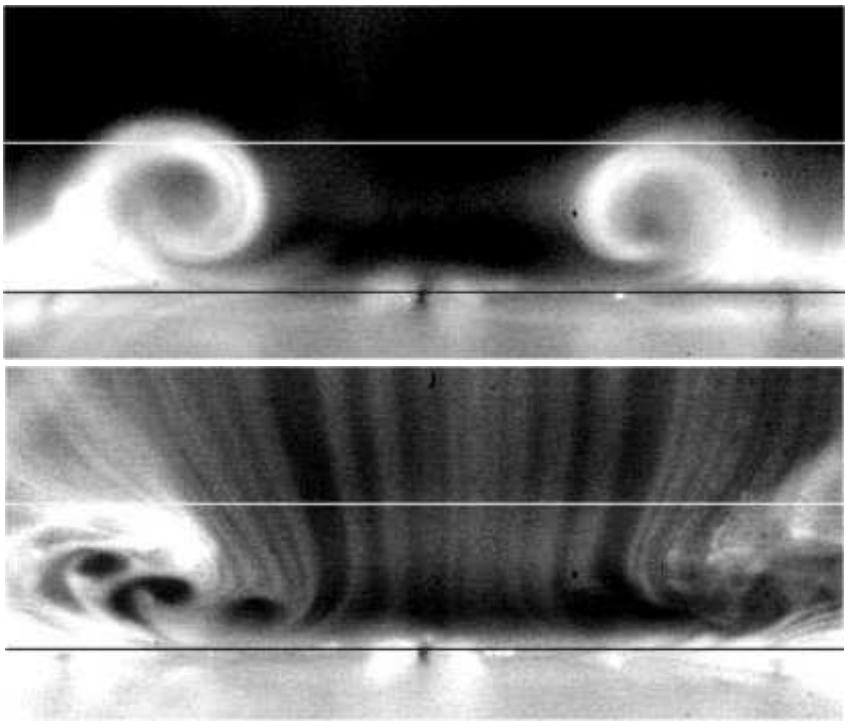

Figure 4.3.13. Smoke wire flow visualization images around the symmetric plasma electrode. The plasma electrode can be seen in the centre of the images and the smoke wire is located 10mm below. Note that the images have been rotated 180°. Horizontal field of view is 24mm ($x = \pm$ 12mm). Lines show the location of $y = 0$mm and $y = 4$mm. a) $t = 0.04$s; b) $t = 0.95$s.

The development of the jet profile can be seen in Fig. 4.3.14. This shows the nondimensional flow velocity, $U^* = U/U_{max}$, and the wall normal distance, y^*, at various times throughout the plasma pulse. Data at 6mm on either side of the electrode is shown since the data is fine enough to encapsulate the location of the maximum velocity and the velocity magnitude is significant ($U_{max} \approx$ 0.25m/s, see Fig. 4.3.10). The final velocity profile, taken as the average velocity profile for $t > 0.8$s, is identical at both of the streamwise locations and it is expected that the evolution of the jet is similar to either side of the electrode. The flow field seems to primarily develop in the outer region, with the velocity overshooting the final profile whilst the near wall flow increases in magnitude more slowly. This distortion in the outer jet profile is observed traveling away from the wall with time ($y^* > 0.5$) and has moved past this hot-wire location by $t^* = t.U_{max}/\delta_{½} \approx 7$. This motion is related to a pair of vortices created at the electrode at the moment of plasma creation, which can be clearly seen in the flow visualization of Fig. 4.3.13 and the temperature profile of Sec. 4.3.5. There is no evidence to suggest that the plasma forms differently during each pulse envelope and consequently it is believed that the momentum imparted into the flow is the same each time. For $t^* > 10$, the pulse averaged velocity profile becomes time invariant. The induced flow is therefore a quasi-steady pulsed laminar wall-jet, with small fluctuation in velocity between pulse envelopes, preceded by a development period in which vortices are created. These initiation vortices are inherent in the plasma flow due to the slip wall condition within the plasma and the non-slip boundary condition outside.

The variation of U_{max} and $\delta_{½}$ for the steady-state pulse averaged velocity profile with downstream distance, x, is plotted logarithmically in Fig. 4.3.15,

together with a best-fit line to the data. Glauert (1956) predicted that for a plane laminar wall jet the velocity varies as $u \propto x^{-1/2}$ and the jet thickness varies as, $\delta_{1/2} \propto x^{3/4}$. It can be seen that the best fit exponents are in reasonable agreement to that expected from a laminar wall-jet, given the lack of data in the downstream direction.

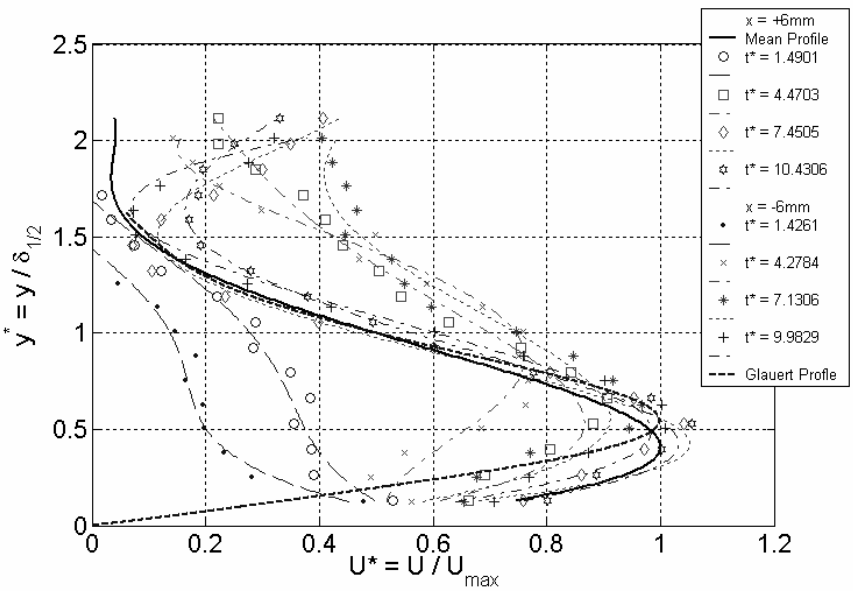

Figure 4.3.14. Development of the wall jet. Pulse-averaged velocity plotted nondimensionally at x = 6mm (open symbols) and x = -6mm (crossed symbols) at various midpulse times, $t^* = t.U_{max}/\delta_{1/2}$.

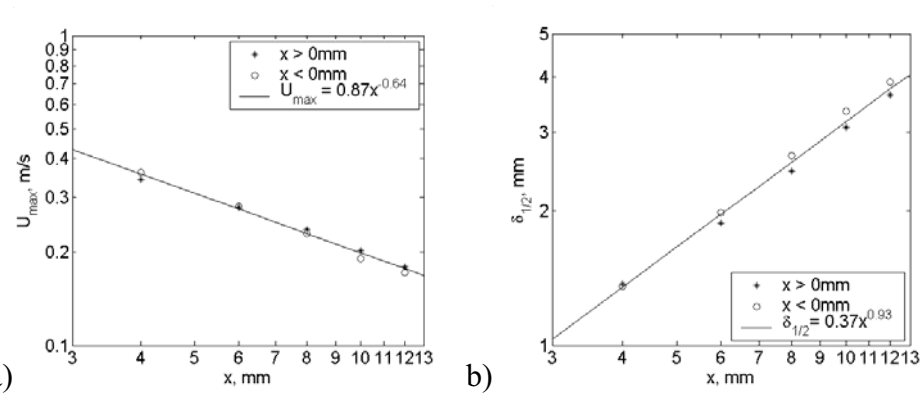

a) b)

Figure 4.3.15. Variation of steady-state pulse-averaged parameters with distance from electrode centerline. a) variation of maximum velocity and b) variation of jet half-width.

4.3.5. Temperature Profile

A similar technique has been applied with a cold-wire probe operated in constant current mode to obtain the temperature variation around the electrode in initially static air. Here the symmetric electrode case is studied and the plasma parameters are identical as for the results presented in Sec. 4.3.4. The contour plot of the ensemble averaged data after a single plasma pulse is shown in Fig. 4.3.16 at t = 4ms and t = 8ms. These show a pair of high temperature regions moving along the wall, away from the electrode centerline with maximum temperature difference of 2.0 ± 0.1ºC (compare Figs. 4.3.16a and 4.3.16b). Using the temperature as a passive tracer, these have an estimated convection velocity of 0.5 m/s. It is expected that the temperature is higher closer to the electrode. Thus there is some heat transferred to the air at the plasma-gas interface. After each individual plasma pulse, the heated air is convected laterally with the resulting wall jet flow.

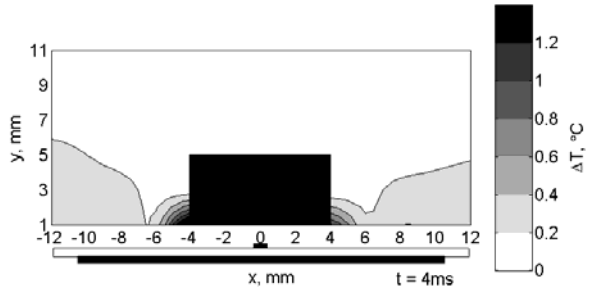

a)

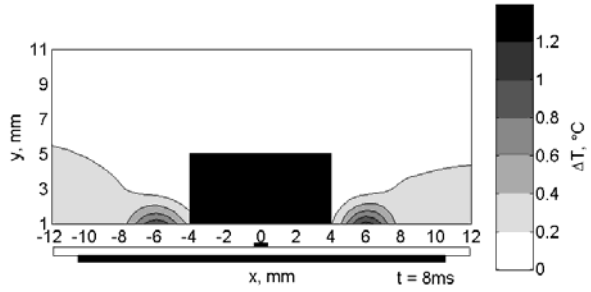

b)

Figure 4.3.16. Phase-averaged temperature contours around a single symmetric electrode. a) t = 4ms and b) t = 8ms.

The contour plot of the temperature change, based on time-averaged data between plasma pulses, is shown at t = 0.11s and t = 1.01s in Fig. 4.3.17. The initiation of the plasma causes two high temperature regions to be ejected away from the electrode centreline, corresponding to the two vortex cores (Fig. 4.3.17a). These have a convection velocity of 0.1m/s and travel at an angle of 25° to the wall. The maximum temperature difference is 0.5ºC. After about 0.3s, these have diffused and exited the measurement area. A steady increase in wall temperature is observed after this time, to a maximum of 0.8ºC at the end of the plasma-on period. The pulse averaged temperature profile on either side of the electrode at t = 1.01s is shown in Fig. 4.3.18. Similar to the velocity data this is nearly symmetric, as expected from the electrode geometry.

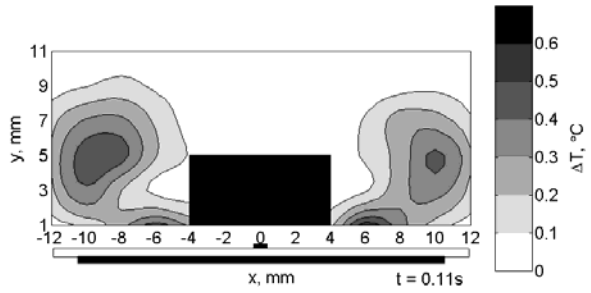

a)

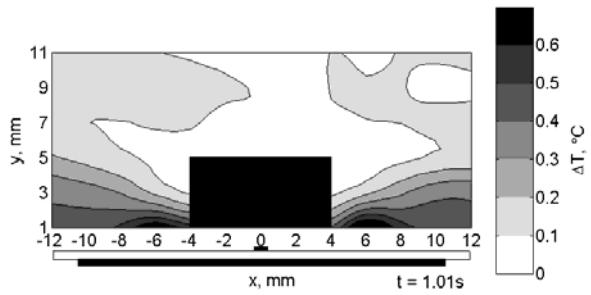

b)

Figure 4.3.17. Pulse-averaged temperature contours around a single symmetric electrode. a) t = 0.11s and b) t = 1.01s.

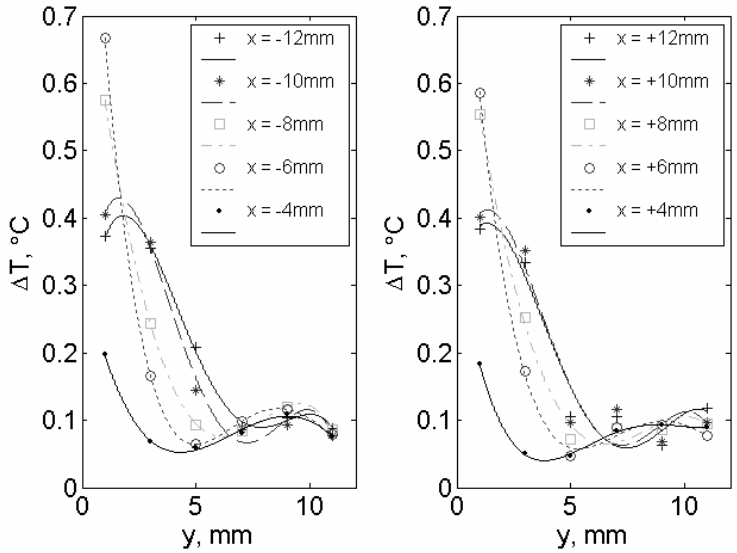

Figure 4.3.18. Pulse-averaged temperature profiles on either side of the symmetric electrode. Curves are polynomial fits to the data points. t = 1.01s.

The temperature of the induced airflow is not significantly above ambient temperature. Assuming a maximum temperature difference of 50°C occurs at the plasma-air boundary (a generous approximation given the temperature profile), and a length scale of 4mm (total length of plasma formation on both side of the electrode), the Grashof number of the configuration is Gr = 470. If the inertial force created by the temperature gradient were of the same order of magnitude as the buoyancy force, then $Re \sim Gr^{1/2}$. Thus, a flow of ~ 0.1m/s is expected. The observed flows are of greater magnitude and contrary to that expected from buoyant flow. We therefore expect that the thermal effect of the plasma is not responsible for the observed airflow.

4.3.6. Conclusions

Two-dimensional hot-wire and cold-wire surveys have been performed around a symmetric and an asymmetric RF glow discharge plasma electrode in initially static air at atmospheric pressure. The velocity profiles show that plasma imparts momentum into the air, such that a laminar wall jet is produced emanating away from the electrode centerline. Since the plasma induced flow is not a source of fluid, there is expected to be an entrainment region from above the electrode, whereby fluid is drawn towards the plasma to replace that ejected laterally.

The velocity profile and temperature profile show that vortices are created at the first instance of plasma formation in initially static air. These move at an angle of around 25° to the electrode sheet with a convection velocity of 0.1m/s. After an initiation period of $t^* \approx 10$, the flow forms a pulsed, quasi-steady laminar wall jet.

The temperature profiles show a maximum air temperature difference of 2°C occurs at 1mm away from the electrode sheet surface. It is unlikely that the thermal nature of the plasma is responsible for inducing the observed airflow since the temperature differences are small, and the observed flow is contrary to that expected from buoyancy driven flow. The origins of the induced flow field remain unclear. The fact that the induced flow only occurred when plasma was present does suggest that the flow is induced by some interaction between the plasma particles and the neutral gas, and not just the presence of the electric field. It has been suggested that the steep electric field gradients within the plasma accelerate ions, which exchange momentum with the neutral

background gas through ion-neutral collisions, and thus induce a flow (Roth 2001, Wilkinson 2003, Roth *et al.* 2000).

The magnitude of the induced flow field can easily be controlled by variations of the plasma excitation parameters and the observed trends suggest that higher flow speeds could be possible. The generated flow profiles are always similar to a laminar wall-jet at the low Reynolds numbers observed in these experiments. A peak velocity of 2.5 m/s has been recorded, although the true velocity will be greater at the plasma-air boundary. It is also observed that the asymmetric electrode configuration will confine the forcing in one direction and produce a jet velocity nearly double that of the symmetric actuator.

This study has been performed as a feasibility study for using the plasma actuator for flow control in the turbulent boundary layer. For successful flow control by mechanical spanwise wall oscillation, Choi *et al.* (1998) found that a drag reduction of 45% occurred with a nondimensional wall velocity, $w^+ = \Delta Z.\omega/2u^* \approx 15$, where Δz is the amplitude of wall oscillation, ω ($= 2\pi f$) is the angular velocity of wall oscillation, u^* is the friction velocity and f is the oscillation frequency. Choi *et al.* (1998) used f = 7Hz, Δz = 70mm with a free stream velocity, U_∞, of 2 m/s. The maximum wall velocity during the sinusoidal motion was 1.5 m/s. The flow velocities generated here are certainly capable of meeting these criteria, and it is concluded that plasma actuators will produce significant effects in low speed test facilities.

4.4. Induced Flow with Continuous Plasma Activation

In addition to the pulsed plasma tests described above, the effect of continuous plasma excitation has been studied on the symmetric plasma actuator of Sec. 4.3. Here, the hot wire was fixed at x = 4mm, y = 0.5mm from the electrode centreline (i.e. the point of maximum velocity within the measurable area) and the plasma was fired continuously for 1s with various applied voltage, E_{max}, and frequency, PRF. Note that this approach caused severe wear on the electrode sheet and it is not recommended for extended periods due to heating of the dielectric material. The power supply was not designed for this purpose and during similar tests using the thermal camera (see Ch. 6), several components within the power supply failed.

Figure 4.4.1 shows a typical hot-wire signal during the plasma event. Note that the induced flow velocity reaches a quasi-steady state after only 7ms. After this time the induced flow is fairly constant, although a slight increase in velocity with time was common, as can be seen in Fig. 4.4.1a. Prior to steady flow, a peak in induced velocity is observed after around 3ms. The exact cause of the high velocity spike at the moment of plasma initiation is not well understood. One can postulate that the initial ionization of the air is very violent during the first few AC cycles whereas for subsequent cycles, due to the presence of pre-ionized air, the process is much weaker. Though the plasma AC cycle has a timescale of the order 0.02ms, the difference between this and the fluid timescales is due to the transit time taken for the fluid to reach the detection probe.

This peak may be important for increasing the mean flow velocity. In the pulsed plasma tests, it was observed that the maximum ensemble averaged

velocity increases up to a limit of *PED* ≈ 3ms, coinciding with the time taken to the peak velocity in the continuous plasma case. Increasing the *PED* further did not increase the induced flow speed. It is therefore of little advantage to activate the plasma for more than this time and it may be possible to increase the induced-flow speed by pulsing the plasma in 3ms duration pulses at high frequency. This is attempted in Fig. 4.4.2, which shows the hot-wire signal at identical plasma and hot-wire conditions as Fig. 4.4.1, except the plasma is pulsed with *PED* = 3ms, *PEF* = 150Hz. The high velocity spikes do occur every pulse envelope and have similar magnitude as for the continuous plasma case. Though the average velocity is lower, it may be possible to increase it by pulsing at still higher frequency (i.e. *PEF* ≥ 250Hz, such that there is less than 1ms gap between envelopes). This will also have an associated energy saving by the introduction of some plasma off time. Unfortunately, the power supply was designed for plasma excitation between two channels. As a consequence, a duty cycle above 50% is impossible to achieve and it was not possible to test this hypothesis.

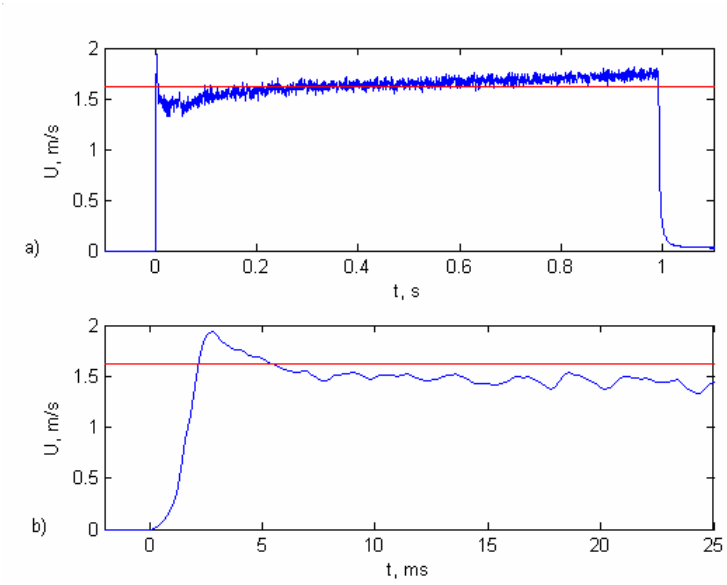

Figure 4.4.1. Hot-wire signal (-) and mean velocity (-) during 1s of continuous plasma forcing. Excitation at PRF = 50.3kHz, E_{max} = 3.1kV. a) Signal over entire 1s of plasma forcing and b) close up of initiation period.

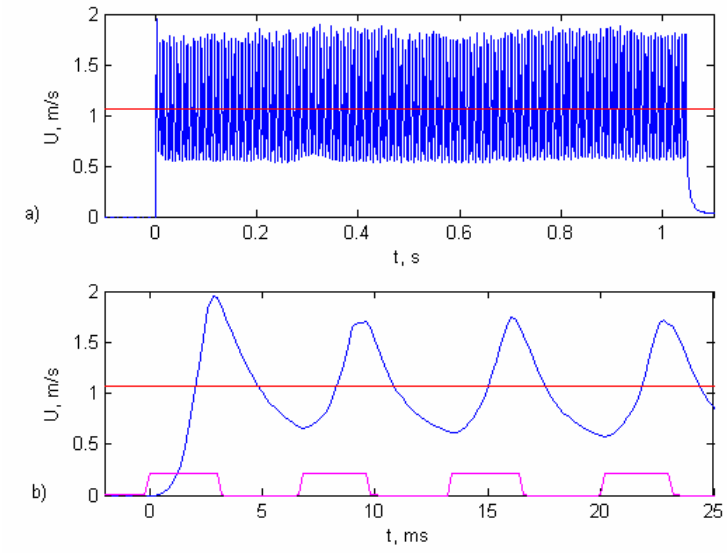

Figure 4.4.2. Hot-wire signal (-) and mean velocity (-) during 1s of pulsed plasma forcing. Excitation at PRF = 50.3kHz, E_{max} = 3.1kV, PED = 3ms, PEF = 150Hz. a) Signal over entire 1s of plasma forcing and b) close up of initiation period and pulse envelopes (-).

The variation of time-averaged velocity with voltage has been plotted for continuously fired plasma at different frequencies in Fig. 4.4.3. Here, an exponential fit has been applied to the data and a contour plot is shown in Fig. 4.4.3b. For an applied voltage above 2kV, the plasma formation threshold in atmospheric pressure air, a rapid increase in induced velocity is observed through increasing the voltage. The average velocity appears to vary with E_{max}^2, although the exact exponent increases with *PRF*.

The variation of average velocity with *PRF*, at several excitation voltages is shown in Fig. 4.4.4. Here, the contour plot of Fig. 4.4.3b has been interpolated to obtain the required information. A reasonably linear variation is observed, consistent with Roth *et al*. (2004 and 2005). It may therefore be inferred that the momentum coupling to the flow is the same during each AC cycle for a given voltage. Therefore by increasing the *PRF*, the amount of force per unit time is increased and the induced flow speed rises accordingly.

In contrast, the amount of momentum coupling per AC cycle is increased with E_{max}^2, indicating that the electric field strength and the plasma volume increases with voltage. Enloe *et al.* (2004b) showed that the spatial extent occupied by the plasma varies with *E* and that the propagation speed of the plasma varies proportionally to *E*. Gibalov and Pietsch (2000), also state that an increase in voltage leads to an enlargement of the discharge area on the dielectric. This will also be shown in the thermal imaging results in Ch. 6. Noting that the charge transfer takes place in a thin layer on the dielectric surface, the plasma volume, *V*, is subsequently expected to vary linearly with *E*, along with the quantity of charge contained within the plasma, $q = \rho_c V$.

Following Orlov and Corke (2005), the body force vector per volume of plasma, $\mathbf{f}_b$, is given by:

$$\mathbf{f}_b = \rho_c \mathbf{E} \qquad (2.3.14)$$

$$\text{i.e.} \qquad \mathbf{F}_b = \rho_c \mathbf{E}.V = q\mathbf{E}$$

Thus, through increasing the voltage, there is an increase in the electric field as well as the amount of charge, so that the force generated by the plasma is expected to vary as E^2.

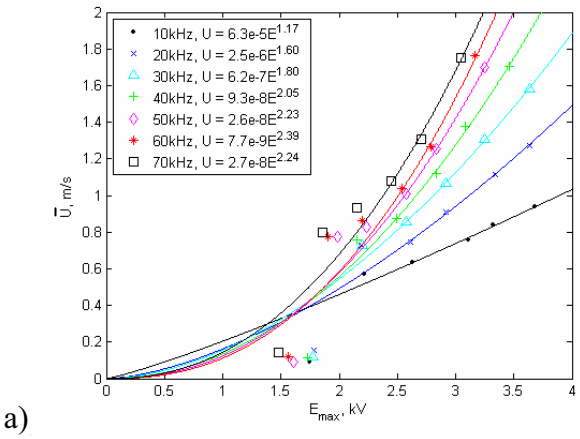

a)

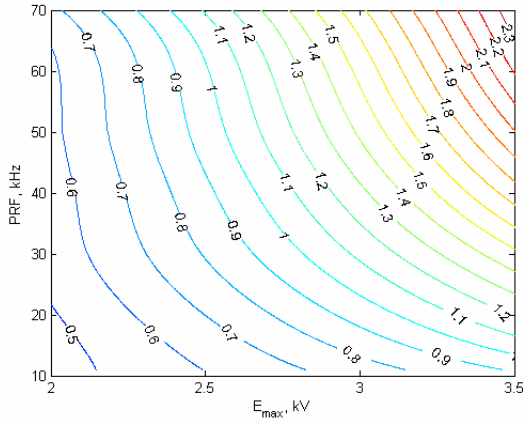

b)

Figure 4.4.3. Variation of time averaged velocity with maximum applied voltage, E_{max}, for several pulse repetition frequencies, *PRF*. Continuous plasma activated for 1s. a) Data fit to power law, $\overline{U} = AE_{max}^{n}$, and b) contour plot with average velocity marked on each contour.

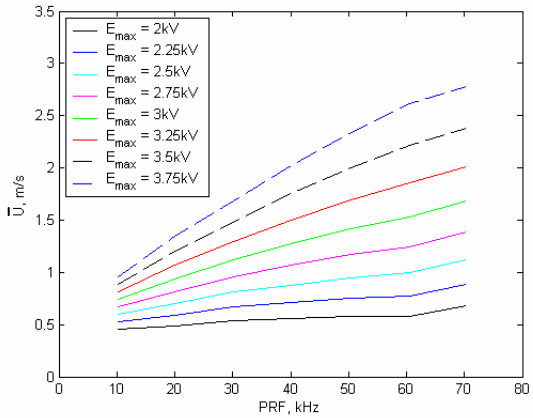

Figure 4.4.4. Variation of time averaged velocity with PRF for several excitation voltages. Continuous plasma activated for 1s. Data is interpolated from polynomial fit in Fig. 4.4.3b.

4.5. Consideration of Errors

All of the conclusions so far have been based on hot-wire measurements within 12mm of the plasma actuators. Such measurements were difficult to make and in this section, the effect of flow direction, probe position and ambient temperature changes will be considered in relation to the accuracy of the results.

4.5.1. Flow Direction

Hot-wire probes respond to the velocity normal to (i.e. u and v in these experiments) and tangentially to the wire (w) (Bruun, 1995). In the preceding sections it was assumed that the hot wire only measured flow parallel to the wall (i.e. u-component only). With an increase in v- and w-component velocities, significant measurement errors result from this assumption. In the plasma-induced wall jet the hot wire will inevitably be contaminated from v-component velocity. It will be shown later in Sec. 5.3.1 that the flow is directed towards the wall above the electrode and in the outer regions of the jet due to entrainment. Cross-wire probes could be used to decompose the velocity into u and v-components, but their physical size prevents their use in the region of interest in this study (typical X-wire dimensions are 2x2mm, while the region of interest is $x < 12$mm, $y < 4$mm). PIV measurements should also give erroneous readings near the wall due to surface reflections and the influence of the electric field on tracer particles. Thus, direct measurement of the v-component velocity has not been possible.

The analytical solution for a laminar wall jet emanating from a thin slit has been given by Tetervin (1948). This result was used to estimate the flow angle

and associated hot-wire error for the plasma wall jet flow. It is herein assumed that the plasma wall jet flow is identical to the wall jet emanating from a thin slit. It will be shown that the *u*-component velocity fields are similar, which leads one to believe that the *v*-component fields are also similar.

The non-dimensional *u*-component velocity, U^*, for a laminar wall jet is given by (Tetervin, 1948):

$$U^* = \frac{9^{2/3}}{3} Ra^{1/3} \frac{\overline{\frac{dG}{d\xi}}}{x^{*1/2}} , \qquad (4.5.1)$$

where $U^* = U/U_{ref}$, $Ra = U_{ref}\, a/\nu$, $x^* = x/a$; a is a reference length and U_{ref} is a reference velocity.

The non-dimensional *v*-component velocity, V^*, for a laminar wall jet is given by:

$$V^* = \frac{9^{1/3}}{Ra^{1/3}} \frac{1}{x^{*3/4}} \left(\frac{3}{4} \xi \frac{dG}{d\xi} - \frac{G}{4} \right) , \qquad (4.5.2)$$

where,

$$\xi = \frac{9^{1/3} Ra^{2/3}}{3} \frac{y^*}{x^{*3/4}} \qquad (4.5.3)$$

and, $y^* = y/a$. The functions $dG/d\xi$, ξ, G and $dG/d\xi$ were tabulated by Tetervin (1948).

A theoretical wall-jet flow can be computed which is similar to that induced by the plasma by taking the reference length, a, as the jet half thickness at x = 3mm and the reference velocity, $U_{ref,}$ as the maximum jet velocity at this location. With reference to Fig. 4.3.15, U_{ref} = 0.4m/s and a = 1mm at x = 3mm and thus Ra = 26. This allows calculation of *u*- and *v*-component velocity at different x locations, as shown in Fig. 4.5.1. The measured velocity (assumed

u-component) around the plasma electrode is also plotted, which shows reasonable agreement with the analytical solution. Figure 4.5.2 shows the flow angle relative to the wall direction. In addition, Fig. 4.5.3 presents a vector diagram of the calculated flow field. It can be seen that close to the wall, the flow is virtually parallel to it. In fact, for y < 2.5mm the flow direction is within 11° to the wall.

Recall that the wire is oriented parallel to the electrode with the probe stem in the wall normal direction. The tangential velocity component over the probe can be assumed zero since the plasma electrode is long compared with the hot wire (i.e. W = 0, 2D flow). Thus, the effective velocity detected by the hot wire, V_{eff}, is given by (Bruun, 1995);

$$V_{eff}^{\ 2} = V^2 + h^2U^2 = V^2 + 1.21U^2 \qquad (4.5.4)$$

where h = 1.1 has be used for the unplated single-wire probe. The effective velocity is shown in Fig 4.5.4, whereby the above response equation has been applied to the computed U and V (Fig 4.5.1a). Also plotted is the experimental error associated with assuming that V_{eff} = U. It is observed that the error associated with ignoring the v-component velocity is around 9% at x = 4mm, y = 0.5mm. By comparing Figs. 4.5.4 and 4.5.1, it can also be seen that the absolute difference between the sensed velocity, V_{eff}, and the true u-component is expected to be less than 0.04m/s in the entire measurement area.

a)

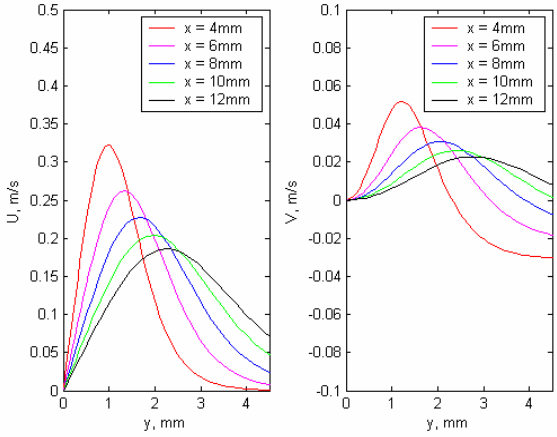

b)

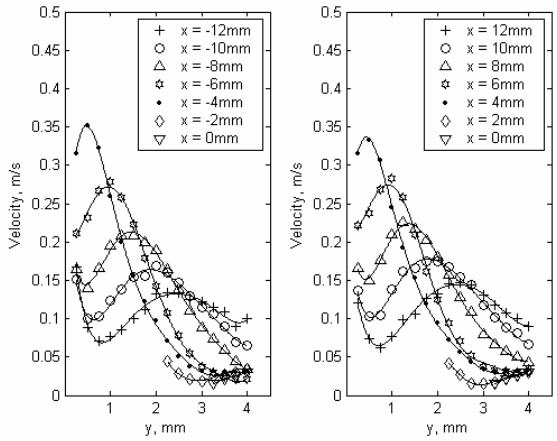

Figure 4.5.1. a) Calculated U and V from Tetervin (1948) with U_{ref} = 0.4m/s, a = 1mm. b) Time averaged velocity profile measured on either side of the symmetric, 250µm thick, Mylar plasma actuator excited at E_{max} = ±3.7kV, PRF = 50kHz, PED = 1ms and PEF = 50Hz.

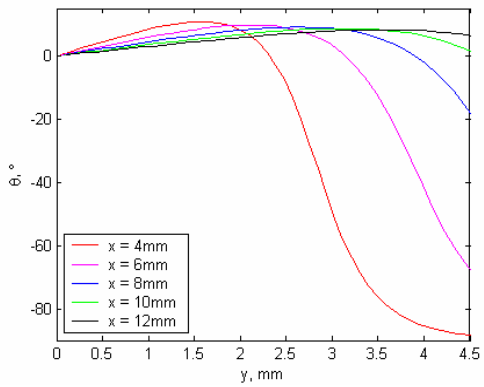

Figure 4.5.2. Flow angle calculated from Tetervin (1948) with U_{ref} = 0.4m/s, a = 1mm.

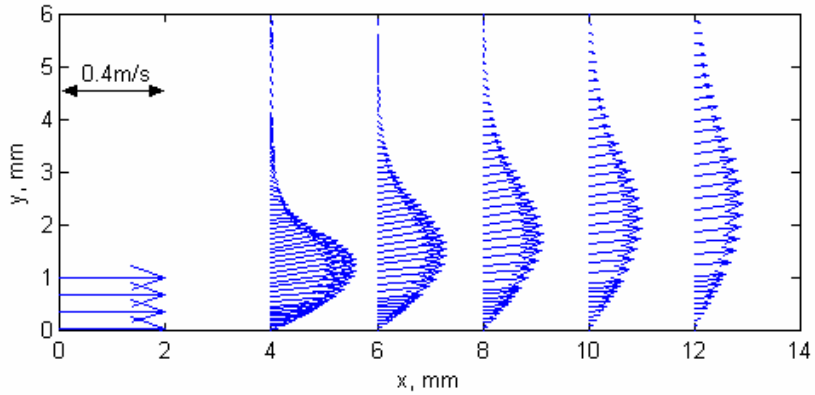

Figure 4.5.3. Vector plot of flow velocity from Tetervin (1948) with U_{ref} = 0.4m/s, a = 1mm. The inlet condition for the wall jet can be seen at x = 0mm. A vector length of 2 units corresponds to a velocity of 0.4m/s.

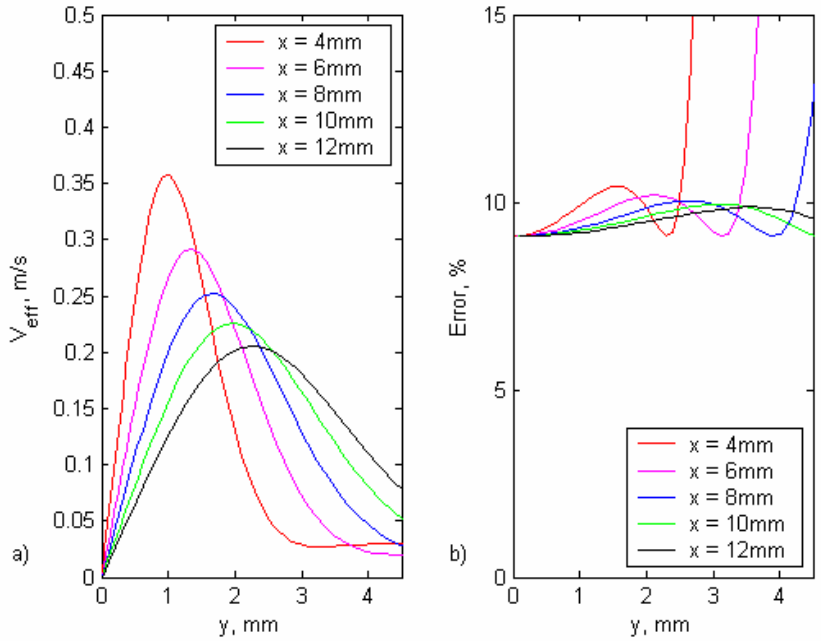

Figure 4.5.4. a) Effective velocity, V_{eff}, sensed by the hot wire and, b) hot-wire error associated with assuming $V_{eff} = U$.

4.5.2. Probe Positioning

The probe position relative to the electrode centreline was achieved using a CCD camera with a zoom lens. The positional accuracy is believed to be better than ± 0.2mm in x and y.

In the parametric testing performed in this chapter, the probe was fixed at x = 4mm, y = 0.5mm. This was the position of the maximum induced velocity for which measurement is possible while avoiding high voltage flashover. The position is, however, in a region of high shear and consequently large error in the maximum velocity may result from only small error in the probe location. Figure 4.5.5 illustrates this point, where the velocity has been computed from Tetervin (1948), at $x = 4 \pm 0.2$mm. The theoretical maximum velocity actually occurs at y = 1mm (as opposed to y = 0.5mm in experiments), due to the difference in the two flow configurations and the assumptions made of the reference length and velocity. Nevertheless, this illustrates the point well. It is observed that the velocity within position boundaries $x = 4 \pm 0.2$mm, $y = 1 \pm 0.2$mm, could have the possible values of 0.294m/s to 0.3305m/s (i.e. 0.312 ± 0.018m/s). Thus, the error in the u-velocity measurement due to wall positioning uncertainty is around ±6%.

Note however, that the probe was not moved during the parametric studies. Thus positional error does not affect the trends in induced flow velocity with E_{max}, *PRF*, *PED* or *PEF*.

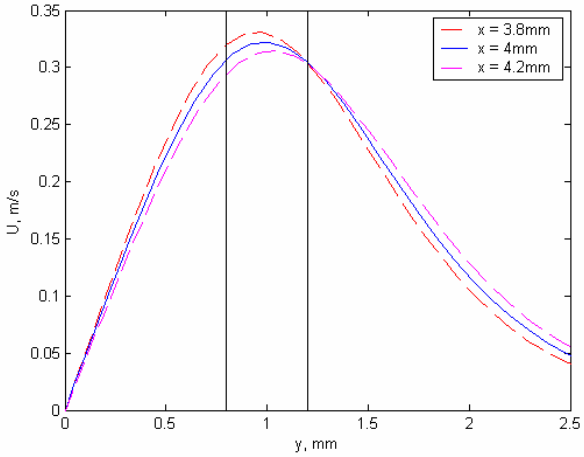

Figure 4.5.5. Computed laminar wall jet profile at $x = 4 \pm 0.2$mm. Lines mark the boundary of $y = 1 \pm 0.2$mm.

4.5.3. Ambient Gas Temperature Change

It was shown in Sec. 4.3.5 that the plasma causes localised heating of the gas. The maximum air temperature rise was 2°C above ambient and the maximum time-averaged change was 0.6°C. From hot-wire calibrations at different ambient temperatures, it is apparent that a 1°C temperature increase will cause a shift in the calibration curve, thus causing the hot-wire velocity to be calculated around 0.05m/s too low. Note that the plasma will only act to raise the gas temperature and consequently the measured velocity will only be decreased from its true value.

Only the velocity data presented in Sec. 4.3.4 have been corrected for the air temperature change due to plasma because of the prohibitive time taken to measure velocity and temperature for every experiment condition. In the temperature correction, the maximum increase for the ensemble-averaged velocity was 0.039m/s. It is therefore expected that the temperature of the plasma will cause errors of up to -8%, approximately.

4.5.4. Overall Uncertainty

In addition to the above uncertainties, errors will also be introduced by the effect of the wall and the hot-wire calibration. The wall effect results from the increased heat loss from the probe as it approaches the wall and is a function of both the flow speed and the wall material (Wills, 1962). The wall effect caused a velocity reading of up to +0.06m/s in still air, 0.5mm above the Mylar sheet. Note also that the wall effect will tend to increase the measured velocity, whereas the increase in air temperature will act to decrease it. Calibration errors result from the uncertainty of the FlowMaster readings at low speed. Both of these errors will be significantly reduced as the flow speed increases, and are expected to be considerably less than the error sources described in Sec. 4.5.1-4.5.3.

The total uncertainty in the velocity measurement consists of contributions of all of the uncertainties described above. Note that some of the quoted uncertainties are interdependent. For example, an error in the wall positioning will affect the error caused by non-parallel flow and the thermal error will counteract the wall effect. The overall uncertainty can be evaluated using the method of Kline and McClintock (1953). For the 250μm thick Mylar actuator, many full 2D traverses of the plasma electrode were performed over a period of many months, where one experimental condition was repeated many times. This data set is representative of all error sources described above, and in addition, the atmospheric conditions varied considerably. The variation in the maximum velocity at x = 4mm, y = 0.5mm in these experiments was 0.51 ± 0.05m/s (20:1 odds). Consequently, the error at this location in the velocity measurement is expected to be around ± 10%.

Chapter 5

Effects of Dielectric Material and Geometry

5.1. Introduction

In the previous chapter, it was shown that plasma actuators with 250μm thick Mylar dielectric are capable of inducing a laminar wall jet flow with magnitude of up to 2.5m/s. This flow speed is rather low and perhaps too low to cause discernible effects in real aerospace applications where the free-stream speed is expected to be several hundred meters per second. In this chapter, the effects of dielectric thickness and dielectric material on the speed of the plasma induced flow are explored. It is hoped that the induced-flow velocity can be increased by enhancing the charge stored on the dielectric surface (and hence body force).

A review of dielectric material properties is presented in Sec. 5.2, followed by a study of a symmetric plasma actuator with 125μm thick Mylar dielectric in Sec. 5.3. Comparison is made with the 250μm thick Mylar symmetric and asymmetric actuators from Ch 4. Section 5.4 presents experimental results using ceramic dielectrics. Two different dielectric materials (Si_3N_4 and AlO_3) with various thicknesses are studied.

5.2. Dielectric materials

The term dielectric refers to a material which is a poor conductor of electricity but an efficient supporter of electrostatic fields. These electric fields are maintained by the process of polarization within the dielectric. In essence, the

charges in a dielectric will not experience bulk motion due to an electric field (like a conducting media), but they will rearrange themselves to cancel as much of the applied field as possible, i.e. negative charges will be displaced towards the positive electrode and vice versa (Frohlich, 1958). The exact process of polarization depends on the nature of the dielectric material. For example, electrons may be displaced relative to their atomic nuclei (electronic polarization), atoms can be displaced relative to each other (atomic polarization), or molecular dipoles can be rotated (dipole polarization), (Kroschwitz et al. 1986). Dipole polarization is most common in polymers, like Mylar. Through polarization, the dielectric material establishes an electric field within itself that will oppose the polarity of the applied field. Consequently, the electric field strength will decrease within the dielectric material (Frohlich, 1958), and it can store electrical energy; hence their widespread application as capacitors.

In a parallel plate geometry, typical of capacitors, the ratio of the charges on the capacitor plates with and without the dielectric is defined as the dielectric constant (relative permittivity) of the material, ε. Thus, if the dielectric constant is increased, a higher amount of charge can be retained across the dielectric. In the case of the plasma actuator, this means that a material with higher dielectric constant will be able to support more surface charge. If the electric field is not altered by the material's dielectric properties, the presence of additional surface charges / charge density will generate more body force since $\mathbf{f}_b = \rho_c \mathbf{E}$ (Orlov and Corke, 2005). There will however, be a complicated modification of the electric field by the dielectric.

When a dielectric is placed in an AC field, the polarization of charge takes place cyclically. However, there is a finite time taken for the dipoles to rotate because their motion is impeded by molecular friction. This is known as dielectric relaxation. Consequently, the current flowing in the dielectric is out of phase with the applied voltage. This phase lag can be expressed by the loss tangent, or dissipation factor, tan5. The rotation also leads to internal heating through the frictional action of the rotating charge – commonly known as dielectric heating. Microwave heating, used in household microwave ovens, is achieved by this process. The power lost to dielectric heating, P, is given by:

$$P = 2\pi f C E^2 \tan\delta \qquad (5.2.1)$$

where, f is the applied frequency, C is the capacitance and E is the applied voltage (Kroschwitz et al. 1986). Thus, plasma actuators should be constructed from dielectric materials with low tan5 such that dielectric heating losses are minimise and the efficiency is increased.

In general, the dielectric constant and loss tangent are functions of temperature and frequency. For polymers, both of these variations largely depend upon the molecular structure, especially whether the material is polar on non-polar. For non-polar materials, such as PTFE, e and tan5 are nearly constant over a wide frequency range and for temperatures below the softening point. For polar materials, such as Mylar, e generally decreases with an increase in frequency, whereas tan5 increases and decreases in a cyclic manner (changes with temperature are similar). The exact variations for Mylar are shown in Figs 5.2.1 and 5.2.2. At constant frequency, e increases as the temperature of the film increases above 65°C. At constant temperature, e decreases with frequency. The cyclic nature of tan5 can be seen in Figure 5.2.2. Note that in

Figure 5.2.2b, tan5 begins to decrease at very high frequencies outside the range of the figure.

Dielectric materials are observed to fail by three mechanisms; intrinsic breakdown, thermal breakdown and avalanche breakdown (O'Dwyer, 1964). Intrinsic breakdown depends on the migration of electrons though the dielectric. Thermal breakdown occurs by changes in conductivity with temperature and can produce local heating beyond that which can be readily dissipated: a cycle that leads to catastrophic failure. Avalanche breakdown occurs when a single electron causes an avalanche of sufficient size to destroy the insulating properties of the dielectric. This is the "solid state" equivalent to creating plasma in a gas. Further to this, failure may occur in voids in the dielectric (Kroschwitz et al. 1986), whereby the electric field is higher within the void than the surrounding dielectric which causes breakdown of gas within it. This leads to oxidation, carbonization and increased gas pressure/temperature within the void which produces cracking. Also, in the case of the plasma actuator configuration, the ion bombardment from the plasma onto the dielectric surface will modify the surface and change the material properties. In practice, the exact mechanism of dielectric breakdown is complex and may be different in experiments which are, as far as possible, identical (O'Dwyer, 1964).

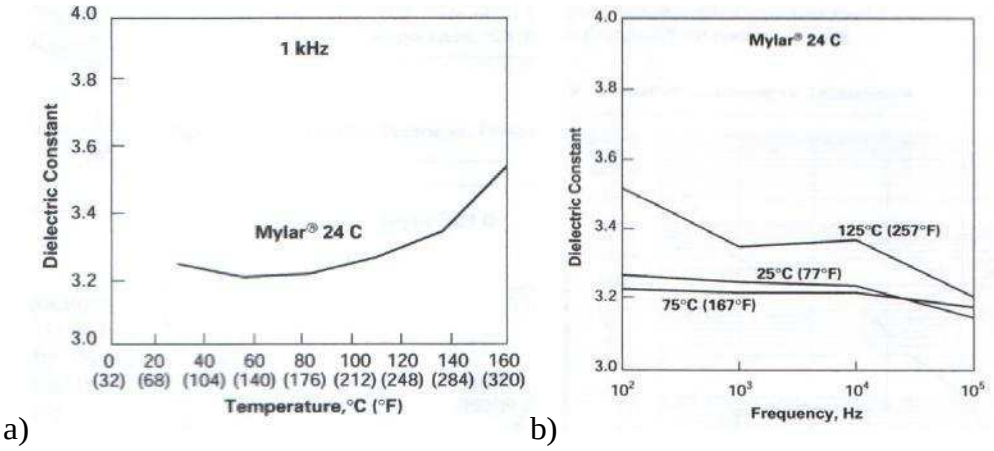

a) b)

Figure 5.2.1. Dielectric Constant, ε', variation with temperature (a), and frequency (b) for Mylar. From DuPont Teijin Films product information.

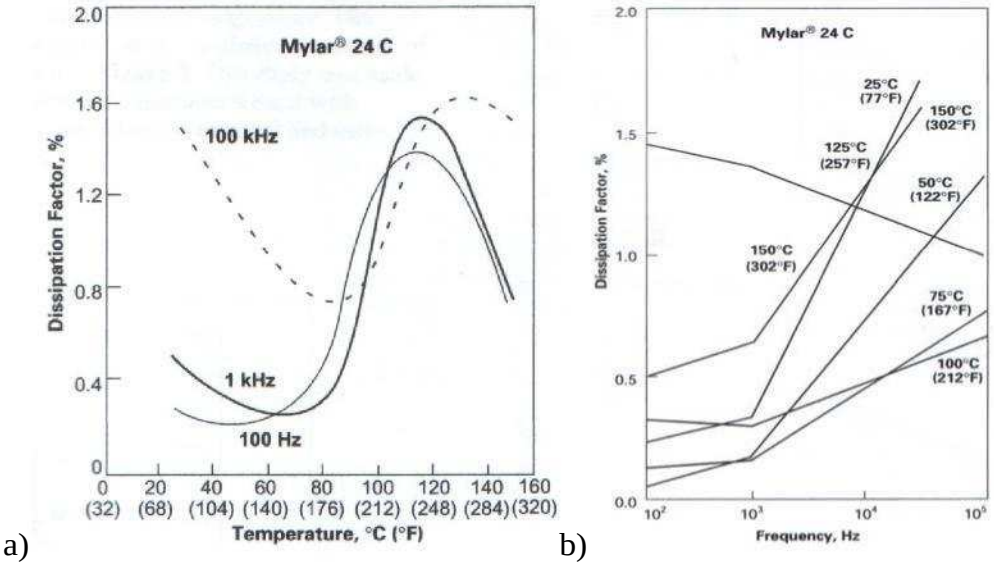

a) b)

Figure 5.2.2. Dissipation factor, tanδ, variation with temperature (a), and frequency (b) for Mylar. From DuPont Teijin Films product information.

5.3. Effect of Dielectric Thickness

In this section, a plasma actuator with reduced dielectric thickness is studied. Here, a symmetric configuration with 125pm Mylar dielectric has been tested with the methodology as described in Sec. 4.2. A 2D survey with a hot-wire probe was performed for identical plasma parameters as used for the 250pm Mylar symmetric actuator and the 250pm Mylar asymmetric actuator in Sec. 4.3, namely E_{max} = 3.6kV, PRF = 50kHz, charge time = 7ps, PED = 1ms, PEF = 50Hz. In addition, the effects of each plasma parameter was studied by fixing the hot wire at x = 4mm, y = 0.5mm from the electrode centreline and varying each parameter independently. Direct comparison of the induced velocity is made with the other Mylar plasma actuators. The physical dimensions of the three plasma actuators are summarized in Table 5.3.1.

The 125pm Mylar symmetric sheet is shown in Fig. 5.3.1, and Fig. 5.3.2 shows the sheet with plasma. The plasma formation was observed to be symmetric around the electrode when viewed though a video camera. Frequent burn-through occurred between the upper high voltage electrode and the lower, ground electrode due to the reduced thickness of this sheet. It appears that this thickness of Mylar is very close to dielectric breakdown when a voltage of 3.6kV is applied.

		250μm Symmetric Mylar	250μm Asymmetric Mylar	125μm Symmetric Mylar
Upper Electrode	Length, mm	90	85	115
	Width, mm	0.2	1.0	0.1
	Thickness, μm	17	17	17
Lower Electrode	Length, mm	110	85	150
	Width, mm	170	9	100
	Thickness, μm	17	17	17
Dielectric	Material	Mylar	Mylar	Mylar
	Thickness, μm	250	250	125
Configuration		Symmetric	Asymmetric	Symmetric

Table 5.3.1. Details of Mylar plasma actuators. All electrodes are Copper.

a) 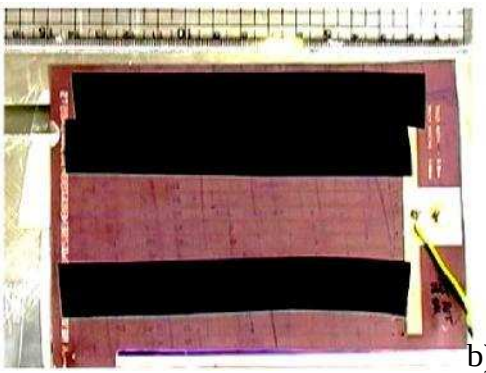 b) 

Figure 5.3.1. 125μm thick Mylar electrode sheet. a) Entire sheet and b) close up of connection bus and plasma electrode. Insulating tape shown in the photographs is used to suppress unwanted plasma formation.

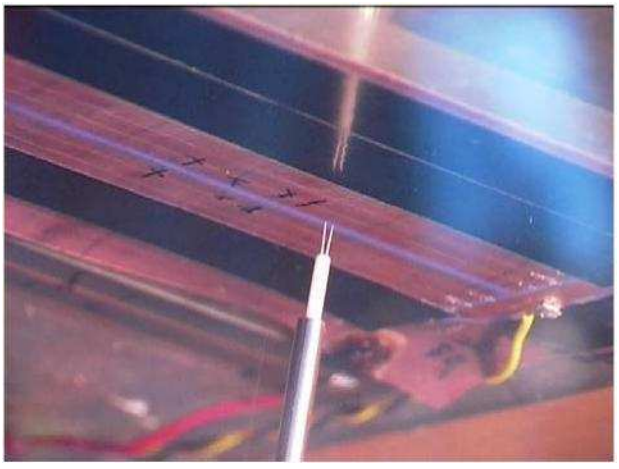

Figure 5.3.2. 125μm thick Mylar electrode sheet during testing. Note symmetric formation of plasma around the electrode, occurring as a light purple glow.

5.3.1. Induced Flow Field – Steady State

The time-averaged velocity profile around the 125pm Mylar actuator is shown in Figure 5.3.3a. The blacked-out area of the plot represents the region for which no data was taken due to the risk of arcing between the electrode and the hot-wire probe. Figure 5.3.3b and 5.3.3c show respectively the time-averaged velocity profile of the 250pm symmetric and 250pm asymmetric actuators.

It is observed that the induced flow characteristics are very similar to that of the 250pm thick Mylar sheet, whereby a laminar wall-jet is created in either direction away from the electrode. However, the magnitude of the velocity has increased due to the reduction in dielectric thickness. Figure 5.3.4 gives a comparison of the velocity profiles of the three actuators. It can be seen that the induced flow velocity of the 125pm symmetric actuator was increased by

around 30%, compared to the 250pm symmetric case (i.e. 30% increase in U for a 50% reduction in dielectric thickness). One also observes that the magnitude of the induced airflow of the 250pm asymmetric actuator was increased by around 50% relative to the 250pm symmetric case (on the plasma side of the electrode only). In fact, the velocity profile of the 250pm thick asymmetric actuator and one side of the 125pm thick symmetric actuator are very similar.

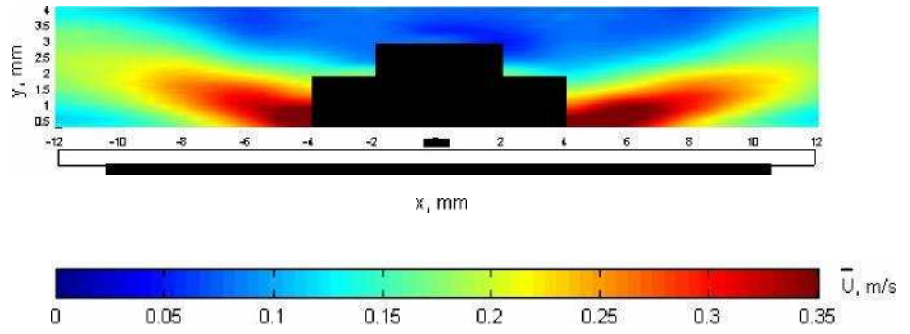

a)

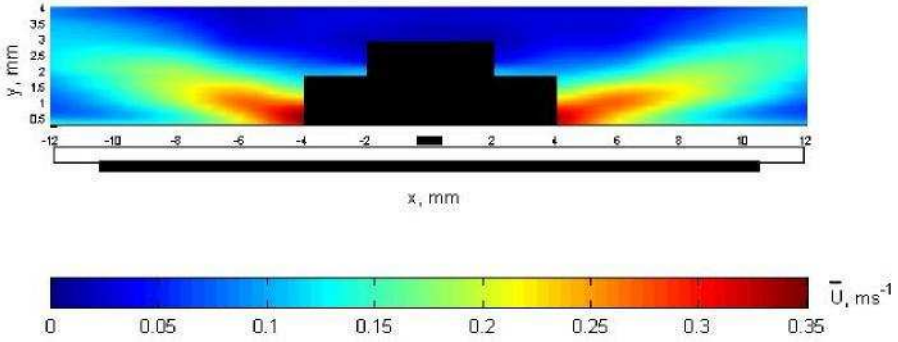

b)

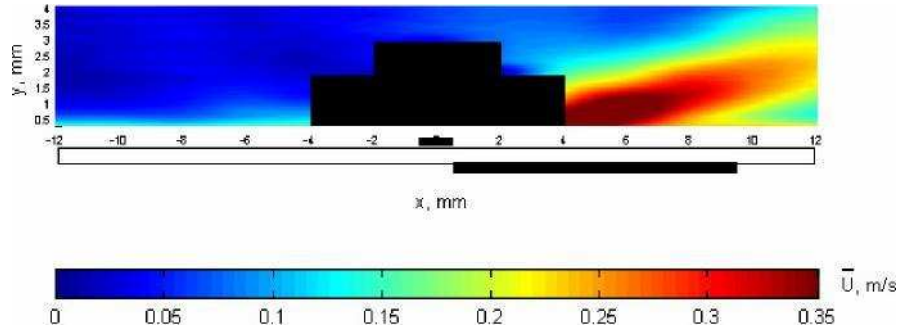

c)

Figure 5.3.3. Velocity profile around: a) 125μm thick Mylar plasma actuator; b) 250μm thick actuator; c) 250μm thick asymmetric actuator. Contours show time-averaged velocity magnitude over 1.4s of plasma forcing. Flow direction is in –x direction for $x < 0$ and in +x direction for $x > 0$. Plasma excitation at $E_{max} = \pm 3.7$kV, PRF = 50kHz, PED = 1ms and PEF = 50Hz.

a

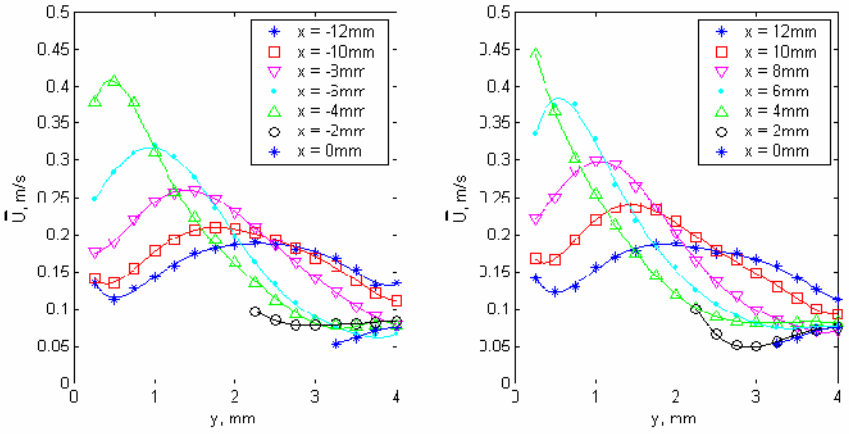

c

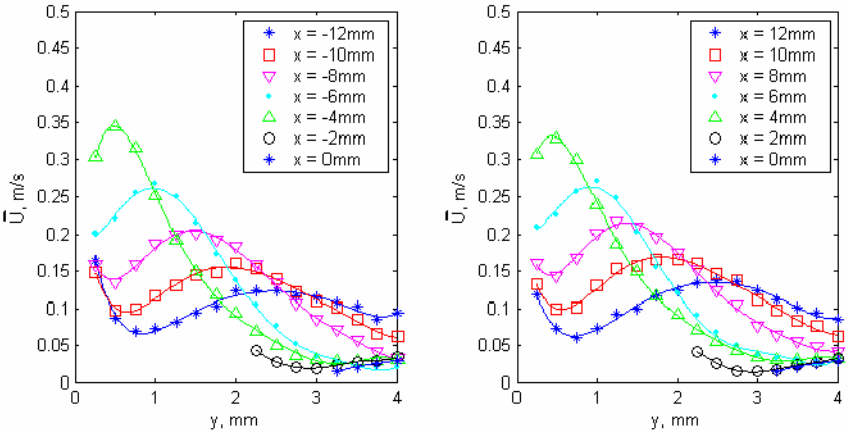

e

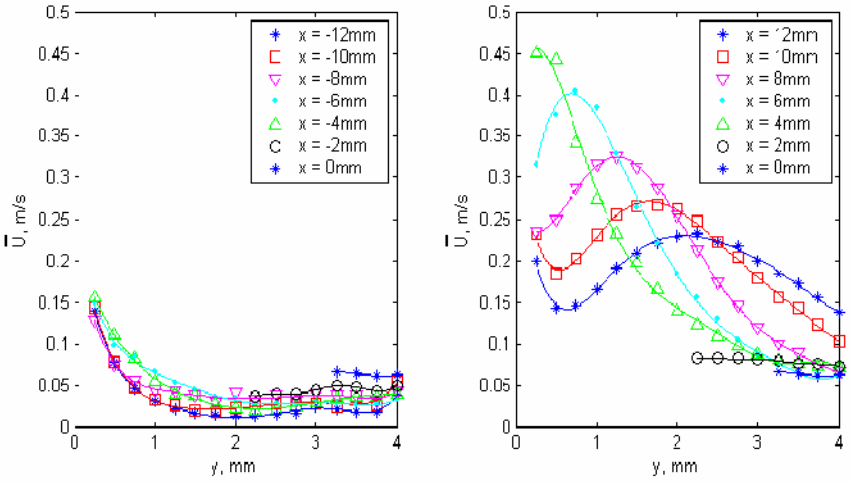

Figure 5.3.4. Mean velocity profile on either side of the plasma electrode: a) 125μm thick Mylar actuator; b) 250μm thick Mylar actuator; c) 250μm Mylar asymmetric actuator.

The time-averaged spanwise vorticity, ω_z, and velocity vectors are shown for the three plasma actuators in Fig. 5.3.5. Here, the wall-normal velocity component, V, was obtained by integrating the continuity equation from the wall outwards, with the assumption that the flow is two-dimensional (i.e. W = 0). This is reasonable since measurements were taken at the mid-point of electrodes more than 85mm long. In addition, this scheme presumed that the hot-wire signal comprised the streamwise velocity component, U, only. This assumption is compromised near the electrode centreline since there is expected to be a large negative V-component which contaminates the hot-wire signal. Also, it was necessary to interpolate the velocity across the region without hot-wire measurements to allow integration in the wall-normal direction (i.e. for $-4 < x < 4$, $y < 2$mm). This was performed by cubic interpolation in x and y. Hence, large errors are expected in V and ω_z near the plasma centreline. However, qualitative observations for $x < -4$mm and $x > 4$mm are expected to be valid.

Figure 5.3.5 shows that the velocity vectors are mainly parallel to the wall suggesting that the hot-wire signal is dominated by U, as assumed. The broadening and deceleration of the jet profile is also obvious from this figure and it is clear that the plasma entrains fluid from above it to replace that forced laterally. The increase in induced velocity by reducing the dielectric thickness is clearly visible, along with the uni-directional flow created by the asymmetric actuator.

A reduction in dielectric thickness evidently increases the plasma-induced wall jet velocity and it is expected that the reason for this is the increased capacitance of the sheet. For a parallel plate capacitor, the charge stored, Q:

$$Q = CV = \frac{\varepsilon_r \varepsilon_0 A}{d} V, \qquad (5.3.1)$$

where C is the sheet capacitance, V is the applied voltage, ε_r is the dielectric constant, ε_0 is the permittivity of free space, A is the electrode area and d is the sheet thickness. Thus, the charge stored for a given applied voltage is proportional to 1/d. Although the geometry is much more complicated for the plasma actuator, one would still expect the capacitance to increase and thus the amount of surface charge will be increased. Hence more charge exists within the electric field and greater force is produced. In addition, the electric field strength will be increased due to the decrease in dielectric thickness which will further enhance the force produced.

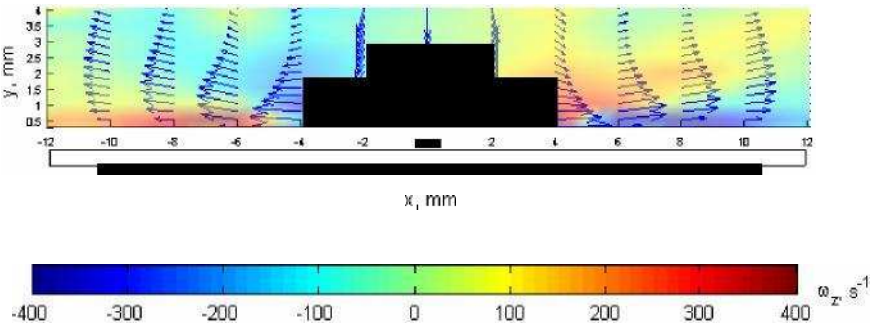

a)

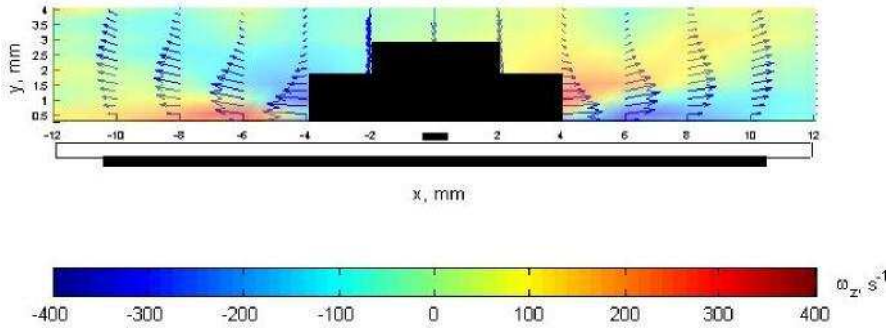

b)

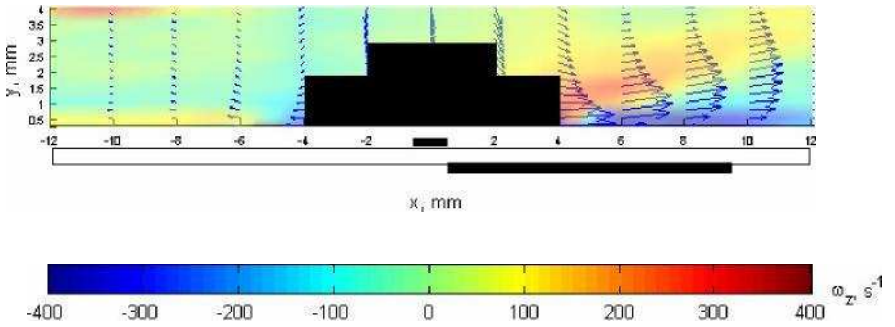

c) Figure 5.3.5. Time-averaged vorticity contours and the velocity vectors in initially static air around: a) 125 μm thick Mylar plasma actuator; b) 250 μm thick Mylar actuator; c) 250 μm thick asymmetric actuator. Positive vorticity implies counter-clockwise rotation. Plasma excitation at E_{max} = ±3.7kV, PRF = 25kHz, PED = 1ms and PEF = 50Hz.

5.3.2. Induced Flow Field – Flow Initiation

Figure 5.3.6 shows the instantaneous velocity vectors and vorticity field from generating plasma with the 125$_p$m thick Mylar dielectric actuator. Slight asymmetry was observed in the flow field, possibly caused by probe location errors or by irregularities in the plasma formation. Figure 5.3.7 shows the flow development for the 250$_p$m thick Mylar actuator at identical times to Fig 5.3.6. It is apparent that the transient development of the flow field is nearly identical in both cases, except that the magnitude of the induced flow velocity was increased by the reduced thickness dielectric.

At the first timestep in both Fig. 5.3.6 and Fig. 5.3.7, there appears to be two regions of strong vorticity alternating in opposite senses located at x § ±6mm, y § 3mm. The velocity vectors show a rotation of fluid around these regions, which are the vortices created by the initiation of plasma. Recall that these vortices are observed at similar positions and times as the temperature measurements and flow visualisation of Sec. 4.3, which are reproduced in Fig. 5.3.8 and Fig. 5.3.9 for clarity.

For t > 0.4s, the flow appears more uniform and uni-directional since the vortex cores have been convected outside of the measurement region. However, regions of high vorticity were also observed to be convected away from the electrode centre line throughout the entire plasma forcing period. These issued from the plasma region after each pulse envelope (PEF = 50Hz) and travelled along the wall with the same rotation sense and location as the rolled up wakes in the flow visualisation of Fig 5.3.9c. One such region can be made out at x = +6mm, y = 1.5mm in Fig. 5.3.6c.

Similar phenomena can be observed in Fig. 5.3.10, which shows the development of the flow field for the asymmetric actuator. Here, the induced flow is mainly unidirectional (i.e. to the right in the view of the figure). It was observed, however, that during the initial stage of plasma forcing, a jet was produced in both directions. This quasi-symmetric forcing was present for $t < 0.2s$ only (i.e. first 10 pulse envelopes), and the magnitude of the jet velocity on the 'no plasma' side of the electrode was approximately half that on the 'plasma' side. On closer inspection with a digital video camera, it appeared that some plasma did form on both sides of the electrode for the first part of the plasma on period, as shown in Fig. 5.3.11. This will produce bi-directional forcing, like the symmetric actuator. It is expected that this plasma can be suppressed by increasing the width of the upper electrode so that there is a greater distance between the upper electrode edge and the lower electrode. This behaviour could be linked to the results in Sec. 4.4, where it was observed that the magnitude of the induced flow velocity was greater for the first few plasma cycles. It was postulated that the initial ionization of the air is more energetic during the first few AC plasma cycles whereas for subsequent cycles, due to the presence of pre-ionized air, the process is much weaker.

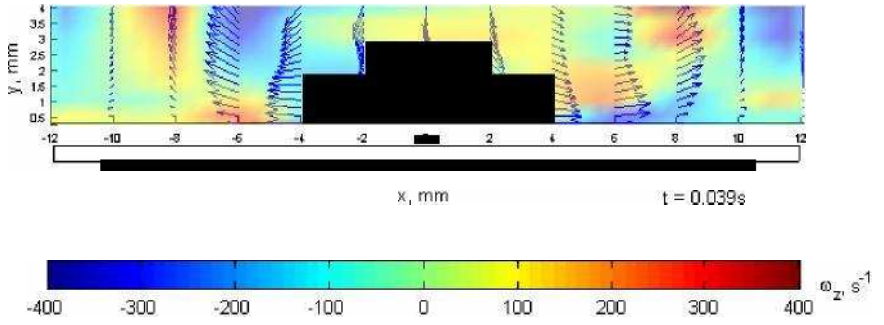

a)

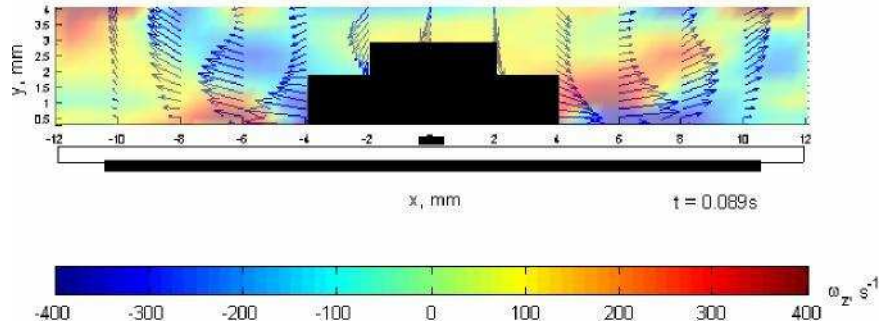

b)

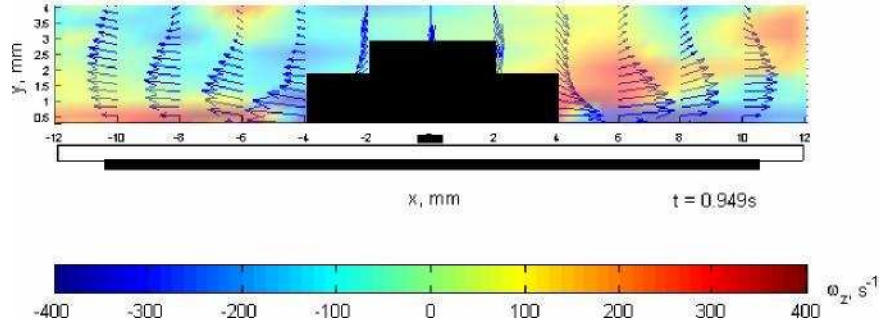

c)

Figure 5.3.6. Instantaneous vorticity contours and velocity vectors around the 125μm Mylar plasma actuator at: a) t = 0.039s; b) t = 0.089s; c) t = 0.949s. Towards the end of the plasma forcing (c), the flow is predominately in the ±x direction.

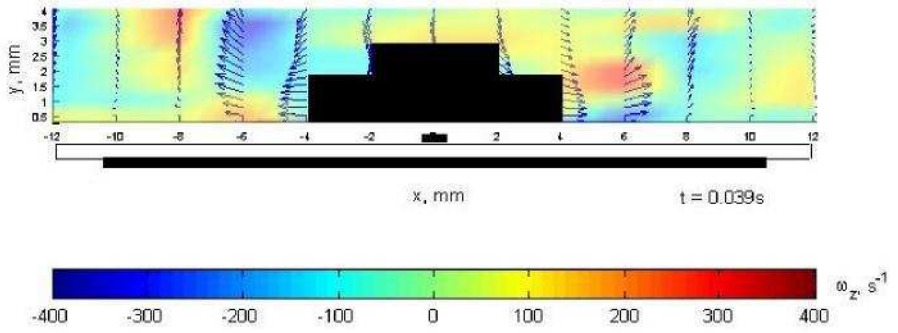

a

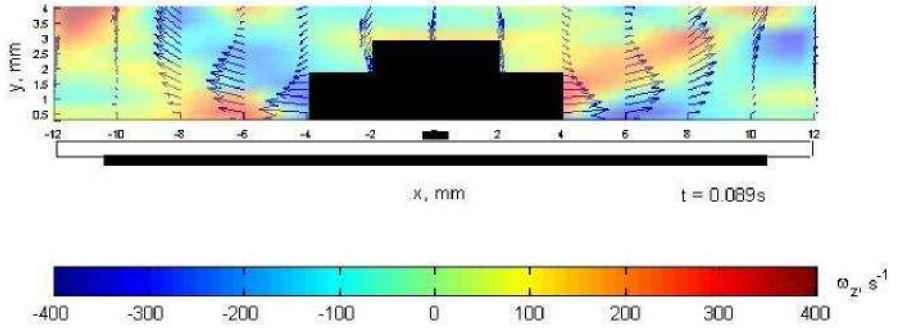

c

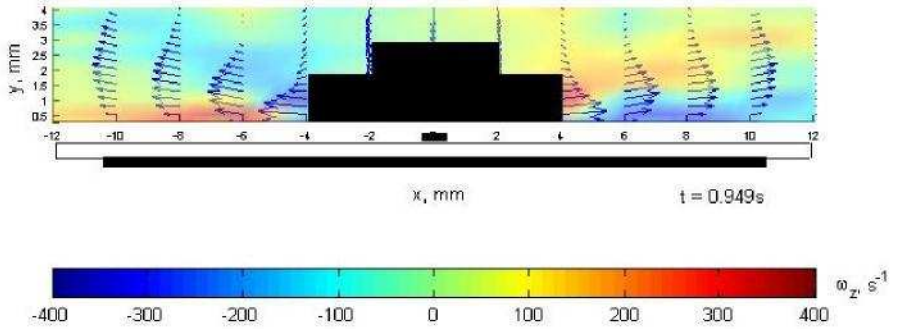

e

Figure 5.3.7. Instantaneous vorticity contours and velocity vectors around the 250m Mylar plasma actuator at: a) t = 0.039s; b) t = 0.089s; c) t = 0.949s.

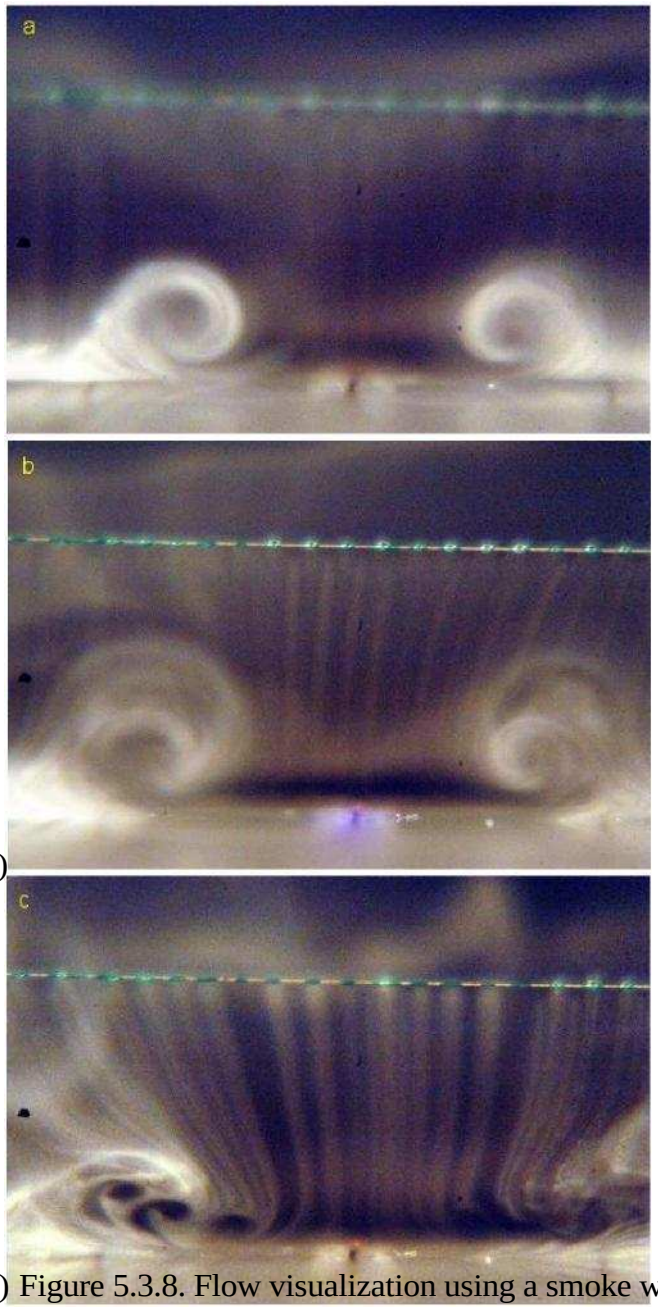

a)

b) Figure 5.3.8. Flow visualization using a smoke wire located 10mm below the

250μm Mylar plasma actuator. Note the pictures have been rotated 180°. The electrode is at the centre of each photo and runs into the page. Picture scale is 26mm horizontally x 18mm vertically. a) t = 0.04s; b) 0.09s; c) 0.95s. The plasma forcing initially creates a pair of vortices (a and b, note visible plasma in b). For t > 0.4s (c), a series of pulsed wall jets occur, each exhibiting vortex roll-up in the outer region.

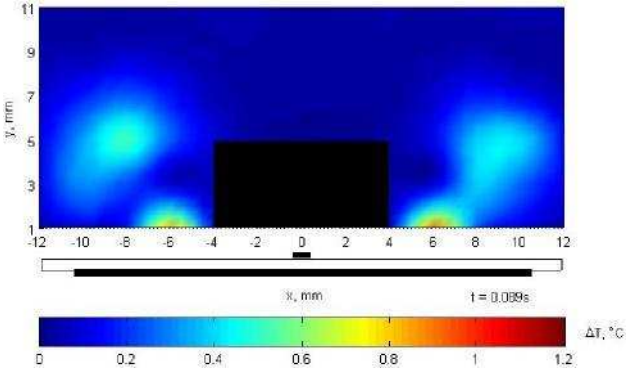

c).

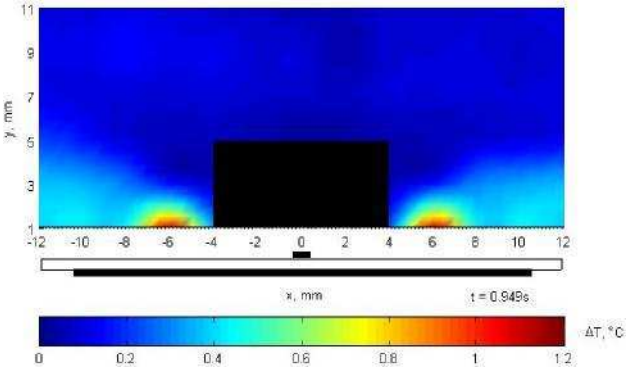

d) Figure 5.3.9. Instantaneous gas temperature field around the 250μm Mylar plasma actuator at: a) t = 0.039s; b) t = 0.089s; c) t = 0.949s. The path of the initiation vortices can be seen in a) and b), travelling at 25° to the electrode

surface. At much later times (c), the initiation vortices have exited the experimental area and regions of hotter fluid travel in the ±x direction only.

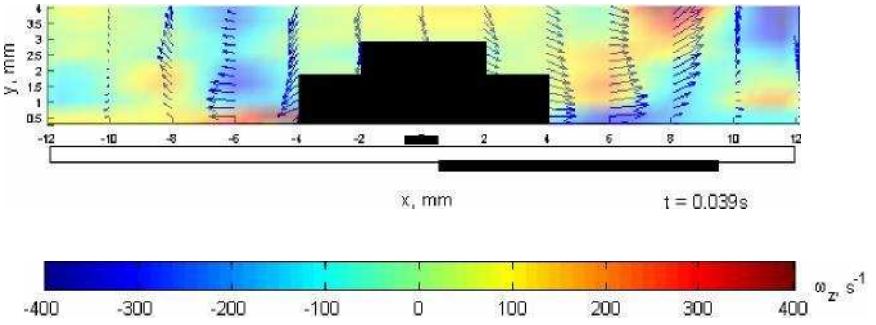

a)

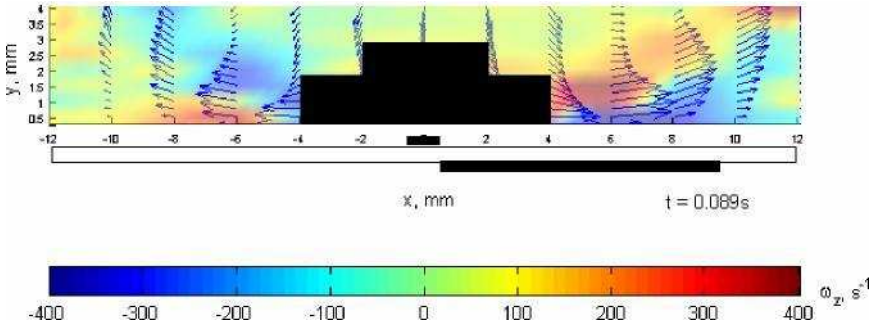

b)

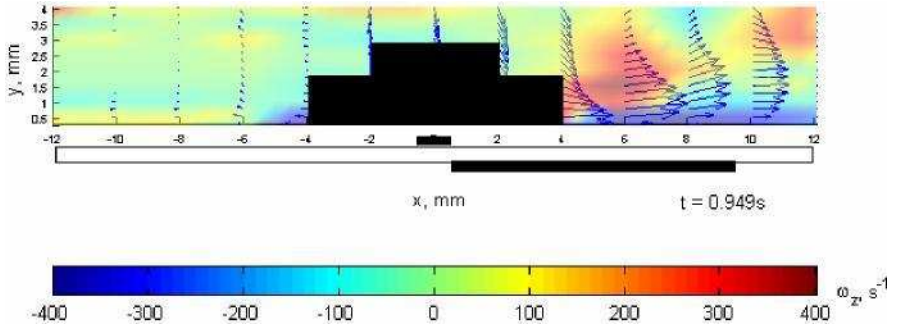

c)

Figure 5.3.10. Instantaneous vorticity contours and velocity vectors around the 250μm thick Mylar asymmetric plasma actuator at: a) t = 0.039s; b) t = 0.089s; c) t = 0.949s.

a

c)

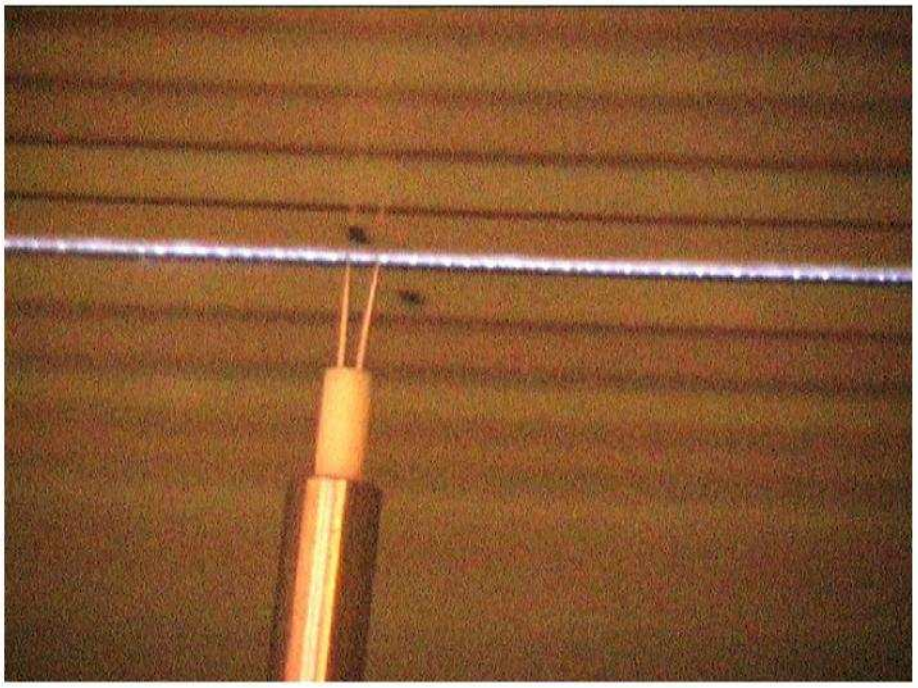

Figure 5.3.11. Colour enhanced images of the asymmetric plasma actuator at: a) $t \approx 40$ms; b) $t \approx 80$ms after plasma initiation. Hot wire shown in figure and the prongs have 1.25mm spacing at their tip. The plasma occurs on both sides of the electrode at initiation (a), although the plasma on the near side appears to be brighter and more uniform. After the first few pulses (b), the plasma formation is entirely one-sided.

5.3.3. Effect of Plasma Parameters

The hot wire surveys in Sec 5.3.2 showed that the maximum jet velocity in the experimental area always occurred at x = 4mm, y = 0.5mm. In this section, the hot-wire probe was fixed at this location and the effect of each plasma parameter on the magnitude of the induced flow was studied. Each plasma parameter was varied independently, as in Sections 4.3.3. The variation of induced velocity with applied voltage was studied by varying E with fixed plasma conditions of PRF = 60kHz, charge time = 7μs, PED = 2ms, PEF = 100Hz. The variation of induced velocity with PRF, PED and PEF was studied through independent variation of the parameters from E_{max} = 3.6kV, PRF = 50kHz, charge time = 7μs, PED = 1ms, PEF = 50Hz. All tests were performed with the plasma activated for a total of 1.4s. Additional care was taken to avoid probe positioning errors but undoubtedly there will be some variation between the exact probe positions for each of the three plasma actuators. Thus, the comparison between different configurations should be made with some caution.

The base case experimental condition (E_{max} = 3.6kV, PRF = 50kHz, charge time = 7μs, PED = 1ms, PEF = 50Hz) was repeated several times. The scatter in the velocity measurement at this condition is small (< 0.1m/s) and reflects errors due to ambient temperature drift, changes in the probe characteristics and electrode sheet wear.

5.3.3.1. Effect of the Excitation Voltage, E

Figure 5.3.12 shows the effect of the applied voltage on the maximum ensemble-averaged velocity throughout the plasma pulse, $\langle U \rangle_{max}$. Here, the maximum voltage, E_{max}, has been used to represent the applied voltage. Figure 5.3.13 shows the effect of E_{max} on the mean velocity, $\bar{U}$, throughout the 1.4s of plasma forcing.

For all the electrode sheets there appears to be a lower cut-off voltage for which no flow is generated. This critical voltage is around 2kV and corresponds to the minimum voltage for which glow discharge plasma will occur in atmospheric pressure air.

Figure 5.3.12 shows that the magnitude of $\langle U \rangle_{max}$ was increased by around 25% by reducing the dielectric thickness by 50%, similar to that observed in Sec. 5.3.1. However, there appears to be a saturation for $E_{max} > 3.3$kV, whereby no further increase in velocity was achieved by increasing the voltage. This is likely to be due to a saturation of the dielectric material itself, where the dielectric properties start to break down as the limit of its dielectric strength is approached (17kV/mm for Mylar). Assuming a parallel plate geometry, the electric field strength with 3kV applied to the electrode sheet is 12kV/mm and 24kV/mm for the 250μm and 125μm electrode sheets, respectively. This high electric field is likely to alter the material properties and hinder charge storage. This also explains the reason for the frequent dielectric breakdown for the 125μm case. Problems with the power supply prevented testing asymmetric electrodes at $E_{max} > 3.3$kV and it is uncertain if the same saturation is experienced for this electrode configuration.

The maximum velocity data has been least-squares fit to a power law in the form $<U>_{max} = AE_{max}^{n}$, as shown in Fig. 5.3.12. Data below the onset of plasma formation and above the saturation region have been ignored in the curve fitting procedure. For the symmetric electrode sheets, the trend seems to follow $<U>_{max} \propto E_{max}^{7/2}$, as also found by Orlov and Corke (2005) and Enloe et al. (2004a). Comparison with their data can be made in Fig. 5.3.12b, where they have plotted peak-to-peak voltage against maximum induced velocity ($V_{p\text{-}p} \approx 2E_{max}$). Their data are taken from PIV measurements around an asymmetric electrode comprising copper foil electrodes and 300μm Kapton dielectric (dielectric constant = 4, similar to Mylar). Also, their plasma is fired continuously and excited by triangular shaped waveforms at 5kHz. There is a large difference between the magnitudes of the induced flow between the two data sets. This is a direct result of the different excitation frequencies (5kHz and 50kHz). As we will see in the next section, a 10-fold increase in applied frequency will tend to increase the induced flow velocity by a factor of 15, which accounts for the differences between the results. There may also be some effect from the applied waveform. It was not possible to study the effect of waveform with the experimental setup used in this study.

However, the variation of $<U>_{max}$ with E_{max} is quite different for the asymmetric actuator. Firstly, there is a large jump in induced velocity as soon as the applied voltage is high enough for plasma to form. Secondly, the variation of maximum velocity appears to vary as $<U>_{max} \propto E_{max}^{2}$, which is a similar variation observed for the continuously fired plasma tests in Sec 4.4.

Fig. 5.3.13 shows a nearly linear variation in U with E_{max} above the lower cut-off voltage and below that of dielectric saturation. This indicates that

although the maximum velocity is increased through increasing the voltage, the duration of the plasma induced flow is not. Figure 5.1.14 illustrates the ensemble-averaged velocity profile for several applied voltages for the asymmetric electrode sheet. This shows that as the voltage increases, and the corresponding gas velocity increases, the affected gas takes a shorter time to arrive at the probe. However, the duration of the affected gas to pass through the probe is similar in all cases ($\lesssim$ 8ms), such that the time-averaged velocity does not follow the same power laws as $<U>_{max}$.

a)

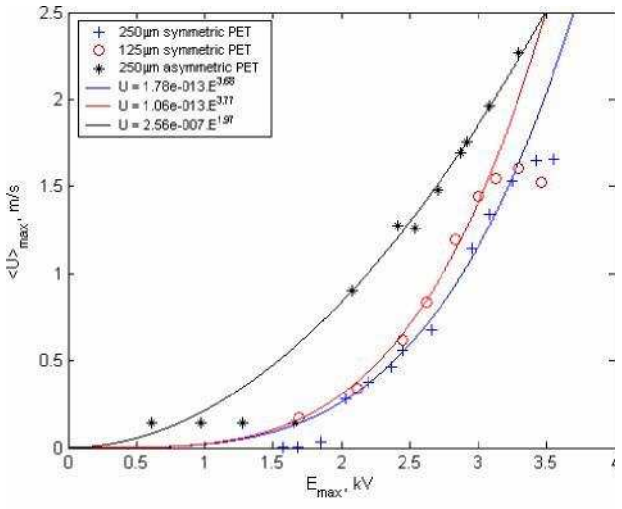

b)

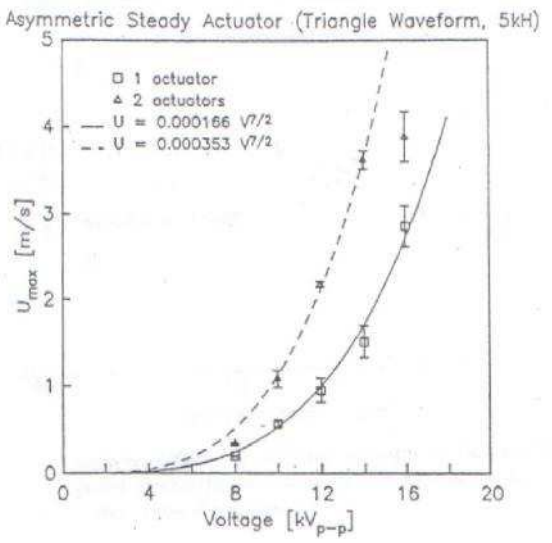

Figure 5.3.12.a) Variation of the maximum ensemble-averaged velocity, $<U>_{max}$, with the applied voltage, E_{max}, for the 250pm symmetric (-), 125pm symmetric (-), and 250pm asymmetric (-), electrode sheet configurations. Square wave excitation with PRF = 60kHz, charge time = 7ps, PED = 2ms, PEF = 100Hz. b) PIV data from Enloe et al. (2004a) for an asymmetric configuration with 300pm thick Kapton polyimide dielectric. Excitation by triangular waveform at 5kHz. Note their formulae are for E_{p-p} in kV.

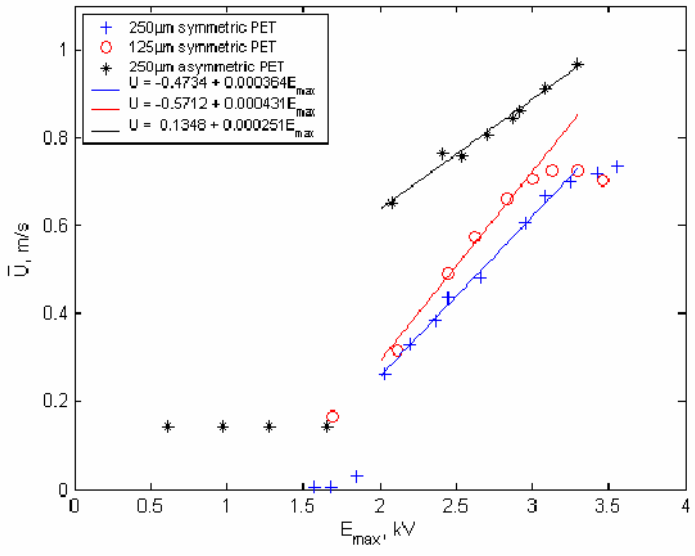

Figure 5.3.13. Variation of the time-averaged velocity, U , with the applied voltage, E_{max}, for the three electrode sheet configurations.

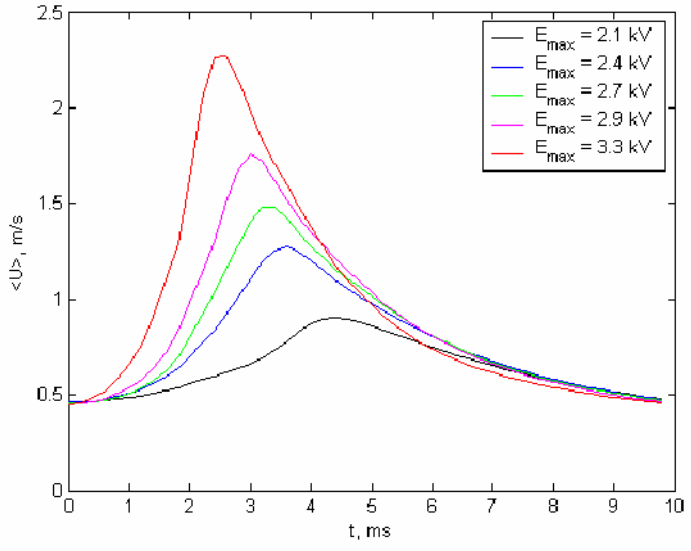

Figure 5.3.14. Ensemble-averaged velocity, <U>, between plasma envelopes at different applied voltages. Asymmetric electrode configuration.

5.3.3.2. Effect of the Pulse Repetition Frequency, PRF

Figures 5.3.15 and 5.3.16 show the effect of the PRF on $_{max}$ and U , respectively. The experimental condition with PRF = 50kHz has been repeated several times to indicate the scatter of the experimental data. Note that the 250pm symmetric Mylar data were taken over a period of several months, during which different probes were used and atmospheric conditions changed considerably. The scatter was still within only .0.05m/s (10%).

The trend in $_{max}$ with PRF is consistent for all three plasma actuators, whereby the maximum velocity appears to vary as $<U>_{max} \propto PRF^{1.2}$. This variation is nearly linear, which would suggest that the PRF simply controls the amount of force produced per unit time, whereas the applied voltage controls the amount of body force produced per AC cycle.

The 125pm thick dielectric actuator induced a velocity around 25% higher than the 250pm actuator, as also observed in Sec. 5.3.1 and 5.3.3.1. The 250pm thick asymmetric configuration induces a velocity nearly 90% higher than the 250pm thick symmetric case.

The trend in time-averaged flow velocity is also similar for the three plasma actuators, where $U \propto PRF^{0.4}$. Figure 5.3.17 shows the ensemble-averaged velocity at different PRF for the asymmetric actuator. This shows that although the peak velocity increases with PRF, the duration of the peak remains approximately the same, as was observed in Fig. 5.3.14.

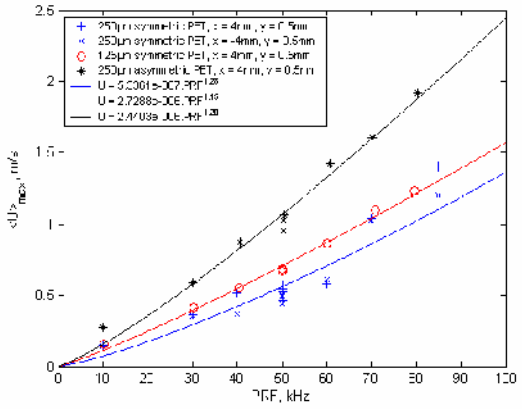

Figure 5.3.15. Variation of the maximum ensemble-averaged velocity, $\langle U \rangle_{max}$, with the pulse repetition frequency, PRF, for Mylar electrode sheets.

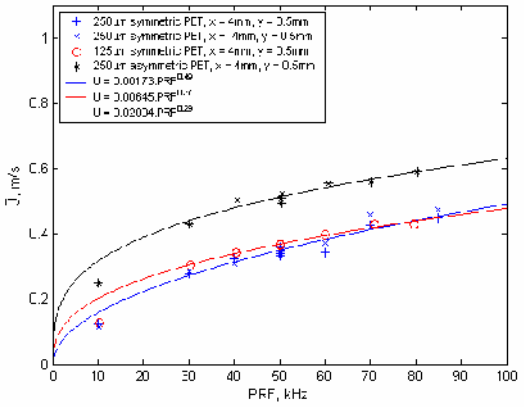

Figure 5.3.16. Variation of the time-averaged velocity, U , with the pulse repetition frequency, PRF, for the three electrode sheet configurations.

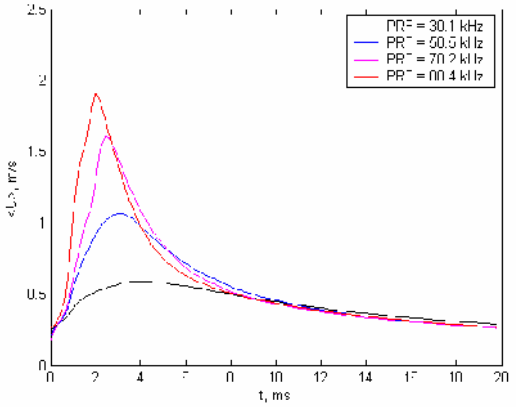

Figure 5.3.17. Ensemble-averaged velocity, $\langle U \rangle$, between plasma envelopes at various PRF. Asymmetric electrode configuration.

5.3.3.3. Effect of the Pulse Envelope Duration, PED

Figures 5.3.18 shows the effect of the PED on $\langle U \rangle_{max}$. Again, the trend is similar for all three electrode sheets, whereby $\langle U \rangle_{max}$ increases linearly until a saturating limit at PED = 3ms. In the continuously fired plasma tests of Sec. 4.4, it was observed that the induced-flow speed was much higher for the first few milliseconds of plasma excitation. It was suggested that this was due to more energetic plasma occurring during the first few AC cycles, and thus there is little benefit in increasing beyond PED = 3ms. Note in Sec 5.3.2 that plasma formation occurred around both sides of the asymmetric plasma actuator for the first few plasma pulses only, which further supports this conclusion. For PED < 3ms, the 125μm thick actuator showed a 35% increase in $\langle U \rangle_{max}$ as compared to the 250μm actuator, consistent with the results of Sec. 5.3.3.1 and 5.3.3.2. The asymmetric sheet shows a 100% increase, again consistent with the previous results.

The variation of U with PED is shown in Fig. 5.3.19. Sudden saturation is not evident for PED > 3ms, although the rate of increase with PED is continually diminishing ($U \propto PRF^{0.4}$). Figure 5.3.20 shows the ensemble-averaged velocity at different PED for the asymmetric actuator. It appears that the PED will increase the maximum induced velocity up to the saturation limit, but once the limit is exceeded the flow velocity will naturally start to decrease, whether plasma is present or not. The reduction in flow speed is not as rapid

when the plasma is on, such that U can still be increased through increasing the PED. For PED > 3ms, the natural decay in velocity is merely postponed.

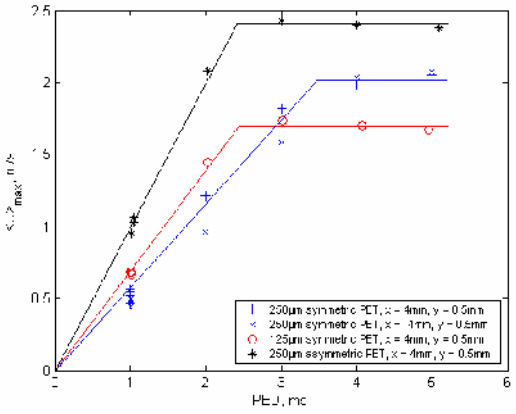

Figure 5.3.18. Variation of the maximum ensemble-averaged velocity, $\langle U \rangle_{max}$, with the pulse envelope duration, PED, for Mylar electrode sheets.

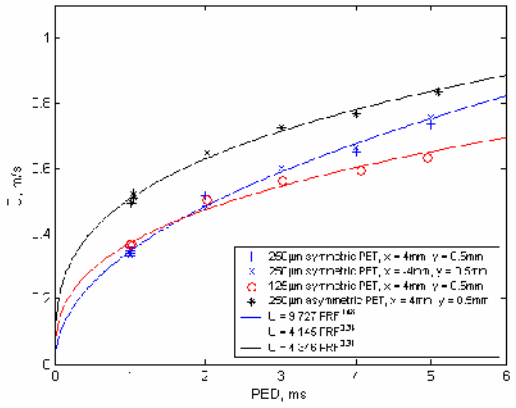

Figure 5.3.19. Variation of the time-averaged velocity, U , with the pulse envelope duration, PED, for the three electrode sheet configurations.

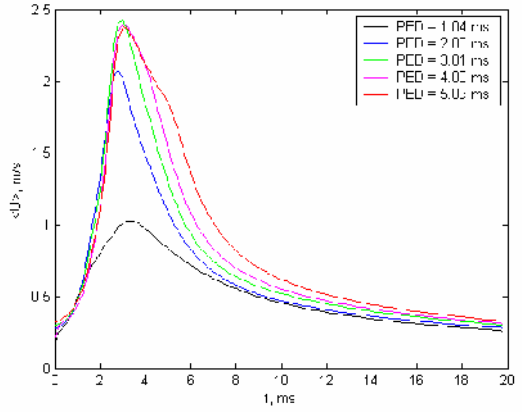

Figure 5.3.20. Ensemble-averaged velocity, $\langle U \rangle$, between plasma envelopes at various PRF. Asymmetric electrode configuration.

5.3.3.4. Effect of the Pulse Envelope Frequency, PEF

Figures 5.3.21 and 5.3.22 show the effect of the PEF on $_{max}$ and U , respectively. The variation in $_{max}$ is near linear for the experimental conditions used here and no saturation appears to be reached. Whilst there is a slight increase in the observed velocity with PEF, the rate of change is much weaker than observed for the other parameters. Consequently, the induced velocity cannot be significantly raised through increasing the PEF. The 125 m sheet shows a 35% increase in $_{max}$ as compared to the 250 m symmetric sheet and the asymmetric sheet shows a 90% increase, consistent with the results of the previous sections.

The time-averaged velocity appears to vary as U $\propto$ $PEF^{1/2}$ for all three actuators. The PEF appears only to dictate the flow speed that will be present at the start of the next plasma envelope (i.e. how much the flow speed will decay during the plasma off part of the cycle). This is clearly demonstrated in Fig. 5.3.23. Thus, if the air velocity is already high (in the case of high PEF), the additional forcing provided by the plasma will further increase the gas speed. Note, however, that this process cannot continue indefinitely because the fluidic losses (i.e. viscous damping) will increase with flow velocity.

In conclusion, $_{max}$ controls the amount of force produced by the plasma per AC cycle and the PRF controls the amount of force produced per unit time. The PED alters the duration for which the flow 'sees' the force and should be set so that the flow has enough time to react to the stronger excitation during the first few ms. The PEF controls the minimum flow speed between envelopes and thus dictates the gas velocity at the time of the next plasma pulse.

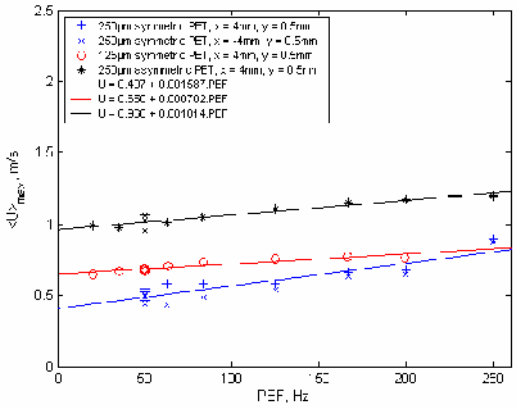

Figure 5.3.21. Variation of the maximum ensemble-averaged velocity, $\langle U \rangle_{max}$, with the pulse envelope frequency, PEF, for Mylar electrode sheets.

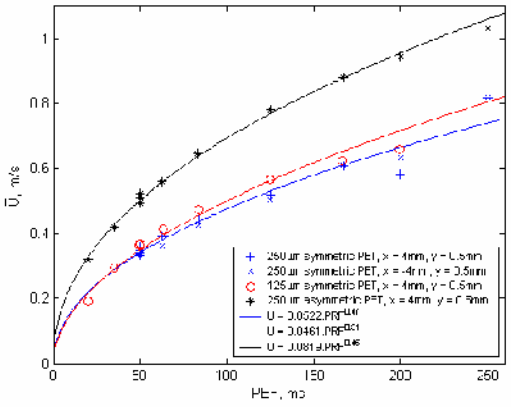

Figure 5.3.22. Variation of the time-averaged velocity, U , with the pulse envelope frequency, PEF, for the three electrode sheet configurations.

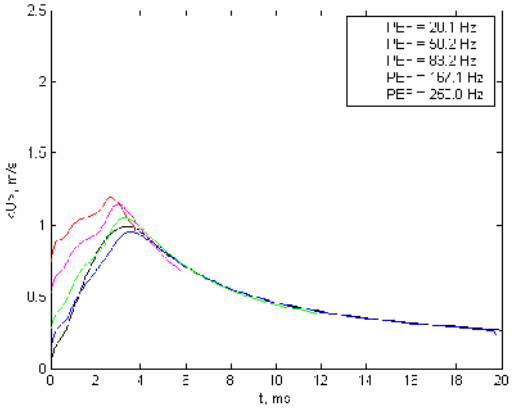

Figure 5.3.23. Ensemble-averaged velocity, <U>, between plasma envelopes at various PEF. Asymmetric electrode configuration.

5.3.3.5. Velocity Variation with Applied Power

Figure 5.3.24 and Figure 5.3.25 show the variation of $\langle U \rangle_{max}$ and U with applied power for the symmetric Mylar plasma actuators. Here, the power, P, has been calculated from the voltage and current waveforms measured using a 200MHz digital oscilloscope:

$$P = \frac{PRF}{2} \cdot PED \cdot PEF \cdot \int_0^{t_{AC}} (EI)\, dt \qquad (4.3.1)$$

where, t_{AC} is the time to complete one AC cycle (i.e. 2/PRF) and the voltage and current waveforms were obtained from the average of 128 cycles to eliminate random noise. The figures show the power per unit length of electrode, where the length used is the total length of the electrode over which plasma forms (i.e. including bus connections to electrodes, etc.). The gradient of the data in these figures thus constitutes a measure of how effective the plasma is at converting electrical power into flow velocity.

Figure 5.3.24 shows a reasonable collapse of the data through variation of the PRF, PED and E_{max}, suggesting that the maximum induced velocity is proportional to the power delivered to the electrode sheet. In Figure 5.3.25, a reasonable collapse is observed for all plasma parameters. It is clear that the gradient through the data points is increased by using a thinner dielectric, suggesting that the 125μm thick Mylar dielectric is at least twice as effective as the 250μm sheet at converting electrical energy to momentum.

Unfortunately there was a problem with the voltage and current waveforms for the asymmetric electrode case, where the measured current did not return to zero between the high voltage burst due to a problem with the current shunt. Upon integration, this caused the calculated power to be negative – a physically impossible result.

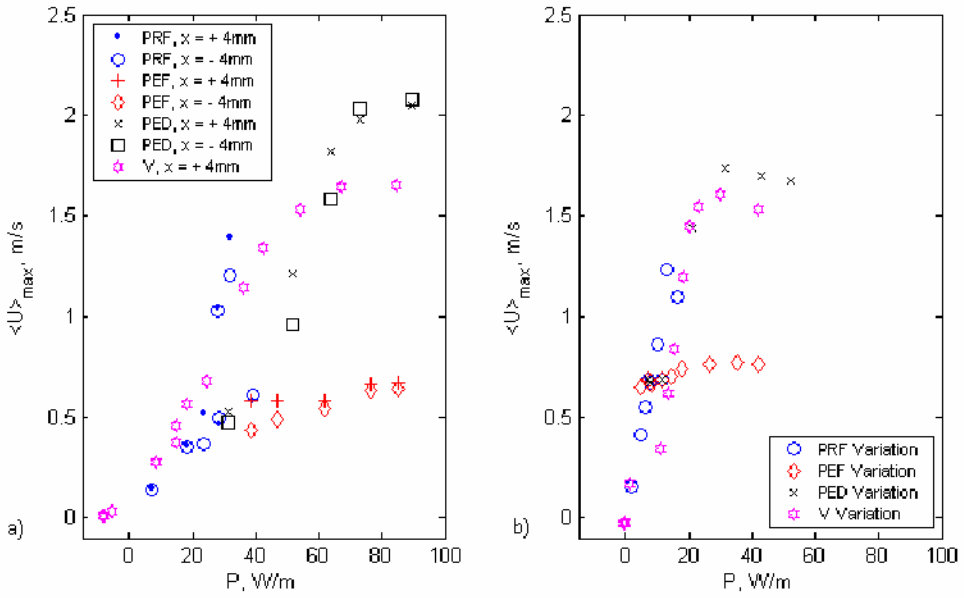

Figure 5.3.24. Variation of maximum ensemble averaged velocity with plasma power per unit electrode length. a) Symmetric 250pm Mylar dielectric and b) symmetric 125pm Mylar dielectric

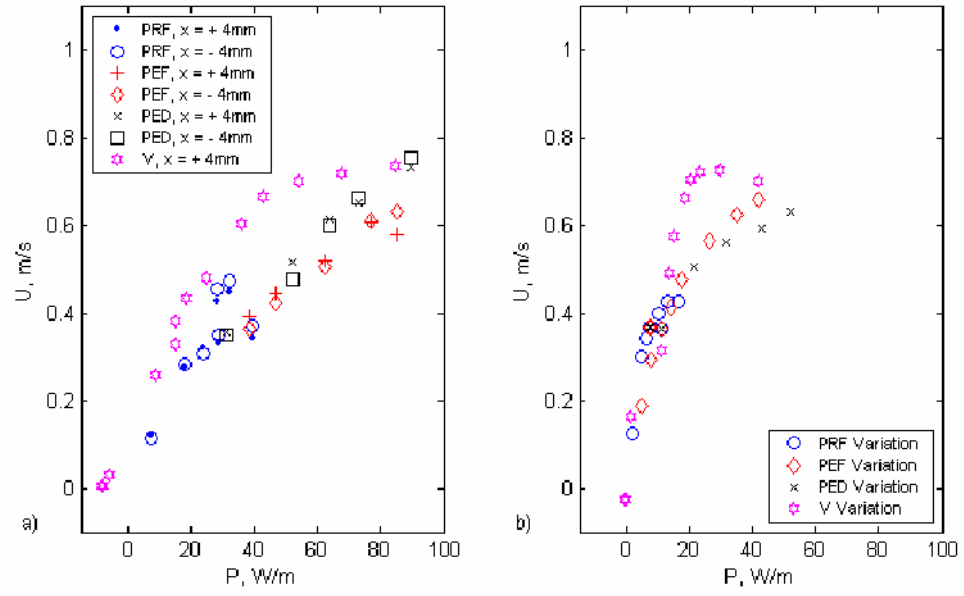

Figure 5.3.25. Variation of time averaged velocity with plasma power, calculated by integrating voltage and current waveforms. a) Symmetric 250pm Mylar dielectric and b) symmetric 125pm Mylar dielectric.

5.4. Effect of Dielectric Material

The previous section showed that the plasma-induced jet velocity could be increased by decreasing the dielectric thickness. However, limited gains were made with this approach because the increase in electric field strength (for a given applied voltage) became close to the breakdown strength of the Mylar, thus leading to dielectric failure. In this section, several ceramic dielectric actuators with higher dielectric strength are explored.

Ceramic materials generally have higher dielectric constants than Mylar. In fact, some ceramics have dielectric constants of well over 1000 (recall ε_{Mylar} = 3.1). It is expected that the surface charged stored (c.f. Eq. 5.3.1), and the corresponding plasma force will be increased for a given voltage thus causing a higher jet velocity to be induced. The dielectric strength of ceramics are also higher than Mylar (typically ten times), such that the frequent burn-through can be avoided. In addition, the loss tangent for ceramics is typically 100 times less than Mylar, and hence less energy is expected to be lost through dielectric heating (c.f. Eq. 5.2.1). This is expected to lead to more energy efficient actuators.

Ceramic materials are also less prone to wear, are generally good thermal insulators and have excellent thermal shock resistance. They may, therefore, be more reliable and have a longer life span than plastics. The disadvantages of using ceramics are that they are brittle and the manufacture of large, thin plates is difficult. One must also be careful to avoid voids/porosity as these will allow plasma to form within the ceramic which could lead to cracking and catastrophic failure.

Samples of Silicon Nitride (Si_3N_4) and Alumina (Al_2O_3) were kindly provided by Dr. Yoshida and Dr. Segawa at the National Institute of Advanced Industrial Science and Technology, Japan. Silicon Nitride is a sintered ceramic, typically used for advanced gas turbine blades and for engine parts. Three samples of different thicknesses were tested (600pm, 440pm and 270pm), which were all machined from 3mm thick plate. Alumina is a very common engineering ceramic and has been used for some time as the dielectric material for plasma actuators by Roth (2004). Our sample had a thickness of 400pm. The properties of Mylar, Silicon Nitride and Alumina are compared in Table 5.4.1.

The ceramic plasma actuators were manufactured by adhering 76pm thick copper shielding foil to the ceramic and carefully trimming to shape. The lower electrode was 10mm wide and the upper electrode was 1mm wide and around 50mm long, such that all of the actuators were symmetric type. The exact electrode length differed for each electrode sheet. Care was taken to avoid any sharp edges on the exposed electrode and the soldered electrical connection to the exposed electrode was covered with insulating tape. The Si_3N_4 and Al_2O_3 ceramic plasma actuators are shown in Fig. 5.4.1.

	Mylar	Si_3N_4 Ceramic	Al_2O_3 Ceramic
General Description	Polyethylene terephthalate - a thermoplastic, often referred to as 'polyester' or PET. Mylar is a flexible, opaque PET film commonly used for capacitors.	A pressed and sintered ceramic, dark grey in appearance. Typically used for engine parts and gas turbine blades due to its high strength at elevated temperatures and excellent thermal shock resistance.	Alumina has good thermal shock resistance, and is used for furnace crucibles and thermocouple sheaths. Very Good electrical insulation at elevated temperatures, good wear resistance and high hardness.
Density, g/cm^3	1.3-1.4	3.4	3.9
Young's Modulus, GPa	2-4	309	300
Dielectric Constant @ 1MHz	3.1	7.9-8.1	9-10
Loss Tangent @ 1MHz	0.013	0.0005-0.0009	0.0004
Dielectric Strength, kV/mm	17	$210\text{-}10^3$	10-35
Thermal Conductivity, W/mK	0.13-0.15	20-30	26-35
Upper continuous use temperature, °C	≤ 80	1100-1650	1700

Table 5.4.1. Comparison of dielectric material properties. Sources: CRC Material Science and Engineering Handbook, Encyclopaedia of Polymer Science and Engineering, Kyocera Corporation product information and Goodfellows online source (http://www.goodfellow.com)

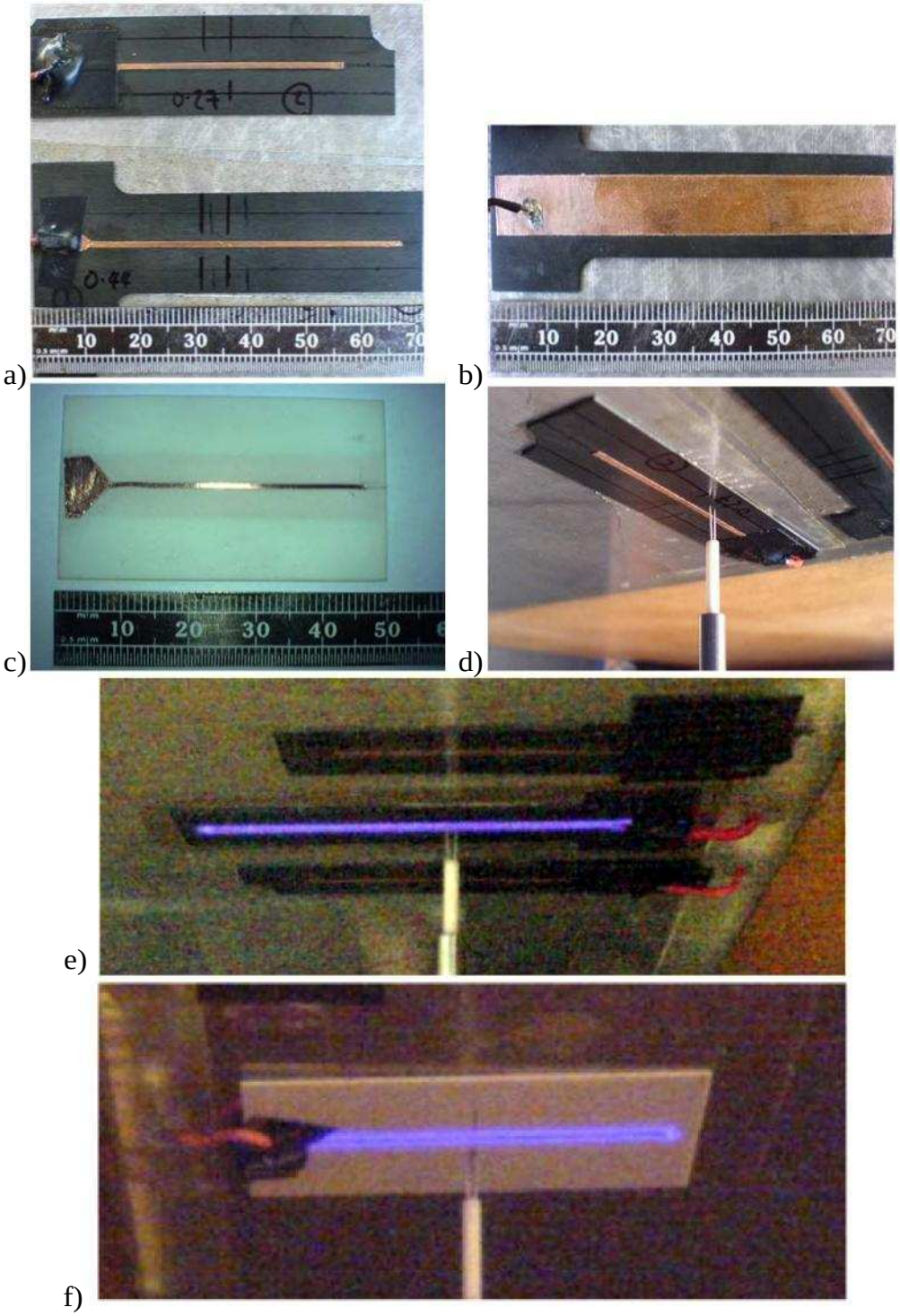

Figure 5.4.1. Detail of the ceramic plasma actuators. a) upper (exposed) surface of the 270pm (top) and 440pm (bottom) thick Si_3N_4 ceramic plasma actuator. b) lower surface of the 440pm thick Si_3N_4 actuator. c) Upper surface of the 400pm thick Al_2O_3 ceramic plasma actuator. d) hotwire position during experiments. e) and f) plasma formation around the 440pm Si_3N_4 actuator and 440pm Al_2O_3 actuator, respectively.

5.4.1. 600,m $_{Si3N4}$ Ceramic Actuator

In order to compare the flow field induced by the ceramic and Mylar plasma actuators, a hot-wire probe was used to survey the induced velocity around the 600pm thick $_{Si3N4}$ actuator. This was identical to the technique described in Sec. 4.2. Again, the plasma parameters were set with E_{max} = 3.6kV, PRF = 50kHz, Charge Time = 7ps, PED = 1ms, PEF = 50Hz.

Figures 5.4.2 and 5.4.3 present the time-averaged velocity magnitude contours, and the time-averaged velocity vectors and vorticity contours, respectively. The induced flow is observed to be symmetric with respect to the electrode, and is similar in profile to the flow formed by symmetric electrode sheets with Mylar dielectric (c.f. Fig. 5.3.3). Figure 5.4.4a shows the velocity distribution on either side of the 600pm thick $_{Si3N4}$ actuator. Fig. 5.4.4b shows the velocity distribution for the 250pm symmetric Mylar actuator for comparison. The magnitude of the induced flow velocity is comparable to the Mylar case, but the ceramic material being used is nearly 2.5 times as thick. It should also be noted that the dielectric constant of this ceramic is 2.5 times greater than that of Mylar.

The velocity distribution non-dimensionalised by $_{Umax}$ and $_{51/2}$ is given in Fig. 5.4.5. The collapse of this data onto a self-similar profile does not appear to be as good as the Mylar cases. Though this is partly due to positioning error, the main cause is the ceramic sample was only 18mm wide, as depicted in Figs 5.4.2 and 5.4.3. Hence, some data is taken without the ceramic directly underneath the probe and is responsible for the apparent discontinuity at around x = -6mm in Fig. 5.4.2. This 'backward facing step' configuration will inherently alter the wall jet at distances downstream of this location.

Unfortunately this was unavoidable because of the small size of the ceramic samples.

Figures 5.4.6 and 5.4.7 show the instantaneous velocity and vorticity profiles throughout the plasma on period, respectively. Although the velocity appears to have decreased in magnitude towards the end of the plasma-on time (Fig. 5.4.6c), this is merely due to the choice of timestep since the pulse averaged velocity, $\hat{U}(x,y,t)$ (not shown), was constant with time after the flow initiation period ($t > 0.4s$). The induced flow field does not appear as smooth as the flow over the Mylar sheets. This is partially attributed to the absence of dielectric underneath some measurement locations, which modifies the wall-jet flow. In addition, there may be irregular plasma formation because of the lower quality hand-made foil electrodes (i.e. the foil electrode edge is much more ragged than the photochemically-etched Mylar sheets). One should also note that the plasma itself appeared weaker during experiments: it was less bright to the naked eye and produced less audible noise.

The fact that the same flow velocity was induced by an actuator 2.5 times as thick with a dielectric constant 2.5 times greater indicates that the induced flow varies in the same proportion to dielectric constant as the inverse of thickness. If the momentum coupling were to increase as material thickness decreases, as suggested by the 125μm Mylar electrode sheet, greater induced flow speed could be possible by using thinner ceramic materials. This hypothesis will be tested in the next section.

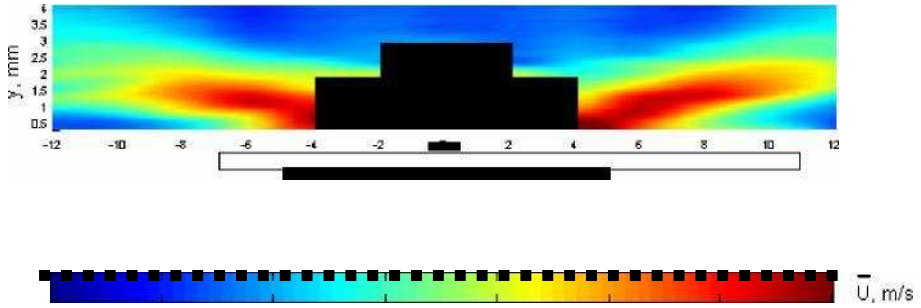

Figure 5.4.2. Velocity profile around the 600μm thick Si_3N_4 plasma actuator. Contour show average velocity magnitude over 1.4s of plasma forcing. The blackened region indicates where no data was taken due to the possibility of high voltage arcing from the electrode to the probe. Plasma excitation at E_{max} = ±3.7kV, PRF = 50kHz, PED = 1ms and PEF = 50Hz.

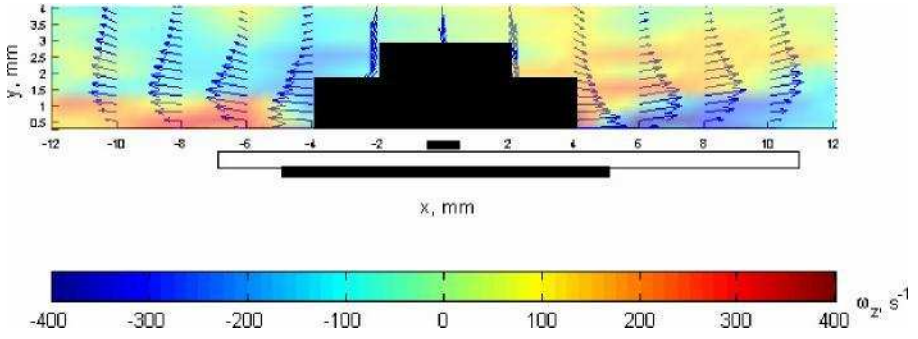

Figure 5.4.3. Vorticity profile around the 600μm thick ceramic plasma actuator in initially static air (contours) with the velocity direction (vectors), averaged over 1.4s of plasma forcing. Positive vorticity implies counter clockwise rotation. Plasma excitation at E_{max} = ±3.7kV, PRF = 25kHz, PED = 1ms and PEF = 50Hz.

a)

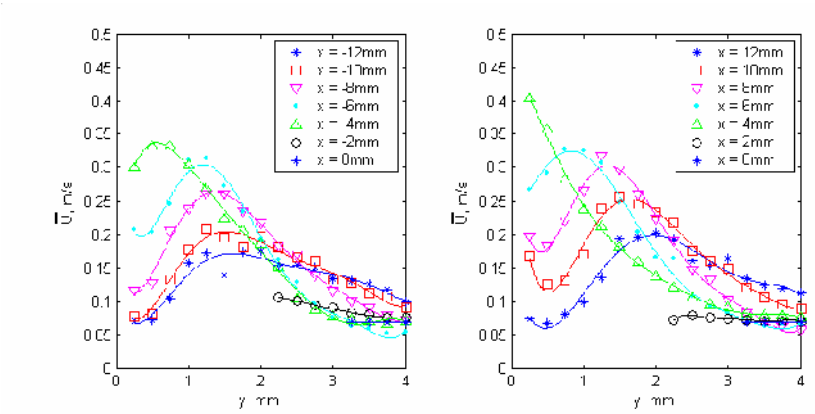

b)

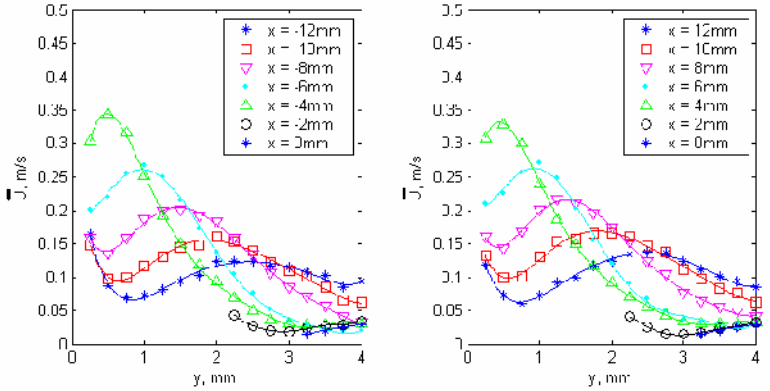

Figur

e 5.4.4. Mean velocity profile on either side of the plasma electrode. a) 600μm thick Si_3N_4 ceramic dielectric and b) 250μm Mylar dielectric with symmetric configuration.

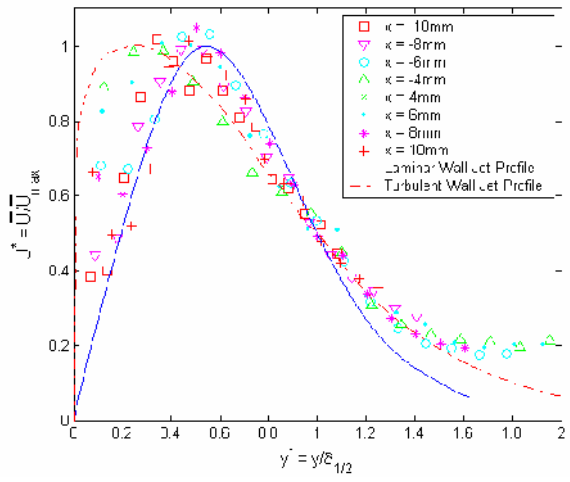

Figure 5.4.5. Mean velocity profile of the plasma induced flow normalized with the maximum jet velocity, U_{max}, and the jet half width, $\delta_{1/2}$. 600μm thick ceramic dielectric.

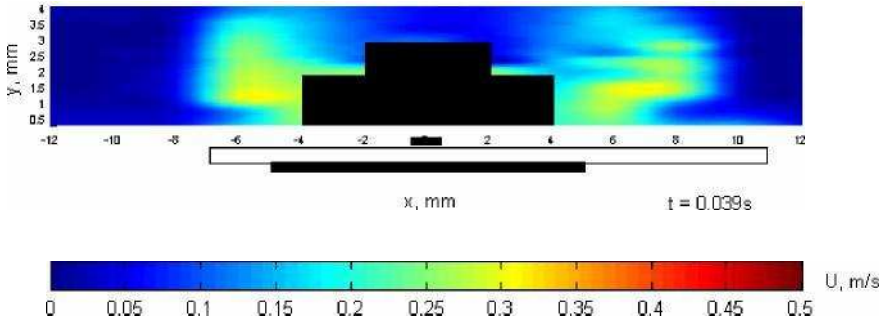

a)

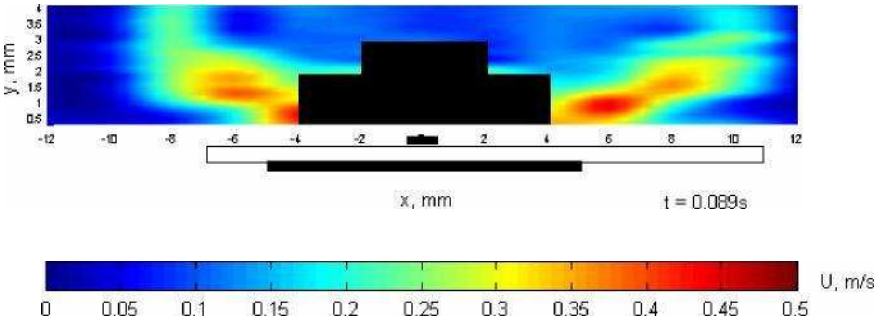

b)

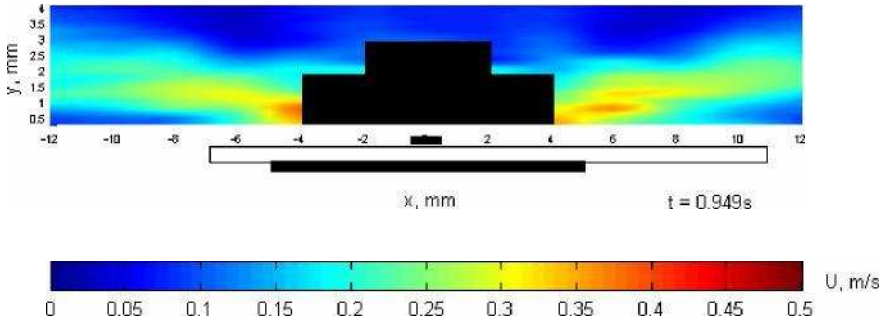

c)

Figure 5.4.6. Instantaneous velocity field around the 600μm thick ceramic plasma actuator at: a) t = 0.039s; b) t = 0.089s; c) t = 0.949s.

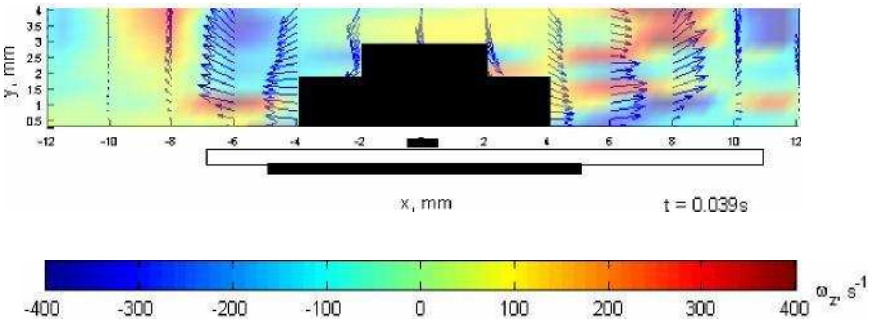

a)

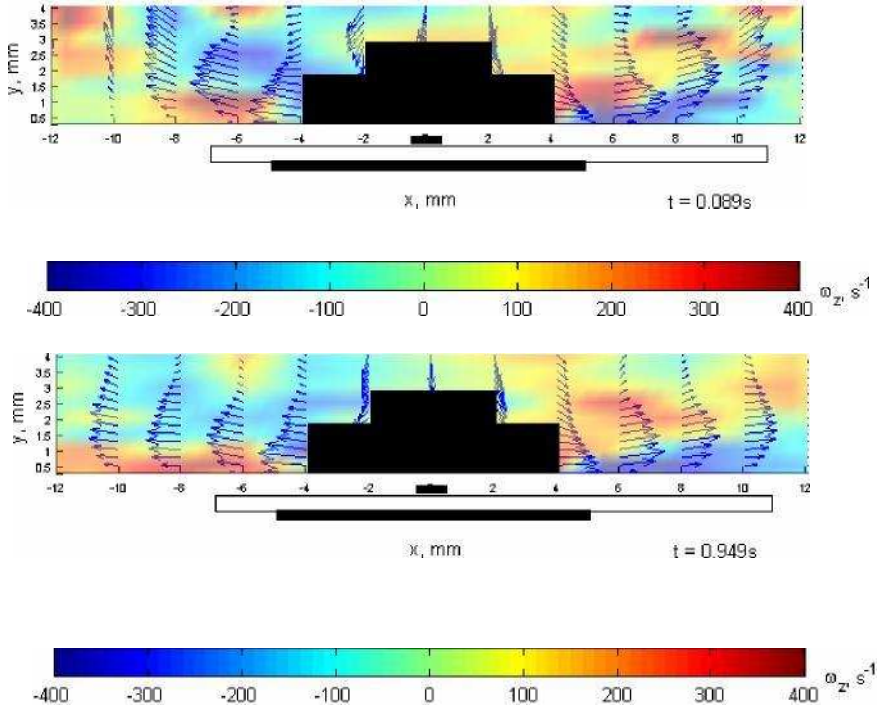

b)

c) Figure 5.4.7. Instantaneous vorticity contours and velocity vectors around the 600μm thick ceramic plasma electrode at: a) t = 0.039s; b) t = 0.089s; c) t = 0.949s.

5.4.2. Parametric Testing of Ceramic Actuators

The induced-flow velocity at different voltages is shown for the 600μm, 440μm and 270μm Si_3N_4 ceramic plasma actuators, the 400μm thick Al_2O_3 actuator, and the 250μm thick Mylar actuator in Figs. 5.4.8 and 5.4.9. Here, the hot wire was fixed at x = 4mm, y = 0.5mm, and E was varied from fixed plasma conditions of PRF = 60kHz, charge time = 7μs, PED = 2ms, PEF = 100Hz, as in Sec. 5.3.3.

For all ceramic actuators, both the maximum induced-flow velocity and the mean-flow velocity was higher than that for the Mylar actuator, and this is believed to be due to the higher dielectric constant of these materials. Gibalov and Pietsch (2000) studied PETG (ε = 2.4), Al_2O_3 (ε = 9.8), and various glass-based actuators (up to ε = 1000), and stated that the lateral extent of the plasma region becomes shorter as the dielectric constant increases, while the charge transferred to the surface increases. Thus more charge is held in the electric field leading to a greater induced force. Figure 5.4.8 shows that the maximum flow velocity is increased by around 200% for the 270μm thick Si_3N_4 ceramic compared with the 250μm Mylar actuator. The ratio of dielectric constants is 2.5, suggesting that the induced-flow velocity is approximately proportional to the dielectric constant.

The induced-flow velocity clearly increases through reducing the ceramic thickness. The 440μm Si_3N_4 actuator shows a 35% increase in maximum induced velocity compared to that for the 600μm sheet. The 270μm Si_3N_4 actuator shows a 70% increase. Thus, the induced velocity appears to be inversely proportional to the actuator thickness, as suggested in Sec. 5.3. It can also be seen that the induced-flow velocity from the 400μm Al_2O_3 actuator is

very similar to that of the 440pm $_{Si3N4}$ ceramic actuator, as expected from two actuators of similar thicknesses and similar dielectric constants.

Through changing the dielectric material, the maximum induced velocity was still only 2.3m/s, which is not significantly above that observed from the Mylar electrode sheets. This is because the minimum thickness of ceramic available was 270pm (i.e. thicker than the 250pm Mylar actuator). Unfortunately, it was not possible to create thinner samples of the ceramic due to the extremely brittle nature of this material.

Figs 5.4.10 and 5.4.11 show the maximum and mean velocity with plasma power through variation of the $_{Emax,}$ PRF, PED and PEF. With comparison to Figs. 5.3.24 and 5.3.25, which show similar data for Mylar actuators, it can be seen from the gradients that the ceramic actuators are considerably more effective at creating flow. For the 250pm Mylar actuator of Fig. 5.3.24, the maximum induced velocity was linearly proportional to electrical power consumption, with a gradient of approximately $0.025m^2/Ws$. For the 600pm Si_3N_4 actuator, the ratio is more like $0.1m^2/Ws$; an improvement of 400%. This improves further through reducing the dielectric thickness, where the gradient for the 440pm $_{Si3N4}$ actuator is around $0.15m^2/Ws$. Note also that the 400pm $_{Al2O3}$ actuator has similar characteristics to the 440pm $_{Si3N4}$ actuator, as expected from their similar geometry and material properties. The trend does not continue to the 270pm $_{Si3N4}$ actuator case because the induced velocity saturated at high voltages, as can be seen in Fig. 5.4.8. The applied voltage was above that at which saturation occurred during the PRF, PED and PEF parametric tests for this actuator. It is not clear whether this saturation is due to the actuator or due to limitations of the power supply.

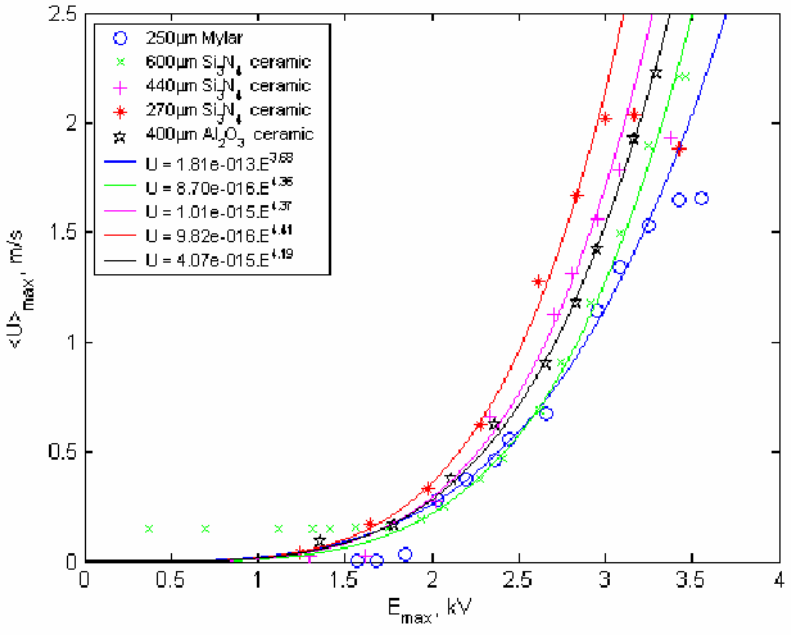

Figure 5.4.8. Variation of maximum induced velocity with applied voltage at x = 4mm, y = 0.5mm for 250jtm thick Mylar, three thickness of $_{Si3N4}$ ceramic and 440jtm thick $_{Al2O3}$ ceramic. PRF = 60kHz, charge time = 7jts, PED = 2ms, PEF = 100Hz.

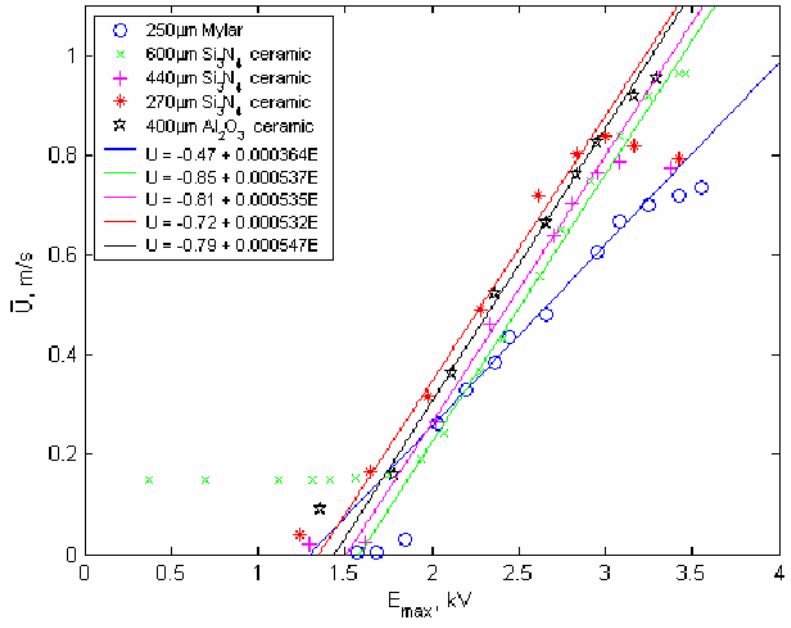

Figure 5.4.9. Variation of mean velocity with applied voltage at x = 4mm, y = 0.5mm. Plasma excitation at PRF = 60kHz, charge time = 7jts, PED = 2ms, PEF = 100Hz.

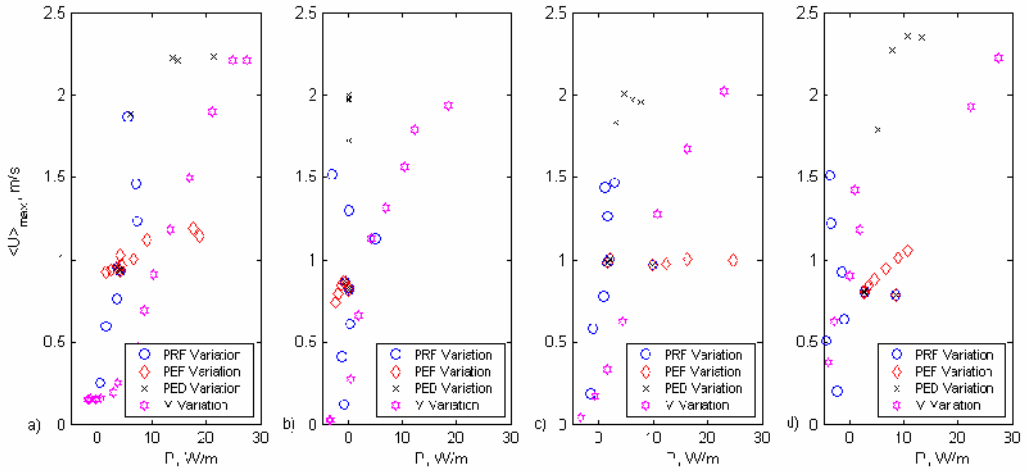

Figure 5.4.10. Variation of maximum induced velocity against plasma power per unit length. a) 600pm Si_3N_4 ceramic, b) 440pm Si_3N_4 ceramic, c) 270pm Si_3N_4 ceramic, d) 400pm Sl_2O_3 ceramic

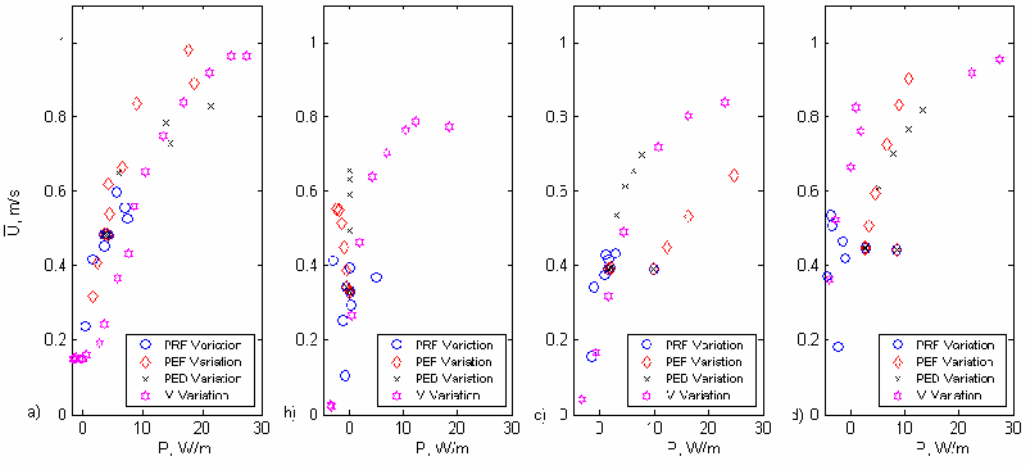

Figure 5.4.11. Variation of time-averaged velocity against plasma power per unit length. a) 600pm Si_3N_4 ceramic, b) 440pm Si_3N_4 ceramic, c) 270pm Si_3N_4 ceramic, d) 400pm Sl_2O_3 ceramic.

Chapter 6

Measurement of Plasma Temperature

6.1. Introduction

In the preceding chapters it was observed that the gas heating due to the plasma was relatively small. In Sec. 4.3.5, the gas temperature increase in the initiation vortex cores was only around 0.5°C above ambient and the air near the wall had increased by 2°C at the end of 1.4s of plasma excitation. This small temperature increase was deemed insufficient to contribute in inducing the wall jet flow. However, the question still remains as to how hot the plasma is and how the temperature varies with excitation parameters.

In this chapter, the surface temperature of the electrode sheet was studied using infrared (IR) thermography. A FLIR Systems ThermaCAM SC3000 thermal camera was kindly loaned from the EPSRC. This device uses a Quantum Well Infrared Photon (QWIP) detector and is cooled using a Stirling engine. This has the advantage of being able to operate the camera pointing vertically upwards, unlike the liquid nitrogen models that require the camera to be used virtually level to avoid coolant spillage. The system had image resolution of 320x240 pixels with sensitivity of 30mK at room temperature.

6.2. Thermal Camera Operating Principles

The FLIR Systems ThermaCAM SC3000 measures electromagnetic radiation in the 8-9μm spectral range (far infrared) emitted from an object. The amount of emitted radiation is a function of surface temperature and hence images of instantaneous temperature can be created. However, the IR radiation that the

camera receives will not only be that emitted due to the thermal kinetic energy of the object, but also that reflected from the surroundings and transmitted through the object. These are also modified by the atmosphere between the subject and the camera.

The plasma electrode sheets studied here were constructed from 17μm-thick lower copper electrode, 250μm thick Mylar dielectric and 17μm-thick upper electrodes in a symmetric actuator configuration (c.f. Fig 4.2.1). Since the plasma spreads out to either side of the upper electrode, the surface temperature of the dielectric around the electrode is of interest. The general case of what the camera observes is as shown in Figure 6.2.1. Thermal images were also taken from the side of the electrode (i.e. into the plane of Fig. 6.2.1) and it was confirmed that the plasma did not emit at IR frequencies. Thus it is assumed that the IR radiation from the Mylar surface is transmitted through the plasma without modification. This will be discussed further in Sec. 6.6.

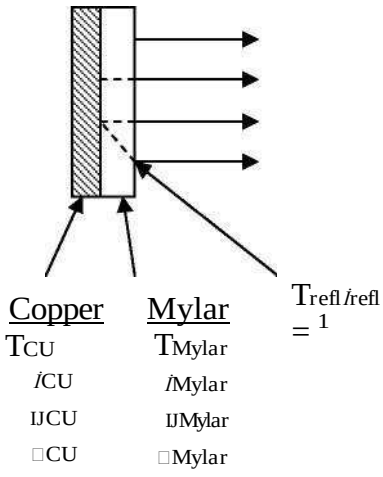

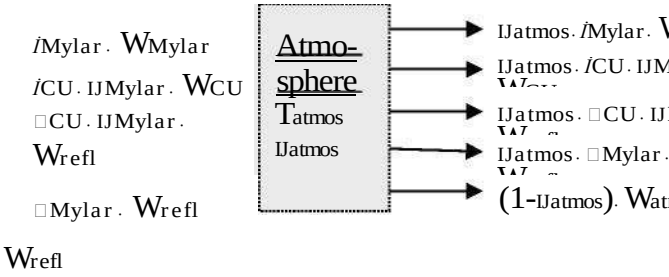

i = spectral emissivity
IJ = spectral transmittance
□ = spectral reflectance
W = radiation power

T = temperature

Figure 6.2.1. General schematic of thermographic measurement.

The total IR radiation arriving at the camera is the sum of the following:

1. Emission from the Mylar sheet:

$$\text{IJatmos} \cdot \text{İMylar} \cdot \text{WMylar} .$$

2. Emission from the Copper sheet through the Mylar:

$$\text{IJatmos} \cdot \text{İCU} \cdot \text{IJ}Mylar \cdot \text{WCU} .$$

3. Reflected emission from ambient sources on the copper, through the Mylar:

$$\text{IJ}atmos \cdot \square CU \cdot \text{IJ}Mylar \cdot \text{Wrefl} .$$

4. Reflected emission from ambient sources on the Mylar:

$$\text{IJ}atmos \cdot \square Mylar \cdot \text{Wrefl} .$$

5. Emission from the atmosphere:

$$(1\text{-IJatmos}) \cdot \text{Watmos} .$$

Thus, the total radiation detected by the camera is:

$$\text{Wtotal} = \text{IJ}atmos \cdot \text{İ}Mylar \cdot \text{WMylar} + \text{IJ}atmos \cdot \text{İ}CU \cdot \text{IJ}Mylar \cdot \text{WCU} + \text{IJ}atmos \cdot \square CU \cdot \text{IJ}Mylar \cdot \text{Wrefl} + \text{IJ}atmos \cdot \square Mylar \cdot \text{Wrefl} + (1\text{-IJatmos}) \cdot \text{Watmos} . \quad (6.2.1)$$

For non-blackbody emitters the spectral absorptance (İ), spectral reflectance ($\square$), and spectral transmittance (IJ), must add up to unity. Hence:

$$\text{İ} + \square + \text{IJ} = 1 . \quad (6.2.2)$$

Also, through Kirchoff's law, the spectral emissivity, İ, is equal to the absorptance:

$$\text{İ} = \text{İ} . \quad (6.2.3)$$

The copper sheet is known to be opaque in the IR spectrum ($\tau_{CU} = 0$) and is highly reflective. Making the assumption that the copper emissivity tends to 0 (for polished copper, $\varepsilon = 0.02$), then using (6.2.2):

$$\tau_{CU} = 0,\ \varepsilon_{CU} = 0,\ \rho_{CU} = 1\ . \qquad (6.2.4)$$

Inserting (6.2.4) into (6.2.1) and noting $\rho_{Mylar} + \tau_{Mylar} = 1 - \varepsilon_{Mylar}$, from (6.2.2):

$$W_{total} = \tau_{atmos} \cdot \varepsilon_{Mylar} \cdot W_{Mylar} + \tau_{atmos} \cdot (1 - \varepsilon_{Mylar}) \cdot W_{refl} + (1 - \tau_{atmos}) \cdot W_{atmos}\ . \qquad (6.2.5)$$

The camera is calibrated to a blackbody source such that it generates a voltage proportional to the radiation power input (linear power device) such that:

$$E_{source} = CW_{source}\ , \qquad (6.2.6)$$

where:

E_{source} = output voltage of camera when directed at a blackbody

C = constant of proportionality

W_{source} = radiative power of blackbody.

Thus, multiplying (6.2.5) by C and solving for E_{Mylar}:

$$E_{Mylar} = (1/\varepsilon_{Mylar} \cdot \tau_{atmos})E_{total} - [(1 - \varepsilon_{Mylar})/\varepsilon_{Mylar}] \cdot E_{refl} - [(1 - \tau_{atmos})/\varepsilon_{Mylar} \cdot \tau_{atmos}] \cdot E_{atmos}\ . \qquad (6.2.7)$$

The voltage measured by the camera detector, E_{total}, can then be adjusted so that the only the emission from the Mylar sheet remains, thus allowing the temperature of the Mylar sheet to be measured. Eq. 6.2.7 shows that it is necessary to know the surface emissivity of the Mylar, ε_{Mylar}, the atmospheric transmittance, τ_{atmos}, the reflected voltage, E_{refl}, and the atmospheric voltage,

E_{atmos}. The atmospheric transmittance is computed internally by the thermal camera through knowledge of the distance to the object, relative humidity and atmospheric temperature. The camera calculates E_{refl} internally though knowledge of the surrounding surface temperatures and assuming these are perfect emitters. The camera also calculates E_{atmos} through knowledge of the ambient air temperature. However, the emissivity of the Mylar must be known accurately and requires calibration.

The sensitivity of the surface temperature measured by the thermal camera on the material emissivity is presented in Fig. 6.2.2. The emissivity dramatically affects the absolute temperature, T, and temperature difference, ΔT (obtained by subtracting images before and during plasma). Thus, the material emissivity must be accurately known in order to achieve correct temperature measurements with the thermal camera.

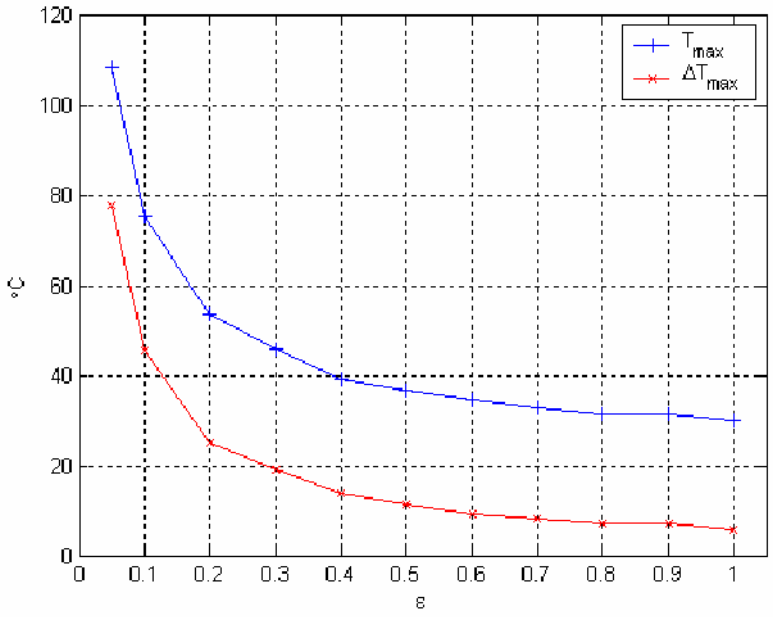

Figure 6.2.2. Sensitivity of absolute Mylar temperature (-) and temperature difference (-) to assumed emissivity, ε, after 5s of plasma formation. Plasma excitation at E_{max} = 3.4kV, PRF = 50kHz, PED = 1ms, PEF = 100Hz. Camera acquisition at 50Hz.

6.3. Equipment Set-up

The ThermaCAM was mounted within the wind tunnel so that the camera pointed vertically upwards onto the plasma sheet, as shown in Fig. 6.3.1. A close-up lens was fitted to the camera with details given in Table 6.3.1. The rear of the camera was rested upon a plate on the wind-tunnel floor such that the front of the camera lens was 100mm away from the electrode sheet. The camera was then focused onto the plasma actuator surface.

In order to ensure a uniform reflection from surrounding objects, a large insulation tile was mounted on the front of the camera, with a hole cut for the camera lens. This was painted matt black such that it was close to a perfect emitter and spanned the whole width of the wind tunnel. Also, the rear of the board was covered by a disposable foil blanket with a radiant heat reflectance of over 90%. This foil shielded the test piece from reflections from the camera casing, which was warm to touch during experiments.

Measurement of the ambient air temperature was made using a Platinum Resistance Thermometer (PRT), thus allowing compensation for atmospheric emission. Measurement of the relative humidity was taken using an Oregon Scientific hygrometer in order to compensate for the atmospheric transmittance. Measurements of the surface temperature of the insulating board were made using a K-Type surface mountable thermocouple via a Tenma 72-2060 digital readout unit. This compensated for radiation reflected from the surroundings. The surface mount thermocouple was previously calibrated to the PRT temperature in purified water.

Lens	Spot Size	Working Distance	FOV (Hor x Vert)	Focus Depth
Close-Up	0.11mm	100mm	34 x 26mm	0.25mm

Table 6.3.1. Thermal camera close-up lens optics data

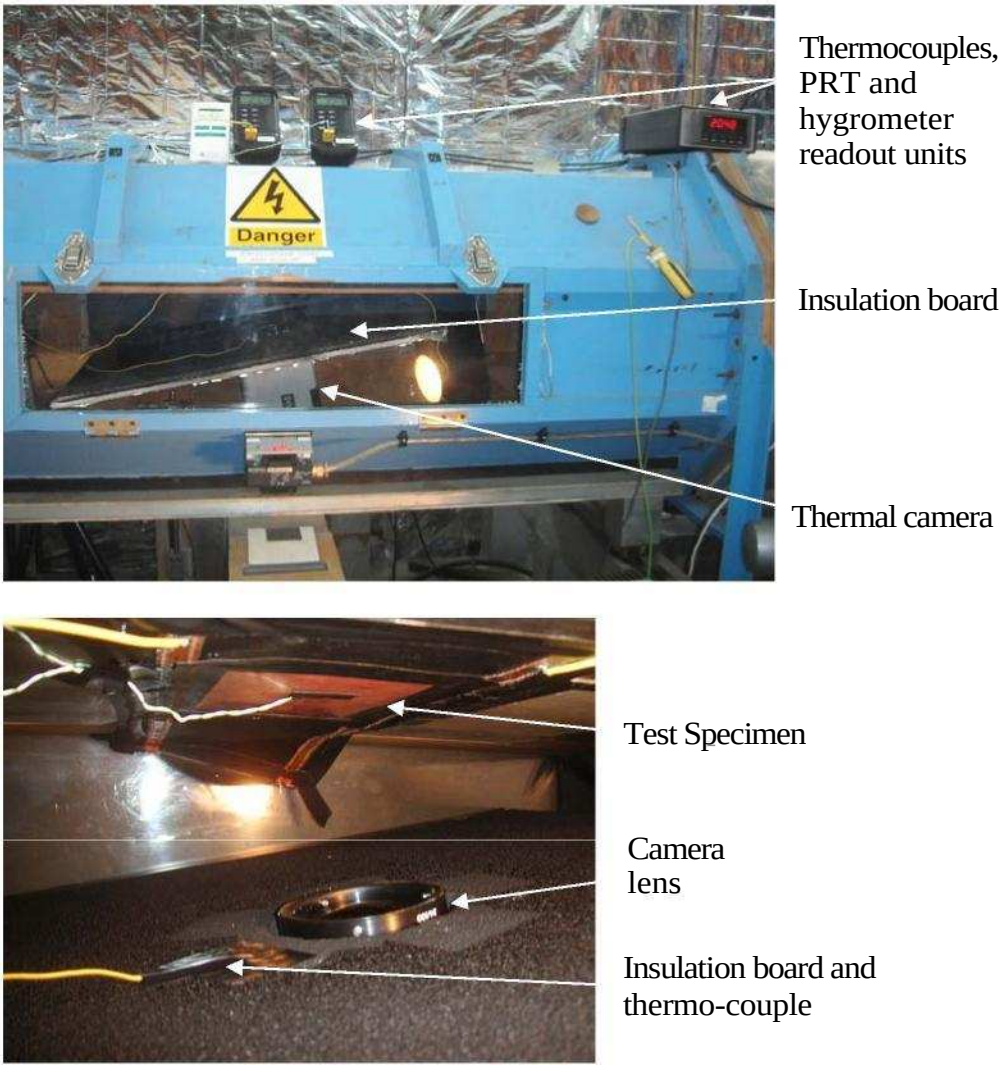

Figure 6.3.1. Experimental arrangement of thermal camera in the wind tunnel.

6.4. Thermal Reflections

At such close distances to the test specimen, problems were encountered with the thermal camera receiving reflections of its own QWIP detector. This takes the form of a cold spot in the centre of the image, as illustrated in Fig. 6.4.1. Note that the reflected image showed a much colder temperature for the copper surface because it is more reflective.

In order to receive a true temperature reading of the test material, it was necessary to set the camera at some angle to the normal in order to avoid such reflections. Tests were conducted on the Mylar/copper sheet in order to determine an optimum angle and it was observed that the camera must be placed at an angle of at least 8°. The thermal camera was consequently set at an angle of 10° to the normal (about x axis) in these experiments.

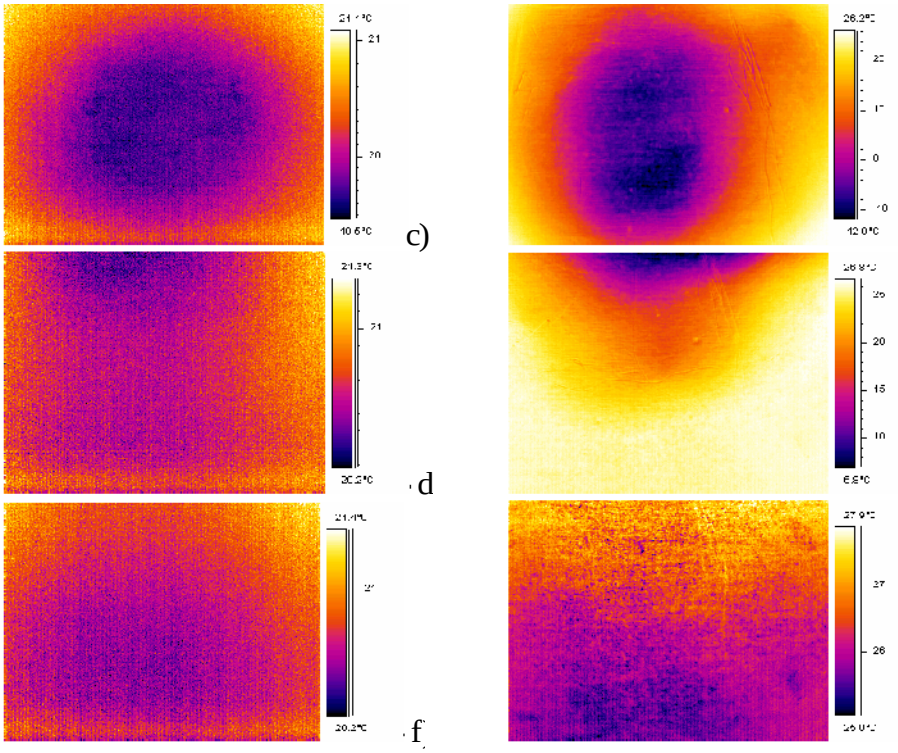

Figure 6.4.1. Variation in IR image with viewing angle. Mylar material: a) 0°, b) 5°, c) 10°. Copper material: c) 0°, d) 5°, e) 10°.

6.5. Emissivity Calibration

Emissivity calibration was performed by using a small sample of the 250μm thick Mylar electrode sheet with the copper etched away on one side only. This was then attached to a heating mat that was used to increase the temperature of the electrode sheet to 60°C. The heating mat was studied with the thermal camera prior to calibration so that the sheet was attached to a location with uniform temperature. The assembly was then fixed to the plate in the wind tunnel in order to replicate the scenario of the plasma experiments.

The Mylar surface temperature was measured using the K-Type thermocouple. This was attached to the sheet using black insulating tape (ε 0.97) and the camera was focussed onto it. The heating mat was adjusted to several different temperatures by altering the DC input into the sheet. The emissivity of the Mylar sheet was calculated within the thermal camera software so that a small area next to the thermocouple was equal to the thermocouple temperature reading. A typical image is presented in Fig. 6.5.1 and the results for the Mylar material are tabulated in Table 6.5.1. The ThermaCAM software only allows an emissivity calculation if the known temperature and ambient temperature differ by at least 3°K. Hence no emissivity calculation was possible for the first few data points. The emissivity calculation is more accurate when the test specimen is at a temperature far from ambient. Thus, ε_{Mylar} 0.93.

Emissivity calculation of the copper material was not possible because it is highly reflective; causing the thermal camera to only "see" the reflection of the insulation tile temperature. The emissivity value for polished copper at 50-100°C given by the ThermaCAM manual is ε_{CU} = 0.02.

T_{atmos} (°C)	RH (%)	IJatmos	$T_{refl} = T_{insulation}$ (°C)	Applied voltage, (V)	T_{Mylar} (°C)	T_{camera} (°C)	Emissivity, i
20.48	56	1.00	24.4	0.0	22.2	22.2	ı > 0.97 (too close to ambient to calculate)
20.49	56	1.00	24.4	5.0	22.4	22.4	
20.53	56	1.00	24.5	10.0	23.5	23.6	
20.55	56	1.00	24.9	12.5	25.2	25.3	
20.57	56	1.00	25.3	15.0	27.6	27.7	
20.60	56	1.00	25.8	17.5	30.3	30.3	1.00
20.63	56	1.00	26.6	20.0	34.6	34.6	0.99
20.64	55	1.00	27.6	22.5	39.7	39.7	0.98
20.68	55	1.00	29.1	25.0	43.2	43.2	0.94 ± 0.04
20.73	54	1.00	30.7	27.5	48.3	48.3	0.93 ± 0.03
20.74	53	1.00	31.9	30.0	53.2	53.2	0.92 ± 0.03
20.44	53	1.00	30.7	25.0	47.0	47.0	0.91 ± 0.03
20.77	53	1.00	29.4	10.0	40.2	40.2	0.93 ± 0.03
20.83	53	1.00	28.3	15.0	33.3	33.3	0.94

Table 6.5.1. Emissivity calibration of the Mylar/copper laminate.

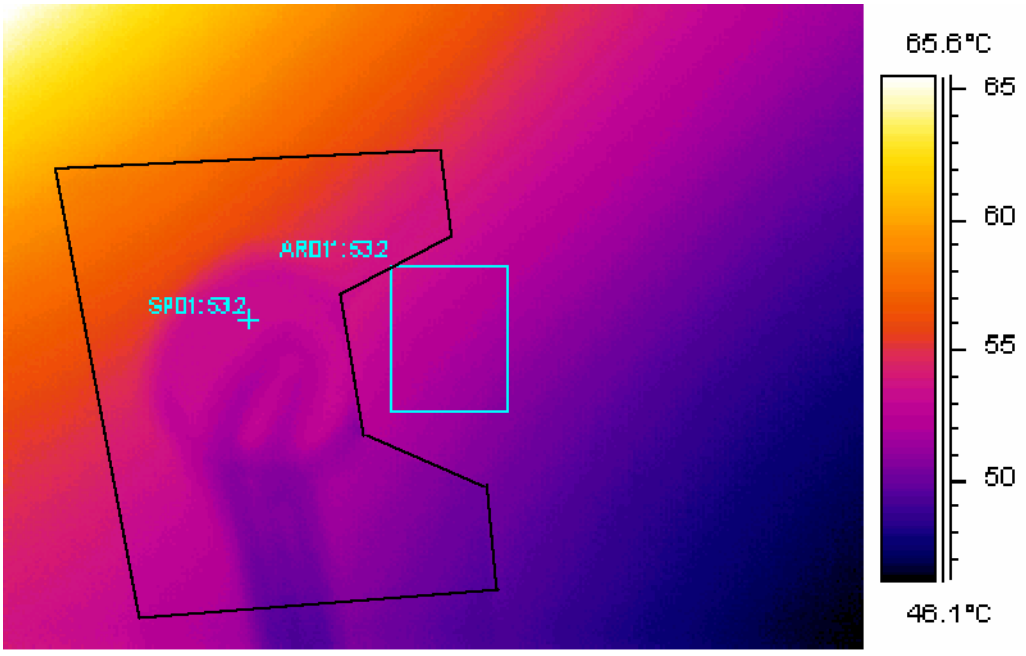

Figure 6.5.1. Thermal Images of the Mylar sheet with 30V applied to the heating mat. Image area is 34 x 26mm. Black lines denote the insulating tape and the surface mount thermocouple is clearly visible on the left. Emissivity calibration was performed by comparing the average temperature of the blue region (Mylar) to the thermocouple reading.

6.5.1. Sensitivity Analysis

The value of ε_{Mylar} was calculated for different input temperatures (T_{atmos}, T_{Mylar} and T_{refl}), within the range of error expected from this experiment. Through variation of T_{atmos}, no change was observed in the calculated emissivity. This is because the distance between the object and camera is very short (0.1m), thus the atmospheric transmission, τ_{atmos}, is equal to unity. Table 6.5.2 demonstrates the variation of emissivity with 30V applied to the heating mat, whereby T_{Mylar} and T_{refl} have been varied by ±1°C in 0.5°C increments to cover the range of error expected from each thermocouple. Error in T_{refl} seems to have only a small influence in the value of ε_{Mylar}, but error in T_{Mylar} has a significant effect. Assuming the thermocouple readings are accurate to ±0.5°C, the emissivity variation is 0.92 ± 0.03.

Applying sensitivity analysis to the calibrations where $T_{Mylar} > 40$°C and averaging the results (Table 6.5.1), it was found that the Mylar laminate has an emissivity of, $\varepsilon_{Mylar} = 0.93 \pm 0.03$. This conclusion is further supported by Fig. 6.5.1. In the images, black insulating tape of $\varepsilon \approx 0.97$ was used to adhere the thermocouple to the surface. The Mylar material is detected to be at slightly lower temperature than the tape. Thus, the Mylar is expected to have an emissivity slightly lower than 0.97.

T_{refl} (°C) / T_{Mylar} (°C)	30.9	31.4	31.9	32.4	32.9
52.17	0.97	0.97	0.97	0.97	0.97
52.67	0.94	0.94	0.94	0.94	0.94
53.17	0.92	0.92	0.92	0.92	0.91
53.67	0.89	0.89	0.89	0.89	0.89
54.17	0.87	0.87	0.87	0.87	0.87

Table 6.5.2. Sensitivity of ε_{Mylar} on reflected and sheet temperature readings.

6.6. Results

As stated in the Sec. 6.2, the plasma itself could not be detected by the thermal camera when the electrode sheet was viewed from the side, which suggests that the plasma does not emit IR radiation. Consequently, direct measurements of the plasma temperature could not be made here. The plasma temperature can, however, be inferred from the electrode sheet surface temperature. Care must be taken in interpreting these results, since the AC electric field will also cause internal heating of the dielectric through dipole polarization, as discussed in Sec. 5.2.

6.6.1. One-Dimensional Analysis

The occurrence of plasma over the laminate electrode sheet can be modelled as a 1D transient heat conduction problem. If the plasma is regarded as a constant temperature gas occurring near the surface of a semi-infinite solid (i.e. the electrode sheet mounted onto a large aluminium heat sink), then at the instant of plasma formation a one-dimensional temperature wave will propagate into the solid walls. Thus, the formation of plasma acts as a step change in temperature at t = 0 and the surface temperature will eventually reach to the temperature of the plasma.

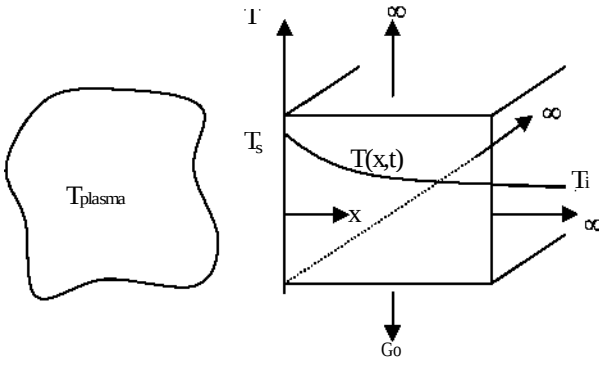

Figure 6.6.1. Schematic drawing of heat conduction into the test plate.

In this model, it is assumed that the plasma is at a constant temperature, T_{plasma}, and the flow of heat is one-dimensional. Futhermore, assuming the solid has no heat sources and has constant physical properties; the general heat conduction equation can be reduced to:

$$\frac{1}{\alpha}\frac{\partial T}{\partial t} = \frac{\partial^2 T}{\partial x^2}, \qquad (6.6.1)$$

where α is the thermal diffusivity of the solid, and other nomenclature is as shown in Fig. 6.6.1. Note that in this section only, x denotes the distance into the dielectric to be consistent with conventional heat transfer nomenclature. For the initial condition, it is assumed that the actuator and aluminium test plate are at constant temperature throughout, i.e. $T(x,0) = T_i$. For the boundary condition far from the surface, the aluminium test plate temperature is assumed to be unaffected by the surface temperature change, $T(\infty, t) = T_i$. Also, the solid surface is assumed to be exposed to plasma through a uniform and constant heat transfer coefficient, h. Thus:

$$-k\left.\frac{\partial T}{\partial x}\right|_{x=0} = h\left(T_{plasma} - T(0,t)\right), \qquad (6.6.2)$$

where k is the thermal conductivity of the solid. This problem has the closed form solution given by Kreith and Bohn (1993):

$$\frac{T(x,t) - T_i}{T_{plasma} - T_i} = \operatorname{erfc}\left(\frac{x}{2\sqrt{\alpha t}}\right) - \exp\left(\frac{h x}{k} + \frac{h^2 \alpha t}{k^2}\right)\operatorname{erfc}\left(\frac{x}{2\sqrt{\alpha t}} + \frac{h\sqrt{\alpha t}}{k}\right). \qquad (6.6.3)$$

However, we are only interested in what the thermal camera "sees", which is the surface temperature of the electrode sheet (i.e. T(0, t)). Thus at x = 0, (6.6.3) becomes:

$$\frac{T(0,t) - T_i}{T_{plasma} - T_i} = 1 - \exp(\tau)\,\mathrm{erfc}(\sqrt{\tau}), \qquad (6.6.4)$$

where, $\tau = h^2\alpha t/k^2$.

Equation 6.6.4 is plotted in Fig. 6.6.2. It can be seen that the temperature at the surface is expected to initially increase very rapidly in response to the sudden change in gas/plasma temperature. However, the rate of increase is very small at later times. For example, the surface temperature is expected to increase to 70% of the plasma temperature by $\tau = 2.5$, but it will take over double this time for the temperature to increase 10% further (i.e. from 70% to 80%). Thus, it is unlikely that the Mylar surface will be close to the actual plasma temperature, even after several seconds of excitation.

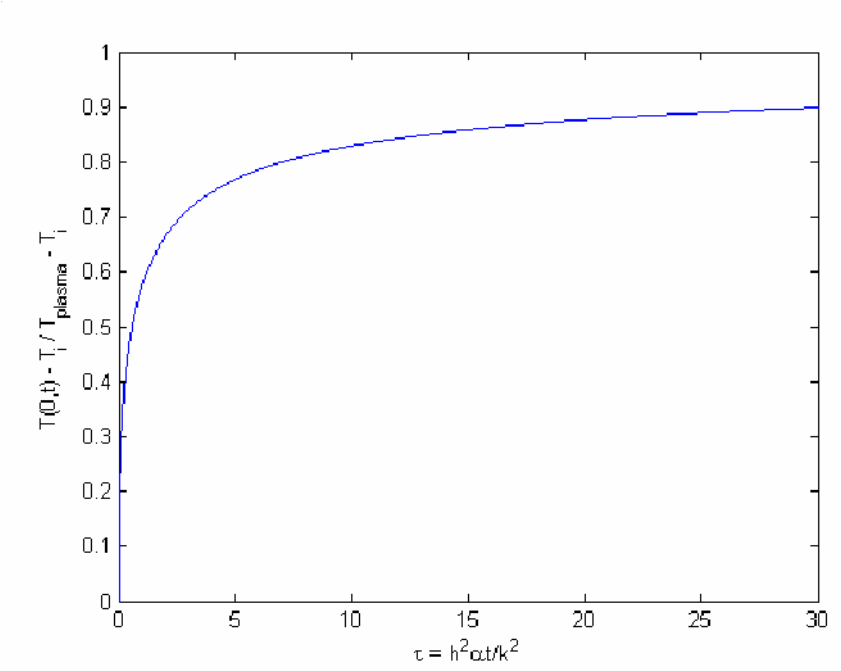

Figure 6.6.2. Variation in dimensionless surface temperature with time for a semi-infinite solid subject to a sudden exposure of the surface to a fluid at different temperature.

6.6.2. Estimation of Plasma Temperature, T_{plasma}

In order to estimate T_{plasma}, the actuator was excited in a non-pulsed mode for 2s. The plasma was activated at various PRF and thermal images were taken at a frame rate of 750Hz. This was the maximum acquisition rate available for the thermal camera which necessitated decreasing the effective field of view to 24mm (x) x 1.6mm (z). The camera was aligned so that 2 plasma electrodes ran vertically across the image area. A typical post-processed image of the temperature profile around one of the electrodes is shown in Fig. 6.6.3, where the plasma was fired continuously at E_{max} = 3.5kV, PRF = 50kHz.

In Fig. 6.6.3a discrete hot-spots can be observed along the electrode length. These are caused by concentrated filaments of plasma which moved about randomly. These hotspots ceased to be observed after around 0.4s of continuous plasma forcing, as shown in Fig. 6.6.3b, and the temperature became reasonably uniform along the electrode length. This is likely to be caused by the averaging effect of these filaments changing location and surface conduction within the dielectric. In order to eliminate any remaining spanwise inhomogeneity, the temperature was averaged in the z direction.

In Fig. 6.6.3a, one can see that the plasma extends for 3mm to either side of the electrode. Note that the dip in the temperature profile at the electrode itself is caused by the differences in emissivity between the Mylar sheet and the copper electrode (ε_{Mylar} = 0.93, ε_{CU} = 0.02). The temperature distribution takes a bell shaped profile, due to the plasma spreading out from the electrode during each formation during the AC cycle. Thus, the plasma nearest the electrode is present for the longest time and it is at this location that one expects to observe the most reliable measurement of its temperature.

Figure 6.6.4 shows the variation in maximum surface temperature at the electrode edge with time, for a range of PRF. The temporal variation is consistent for all excitation frequencies and is very similar to the theoretical model in Fig. 6.6.2. Some meander occurs, especially at high PRF, due to the formation of localised arcs.

In Fig. 6.6.5, the transient temperature profiles of Fig. 6.6.4 have been scaled to fit the theoretical curve based on the 1-D theoretical analysis. Here, the values of $_{Tplasma}$ and $h^2\ell/k^2$ were simultaneously adjusted in Eq. 6.6.4 until the temperature profiles closely matched the theoretical curves. It was found that a value of $h^2\ell/k^2 \approx 0.7$ produced a good fit in all cases, supporting the validity of the 1-D theory. Thus, Fig 6.6.5 shows that the temperature measured at the end of 2s of plasma forcing was roughly 60% of the actual temperature of the plasma. Figure 6.6.6 plots the temperature at the end of 2s forcing and the calculated plasma temperature as a function of PRF.

It is apparent that the plasma gas temperature is considerably hotter than was anticipated, where $_{Tplasma}$ is estimated to be well over 60°C above ambient and increases with the PRF. From the cold-wire anemometer measurements the air temperature was only 2°C above ambient at x = 4mm, y = 1mm from the electrode. This shows that there must be a very steep temperature gradient between the plasma region and where the cold-wire measurements were taken. It seems apparent that very little of the plasmas thermal energy is transferred to the ambient gas and into the resulting flow.

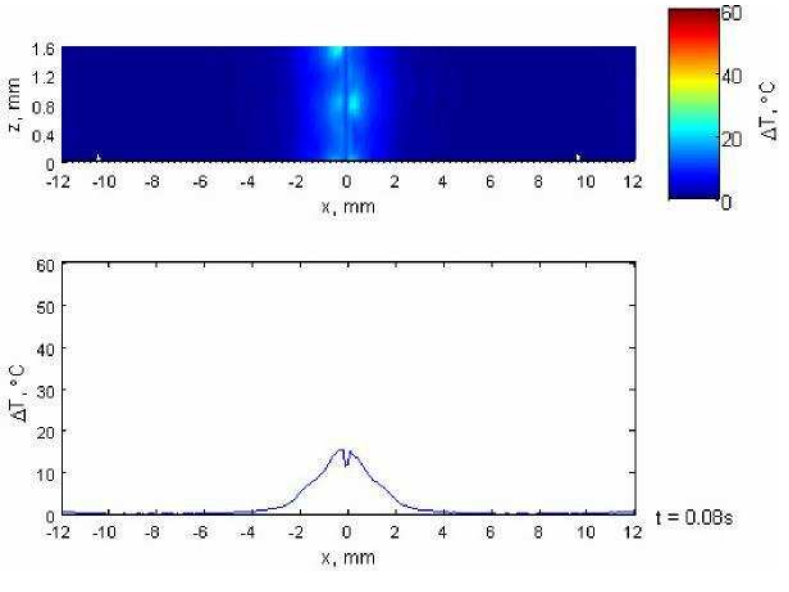

a)

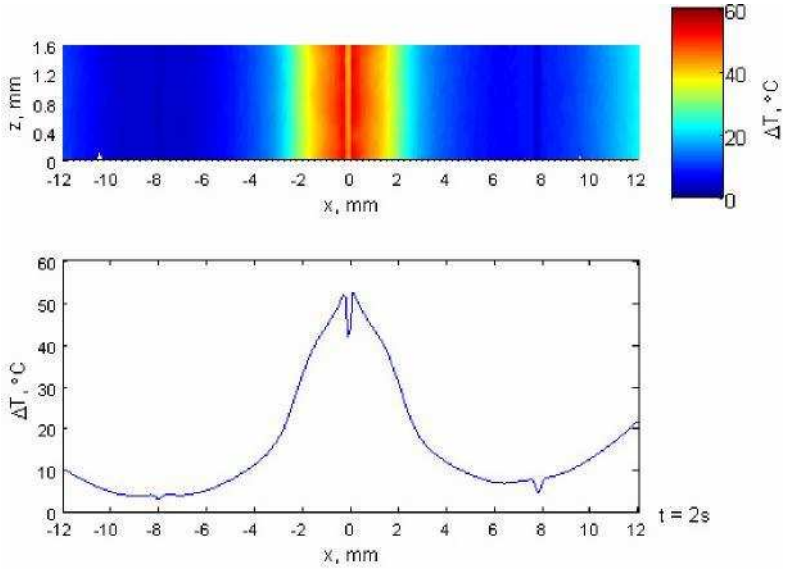

b)

Figure 6.6.3. Instantaneous surface temperature image and surface temperature profile at a) t = 0.08s and b) t = 2.00s. Images have been stretched by a factor of 3 in the z direction to ease viewing. Surface temperature profile is obtained by averaging the temperature in the z direction. The active plasma electrode is located at x = 0, along with two unused electrodes at x = ± 8mm. The sharp drop in temperature at these locations is due to the difference in emissivity of the Mylar dielectric and copper electrodes. Plasma excited continuously at E_{max} = 3.5kV, PRF = 50kHz.

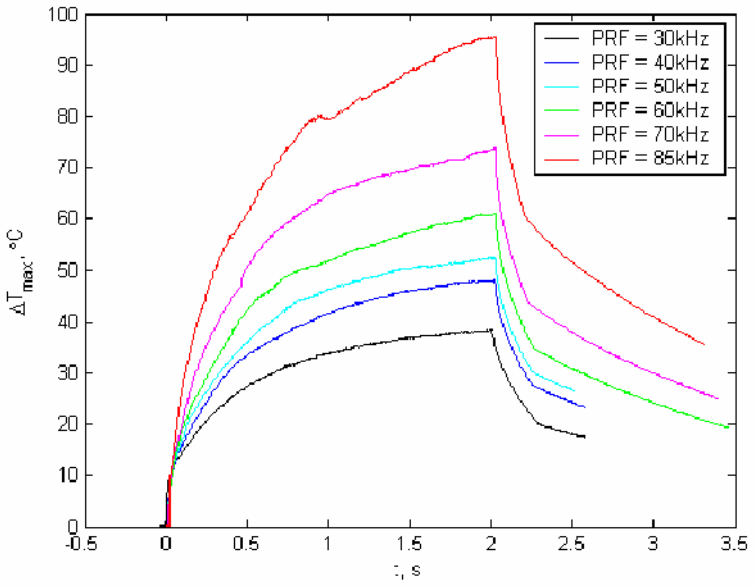

Figure 6.6.4. Variation in maximum spanwise averaged temperature difference with time for continuous plasma forcing for 2s at a range of PRF. E_{max} = 3.5kV.

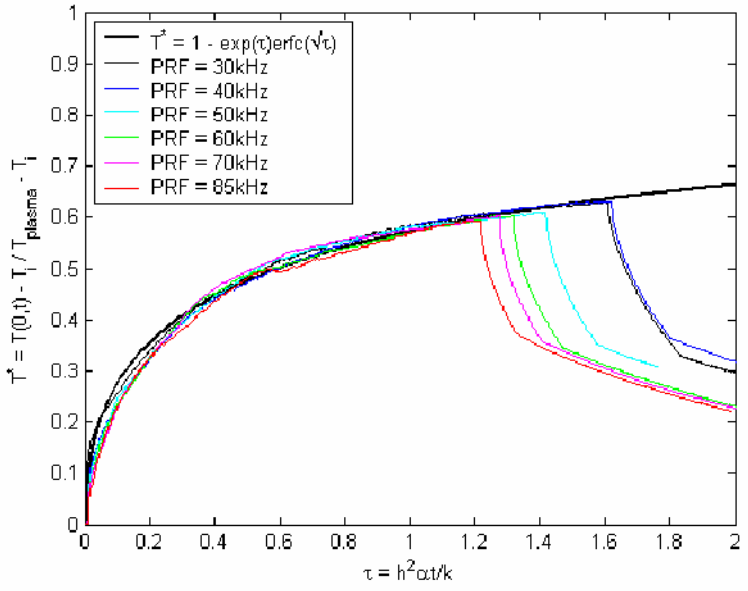

Figure 6.6.5. Variation in dimensionless surface temperature with time for continuous plasma forcing for 2s at a range of PRF. E_{max} = 3.5kV. T_{plasma} calculated by scaling to fit to the theoretical curve of eq. (6.6.4).

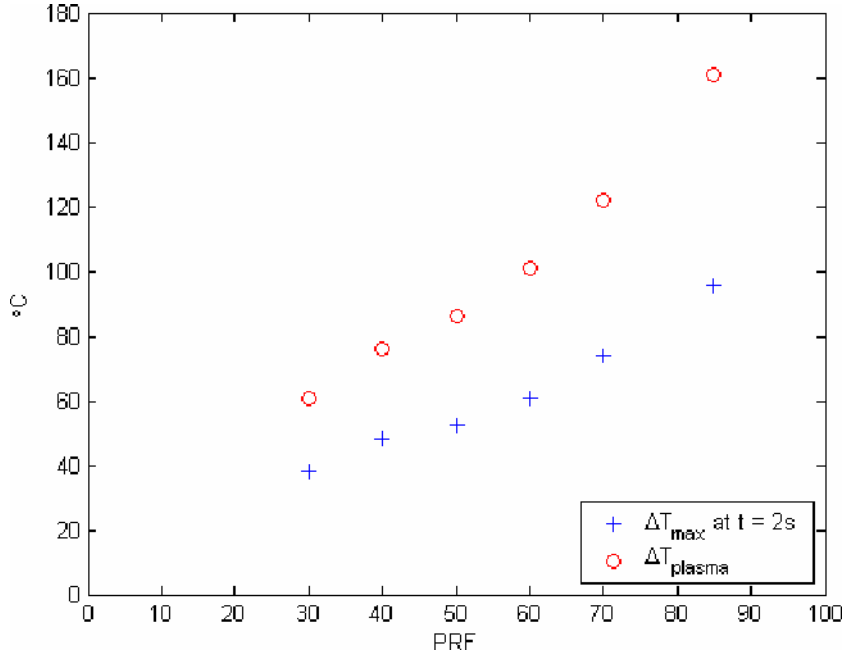

Figure 6.6.6. Variation in maximum spanwise averaged temperature difference with PRF at t = 2s (+), and variation in $_{Tplasma}$ with PRF (o). E_{max} = 3.5kV.

6.6.3. Surface Temperature with Pulsed Plasma

In addition to the estimation of plasma temperature above, the thermal camera was used to study the electrode sheet surface temperature when the plasma is pulsed. Here, it is of interest to observe if the steady state temperature of the sheet is high enough to damage the dielectric, which has an upper continuous use temperature of around 100°C.

The surface temperature distribution and variation with time for plasma excited with E_{max} = 3.6kV, PRF = 50kHz, PED = 1ms, and PEF = 50Hz is shown in Fig. 6.6.7. A maximum surface temperature rise of only 4°C is observed at t = 1s, and the temporal change shows that the surface temperature will not increase significantly above this. Thus, it is unlikely that the electrode

sheet will fail due to thermal breakdown, even if the plasma is maintain indefinitely in this pulsed mode.

A reasonably linear variation in maximum temperature is observed through increasing the applied voltage, as illustrated in Fig. 6.6.8. In this figure, plasma does not form until $E_{max} > 2.2kV$ and the temperature rises linearly thereafter. Note that the thermal camera also detected a surface temperature rise at voltages below that at which plasma forms. This is expected to be due to dielectric heating. Assuming that the dielectric heating varies linearly and continues for $E_{max} > 2.2kV$, it can be seen that it is responsible for nearly 50% of the measured temperature rise, thus emphasising that the plasma temperatures shown above should be treated with much caution. Roth (2005), also found that for $_{Al2O3}$ actuators, the dielectric heating will account for over 50% of the consumed power. The plasma temperature estimates in Sec. 6.6.2 can, however, be regarded as an upper limit of T_{plasma}.

Figure 6.6.9 shows the spatial temperature variation at the corresponding voltages in Fig. 6.6.8. Though the exact extent of the plasma is open to some interpretation because of heat-conduction processes, it is clear that the lateral extent of the plasma increases with applied voltage. Consequently, the volume occupied by the plasma is expected to increase with voltage so that more charge is stored in a stronger electric field. This is expected to increase the body force and hence flow velocity. This supports the conclusions made in Sec. 4.4.

The maximum Mylar temperature varies linearly with PRF, PED and PEF as shown in Figs. 6.6.10 to 6.6.12. For all of these pulsed-plasma tests, the surface temperature was no more than 18°C at the end of 4s of plasma activation. Thus, it is unlikely that the dielectric will overheat in practical

situations, provided the plasma is fired in a pulsed mode. In the continuous mode, the surface temperature very quickly approaches the melting point and this mode of operation should be avoided. Also, during the experiments using continuous plasma, the power supply actually failed due to overloading of the components inside. The variation in surface temperature with applied power is shown in Fig. 6.6.13. The variation is linear for all of the tests, including the continuously fired cases in the previous section.

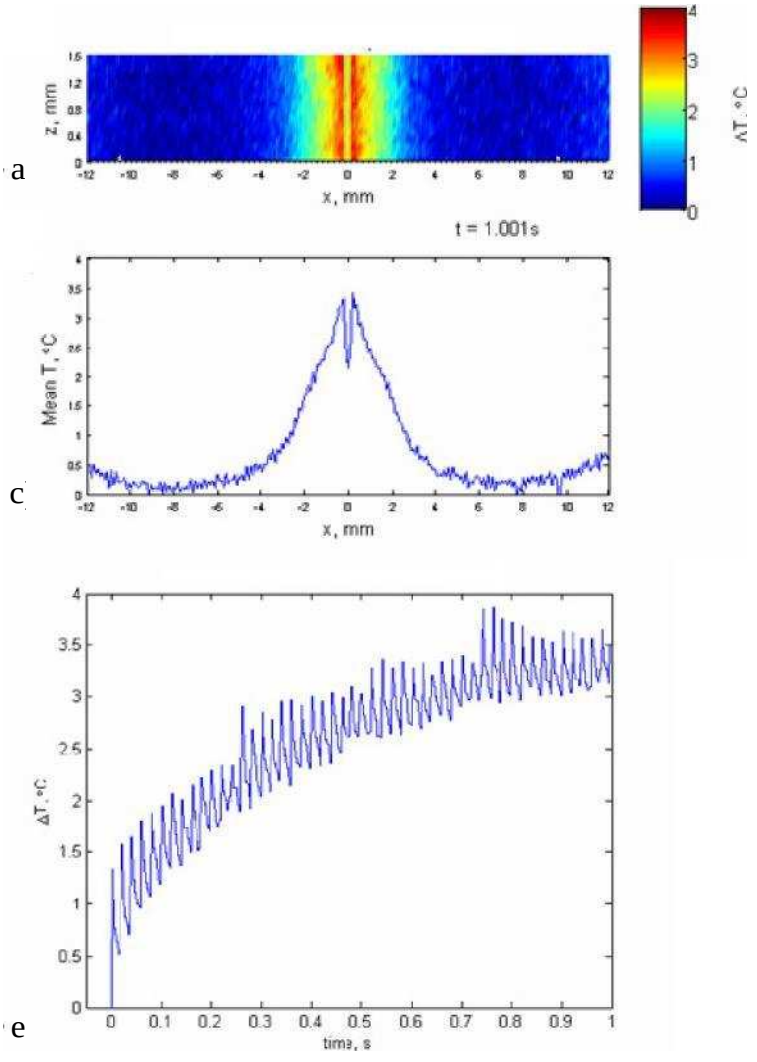

Figure 6.6.7. Surface temperature contour plot (a) and spanwise-averaged variation in temperature (b) at t = 1.001s for a 250μm symmetric Mylar actuator. c) Variation of maximum temperature difference with time. E_{max} = 3.6kV, PRF = 50kHz, PED = 1ms, PEF = 50Hz.

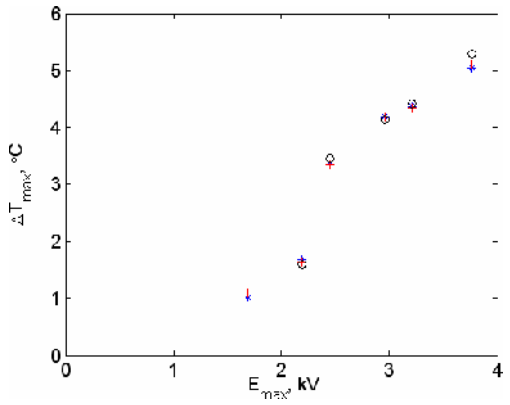

Figure 6.6.8. Variation in maximum spanwise averaged surface temperature with E_{max} at t = 3s. PRF = 50kHz, PED = 1ms, PEF = 50Hz. Note that plasma is only present for E_{max} > 2.3kV.

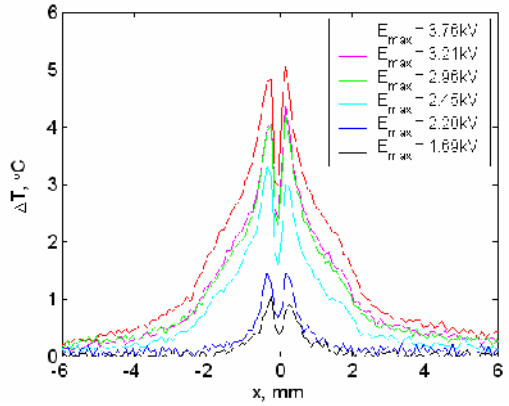

Figure 6.6.9. Lateral variation in spanwise averaged surface temperature at t = 3s at different applied voltage. PRF = 50kHz, PED = 1ms, PEF = 50Hz. Note that plasma is only present for E_{max} > 2.3kV.

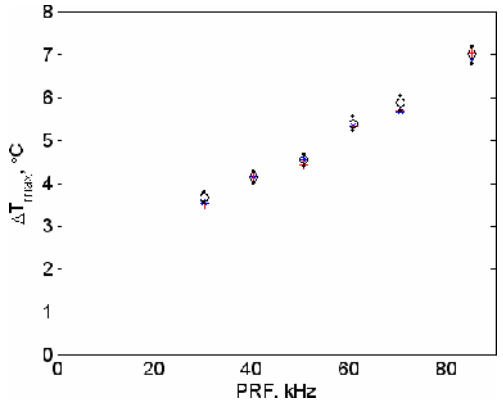

Figure 6.6.10. Variation in maximum spanwise averaged surface temperature with PRF at t = 4s. E_{max} = 3.6kV, PED = 1ms, PEF = 50Hz.

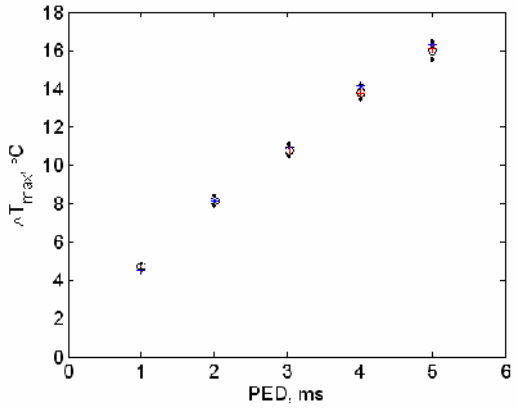

Figure 6.6.11. Variation in maximum spanwise averaged surface temperature with PED at t = 3s. E_{max} = 3.6kV, PRF = 50kHz, PEF = 50Hz.

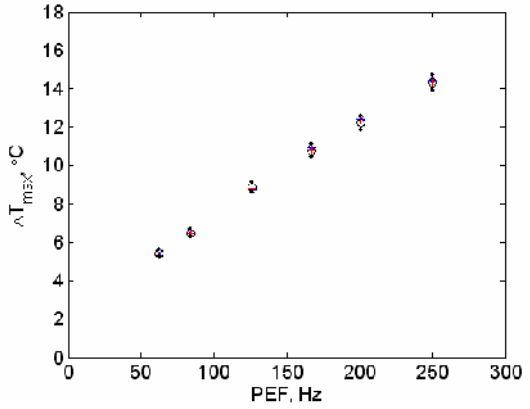

Figure 6.6.12. Variation in maximum spanwise averaged surface temperature with PEF at t = 4s. E_{max} = 3.6kV, PRF = 50kHz, PED = 1ms.

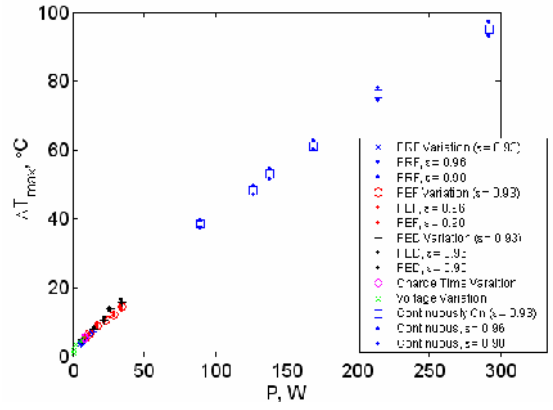

Figure 6.6.13. Variation in maximum spanwise averaged surface temperature with Power through variation of E_{max}, PRF, PED and PEF.

Chapter 7

Plasma Induced Wall Normal Jets

7.1. Introduction

Wall-normal jets have been used for separation control over high-lift devices in order to prevent flow separation and hence reduce profile drag (Gad-el-Hak, 2000). In order to create a wall-normal jet for separation control, holes or slots are typically machined into the surface and fluid is either pumped through the holes (mass addition) or alternately sucked and blown (synthetic jets, Glezer, 2002). These methods involve costly machining of the holes and the necessary ducting adds weight and removes space from the structure. Structural integrity of high lift devices will also be compromised as a result of surface machining. In Chaps 4 and 5, it was shown that a single plasma actuator will initially produce a pair of vortices, and then form a quasi-steady laminar wall jet. Through this work it became apparent that by placing actuators side by side, it would be possible to create a jet of air in the wall-normal direction. The process is shown schematically in Fig. 7.1.1. Note that the wall-normal jet could either be produced along one axis by using long straight electrodes, or could be used to produce axisymmetric jets by using annular ring electrodes. The device would of course need no complicated ducting or precise machining of the aerodynamic surface and may be important for flow control in the future. Vectoring of the 'slot-type' wall-normal jet may also be possible by reducing the plasma force at one electrode or introducing some time delay between firing the plasma on each actuator.

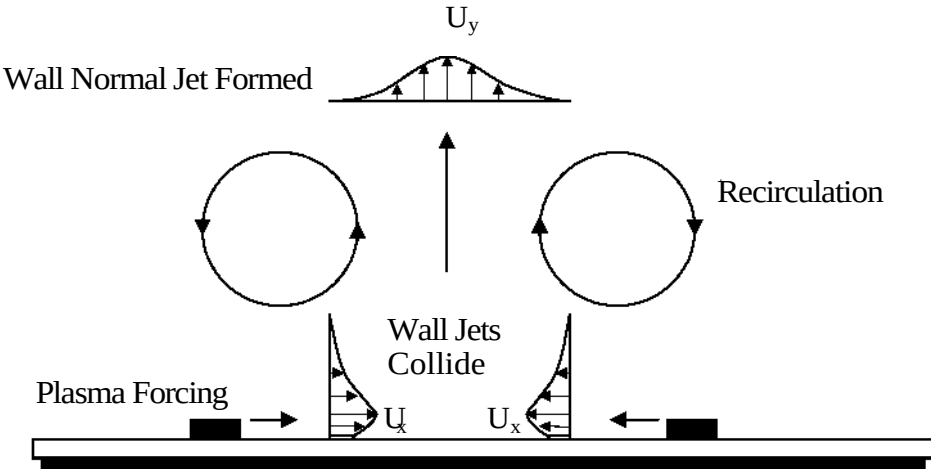

Figure 7.1.1. Schematic of plasma actuators to produce a jet of fluid in the wall-normal direction by using two actuators placed side by side. Each actuator drives a laminar wall jet, which collide and create a flow in the wall-normal direction. Recirculation is expected since each plasma actuator draws air in from above it to satisfy continuity.

7.2. Velocity Measurements and Flow Visualisation

Three wall-normal jet plasma actuators were constructed using 250μm Mylar dielectric with photo-chemically etched upper electrodes, 90mm long. The lower surface was continuous copper such that the actuators were symmetric type. Three pairs of electrodes were manufactured on a single electrode sheet with spacing, s, of 12.7, 19.1 and 25.5mm. Measurements were taken with only one pair of electrodes operating at a time, so that interaction of one jet with another was prevented.

2D hot-wire traverses were performed around each pair of electrodes, with an identical procedure as outlined in Sec. 4.2. In these experiments, measurements were taken at 2.5mm intervals in y ($3.5 < y < 28.5$mm), and

1.6mm intervals in x. Thus the measurement area consisted of between 9 x 11 data points (s = 12.7mm) and 17 x 11 data points (s = 25.5mm). Data were not taken below y = 3.5mm, even between the electrodes, due to the risk of electrical arcing of the hot-wire probe. The plasma was activated with E_{max} = ±3.7kV, PRF = 50kHz, PED = 1ms and PEF = 50Hz, for a total time of 1.4s. These are identical parameters to the single actuator experiments in Sec. 4.3.3, 5.3.1 and 5.4.1.

Figure 7.2.1 shows the time-averaged velocity profile for the two plasma actuators with a spacing of 12.8mm. A wall-normal jet is clearly created, which penetrates for at least 25mm ($\leq$ 2s). The maximum velocity is around 0.25m/s within the measurement area in this experiment. For identical plasma conditions, the maximum time-averaged wall jet velocity for a single, symmetric, 250μm Mylar plasma actuator was 0.35m/s (see Sec. 4.3).

The jet development is shown in Fig. 7.2.2. Primarily, two vortices are created at each plasma electrode which travel along the electrode sheet surface and collide. The slow moving fluid in these vortex cores can be seen to either side of the centreline in Fig. 7.2.2a. Upon contact, these move in the wall-normal direction and establish the jet. Note that the jet takes around 0.4s to fully develop. This is identical to the development time of the wall jet created by a single actuator. After this time, the jet meanders around somewhat, but no decrease in the velocity magnitude was observed near the wall.

A smoke-wire flow visualisation image of all three actuators fired in unison is shown in Fig. 7.2.3 at t = 0.1s. The collision of the initiation vortices is clear, whereby a ‘mushroom’ shape vortex pair develops and moves away from the wall. A steady wall-normal jet soon develops, in which the laminar wall jets

produced by each actuator collide and move away from the wall. The collision is in different stages for each actuator pair in Fig. 7.2.3. For the largest spacing in the figure, the vortices have not yet collided due to the increased distance that they must travel before they meet.

The variation of the time-averaged velocity with wall-normal distance is shown in Fig. 7.2.4. The induced flow from all three actuators is shown for comparison, and all show a similar trend. The jet centreline velocity appears to vary as $U_{max} \propto y^{-2/3}$. The flow has a similar exponent and magnitude to that observed by a single (tangential flow) actuator in Fig. 4.3.15, where it was suggested that $U_{max} = 0.87x^{-0.64}$. Note that for a laminar wall jet emanating from a slit, the jet velocity is expected to vary as $U_{max} \propto x^{-1/2}$ (Glauert, 1956). For a two-dimensional laminar jet, the centreline velocity is expected to vary as $U_{max} \propto y^{-1/3}$ (Mei 2005). The magnitude of the wall-normal velocity also seems to vary linearly with the electrode spacing. The present experimental range is, however, rather limited.

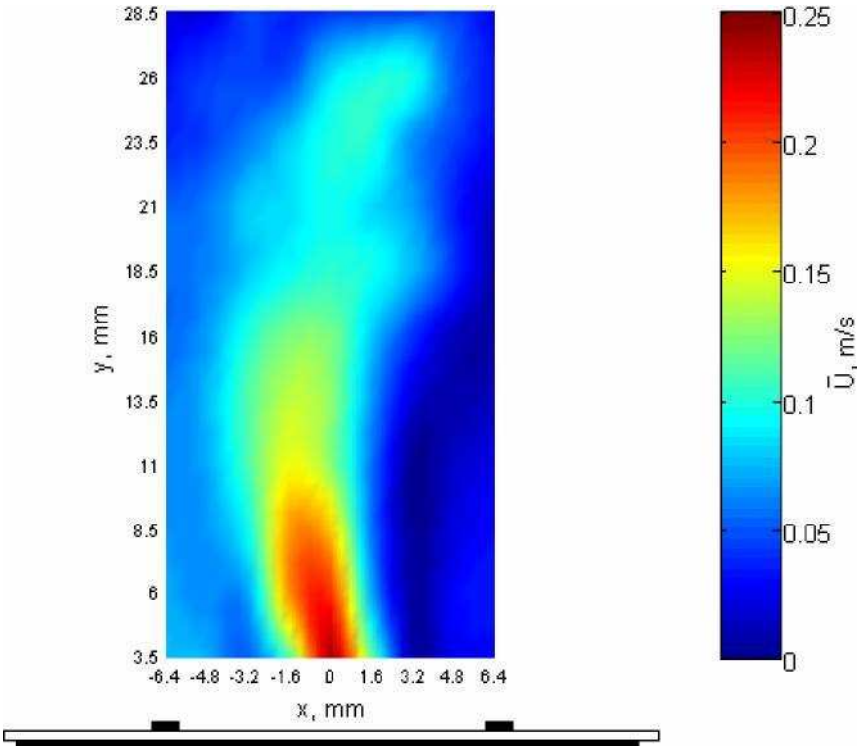

Figure 7.2.1. Mean velocity profile induced by two opposing symmetric plasma actuators spaced 12.8mm apart. Dielectric material is 250μm thick Mylar. Contour show average velocity magnitude over 1.4s of plasma forcing. Plasma excitation at E_{max} = 3.7kV, PRF = 50kHz, PED = 1ms and PEF = 50Hz.

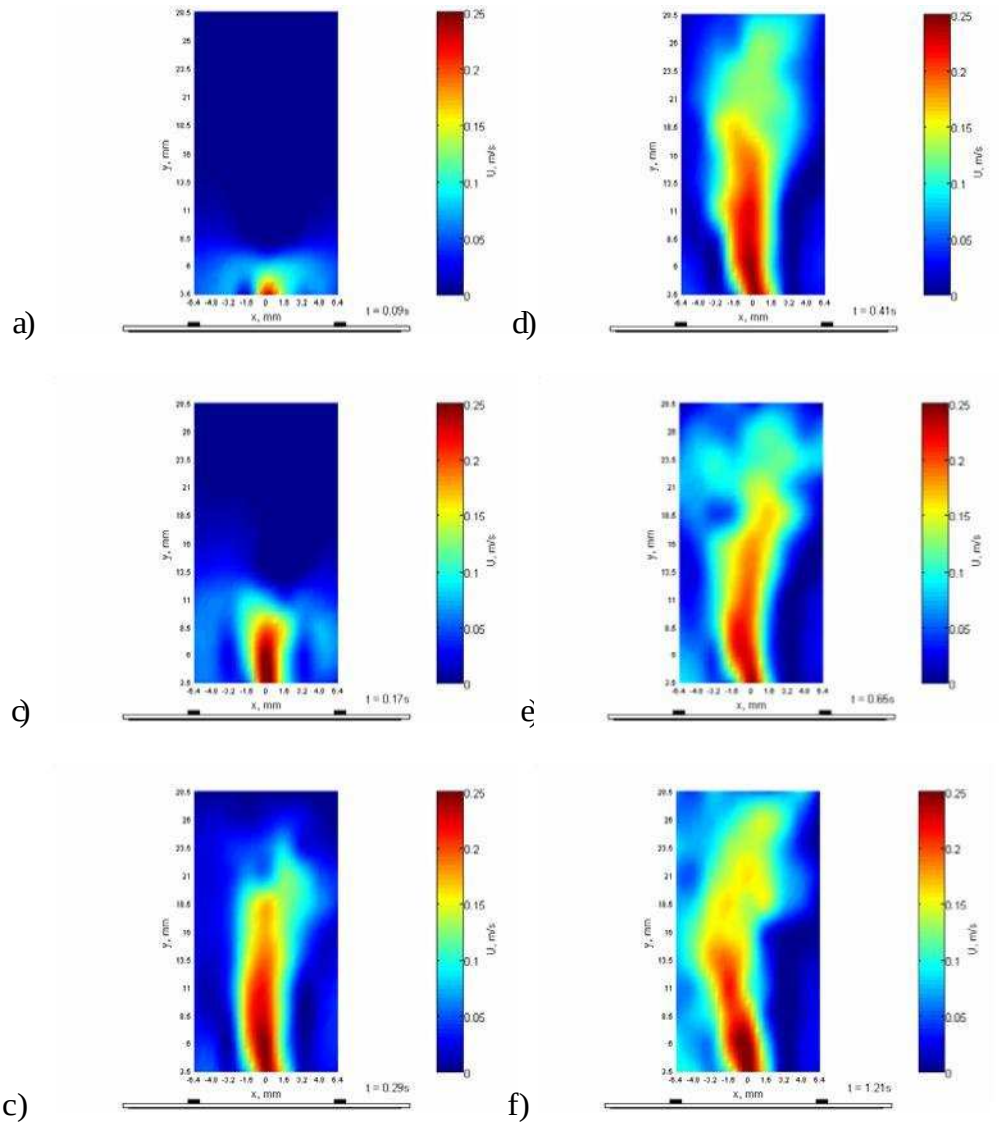

Figure 7.2.2. Velocity magnitude induced by two opposing symmetric plasma actuators spaced 12.8mm apart at different times. a) t = 0.09s; b) t = 0.17s; c) t = 0.29s; d) t = 0.41s; e) t = 0.65s; f) t = 1.21s. Plasma excitation at E_{max} = 3.7kV, PRF = 50kHz, PED = 1ms and PEF = 50Hz.

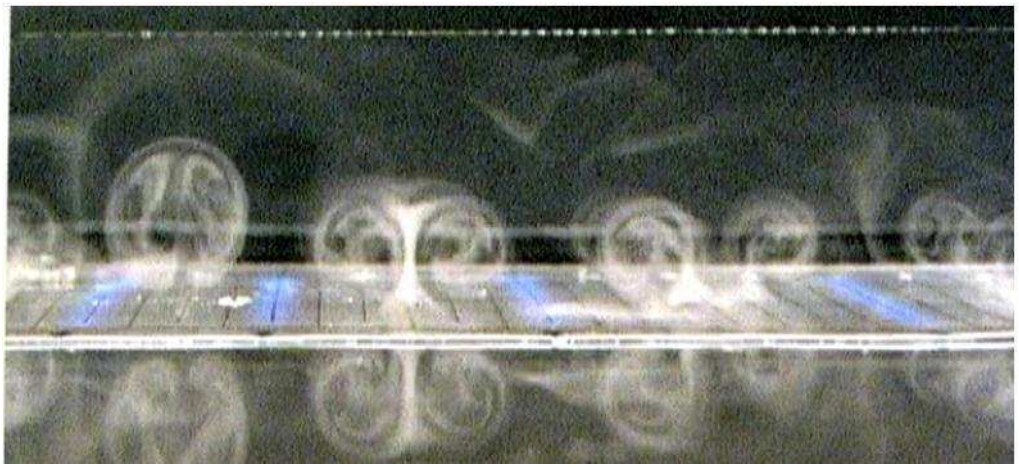

Figure 7.2.3. Flow visualization of plasma induced flow by pairs of opposing actuators. Three different electrode spacings are shown with s = 12.7mm, s = 19.1mm and s = 25.5mm from left to right respectively. The plasma can be seen in blue. The image is taken at t = 0.1s, just as the initiation vortices form each actuator begin to collide and form the wall-normal jet.

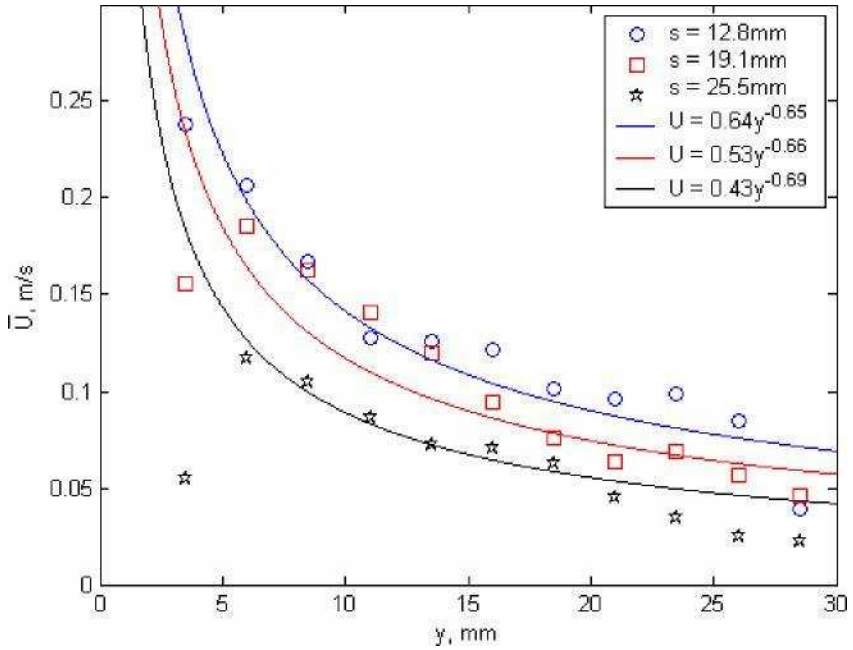

Figure 7.2.4. Variation of mean centerline velocity with wall normal distance for pairs of symmetric plasma actuators with different spacing. s = 12.7mm (-), s = 19.1mm (-), s = 25.5mm (-). Plasma excitation as in Fig. 7.2.

Chapter 8

Spanwise Oscillation Electrode Sheets

8.1. Introduction

For the remainder of this thesis we will focus upon using surface plasma to reduce skin-friction drag in a fully developed turbulent boundary layer occurring over a flat plate. Plasma actuators sheets have been designed such that spanwise forcing occurs near the wall, with characteristics similar to mechanical spanwise-wall oscillation (Choi and Debischop, 2001) and spanwise Lorentz forcing (Pang and Choi, 2004). Hot- and cold-wire anemometry techniques have been used to measure the skin-friction drag and to observe the changes in the turbulent boundary layer structure with and without surface plasma. In this chapter, the operation of the spanwise oscillation electrode sheets is explained and the induced air flow from them is studied in initially static air using flow visualisation. In Ch. 9, a detailed study of the changes in the turbulent boundary layer due to plasma is presented, including u, v, w and T measurements and conditional sampling of the near wall structures. Chapter 10 explores the effect on skin-friction drag for a range of plasma forcing parameters.

8.2. Electrode Sheet Design

8.2.1. Operating Principle

In order to create oscillatory plasma forcing at the wall of a turbulent boundary layer, it was decided to use two sets of opposing asymmetric plasma actuators. Spanwise oscillation using plasma actuators has been attempted before by frequency modulating two offset lower electrodes such that plasma forms sinusiodally on either side of a common upper electrode (Wilkinson 2003). Further details were presented in the Literature Review, Sec. 2.4.3. However, the spanwise oscillation was not effectively maintained by Wilkinson (2003), since a net flow was generated in the wall-normal direction. This was because plasma was present on both sides of the electrodes during part of the oscillation cycle, thus causing adjacent electrodes to producing forcing towards each other, which created wall-normal flow. This is similar to the wall-normal jet that occurred in Ch. 7. The approach used here utilizes two independent electrode sets. This should eliminate the problems using frequency modulation, since each electrode set is activated individually. The approach does, of course, require a dual-channel power supply.

Before discussing the electrode sheet design, let us briefly recap some of the key parameters for turbulent drag reduction in the spanwise-wall oscillation and spanwise Lorentz forcing studies. Jung et al. (1992), simulated a spanwise-wall oscillation and found that for maximum drag reduction the non-dimensional oscillation period, $T^+ = Tu^{*2}/_{\nu}$, should be around 100. Choi et al. (1998), found that the non-dimensional wall speed, $W^+ = (\delta z^+/2).A^+ = .\delta z^+/T^+$, was the important parameter for drag reduction and should be equal

to around 15. Furthermore, Pang and Choi (2004), show that the equivalent wall speed for Lorentz forcing, $W_{eq+} = St.T^+/(2\pi Re_T)$, should also be around 10-15 for maximum drag reduction. Berger et al. (2000) stated that the penetration depth of the Lorentz force into the flow should be set to match the location of the quasi-streamwise vortex cores ($y^+ \approx$ 15-25, Kim et al., 1971). The similarity of the optimum parameters in the two methods suggests that it is the spanwise displacement of low and high-speed streaks relative to the quasi-streamwise vortices that is important for drag reduction (Karniadakis and Choi, 2003). Further details were presented in Sec. 2.3.

The free-stream velocity, U_∞, of 1.8m/s was used in this study. This enabled a thick boundary layer to be developed over the 3m long test plate ($\delta \approx$ 70mm), with a viscous sublayer large enough to enable hot-wire measurements within it so that the skin-friction drag could be evaluate from the near-wall velocity gradient ($y \approx$ 1mm at $y^+ = 5$). This speed also coincides with optimum wind tunnel conditions, based on flow steadiness and minimum free-stream turbulence intensity. Dimensionally (and assuming $u^* \approx U_{0c}/20$), the above optimum spanwise oscillation requirements translate into an oscillation period, $T_{opt} \approx$ 0.14s ($f_{opt} \approx$ 7Hz), wall displacement, $Az_{opt} \approx$ 70mm, and wall speed, $W_{opt} \approx$ 1m/s. The quasi-streamwise vortices occur at y = 2-4mm.

The question now is how to achieve the above criterion with plasma actuators. In the results of the previous chapters we have seen that plasma actuator can be used to create laminar wall jets. For the purpose of designing actuator sheets, it was assumed that several asymmetric plasma actuators placed side by side will create a series of wall jets that superimpose upon one another. This process is illustrated in Fig. 8.2.1. The wall jet from the first actuator was

expected to spread out and lose momentum as it travels to the right in the figure. However, as the jet approaches the next actuator, additional momentum is added, causing the superposition of a new wall jet on the induced velocity profile. It was expected that the wall-jet velocity could be controlled by varying the plasma parameters (e.g. E_{max}, PRF, PED, and note that these have little effect on the jet thickness). Subsequently, it was expected that the mean wall-jet thickness could be controlled by altering the actuator spacing.

Several actuator sheets were manufactured with different electrode spacing and plasma forcing parameters were varied on each sheet. Initially, the plasma parameters were set so that a jet velocity of $U_{max} = W_{opt} \approx$ 1m/s would be produced at $y \approx$ 2-4mm in initially stationary air (i.e. $W^+ \approx 15$ at the centre of the quasi-streamwise vortices). With reference to Fig. 5.3.4c, U_{max} occurs at this distance from the wall when $x \approx$ 10-12mm. Therefore, it was expected that electrode sheets with a gap between co-forcing actuators, 2s, of around 10mm would produce the desired effect. To test this, electrode sheets with 2s = 8-20mm were manufactured and used in the experiments.

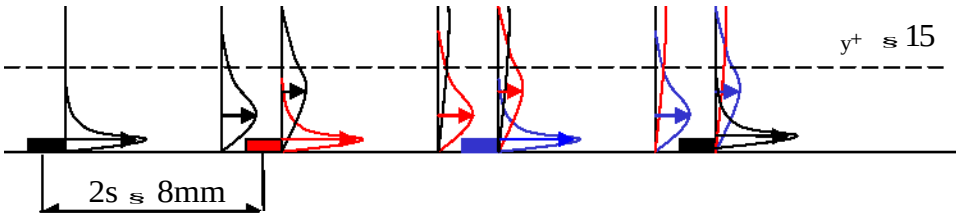

Figure 8.2.1. Schematic of superimposing wall jets occurring due to asymmetric plasma actuators.

In order to create oscillatory spanwise forcing in the near-wall region of the turbulent boundary layer, opposing pairs of asymmetric surface-plasma electrodes were used as depicted in Fig. 8.2.2. Two sets of electrodes were etched onto the upper surface of the electrode sheet with a common ground electrode between opposing pairs. On energizing one electrode set, the plasma formed on one side of the exposed electrode only, due to the offset of the ground. This produced plasma-induced flow of ambient gas in one direction only (e.g. to the right for the red electrode set in Fig. 8.2.2). At a later point in time, the other electrode set was energized, causing plasma to form on the opposite side of these electrodes. This caused the plasma forcing to occur in the other direction (e.g. to the left for the red electrode set in Fig. 8.2.2). Thus, by alternately activating the electrodes it was possible to produce oscillatory forcing near the wall.

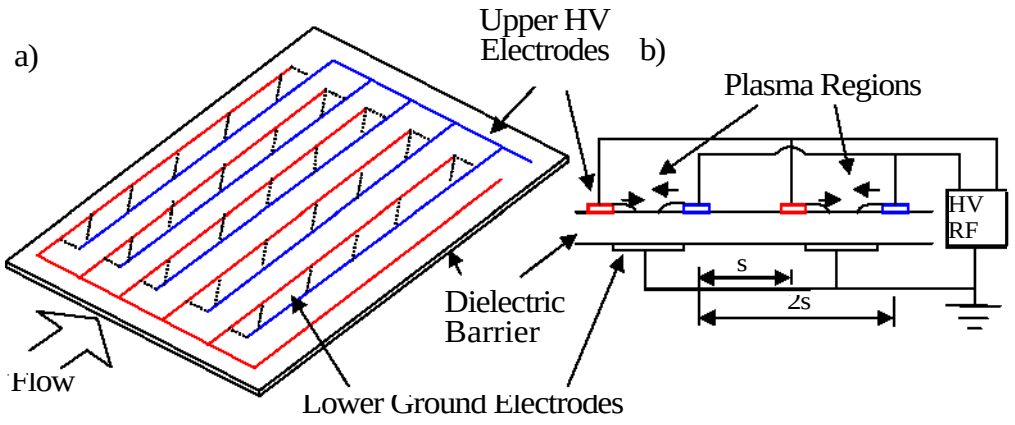

Figure 8.2.2. Spanwise oscillation electrode sheet schematic. Two electrode sets are located on the exposed surface with a common ground between opposing pairs of electrodes. Alternately firing the electrode sets produces oscillatory forcing near the wall. a) Electrode sheet geometry and b) cross section through electrode sheet showing the location of plasma formation and direction of forcing.

Several spanwise-oscillation electrode sheets were photo-chemically etched from copper clad, 250µm thick Mylar dielectric. Each sheet had a usable streamwise length of 366mm and a spanwise width of 304mm (§5 x 45, 1800 x 1500l^+). A CAD drawing of the electrode sheet used in Ch. 9 is shown in Fig. 8.2.3. The sheets were adhered to the aluminium heat sink and flush mounted into the boundary layer test plate, 2m from the leading edge. Gaps between the boundary layer plate and the electrode sheet were within ±0.2mm ($1l^+$). Pressure sensitive tape of 50µm thickness ($0.25l^+$) was used to smooth between the two. An insulating layer of Melonex and silicone sealant was placed between the electrode sheet and the aluminium heat sink. This was necessary to ensure that the plasma formed only on the side of the electrode under which the ground electrode was placed. Without this insulating layer, plasma formed on both sides of the exposed electrode due to the presence of the metal heat sink underneath.

In practice, these electrode sheets took many microseconds to charge to the applied potential due to their large size and increased capacitance. This limited the maximum PRF that could be applied (and thus limited the plasma-induced velocity). The PRF was consequently set to the maximum possible value which allowed the sheets to fully charge during an AC cycle: PRF = 37 kHz. In the future, it may be possible to reduce this charging time, and thus increase the maximum PRF, by removing any unnecessary copper on the sheet underside.

In order to induce the required velocity for the spanwise oscillation at this relatively low PRF, the applied voltage, E_{max}, had to be set to the maximum value obtainable by the power supply (~4kV). However, the applied voltage

had to be reduced slightly for the sheet with s = 4mm because arcs frequently formed between neighbouring electrodes. This was because the inter-electrode gap was smaller that the lateral extent of the surface plasma.

Due to the restrictions on PRF and $_{Emax,}$ only three independent parameters were available to alter the plasma-induced spanwise oscillation: the pulse envelope duration, PED, the electrode spacing, s, and the oscillation period, PEF (= 2/T). The effect of these parameters on the viscous drag will be studied in Ch. 10.

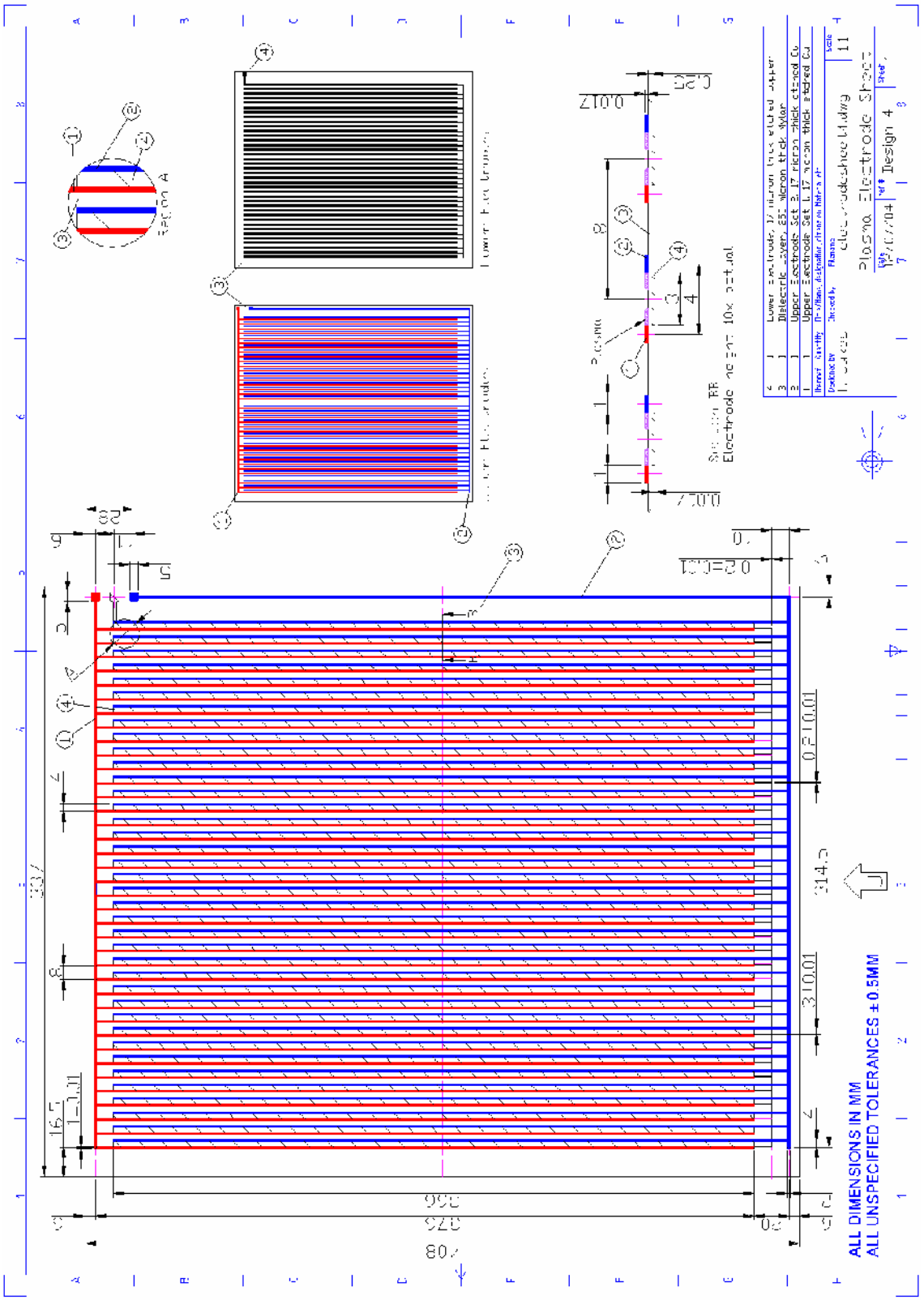

Figure 8.2.3. Spanwise oscillation electrode sheet. This sheet has 8mm spacing between electrodes on the same bus. The spacing between opposing electrodes, s, is 4mm.

8.2.2. End Effects

Due to the electrical nature of the plasma, it was not possible to take hot-wire measurements near the wall of the spanwise oscillation electrode sheets ($y <$ 3mm, $y^+ < 15$). Consequently, analysis of skin-friction drag from viscous sublayer measurements had to be made downstream of the electrode sheet. Preliminary tests showed that some plasma formed at the end electrodes, as illustrated in Figs. 8.2.4a and b. This formation was expected to generate a force in the streamwise direction, just prior to measurement with the hot wire. This may have induced a streamwise wall jet that altered any skin-friction drag reduction caused by spanwise oscillation.

Experiments were conducted to suppress this plasma formation by shortening the electrodes and covering them with insulation. The most effective method was to terminate the electrodes using insulating tape, as shown in Figs. 8.2.4c and d. In the measurements in the following Chapters, a layer of 100μm thick insulating tape ($0.5l^+$) was placed along the rear edge of the electrodes. Hot-wire measurements were then taken above the insulating tape. The author is well aware that this discontinuity will inevitably have some effect on the near wall structures. However, the discontinuity is well below the condition for a hydraulically smooth wall ($y \ll 5l^+$), and the measurements are concerned with a comparison between the boundary layer without and with plasma forcing. It will be shown that the near-wall profile of the boundary layer without plasma compares very well to the DNS results of Moser et al. (1999), proving that the tape had little effect.

It was also noted that if the hot-wire probe was placed near the electrode bus (covered by insulating tape), plasma will form through the tape and onto the

probe as shown in Fig. 8.2.5. Remarkably, no damage was caused to the sensor during this process but the velocity measurements could not be trusted. Measurements were subsequently taken 15mm downstream of the end electrodes (5mm downstream of the connecting bus). At this position in still air for y < 1mm (y^+ < 5, i.e. within the viscous sublayer), the electronic interference during plasma formation caused an increase in the mean voltage of 0.03% (áE < 0.04mV, á*e'* < 0.06mV, áU < 0.0005m/s). This is a negligible level of electronic interference and the hot-wire signals are therefore considered devoid of plasma-induced noise.

For later studies to be discussed in Ch. 10, electrode sheets were manufactured that avoided using a bus at the downstream edge. This enabled measurements to be taken closer to the plasma electrodes. Figure 8.2.6 shows the design of these 'busless' electrode sheets. Both HV buses are located at the upstream edge of the electrode sheet with one HV bus (HV 2), located on the underside. Holes are then drilled through the sheet and silver conductive paint is used to make the electrical connection. Care was taken in ensuring that the holes and paint on the upper surface were smooth. Very few problems were encountered with these 'bi-layer' sheets and they were just as reliable as the other style. This opens many opportunities for complex multi-layer electrode patterns that are limited only by our imagination.

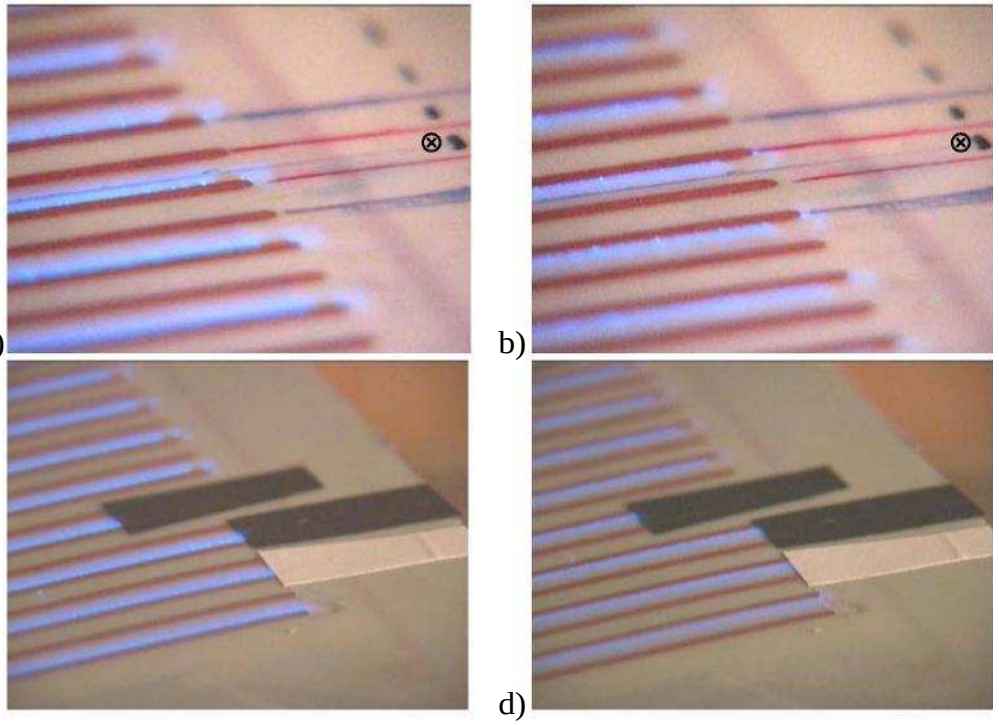

Figure 8.2.4. Photograph of the downstream edge of the electrode sheets. a) and b) show plasma formation around the edge of the electrode during the spanwise forcing cycle; c) and d) illustrate suppression of plasma formation using insulating tapes of different thicknesses. Hot-wire measurements typically taken at .

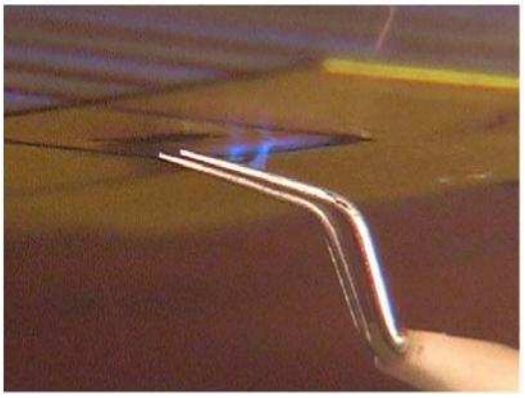

Figure 8.2.5. Insulating tape is used to inhibit plasma formation at the end of the electrodes. However, plasma can be seen to form between the electrode bus (under the tape) and the hot wire, necessitating measurements to be taken an additional 10mm downstream from this position. Remarkably, no damage was caused to the hot wire.

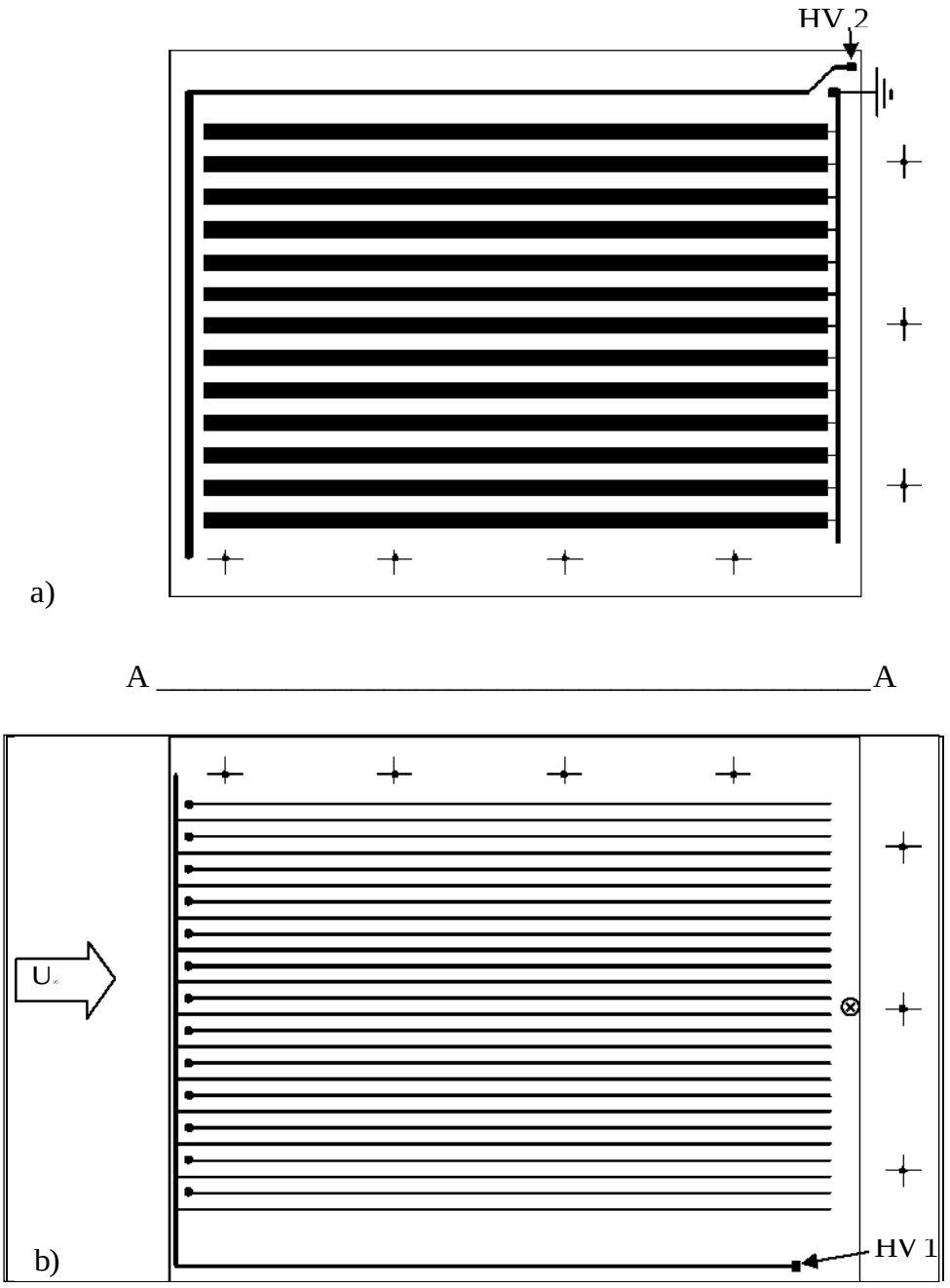

Figure 8.2.6. Template for 10mm spacing electrode sheet with 'busless' design. Lower electrodes are shown in a) and upper (exposed) electrodes in b). Drawing shown mirrored, such that folding along A-A creates the sheet. Flow over upper electrodes is from left to right and measurements are taken at ∞. Holes are drilled through circles on upper sheet and filled with conductive paint in order to connect the second electrode set to the HV bus on the lower surface (HV 2).

8.3. Visualisation of Spanwise Oscillation Plasma Actuators in Still Air

A series of flow-visualisation images of the induced flow by the spanwise oscillation electrode sheet in initially static air is shown in Fig. 8.3.1, and drawn schematically in Fig. 8.3.2. The sheet had 4mm electrode spacing, s, (i.e. 4mm between opposing electrodes, 8mm between like electrodes), and the location of the electrodes have been drawn on the figure. Plasma forcing occurs in frames b, e and h in Fig 8.3.1, with direction as indicated. This is the same sheet that will be studied in the boundary layer experiments of Ch. 9, where the free stream will be into the plane of these figures.

Images were taken using a Canon XM2 video camera at 25fps, with a shutter speed of $1/250^{th}$ s for each frame. In order to capture the oscillation on video camera, the oscillation frequency and pulse duration were reduced slightly from the boundary layer experiments in Chaps. 9 and 10. The plasma conditions were set as PRF = 37kHz, E_{max} = 3.3kV, PED = 1ms, PEF = 8.5Hz (i.e. oscillation period, T = 2/PEF = 0.24s, or $T^+ \leqslant 90$ if there was flow).

Seeding from a fog generator was used to visualise the fluid motion. This smoke was slightly denser than air so that it accumulated in a thin region near the wall prior to plasma forcing (Fig. 8.3.1a). In order to seed the sheet with a relatively undisturbed layer, the smoke was first fed into a large box and then slowly pumped onto the electrode sheet using a CPU fan via 4mm diameter flexible tubing. Controlling the DC voltage to the CPU fan ensured that a laminar flow of smoke was produced with a velocity of less than 0.05m/s.

From the flow visualisation it is clearly observed that a series of co-rotating vortices are created by the plasma in still air. During the first part of the cycle,

counter-clockwise vortices are created and travel to the right in Fig. 8.3.1b-d and shown schematically in Fig. 8.3.2a. For the next part of the cycle, clockwise co-rotating vortices are created which travel to the left (Fig. 8.3.1e-g, Fig. 8.3.2c). The centre of these vortices are at around $y \approx 4$mm ($l^+ \approx 20$); equal to the inter electrode spacing, such that the vortices have a diameter of around 8mm ($l^+ \approx 40$). Note that this is at a similar height to the naturally occurring quasi-streamwise vortices in the turbulent boundary layer at the present experimental condition ($y \approx$ 2-4mm).

These vortices are similar to the initiation vortices observed in the single electrode studies. The presence of these co-rotating vortices was not as originally planned, but is inherent to the spatially discrete nature of plasma. The change from a 'slip' (in the plasma), to a 'no-slip' boundary condition (outside of the plasma region), is expected to create a junction vortex similar to that between a moving and stationary wall (see Allen and Naitoh, 2005).

Looking carefully at frames e and h in Fig. 8.3.1, it is observed that when the plasma is activated, a downwash occurs in the inter-electrode space between electrodes (plasma side) as the plasma entrains fluid from above to replace that ejected laterally. This downwash region occurs at around the same spatial location regardless of forcing direction. This process destroys the vortex directly above the plasma, although it is important to note that the location of the vortices relative to the electrodes when the plasma forcing occurs will depend on E_{max}, PRF, PED (i.e. vortex convection velocity, U_{conv}), and the oscillation frequency, PEF/2.

In the flow visualisation pictures carried out in still air, a tangentially oscillating flow can be observed in the near wall region, as intended. This can

be seen most clearly in the inter-electrode space between no-plasma sides of the electrodes. Spanwise motions also occur between opposing pairs (plasma sides), but the motion is complicated somewhat by the fluid motion towards the wall. It is, however, expected that the spanwise velocity between opposing pairs is much larger because this is the region in which plasma forcing occurs. While the plasma-induced downwash remains approximately stationary during the forcing cycle, the vortex cores do not. In fact, the location of the vortices offset each other by one half the vortex diameter. For example, the cores in Fig. 8.3.1d and 8.3.2a (i.e. just before plasma forcing) are located over the blue electrode set, while the cores in Fig. 8.3.1g and 8.3.2c (again, just before plasma forcing) are located over the red electrode set. This separation ensures that the location of the upwash and downwash sides of the vortices is continually changing.

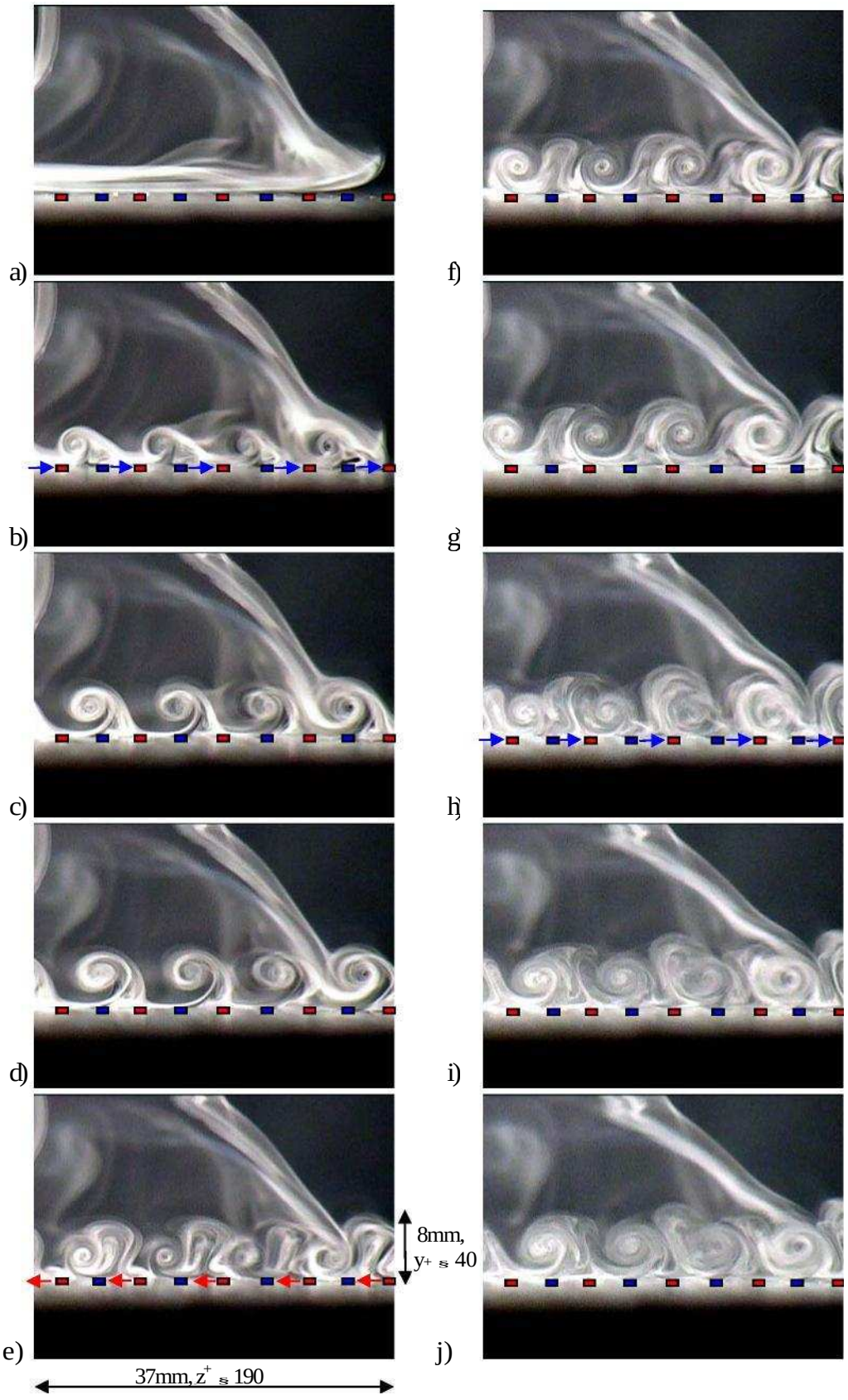

Figure 8.3.1. Oscillatory plasma flow visualisation in static air. FOV = 37 x 28mm at 25fps. Plasma activated in b, e, and h with indicated direction and position. PRF = 37kHz, E_{max} = 3.3kV, PED = 1ms, PEF = 8.5Hz, s = 4mm.

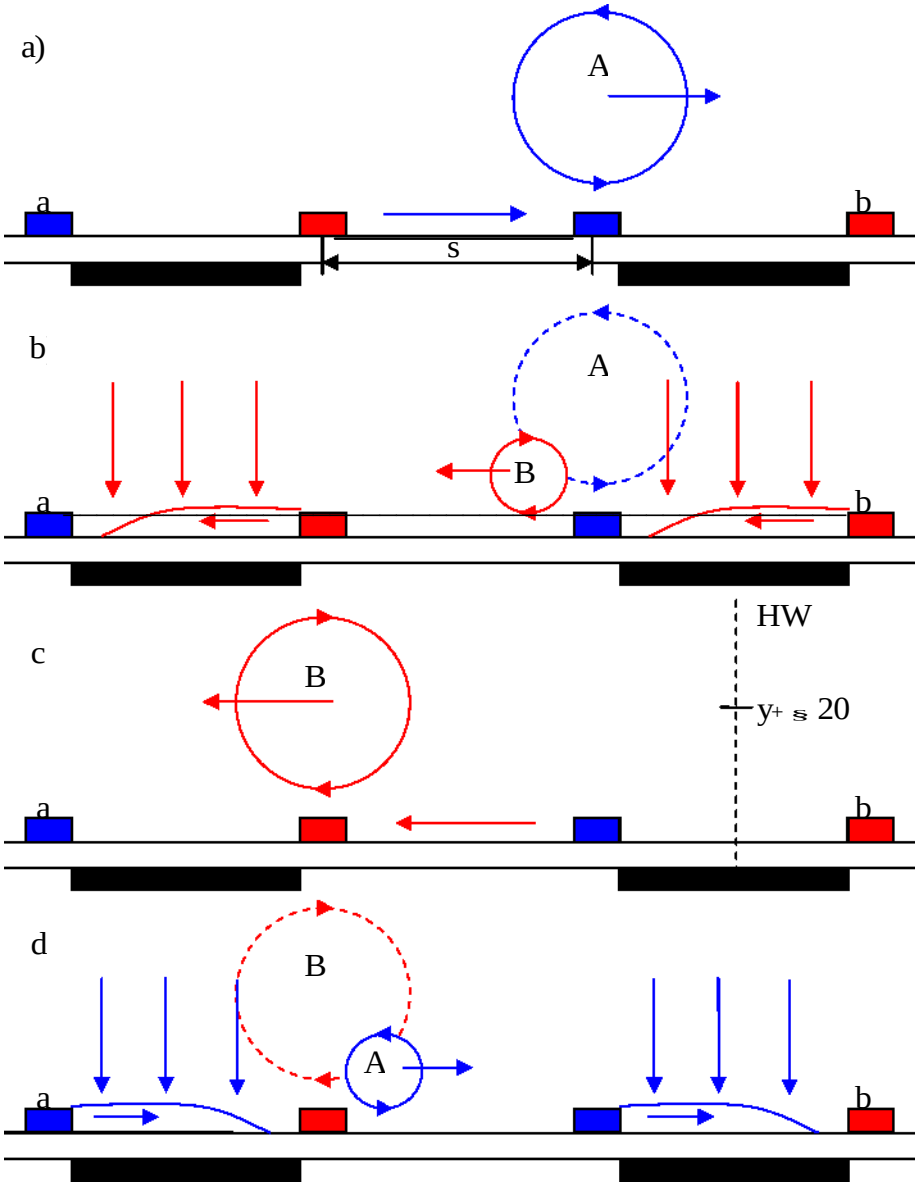

Figure 8.3.2. Schematic of spanwise oscillatory surface plasma motion. a) Initiation vortex (A) from electrode a moves to the right (c.f. Fig. 8.3.1d). b) As A arrives above the next blue electrode set, plasma is activated on the red electrode set. The induced downwash destroys A, and a new vortex forms (B), (c.f. Fig. 8.3.1e). c) Vortex (B) from electrode b moves to the left (c.f. Fig. 8.3.1g). d) As B arrives over next red electrode, blue actuators fire, again destroying the vortex. Note that the downwash occurs in the same position throughout the cycle, whilst the vortices offset each other by the electrode spacing, s. Boundary layer measurements typically taken at HW line in c).

Chapter 9

Plasma Effect on the Turbulent Boundary Layer

9.1. Introduction

In this Chapter, the turbulent boundary layer with and without oscillatory surface plasma is studied in detail at one experimental condition. The electrode sheet used here had an electrode spacing, s, of 4mm (s^+ = 20) between opposing actuator pairs. A CAD drawing was presented in Fig. 8.2.3. Plasma excitation parameters were set with a Pulse Repetition Frequency, PRF, of 38kHz, a maximum applied voltage, E_{max}, of 3.3kV, a Pulse Envelope Duration, PED, of 5ms, and a Pulse Envelope Frequency, PEF, of 21Hz. Thus, the oscillation frequency, f = PEF/2 = 10.5Hz, corresponding to a non-dimensional oscillation period, $T^+ = Tu^{*2}/\nu$ = 38. Although this oscillation period is lower than the optimal value given by Jung et al. (1992), it will be shown later in Ch. 10 that this is near an optimal value for drag reduction using plasma. From measurements of the induced flow by a single asymmetric actuator in initially static air, it was expected that the maximum spanwise wall velocity will be around 1.2m/s at these plasma excitation parameters (i.e. W^+_{max} 15, see Figs. 5.3.15, 5.3.18 and 5.3.21). Most measurements were taken 15mm downstream of the electrodes at the centreline of two opposing actuator pairs. For all tests, the free-stream velocity, U_∞, was set at 1.8m/s. This was so that the viscous sublayer was sufficiently thick to enable measurements within it, and the free-stream flow was of good quality. At the measurement position the boundary layer thickness, δ, was 70mm. The Reynolds number based on

momentum thickness, $Re_\theta = U_\infty \theta / \nu = 920$, and the Reynolds number based on friction velocity, $Re_\tau = u^* \delta / \nu = 380$.

The near-wall positioning technique, skin-friction measurement and scaling methods are outlined in Sec. 9.2. Cold-wire temperature measurements throughout the boundary layer are presented in Sec. 9.3. Single hot-wire measurements are presented in Sec. 9.4.1 (u-component), and X-wire measurements are presented in Sec. 9.4.2 (uv and uw components). Spectral analysis and probability distributions at several key locations in the boundary layer are presented in Sec. 9.4.3. Variable Interval Time Averaging (VITA) is used to study the change in near-wall flow structures in Sec. 9.4.4 and 9.4.5. The phase-averaged spanwise velocity profile is studied in Sec. 9.4.6. Finally, the spanwise variation in U is studied in 9.4.7. A summary of the results presented in this chapter is provided in Sec. 9.5.

9.2. Drag Measurement and Scaling

9.2.1. Skin Friction Measurement and Wall positioning

The skin-friction was obtained by measuring the near wall velocity gradient in the present experiment. This method was used by Andreopoulos (1984) and a review of other techniques for measuring the wall shear stress was given by Winter (1977). This technique relies upon taking velocity measurements within the viscous sublayer ($y^+ < 5$), where the velocity distribution is linear

$$\left. \frac{\partial U}{\partial y} \right|_{y=0} . \qquad (9.2.1)$$

($u^+ = y^+$). By definition:

Thus, the wall shear stress, τ_w, can be determined from the near-wall velocity gradient. This measurement is, in practice, quite difficult due to the interference effect of the wall on the probe (Bruun, 1995). However, the viscous sublayer in the boundary layer used in this study is very thick (> 1mm), enabling many hot-wire measurements to be taken within the linear region. Figure 9.2.1 shows the near wall velocity profile. The 'wall-effect' on the probe does not occur until $y^+ < 3$, in which the probe suffers increased heat loss to the wall and dE/dy changes and becomes negative for $y^+ < 2$. Thus, the near wall gradient could only be calculated in the region $3.5 < y^+ < 5$.

This method also relies upon accurate positioning of the hot-wire probe relative to the wall. Hutchins and Choi (2002), addressed this issue and developed a technique whereby the hot wire is moved to the wall until one of the prongs makes contact with it. A change in voltage gradient (dE/dy) was observed once the contact was made, allowing for computer controlled wall positioning. This method was attempted, but problems were encountered due to the flexible nature of the Mylar dielectric sheet. Inconsistencies were found in the probe positioning routine because the probe deformed the Mylar surface once contact was made. It was also feared that the hot wire was melting the Mylar.

It was decided to initially place the hot wire by eye to within 200μm of the wall. Observing the signal on an oscilloscope then confirmed that the probe was within the wall-effect region (i.e. dE/dy < 0 and $e' \leq 0$, thus $y^+ < 2$; see Fig. 9.2.1). The exact position of the probe was calculated after the experiment by extrapolating the velocity gradient in the viscous sublayer to U = 0 m/s (i.e. at the wall). An iterative procedure was adopted to ensure that the data points

chosen for the linear fit were within the viscous sublayer but out of the wall effect region (i.e. $3.5 < y^+ < 5$). The friction velocity, u^*, and skin-friction coefficient, c_f, were then calculated from the velocity gradient within this region. Thus:

$$u^* = \sqrt{\frac{\tau_w}{\rho}} = \sqrt{\nu \left(\frac{d\overline{U}}{dy}\right)_{y=0}}, \qquad (9.2.2)$$

$$c_f = \frac{\tau_w}{\frac{1}{2}\rho U_\infty^2} = 2\left(\frac{u^*}{U_\infty}\right)^2. \qquad (9.2.3)$$

The friction velocity measured using this near-wall gradient technique was within 5% of the Clauser plot method (Clauser, 1954).

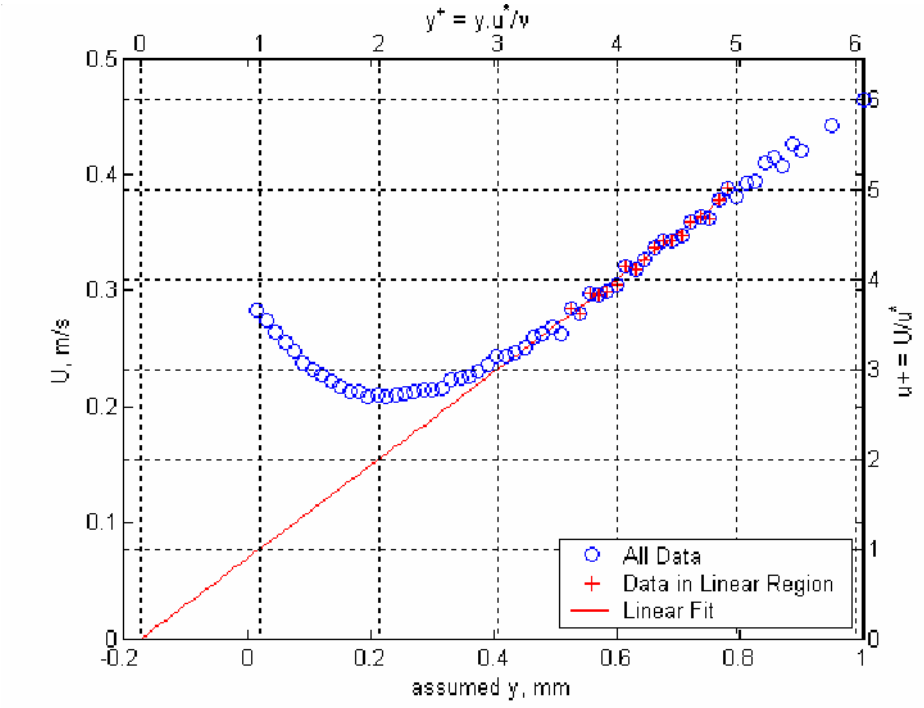

Figure 9.2.1. Near wall velocity profile. Determination of the hot-wire position relative to the wall was achieved by interpolating the mean velocity gradient to U = 0m/s from the region $3.5 < y^+ < 5$. The friction velocity, u^*, and skin-friction coefficient, c_f, were calculated from the slope in this region (Eqs. 9.2.2 and 9.2.3).

A reduction in the near wall velocity gradient thus constitutes a reduction in skin friction drag. The amount of drag reduction was defined such that a positive quantity implies that the drag has been reduced:

$$DR = \frac{c_{f\,canonical} - c_{f\,plasma}}{c_{f\,canonical}}. \qquad (9.2.4)$$

In the above calculations of u^* and c_f, an accurate value of the kinematic viscosity, $\nu = \mu/\rho$, is required. The dynamic viscosity, μ, was obtained from the Sutherland law (White, 1999):

$$\frac{\mu}{\mu_0} = \left(\frac{T}{T_0}\right)^{3/2} \frac{T_0 + S}{T + S}, \qquad (9.2.5)$$

where T_0 = 273K, S = 110.4K (for air), and $\mu_0 = 1.51 \times 10^{-5}$ Ns/m^2. The air density, ρ, was calculated from $\rho = p/RT$, where the molar gas constant, R_{air} = 287 J/kgK, and the air temperature, T, was taken as the mean temperature throughout the linear velocity region ($3.5 < y^+ < 5$).

9.2.2. Outer Scaling

It is found that from experiment to experiment that the calculated value of the boundary layer thickness, δ, differed somewhat despite the flow conditions being as near to identical as possible. Since δ is defined as the distance from the wall at which the local velocity is $0.99U_\infty$ and dU/dy is very small near the edge of the boundary layer, δ is extremely sensitive to the measurement of U_∞. In fact, for the experiments presented in this chapter, the free-stream velocity differed by only 3% between experiments (1.80 ± 0.05m/s). However, the calculated boundary layer thickness varied by around 15% (70 ± 10mm). This

inaccuracy in δ caused problems when outer scaling velocity profiles (i.e. U/U_∞ vs. y/δ). Subsequently, it was decided to normalise the boundary layer profile by the displacement thickness, δ^*, defined as:

$$\delta^* = \int_0^\infty \left(1 - \frac{U}{U_\infty}\right) dy, \qquad (9.2.6)$$

where, for a turbulent boundary layer $\delta^* \approx \delta/8$ (White, 1999). It is to be noted that the ratio, δ^*/δ, does change with Reynolds number for turbulent boundary layers (Clauser, 1956). The following experiments were all conducted at the same Reynolds number and it is thus possible to use δ^* as a substitute for δ. However, because δ^* is calculated by integrating the velocity deficit profile, its value is much more consistent than δ. It was found that δ^* varied by around 5% (11.6 ± 0.6mm) in the experiments; similar to the variation in U_∞.

In the following experiments using surface plasma, we shall see that it was only the inner region of the boundary layer which was affected ($y < 0.4\delta$). Consequently, the boundary layer thickness did not change. However, due to the plasma affecting the mean velocity profiles, the displacement thickness, δ^*, did change. In order to present the results correctly with outer scaling, the boundary layer profile without and with plasma are both normalised with the canonical value of δ^* (i.e. U/U_∞ vs. $y/\delta^*_{canonical}$).

9.3. Thermal Boundary Layer

Measurements of the thermal boundary layer were made with a Dantec 55P31, 1im diameter cold wire probe located 15mm downstream of the plasma region and between two opposing plasma electrodes (c.f. Fig. 8.3.2c). Measurements were taken at 60 wall-normal locations to a maximum height of y = 50mm. The wall-normal measurement locations varied logarithmically with a minimum separation of 0.5mm. At each measurement location, 60s of signal was recorded at 1kHz without plasma. Then a total of 30s of data was taken with plasma, where the plasma was activated in 5s duration bursts, with a 5s gap between each event to minimise thermal damage to the electrode sheet. A 60s pause was included in the automated routine between the last plasma event at one y-location, and the start of data acquisition of the non-plasma condition at the next y-location.

Figure 9.3.1 shows the time-averaged air temperature, AT, throughout the boundary layer without and with plasma. Firstly, one should note that there is a small thermal boundary layer (AT_{max} = 0.5°C) associated with the canonical case. This is due to the residual heat of the electrode sheet after the plasma is activated. The mean thermal boundary layer with plasma shows a maximum air temperature increase of 2.5°C at y = 5mm ($y/5^{*}$ = 0.4, y^{+} = 25). The thermal boundary layer thickness, A, is 32mm. Looking ahead at Fig. 9.4.1, it can be seen that A § 0.45.

The transient development of the thermal boundary layers can be seen in Figs. 9.3.2 and 9.3.3, where the data has been ensemble averaged over each 5s duration plasma burst and time averaged over 0.5s intervals. Mid-interval times are given in the figure. The thermal boundary layer development is

rather rapid, with the majority of the temperature rise occurring within $t^+ <$ 400. After this time, the temperature rises asymptotically and is still increasing towards the end of the plasma forcing period. A maximum temperature of 2.8°C is observed at the end of the 5s duration plasma burst. Note that the location of the maximum temperature remains approximately constant during the development.

The mean temperature profile and the temperature fluctuation profile are non-dimensionalised with 5^*, which are shown in Fig. 9.3.2 and 9.3.4, respectively. A logarithmic horizontal scale has been used to show greater detail for small distances from the wall. Here, 5^* has been calculated from the momentum boundary layer results. It is useful to mention here that the aforementioned figures are plotted on the same scale as will be used to present the velocity profiles in Sec. 9.4.1.

The location of maximum temperature difference closely coincides with the centre of the co-rotating vortices observed in the flow-visualisation pictures of Fig. 8.3.1. The location of the peak temperature fluctuations also appear to correspond to the outer edge of these vortices ($y/5^* = 1$, $y \approx$ 10mm). It will be shown later that this is also the location of maximum w-velocity fluctuations. It appears that a series of co-rotating vortices exist within the boundary layer with characteristics much like the observed behaviour of the vortical structures in initially static air. Since the vortices originate at the plasma, hot fluid is expected to be entrained within, as was observed in Sec. 4.3.5. This leads to the observed maximum in temperature at the location of the vortex cores. Note that the vortices are oscillatory and grow and change location with time. The location of the peak only gives the average vortex core height.

The upwash side of these vortices will act to pump heated air near the wall by the plasma into the outer regions of the boundary layer. Simultaneously, the downwash side of the vortices act to pump cold fluid from the outer region towards the wall. One would subsequently expect large temperature fluctuations at the edge of the vortices as entrained hot and cold fluids intermittently pass over the probe during the oscillatory vortex cycle. This process has lead to the observed peak in temperature fluctuations at $y/\ell^* = 1$ (Fig. 9.3.4).

Figure 9.3.2 shows that the air temperature rise in the near wall region is small ($\Delta T < 1°C$ for $y/\ell^* < 0.06$). This is because the measurement location is downstream of the plasma region, as illustrated in Fig. 9.3.5. A thermal boundary layer develops over the plasma region due to heating near the wall. One would expect the air temperature to increase to a maximum at the wall surface if measurements were taken above the plasma. At the measurement location, however, the wall is at ambient temperature. The mean surface temperature in the plasma region can be estimated by assuming that the thermal boundary layer profile takes the form of a $1/7^{th}$ law ($(T_{wall} - T)/(T_{wall} - T_\infty) = (y/\delta)^{1/7}$). In Fig. 9.3.6, the thermal boundary layer data has been fit to this $1/7^{th}$ law curve for the outer region of the boundary layer (i.e. outside of the vortex region described above, in which the thermal boundary layer is not expected to be canonical). The agreement with the $1/7^{th}$ law in the outer region is reasonable for $y/\delta > 0.5$ ($y/\ell^* > 1.5$), yielding $(T_0 - T_\infty)_{no\ plasma} = 2.9°C$ and $(T_0 - T_\infty)_{plasma} = 12.0°C$.

The absence of near-wall heating at the measurement location is beneficial for the calculation of skin-friction measurement using the near-wall velocity

gradient technique. The momentum boundary layer profile will be corrected for these mean temperature measurements (Fig. 9.3.1). However, the accuracy of this approach relies upon the magnitude of the temperature fluctuations being small. In the near wall region, the RMS temperature fluctuations are less than 0.2°C. The error in the velocity measurement associated with these temperature changes is 1.1%.

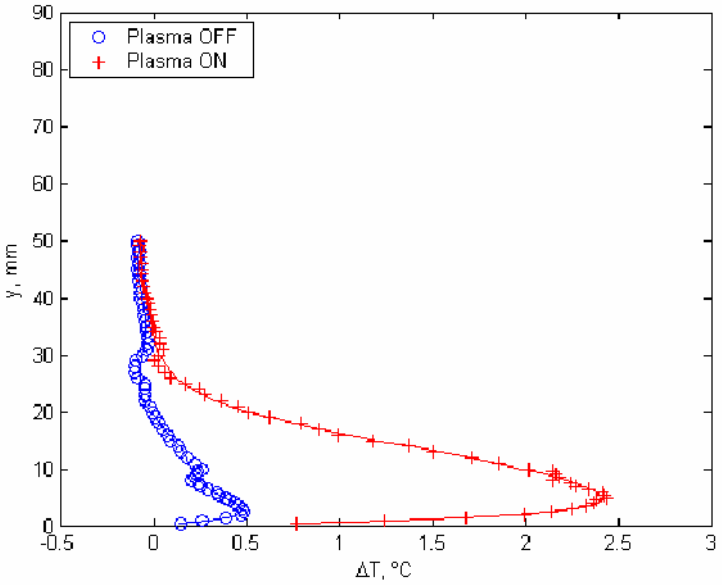

Figure 9.3.1. Mean air temperature profile 15mm downstream of the plasma electrodes without (-), and with (-), spanwise oscillatory plasma forcing. PRF = 38kHz, E_{max} = 3.3kV, PED = 5ms, PEF = 21Hz, U_∞ = 1.8m/s, Re_0 = 900, s = 4mm.

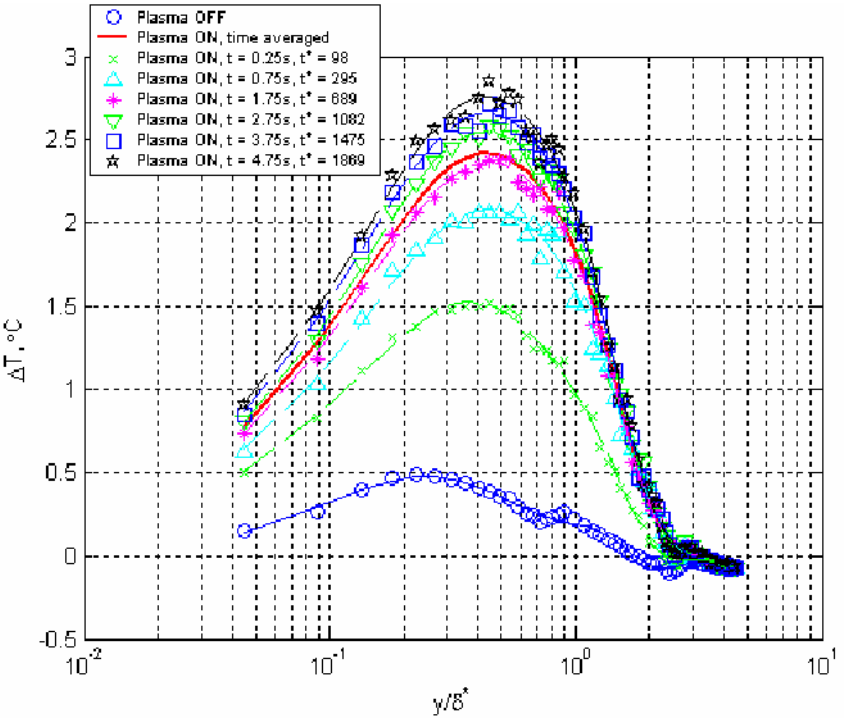

Figure 9.3.2. Air temperature profile with respect to time caused by plasma forcing. Non-dimensionalised with the canonical displacement thickness of Sec. 9.4.1.

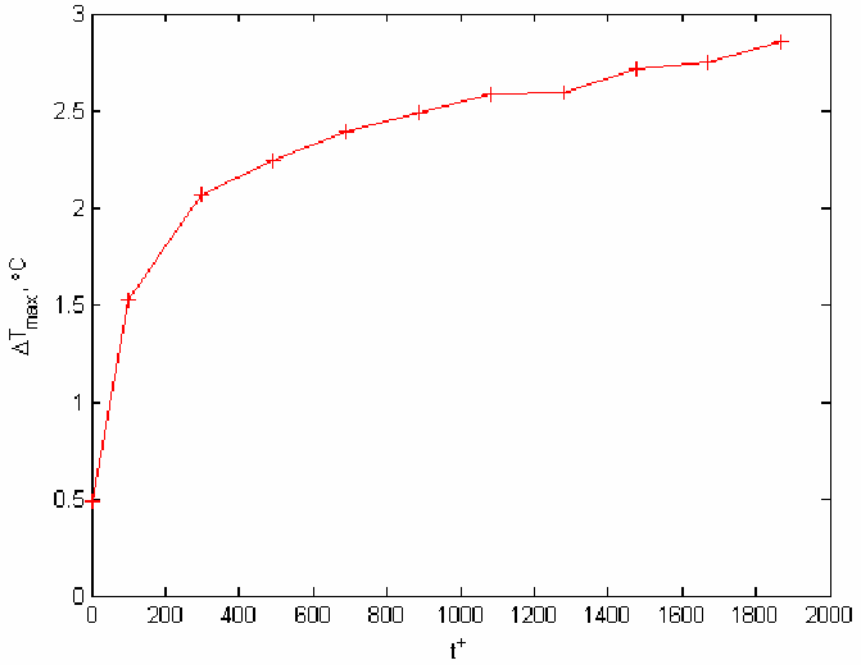

Figure 9.3.3. Maximum temperature difference with respect to non-dimensional time in the thermal boundary layer caused by plasma forcing.

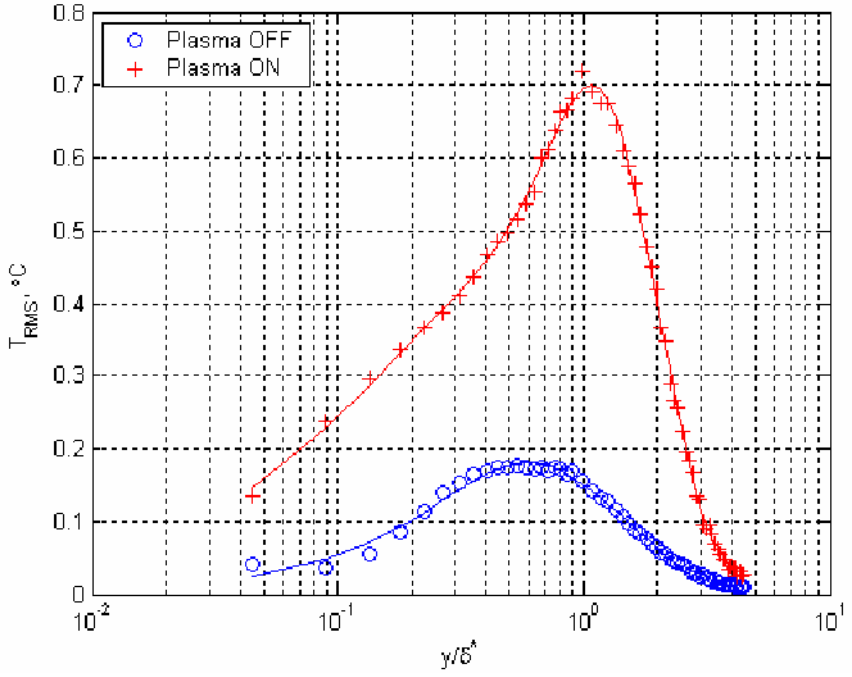

Figure 9.3.4. Temperature fluctuation profile 15mm downstream of the plasma electrodes. Plasma conditions as Fig 9.3.1.

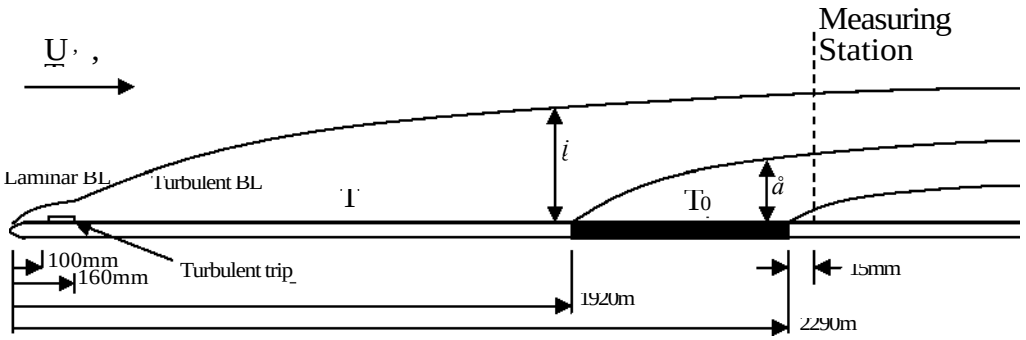

Figure 9.3.5. Momentum boundary layer and thermal boundary layer schematic over the test plate. The thermal boundary layer, δ_t, develops only over the plasma section and is not present in the inner regions of the boundary layer at the measurement location. This ensures small thermal error in the hot-wire measurements in the viscous sublayer.

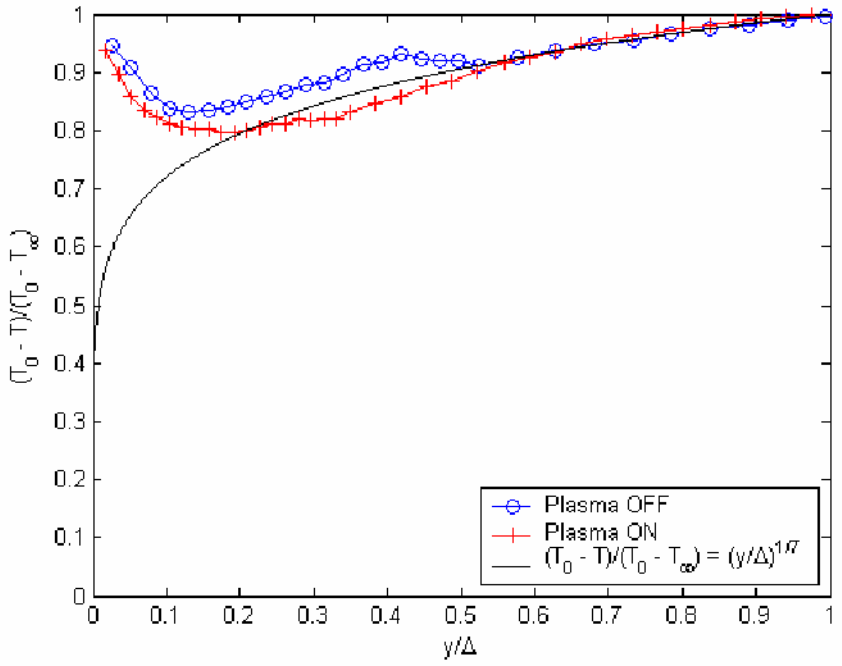

Figure 9.3.6. Non-dimensional thermal boundary layer profile without (-), and with plasma (-). The surface temperature, T_0, has been adjusted such that the profile fits the 1/7th law in the region $y/\delta_t > 0.5$, yielding $(T_0 - T_\infty)_{no\ plasma}$ = 2.9°C and $(T_0 - T_\infty)_{plasma}$ = 12°C.

9.4. Momentum Boundary Layer

9.4.1. *U*-component Velocity

Measurement of the streamwise velocity component were made with a Dantec 55P15, 5pm diameter, boundary layer hot-wire probe located 15mm downstream of the plasma region. Again, data were taken between two opposing plasma actuators (c.f. Fig. 8.3.2c). The probe was operated at an overheat ratio of 1.8 with calibration procedure as described in Sec. 3.4. Measurements were taken at 118 wall normal positions, with 60 of these taken in the first 1.2mm ($y^+ < 7$), with a spacing of 15pm. Measurement positions outside of the viscous sublayer varied logarithmically to a maximum of y = 100mm (1.45).

The hot-wire signal was sampled at 1kHz for 80s without plasma and for a total of 60s with plasma at each measurement location. The plasma was actuated in 5s duration bursts with 5s gap between each such that the thermal damage to the electrode sheet was minimised. A 60s pause was included between successive data acquisitions, as was the case in the cold-wire measurements.

A total boundary layer traverse took around 8hrs to complete and compensation for ambient temperature drift and free-stream velocity was made using the temperature sensor and the free-stream hot wire, respectively. The ambient temperature drift was typically around 1°C and the change in the free-stream velocity was around 0.05m/s. The temperature difference due to the mean thermal boundary layer was added to the ambient temperature measurement (i.e. T(y) = T, + AT(y), AT(y) from Fig. 9.3.1). Calibrations of

the hot-wire probe at different temperatures were then interpolated to give the probe response at each measurement location. Separate corrections were made for the thermal boundary layer with and without plasma.

The mean velocity profile with and without plasma is plotted dimensionally in Fig. 9.4.1. This figure can be directly compared to the thermal boundary layer profile of Fig. 9.3.1. The effect of temperature correction is shown in the figure, and leads to an increase in the mean velocity by up to 10% for $y/5^* > 0.2$. The qualitative results have not been affected.

Figures 9.4.2 shows the outer scaled mean velocity profile with and without plasma forcing. Figures 9.4.3 to 9.4.5 show turbulence statistics, where the turbulence intensity, skewness and kurtosis are shown, respectively. A logarithmic horizontal scale has been used to show greater detail for small distances from the wall.

The mean velocity profile shows a large streamwise velocity deficit in the logarithmic region of the boundary layer (Fig. 9.4.2), extending for $0.1 < y/5^* < 2$ ($6 < y^+ < 110$). Within this region, the mean velocity, U, has been reduced by as much as 40% at $y/5^* \leq 0.5$ ($y^+ \leq 30$). The region of momentum deficit closely corresponds to the thermal boundary layer region, and again, oscillating streamwise vortices are expected to be responsible for this behaviour. A similar behaviour has been observed for streamwise vortices from sub-boundary layer fins (Sandborn, 1981).

The turbulence intensity profile in Fig. 9.4.3 shows that velocity fluctuations, *u'*, have been reduced by as much as 30% for $0.1 < y/5^* < 0.55$ ($6 < y^+ < 30$). This result is similar to drag reducing flows caused by spanwise oscillation (e.g. Choi and Clayton, (2000), Pang et al. (2004), Laadhari et al. (1994), Choi

(1989)). However, the magnitude of the fluctuations has been increased by up to 30% for $0.55 < y/5^{*} < 2.5$ ($30 < y^{+} < 140$) at the same time. This shift indicates that turbulence production has been reduced in the near-wall region yet increased further out, primarily due to the change in mean velocity gradient. The behaviour has some similarity to drag reducing flows caused by vertical blades (Hutchins, 2003).

The skewness and kurtosis in the near wall layer has increased slightly ($y/5^{*} < 0.1$), consistent with the behaviour of Choi (2001) over an oscillating wall. In the velocity deficit region, the skewness and kurtosis are both increased quite dramatically ($0.1 < y/5^{*} < 0.5$, Figs 9.4.4 and 9.4.5), suggesting that the ejection and sweep events have been modified by the plasma. In fact the skewness has changed sign for $0.3 < y/5^{*} < 1$, suggesting that the velocity fluctuations have changed from predominantly large negative fluctuations (i.e. ejection) to large positive fluctuations (i.e. modified sweep events associated with pumping of high speed fluid toward the wall). This will also be supported in the PDFs in Sec. 9.4.3.

Figure 9.4.6 shows the mean velocity profile in the near wall region and Table 9.4.1 gives the measured skin friction with and without plasma. A reduction in near-wall slope is clearly observed with plasma, indicating that the skin-friction coefficient, c_f, has been reduced by 22% by the spanwise oscillatory forcing.

Figures 9.4.7 and 9.4.8 show the inner-scaled mean velocity normalised by the individual friction velocity (i.e. $u^{*}_{canonical}$ and u^{*}_{plasma} accordingly). Various "law of the wall" lines are plotted in Fig. 9.4.8, as suggested by Schlichting (1979), Taylor (1916) and Clauser (1954). Also plotted is the result from the

DNS database of Moser et al. (1999) for turbulent channel flow at $Re_\tau = 395$. For the canonical data, the logarithmic region appears to be offset slightly from the curves of the other authors. There are several reasons for this departure. Firstly, there may be errors in the hot-wire measurements due to the thermal boundary layer and wall positioning, which subsequent affect the calculation of u^*. Secondly, it may be that the boundary layer is not exactly canonical due to wall roughness of electrodes and insulating tape. However, the overall trend of the current velocity profile is very similar to the DNS data of Moser et al. (1999), especially near the wall.

In Fig. 9.4.8, the 22% drag reduction is reflected by the change in the outer boundary layer profile with plasma, showing the increased u^+ at a given y^+. The velocity deficit region caused by the streamwise vortices can be clearly seen for $y^+ > 10$, which have modified the whole of the logarithmic region.

Though the near-wall velocity gradient has been reduced, it is surprising to see that the near-wall velocity magnitude is increased slightly which causes a shift in the virtual origin of the wall (Figs 9.4.6 and 9.4.7). It is believed that the v and w components associated with plasma in the near wall region have caused the apparent increase in measured u-velocity by this single hot-wire probe. Consequently, the probe signal at these locations may be contaminated by the additional velocity components and the measured velocity will increase. It is expected that this is also the reason for the apparent increase in velocity fluctuations in the viscous sublayer. This issue will be further discussed in the two-component velocity measurements with X-wires in Sec. 9.4.2.

	No Plasma	Plasma
dU/dy (s^{-1})	393.63	305.26
u_* (m/s)	0.076578	0.067346
c_f	0.003841	0.002979
0 (mm)	7.86	7.90
δ^* (mm)	11.14	12.78
$H = \delta^*/0$	1.42	1.62
Drag Reduction (%)	-	22.50

Table 9.4.1. Near-wall velocity gradient, skin-friction coefficient, boundary layer integral quantities, and drag reduction with and without spanwise oscillatory plasma forcing. PRF = 38kHz, E_{max} = 3.3kV, PED = 5ms, PEF = 21Hz, U_∞ = 1.8m/s, Re_0 = 900, s = 4mm.

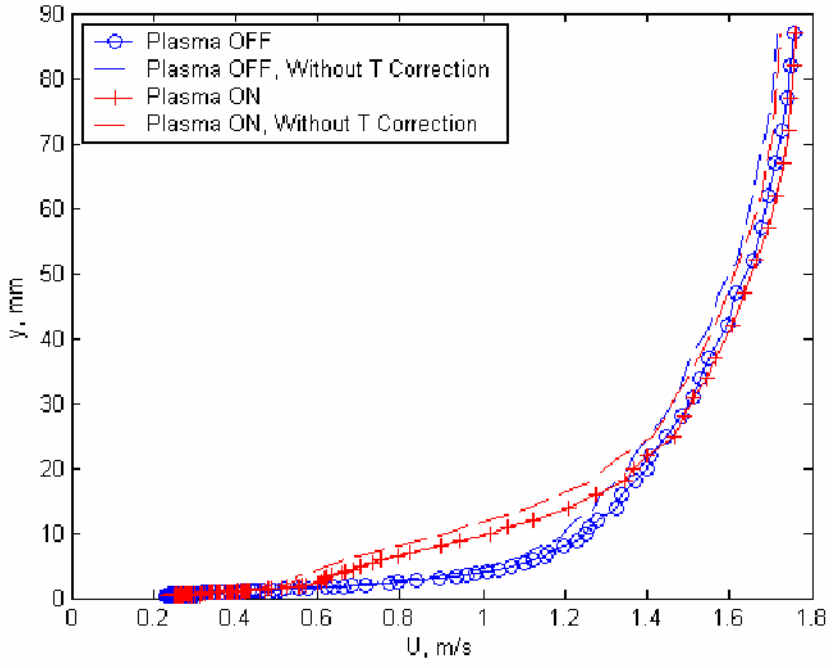

Figure 9.4.1. Mean streamwise velocity profile 15mm downstream of the plasma electrodes showing the effect of temperature correction. Note that the thermal boundary layer primarily affects the region y > 5mm (y^+ > 25).

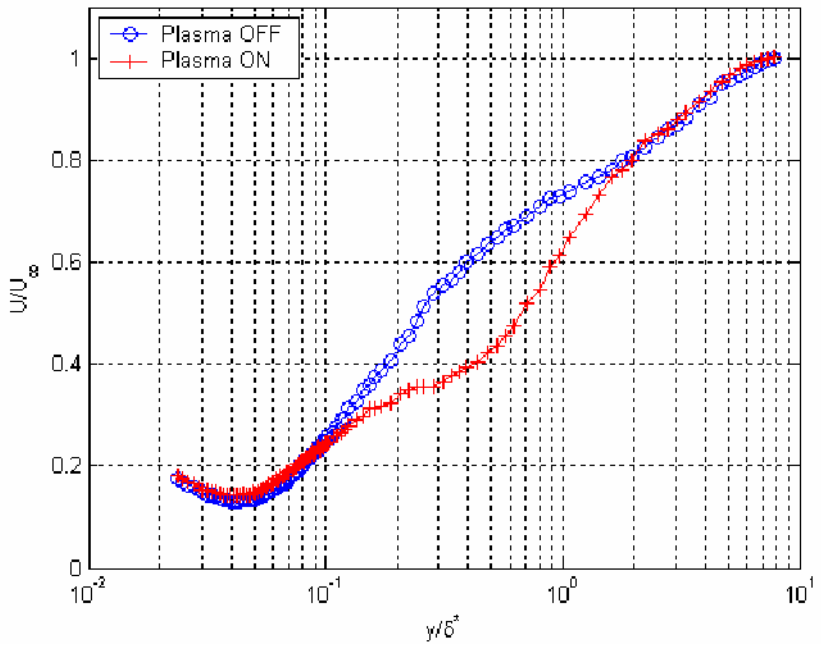

Figure 9.4.2. Mean streamwise velocity profile without (-), and with (-), spanwise oscillatory plasma forcing, corrected for fluid temperature change. PRF = 38kHz, E_{max} = 3.3kV, PED = 5ms, PEF = 21Hz, U_∞ = 1.8m/s, Re_θ = 900, s = 4mm.

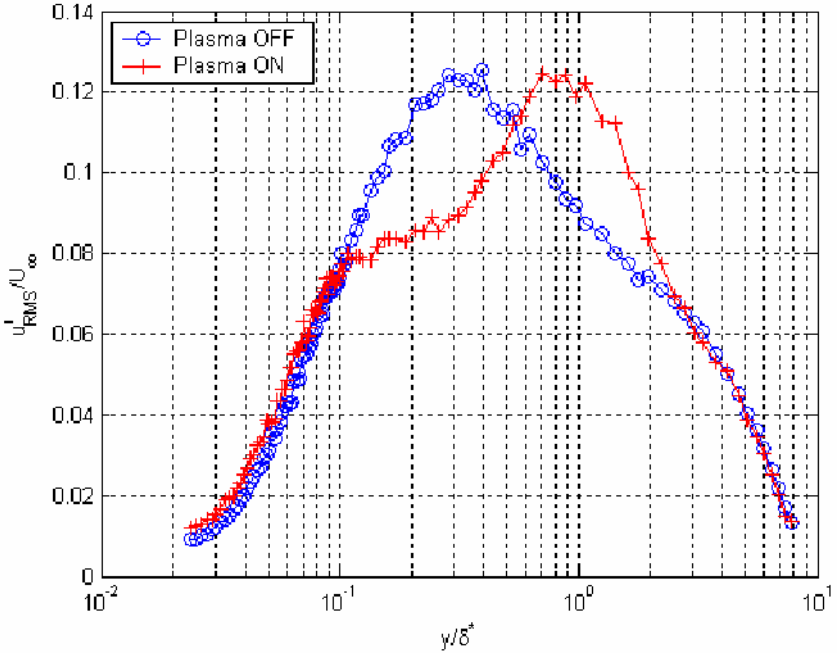

Figure 9.4.3. Turbulent intensity profile without (-), and with (-), spanwise oscillatory plasma forcing, corrected for fluid temperature change. Plasma conditions as Fig 9.4.2.

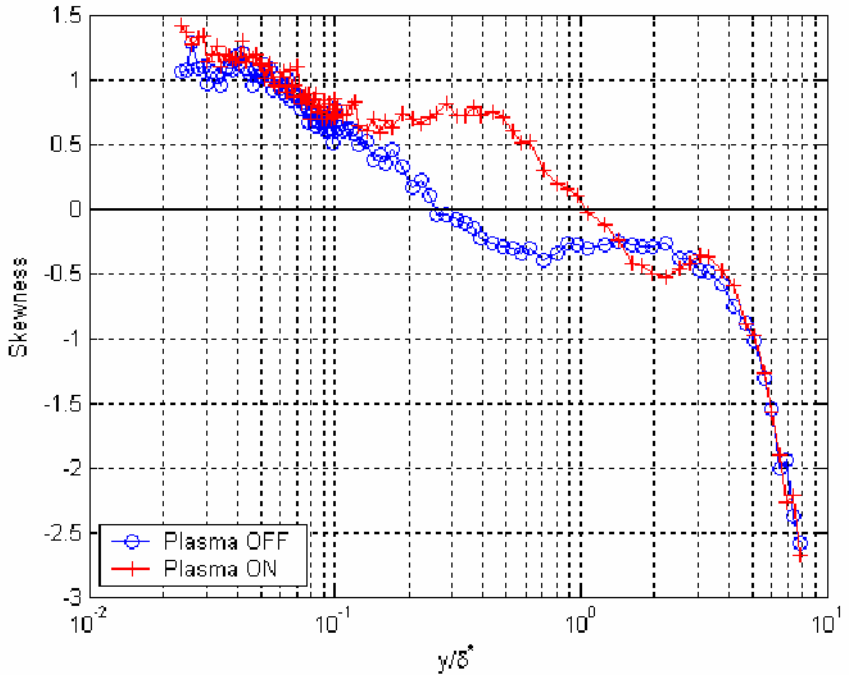

Figure 9.4.4. Skewness profile without (-), and with (-), spanwise oscillatory plasma forcing, corrected for fluid temperature change. Plasma conditions as Fig 9.4.2.

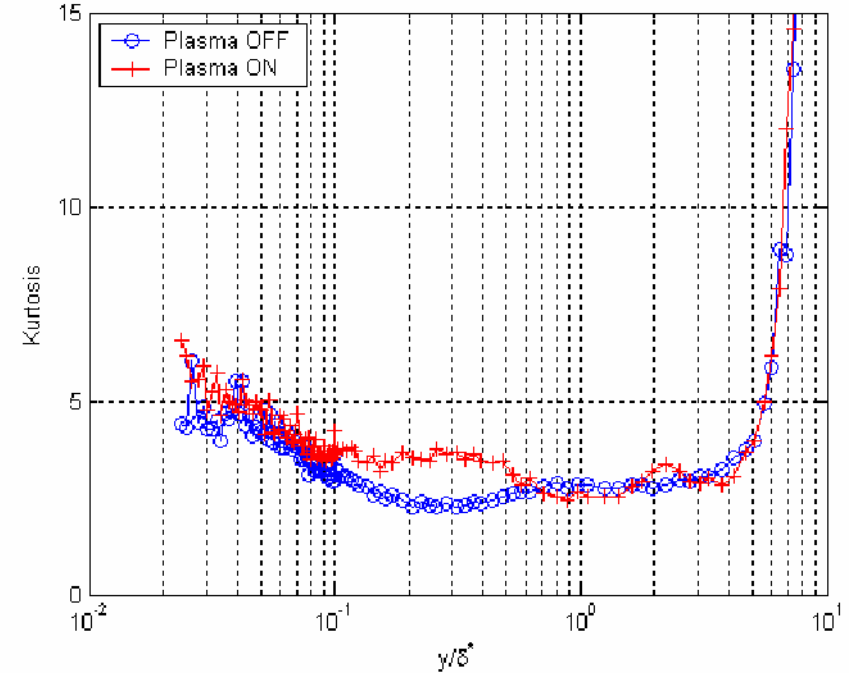

Figure 9.4.5. Kurtosis profile without (-), and with (-), spanwise oscillatory plasma forcing, corrected for fluid temperature change. Plasma conditions as Fig 9.4.2.

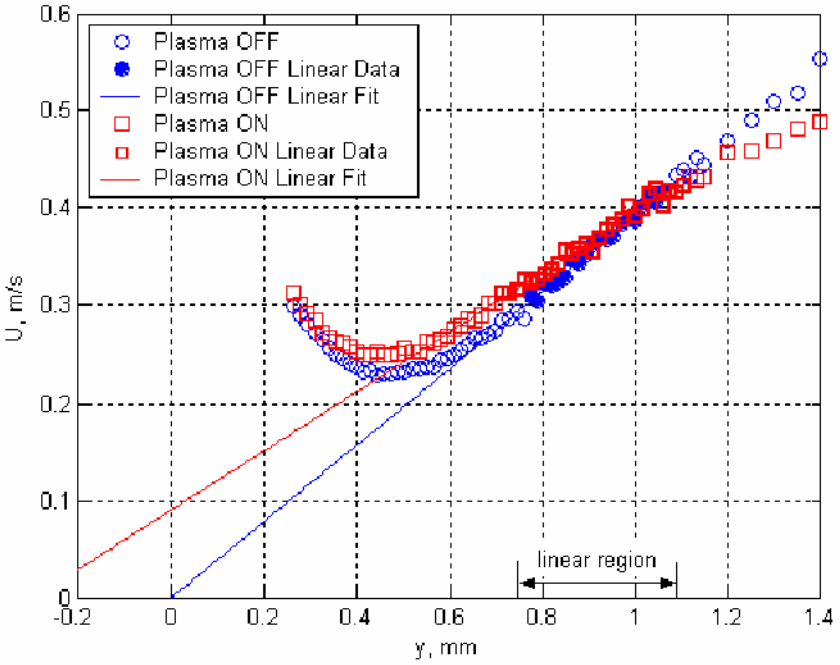

Figure 9.4.6. Near-wall velocity gradient and skin friction without (-), and with plasma (-). Plasma conditions as Fig 9.4.2.

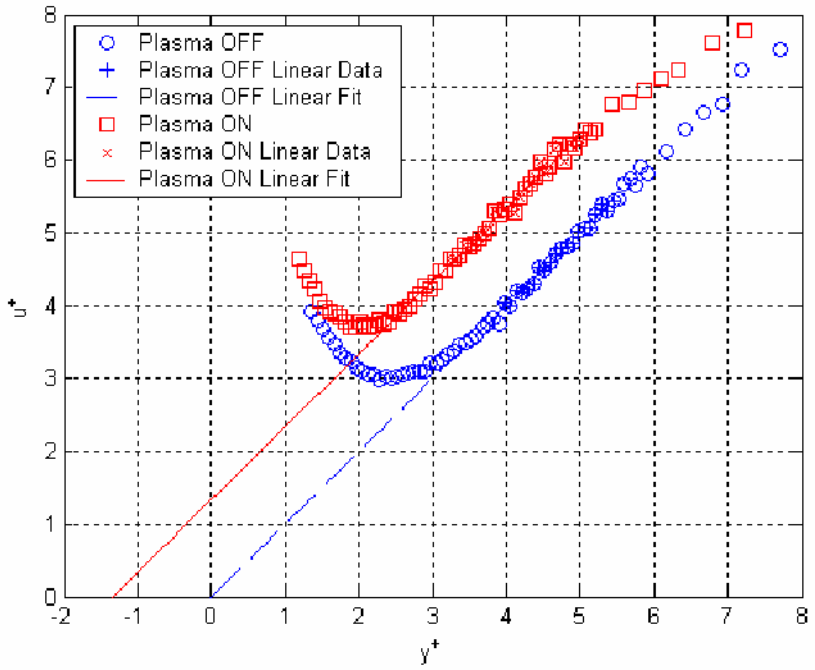

Figure 9.4.7. Inner scaled near-wall velocity profile without (-), and with plasma (-). Plasma conditions as Fig 9.4.2.

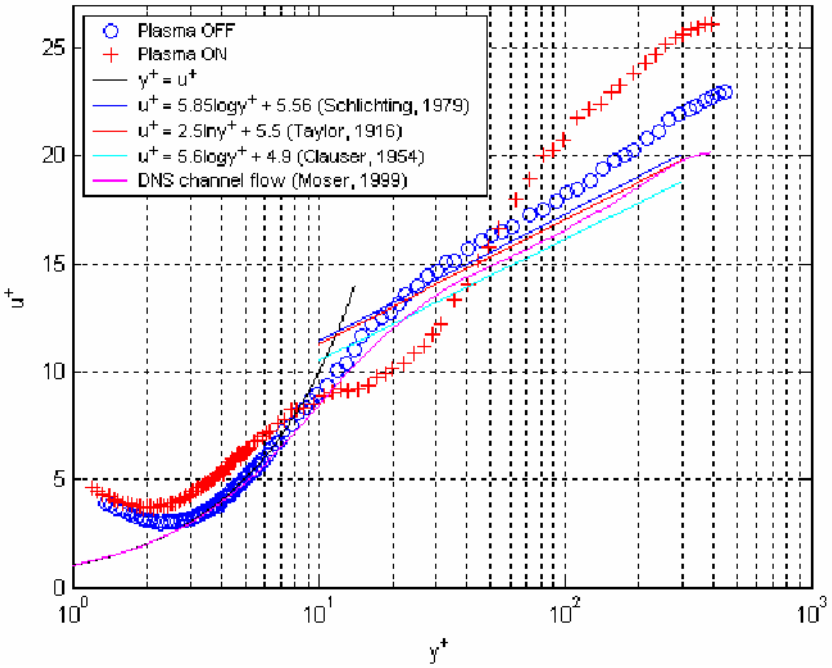

Figure 9.4.8. Inner scaled mean velocity profile without (-), and with (-), spanwise oscillatory plasma forcing, 15mm downstream of the plasma electrodes. Plasma conditions as Fig 9.4.2.

9.4.2. *UV* and *UW* Component Measurements

Sub-miniature X-wire probes were also used to take measurements of U, V and W in the turbulent boundary layer. The probes were specially manufactured by Dantec for near wall measurements and each uses a pair of 2.5μm diameter, 1.5mm long gold-plated platinum wires with an etched length of 0.5mm at the centre (i.e. sensing length = 0.5mm). The wires were separated by a 0.5mm gap such that the volume occupied by the sensing elements is 0.5 x 0.5mm (~2.5 x $2.5l^+$). Both probes were operated at an overheat ratio of 1.5 to reduce thermal cross talk.

The two probe types are shown in Fig. 9.4.9. The UV-type wire of Fig. 9.4.9a/b has two wire elements located in the x-y plane, with separation in the z direction. The wires are inclined at 90° to each other such that simultaneous measurements of U and V components of velocity can be made. In order to allow the UV probe to be traversed to the wall, the probe holder was rotated by 3° about the z axis. As a result, the wires of the array are inclined at +48° and -42° to the streamwise direction. For the UW-type wire in Fig. 9.4.9c/d, the wire elements are located in the x-z plane, with separation in the y direction. Here, the individual wires are located at ±45° to the streamwise direction and simultaneous measurements of U and W are possible. Both of the UV-type and UW-type probes had 'swan-neck' prongs to allow measurement close to the wall, similar to the boundary layer probe used to measure U.

Decomposing the resulting hot-wire signals into velocity component (U and V, or U and W) has been described by many authors including Bruun (1995), Bradshaw (1971), Perry (1982) and Champagne et al. (1967), with many other references within. Here, we adopt the cosine law for simplicity. For the UV

probe, a slightly modified cosine law is used to incorporate the 3° rotation to allow measurement close to the wall. The decomposition is illustrated in Fig 9.4.10.

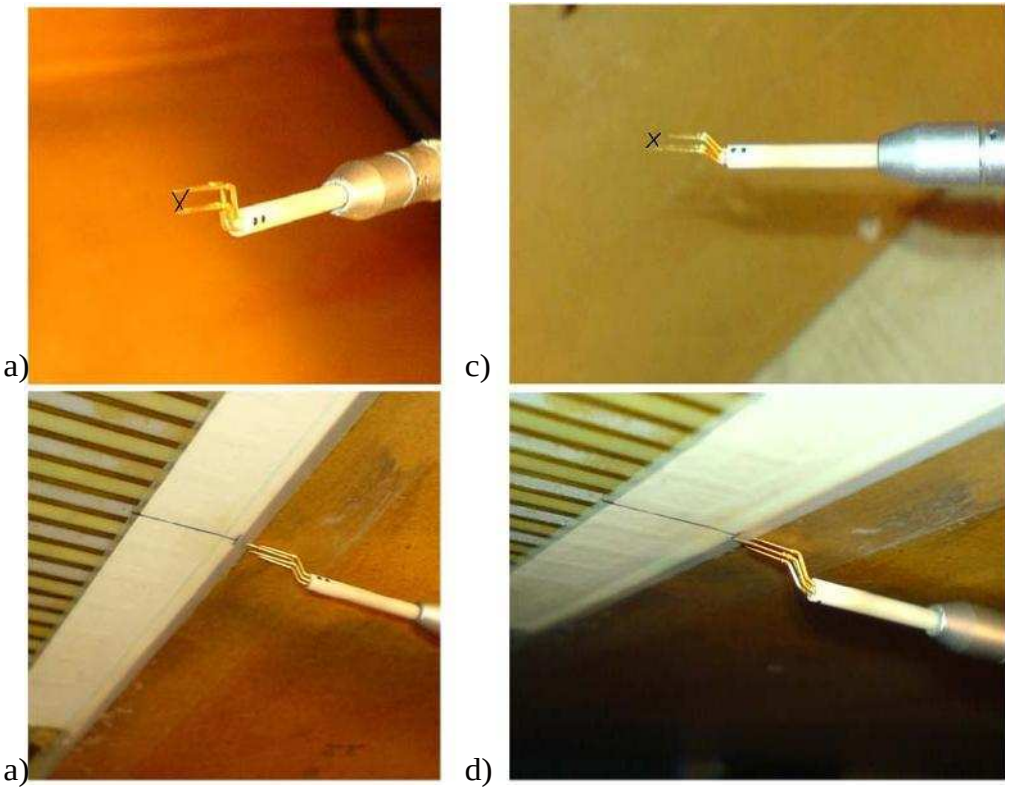

Figure 9.4.9. Sub-miniature X-wire probes used for UV and UW boundary layer measurements. a) and b) UV probe, side view and near wall, respectively. c) and d) UW probe, top view and near wall, respectively. Black lines indicate the wires and flow is from left to right in all images.

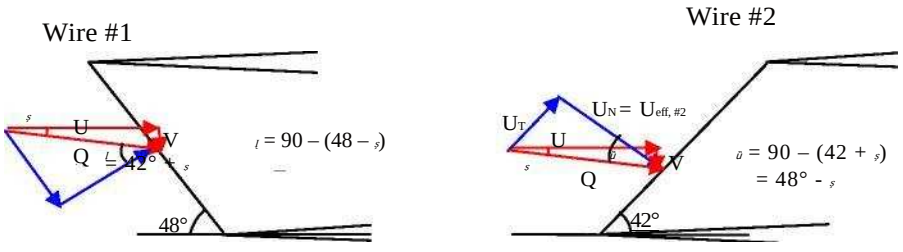

Figure 9.4.10. Decomposition of UV wire velocity components.

The 'effective' velocity, U_{eff}, sensed by the wires is assumed to be the normal component of velocity, U_N, which is related to the flow angle, 0, through:

$$U_{eff,\#1} = \cos(42^\circ)\,U + \sin(42^\circ)\,V$$

$$U_{eff,\#2} = \cos(48^\circ)\,U - \sin(48^\circ)\,V \qquad (9.4.1)$$

Here, 0 is assumed to be small ($\cos(0) \approx 1$, $\sin(0) \approx \tan(0) \approx V/U$, $V^2/U^2 \approx 0$), which assumes small turbulence intensities, and the trigonometric identity, $\cos(a + b) = \cos(a).\cos(b) - \sin(a).\sin(b)$, has been used. Rearranging Eq. 9.4.1 yields:

$$U = \frac{\sin(48^\circ)\,U_{eff,\#1} + \sin(42^\circ)\,U_{eff,\#2}}{\cos(42^\circ)\sin(48^\circ) + \cos(48^\circ)\sin(42^\circ)}$$

$$V = \frac{\cos(42^\circ)\,U_{eff,\#1} - \cos(48^\circ)\,U_{eff,\#2}}{\cos(42^\circ)\sin(48^\circ) + \cos(48^\circ)\sin(42^\circ)} \qquad (9.4.2)$$

For the UW wire, where the $U = \frac{1}{\sqrt{2}}$ wires make an angle of 45° to the mean flow $W = \frac{1}{\sqrt{2}}$ direction, the decomposition is simply:

$$U = \frac{1}{\sqrt{2}}\left(U_{eff,\#1} + U_{eff,\#2}\right)$$

$$W = \frac{1}{\sqrt{2}}\left(U_{eff,\#1} - U_{eff,\#2}\right) \qquad (9.4.3)$$

Calibration of the X-wires was performed in situ, with the wire support prongs located in the mean flow direction. The wires were placed in the free-stream and decomposed into the component of velocity normal to each wire as shown above. The hot-wire output voltage, E, was then related to the effective velocity, U_{eff}, using a 4th order polynomial. Calibrations were performed

before and after the experiments and at a range of temperatures. To check the

validity of the cosine law, calibrations were also performed with each wire normal to the incident flow (i.e. rotated ±45°). The curves obtained were within 0.06m/s across the entire calibration range ($0 < U_\infty < 4$m/s) of those obtained by the cosine law, but are considered less accurate due to the uncertainty in the rotation angle. This also required the probe position to be changed between calibration and experiment, adding further uncertainty in the results.

Figure 9.4.11 shows the mean velocity profile of the turbulent boundary layer measured with a single hot-wire probe, the UV-wire probe and the UW-wire probe. All of the results are corrected for the mean thermal boundary layer with and without the plasma, as described in Sec. 9.4.1. Outer scaling has been applied with the canonical displacement thickness, δ^*. The measurement of the mean streamwise velocity component, U, was in reasonable agreement between all three hot wires. The mean wall-normal, V, and spanwise, W, velocity components were nearly zero ($V, W < 0.025U_\infty$), as expected.

Figure 9.4.12 shows the fluctuating streamwise velocity component measured with the three probes. There is qualitative agreement between the single wire and X-wire measurements, and agreement is especially good for the UW wire. For the plasma off case, the difference between the three measurement techniques is within 15% at $y/\delta^* = 0.2$ (i.e. position of maximum difference between results). The qualitative and quantitative agreement suggests that the X-wires measurements are valid, at least for the streamwise velocity component.

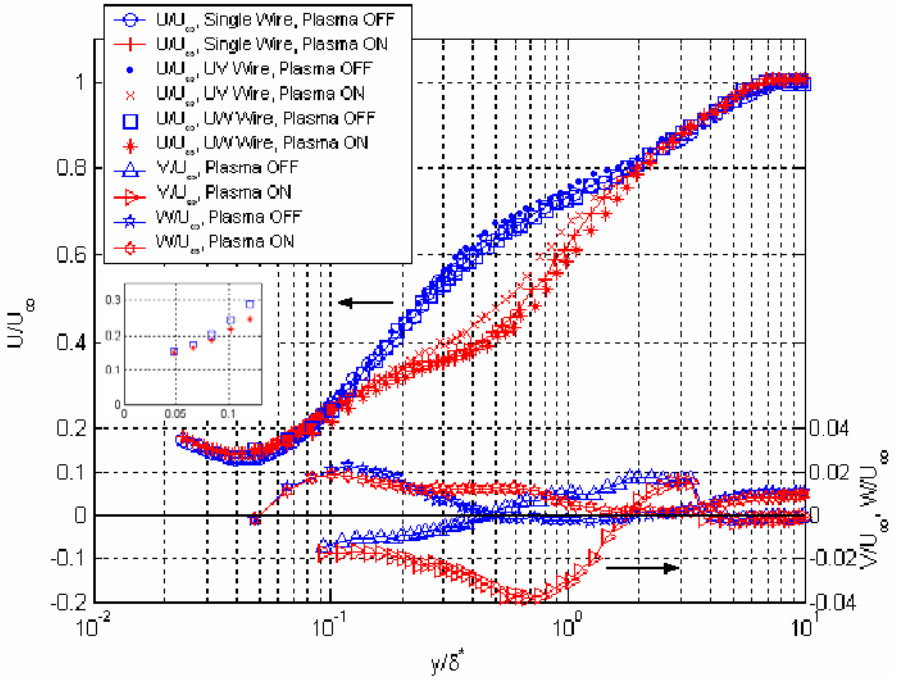

Figure 9.4.11. Mean streamwise velocity profile of the turbulent boundary layer as measured with a single (U) wire, UV X-wire and UW X-wire without (-) and with plasma (-). All results corrected for fluid temperature change. Insert shows UW X-wire result in near wall region on linear axis.

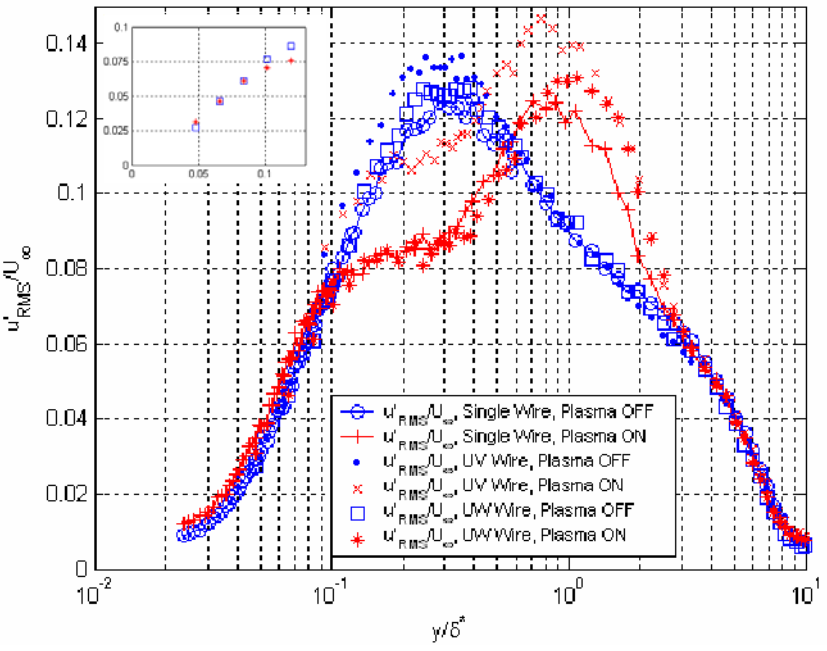

Figure 9.4.12. Streamwise velocity fluctuation profile of the turbulent boundary layer without (-) and with plasma (-) using the single wire and X-wires. Insert shows UW X-wire result in near wall region.

Figure 9.4.13 shows the inner scaled mean velocity, velocity fluctuation and Reynolds stress distribution for the turbulent boundary layer without plasma forcing. The associated distribution with plasma is given in Fig. 9.4.16. The normal and shear stresses have been multiplied by 2 and 10, respectively to ease viewing on the scale. Also plotted in Fig. 9.4.13 is the DNS data of Moser et al. (1999) for comparison to the canonical data. The Reynolds numbers of the two studies are nearly identical ($Re_{\tau,DNS}$ = 395, $Re_{\tau,exp}$ = 380), although the DNS study is for channel flow, such that differences in the outer region are expected. There is good agreement between the two data sets which gives confidence in the measurement of all three velocity components. Qualitatively, the behaviour of all velocity components, fluctuations and Reynolds stresses is similar. There is some quantitative discrepancy between the results, especially for the Reynolds stresses in the inner regions of the boundary layer ($y^+ < 50$). These differences are largely caused by spatial resolution errors, particularly in the near wall region where the velocity gradients are high (see Bruun, 1995).

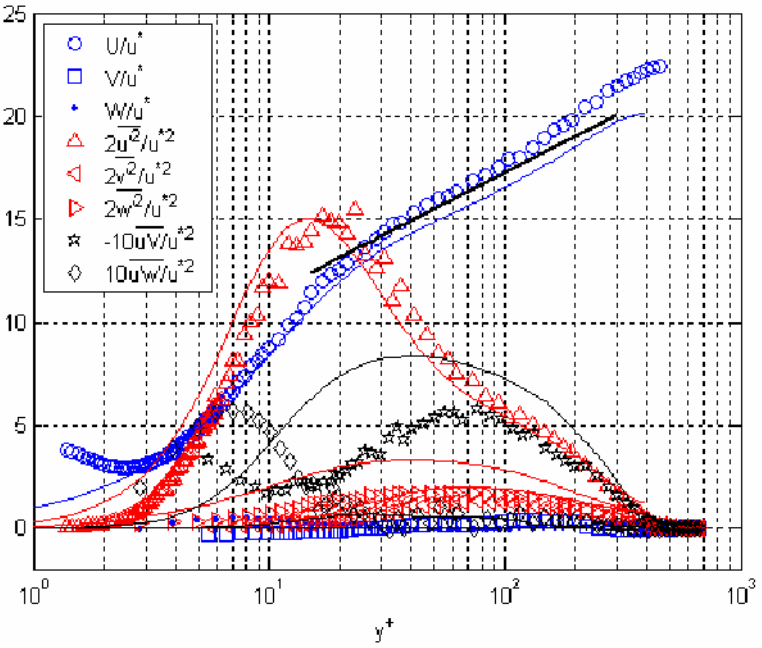

Figure 9.4.13. Inner scaled mean velocity (-), normal stress (-) and shear stress (-) distribution in the turbulent boundary layer without plasma forcing. Hot-wire data at $Re_\tau = u^* \delta / \nu = 380$ (symbols), DNS data of Moser et al. (1999) for turbulent channel flow at $Re_\tau = 395$ (lines), and log law $u^+ = 5.85 \log y^+ + 5.56$ from Schlichting (1979), (thick line).

Figure 9.4.14 shows the outer scaled turbulent intensity profile with and without plasma forcing, and Fig. 9.4.15 shows the associated Reynolds stresses. Figure 9.4.14 shows that the plasma increases the wall normal and spanwise fluctuation significantly for $y/\delta^* < 2$. The wall-normal velocity fluctuations, *v'*, are increased by around 80% throughout the region while the spanwise fluctuations, *w'*, are increased by around 30%. It seems likely that such increases will extend right into the viscous sublayer. It is therefore expected that the increase in U in the viscous layer with plasma (c.f. Fig. 9.4.6), is a result of non-streamwise velocity component contamination of the single-wire probe. Such contamination can only act to increase the measured

velocity since the hot wire is sensitive to velocity magnitude, not direction. Provided that sampling times are long and the magnitudes of fluctuations do not change significantly between $3.5 < y^+ < 5$ ($0.061 < y/\delta^* < 0.087$), the contamination will not affect the mean velocity gradient and the corresponding skin-fiction measurement. If anything, the contamination by *v'* and *w'* becomes worse as one moves away from the wall (c.f. Fig. 9.4.14), so that the velocity gradient is expected to be even lower than measured. Thus, the drag reduction caused by plasma is likely to be greater than 22%. The inserts in Figures 9.4.11 and 12 support this conclusion since U and *u'* with plasma were not increased near the wall when measured with the UW-type probe.

Interestingly, Fig. 9.4.11 shows that the plasma action has caused V to become negative. Thus, between opposing plasma electrodes, there is a tendency for motion towards the wall. This was also observed in the flow visualisation in still air (Fig. 9.3.1), whereby for certain stages of the oscillation cycle, fluid was entrained from above the plasma region to replace that ejected laterally.

With reference to Figs. 9.4.14, 9.4.15 and 9.4.17, it can be seen that the plasma increases *v'* and *w'*. The peak in *v'* occurs at $y/\delta^* = 0.5$, while *w'* has two peaks, occurring at $y/\delta^* = 0.35$ and 1.05. One can interpret these locations as the bottom, centre and top of the plasma induced streamwise vortices. Note that the peak in *v'* also occurs at the position at which *u'* changes from a decrease to an increase (i.e. $\delta u' = u'_{\text{plasma}} - u'_{canonical}$ changes sign), and the peaks of *w'* correspond to maximum and minimum $\delta u'$ (see Fig. 9.4.17). Thus the vortex motion acts to reduce *u'* below the vortex core and increase it above. Also note that the total turbulence intensity is reduced below the vortex cores, as shown in Fig. 9.4.16. At the upper extreme of the vortex, the velocity

fluctuations are increased as low-speed fluid entrained within the vortices moves periodically past the stationary probe. The magnitude of the Reynolds stresses, $u'v'$ and $u'w'$, are shown in Fig. 9.4.15. These are both increased, particularly across the streamwise vortices. This increase in the Reynolds stress seems to contradict the observed drag reduction, although the error in these measurements will increase as the X-wires probes are moved towards the wall.

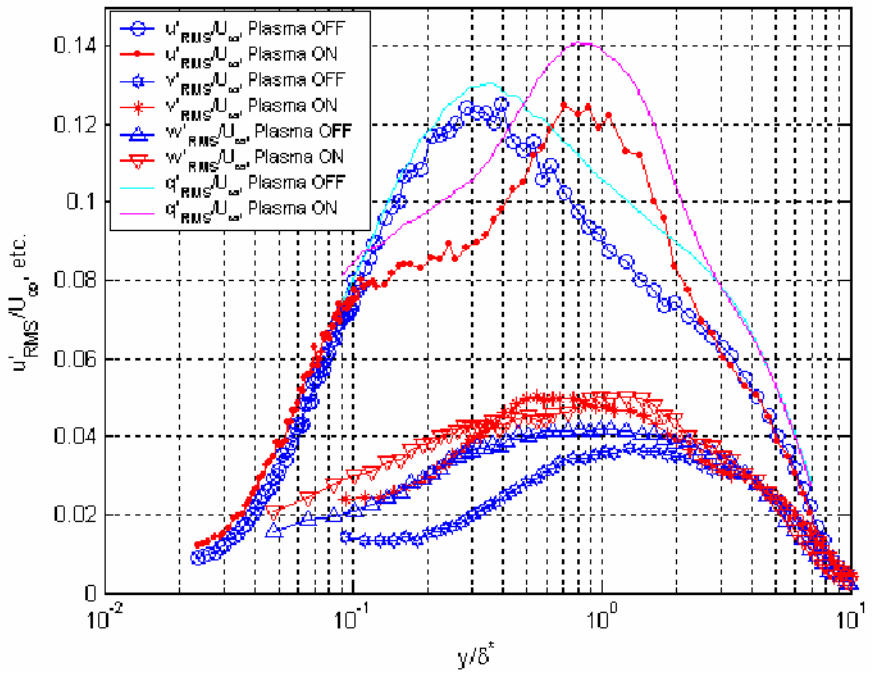

Figure 9.4.14. Turbulent intensity profile in the turbulent boundary layer without (-, -) and with (-, -) plasma. Total intensity, $q'_{RMS} = (u'^2 + v'^2 + w'^2)^{1/2}$.

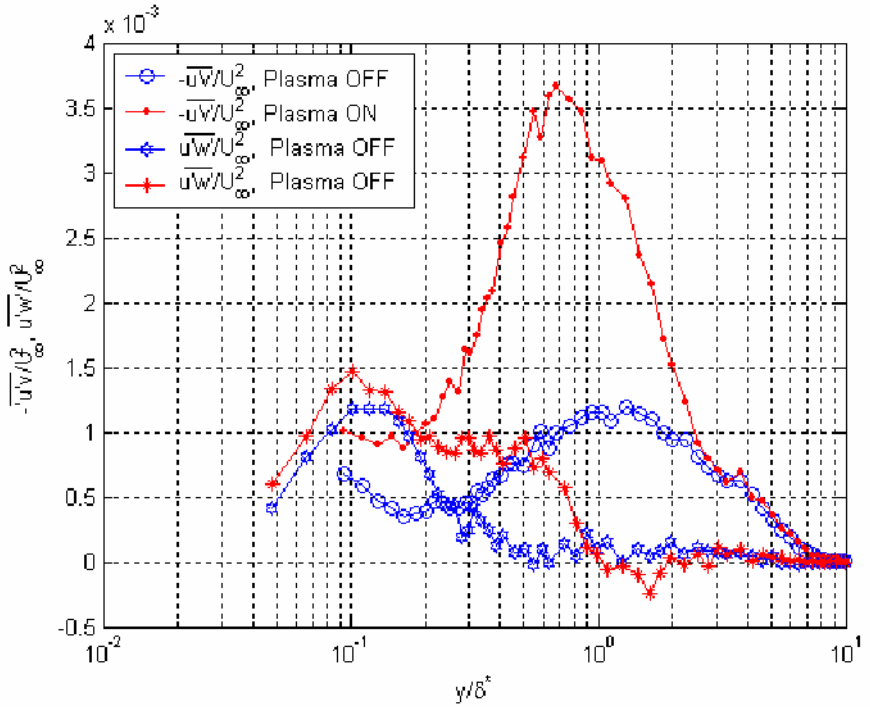

Figure 9.4.15. Reynolds Stress profile in the turbulent boundary layer without (-) and with plasma (-). Plasma forcing as Fig. 9.4.2.

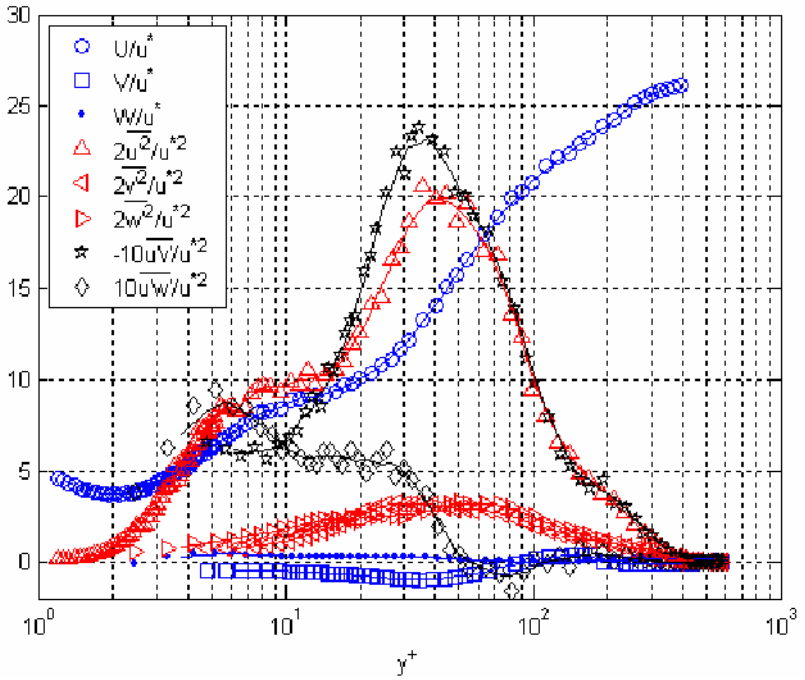

Figure 9.4.16. Inner scaled mean velocity (-), normal stress (-) and shear stress (-) distribution in the turbulent boundary layer with plasma forcing. For comparison to Fig. 9.4.13.

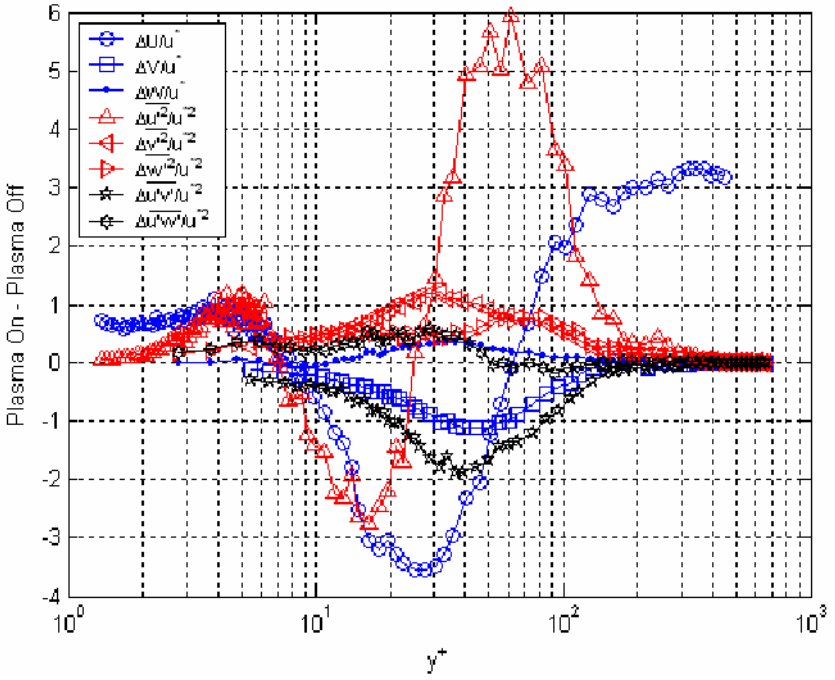

Figure 9.4.17. Absolute change in the mean velocity, normal stresses and shear stresses in the turbulent boundary layer caused by plasma.

9.4.3. Energy Spectra and Probability Distribution Function

So far, our attention has been focused on the changes in the boundary layer profiles with plasma. In order to gain a deeper understanding of how the plasma alters the turbulence structure, the following section will centre on a few key spatial positions in the boundary layer. With reference to Figs. 9.4.17, 9.3.2 and 9.3.4, analysis has been performed at y^+ = 5, 20, 30 and 60 (y/δ^* = 0.09, 0.35, 0.5, and 1.05, respectively). The first position (y^+ = 5) marks the edge of the viscous sublayer. The second position (y^+ = 20) marks the location of the first peak in spanwise fluctuations, *w'*, which is possibly the lower extent of the plasma-induced streamwise vortices due to spanwise induced vortex motions. The third position (y^+ = 30) is the location of maximum temperature change, δT, and maximum wall-normal fluctuations, *v'*. This is possibly the position of the average height of the plasma-induced vortex cores due to the hot, low-momentum fluid entrained within and due to wall-normal induced vortex motions to either sides of the core. The final position (y^+ = 60) is the location of the second peak in *w'* and maximum temperature fluctuations, *T'*. This is possibly the upper extent of the plasma-induced streamwise vortices due to spanwise induced vortex motions and the intermittent passage of these vortices past the probe. Table 9.4.2 summarises these key locations. In this section, the probability density function (PDF) and energy spectra with and without plasma will be presented at each location. VITA analysis of the 'sweep' events will be performed at these locations in Secs 9.4.4 and 9.4.5.

y^+	y/δ^*	U	V	W	T (°C)	u	v	w	uv	uw
5	0.09	2% 0.005	n/a	-	n/a% 1.25	5% 0.005	n/a	40% 0.009	n/a	n/a% 0.0003
20	0.35	35% 0.2	n/a% 0.02	n/a% 0.010	n/a% 2.4	20% 0.025	90% 0.020	15% 0.006	200% 0.0015	n/a% 0.0007
30	0.50	35% 0.22	n/a% 0.04	n/a% 0.015	n/a% 2.4	5% 0.005	75% 0.022	10% 0.005	300% 0.0025	n/a% 0.0008
60	1.05	5% 0.02	n/a% 0.02	n/a% 0.005	n/a% 1.0	30% 0.025	20% 0.01	20% 0.008	100% 0.0011	n/a% 0.0003
> 200	> 3.5	-	-	-	-	-	-	-	-	-

Table 9.4.2. Change in mean velocity and temperature, normal stresses and shear stresses due to oscillatory spanwise plasma forcing in a turbulent boundary layer. Percentages give change due to plasma at each spatial location. Numbers give maximum absolute change with respect to U and U. Note *w'*, *v'*, and the Reynolds stresses contain large errors near the wall.

Figure 9.4.18 shows the energy spectra at these locations which are normalised such that the integral over the entire frequency will give the mean square value of u-component velocity (i.e. u-component kinetic energy). The spectra show that in the near wall region, there is a transfer of energy from large scale eddies to small scale eddies (Figs. 9.4.18a-c). This is especially evident at y^+ = 20 (Figs. 9.4.18b), where the energy contained in the large scale structures (low frequency) is significantly reduced, whilst the energy contained in small scale structures (high frequency) is increased. Thus, the plasma appears to be breaking down the large scale turbulence structures near the wall. At y^+ = 60 (Fig. 9.4.18d), there is higher energy across the full range of frequency reflecting the increased velocity fluctuations. There does not appear to be a shift in the spectra shape.

A spectral peak at the oscillation frequency (10.5Hz), and harmonics thereof, can be seen in the high frequency end of all of the spectra with plasma. Sharp spectral peaks occur from 222Hz and every 10.5Hz thereafter, suggesting that a structure that extends to at least $y^+ = 60$ may be present in the flow. Presumably, the background turbulence has masked the spectral peaks at the lower end of the spectrum.

The probability density functions (PDF) of the u-component velocity fluctuations are shown in Fig. 9.4.19, where the fluctuations have been normalized by their own standard deviation. In the viscous sublayer (Fig. 9.4.19a), the PDF shows a slight positive skewing and narrowing, reflecting an increase in skewness and kurtosis. This behaviour has also been observed in other drag reducing flows (Choi, 2001). Below the plasma-induced vortex cores (Fig. 9.4.19b and c), the plasma maintains a PDF with similar characteristics to that in the canonical viscous sublayer until $y^+ \lesssim 30$. The PDFs at these locations are 'mirrored' relative to the canonical case at the same location, suggesting that the velocity fluctuations have changed to more positive, spikey, excursions of fluid (i.e. modified sweep events). This is also reflected in the increased skewness and kurtosis at these locations (see Figs. 9.4.4 and 9.4.5). These are likely to be associated with the wallward induction of the plasma-induced streamwise vortices. Note, however, that the magnitude of the fluctuations are reduced in this region (by around 20% at $y^+ = 20$, see Fig. 9.4.14), such that these turbulent events are less violent. At $y^+ = 60$ (Fig. 9.4.19d), the PDF has become roughly symmetric. Note that the magnitude of *u'* has, however, increased at this location.

a)

b)

d)

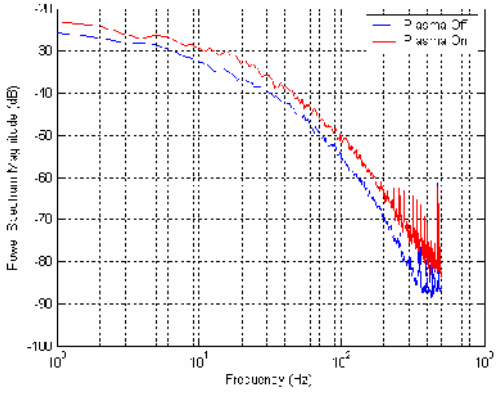
Plasma Off
Plasma On
Power Spectrum Magnitude (dB)
Frequency (Hz)

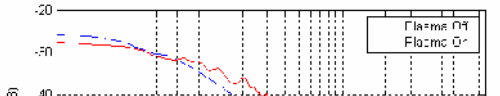
Plasma Off
Plasma On

d) Figure 9.4.18. Energy spectra of *u'* without (-) and with (-) plasma in the turbulent boundary layer at: a) $y^+ = 5$; b) $y^+ = 20$; c) $y^+ = 30$; d) $y^+ = 60$.

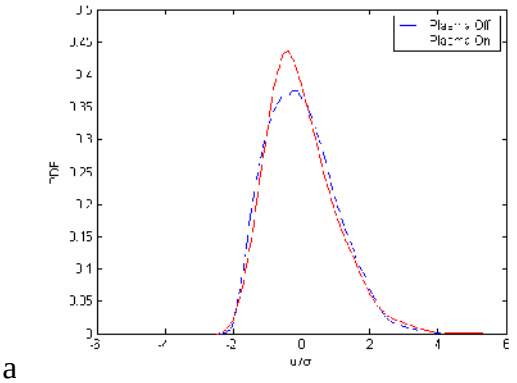

a

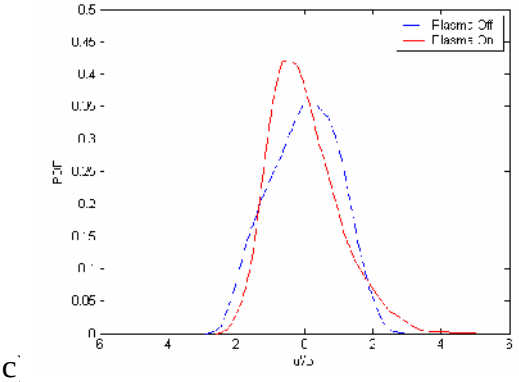

c

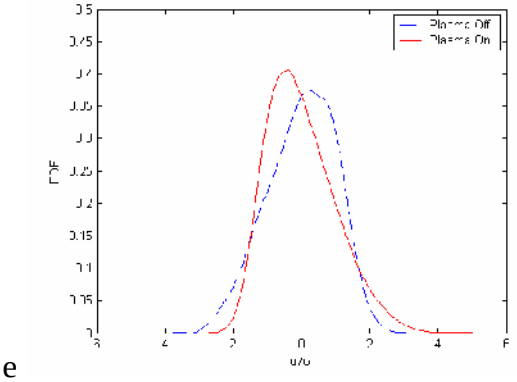

e

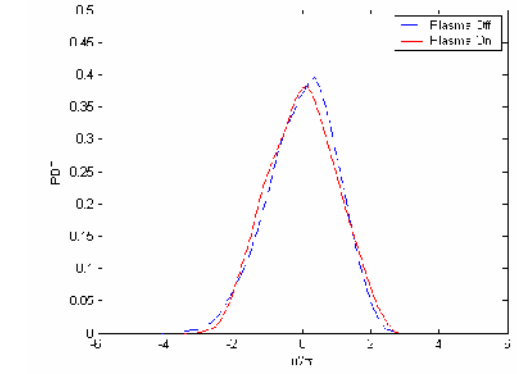

g

Figure 9.4.19. Probability Density Function of *u'* without (--) and with (-) plasma in the turbulent boundary layer at: a) $y^+ = 5$; b) $y^+ = 20$; c) $y^+ = 30$; d) $y^+ = 60$.

9.4.4. Conditional Sampling – VITA Analysis

Variable Interval Time Averaging (VITA) is a conditional sampling technique developed in order to detect coherent turbulent structures. The technique was first used by Blackwelder and Kaplan (1976) to detect burst events in the near wall region of turbulent boundary layers. A review of this and other conditional sampling techniques is given by Antonia (1981). The technique essentially scans a small temporal window of length T_{win} through the signal, and compares the variance across the window to the variance of the entire signal. If this amount is over a threshold value a "hit" is detected, corresponding to a turbulent event of rapidly changing quantity (e.g. velocity) such as a sweep or ejection passing through the detector. For a velocity signal the local mean, $\hat{u}(t, T_{win})$, of the fluctuating velocity component, $u'(t)$, is defined as (Bruun, 1995):

$$\hat{u}(t, T_{win}) = \frac{1}{T_{win}} \int_{t - T_{win}/2}^{t + T_{win}/2} u(s)\, ds \qquad (9.4.4)$$

where T_{win} is the window length. This is a moving average, where the local mean over a given window length is calculated for every temporal position in the velocity signal. The local variance, $var_t(t, T_{win})$ (VITA variance), is defined by:

$$var_t(t, T_{win}) = \hat{u}^2(t, T_{win}) - [\hat{u}(t, T_{win})]^2 \qquad (9.4.5)$$

(i.e. the windowed variance of the signal with respect to the windowed mean). The variance of the entire signal, var(t), is defined as:

$$var(u) = \lim_{t \to \infty} \frac{1}{t} \int_{t_0}^{t} u^2(t)\, dt \qquad (9.4.6)$$

The detection criterion is such that if the local variance, $var_{t(t,Twin)}$, is greater than k.var(t), a VITA event is detected. However, the above criteria will detect on both a rapid positive change of the velocity signal (du/dt > 0, i.e. a sweep event), and a rapid negative change (du/dt < 0, i.e. an ejection event). The detector function, D(t), is thus defined as follows in this study:

$$D(t) = \begin{cases} 1 & \text{if } var_t(t, T_{win}) > k.var(t) \text{ and } du/dt > 0 \text{ (sweep)} \\ -1 & \text{if } var_t(t, T_{win}) > k.var(t) \text{ and } du/dt < 0 \text{ (ejection)} \\ 0 & \text{otherwise.} \end{cases} \quad (9.4.7)$$

An average VITA event can then be obtained by ensemble averaging all events for which detection has occurred over a window of size T_{ens} ($T_{ens} > T_{win}$). In the scheme used in this study, the point of detection was defined as the point of maximum du/dt during each period for which $var_t(t, T_{win}) > k.var(u)$. Further to this criterion, it was decided to ignore multiple detections that occur within the ensembling window, T_{ens}. This ensures that the ensemble averaged event will only contain contributions due to isolated VITA events. In the following analysis, the threshold value of detection is set to equal the entire variance of the velocity fluctuation (k = 1.0) and the window length, T_{win}, was set to $T_{win+} = 10$ (based on canonical u^*). The ensembling window was set to $T_{ens+} = 60$ ($T_{ens+} = -20$ to 40, again based on canonical u^*).

An example of the VITA averaging program is shown in Fig. 9.4.20. The fluctuating u-velocity component measured with a single hot wire at $y^+ = 30$ without plasma is shown at the top of the plot. The local variance is shown in Fig. 9.4.20b, along with the threshold detection level. Figure 9.4.20c shows the raw detection function, D(t), and the detection function after multiple

events have been removed. Consequently, the illustrated part of the signal shows three positive VITA events and one negative event. The ensemble averaged VITA event corresponding to the entire signal is shown in Fig. 9.4.21. Similar analysis for the u-velocity signal with plasma is shown in Figs. 9.4.22 and 23.

The attention should be paid on the locations of Sec. 9.4.3 ($y^+ \cup 60$). In this region, the majority of the events are associated with positive du/dt as can be seen by the quantity of VITA detections in Figs. 9.4.21 and 9.4.23. This is not to say that negative du/dt events (ejections) were rare, but they frequently occurred in groups as can be seen at t = 11.5s in Fig. 9.4.20 (i.e. hairpin packets, as described by Adrian et al., 2000, see Fig. 2.2.10). These are discarded from the ensemble to avoid contaminating the ensemble average to either side of the VITA event. Subsequent analysis will focus only on sweep events. The reader is reminded that sweep events are responsible for the majority of the skin-friction drag (Orlandi and Jimenez, 1994).

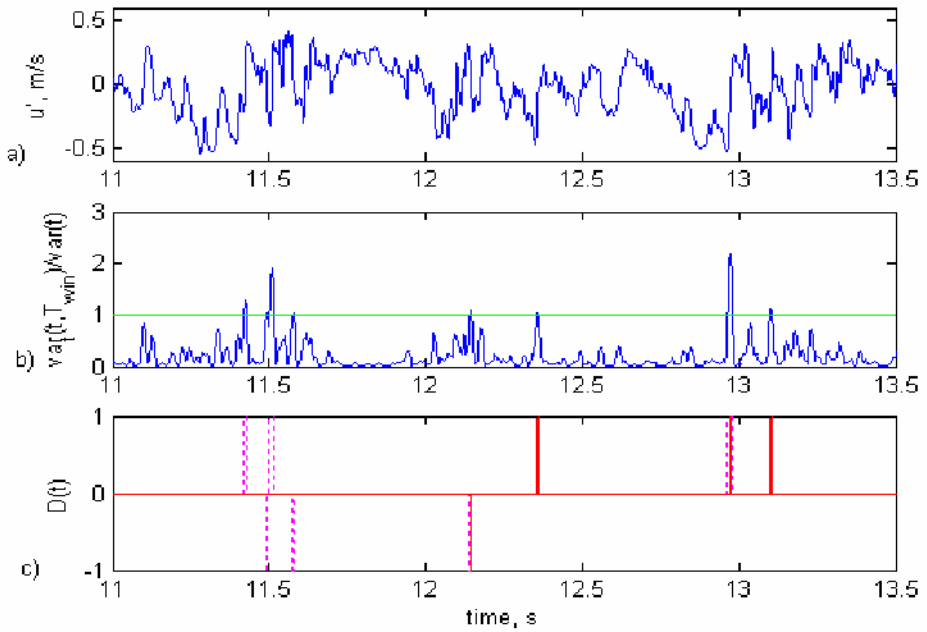

Figure 9.4.20. VITA detection scheme at y^+ = 30 without plasma. a) velocity fluctuation, *u'*. b) ratio of local variance to mean variance and threshold detection level (-). c) detector function, D(t), without discrimination against multiple events (--) and with discrimination (-).

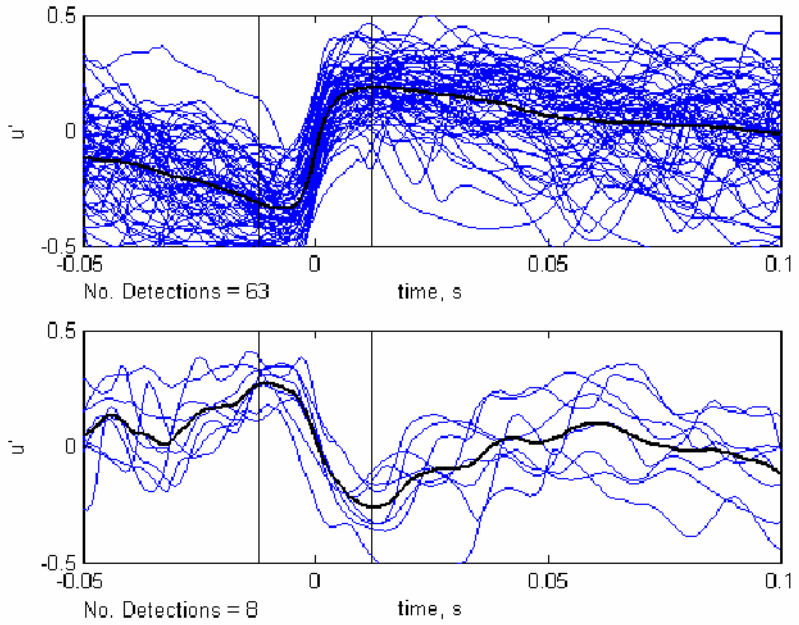

Figure 9.4.21. Ensemble averaged VITA events over the window T_{ens}, without plasma at y^+ = 30. a) du/dt > 0 events and b) du/dt < 0 events. Black lines indicate the window size, T_{win}.

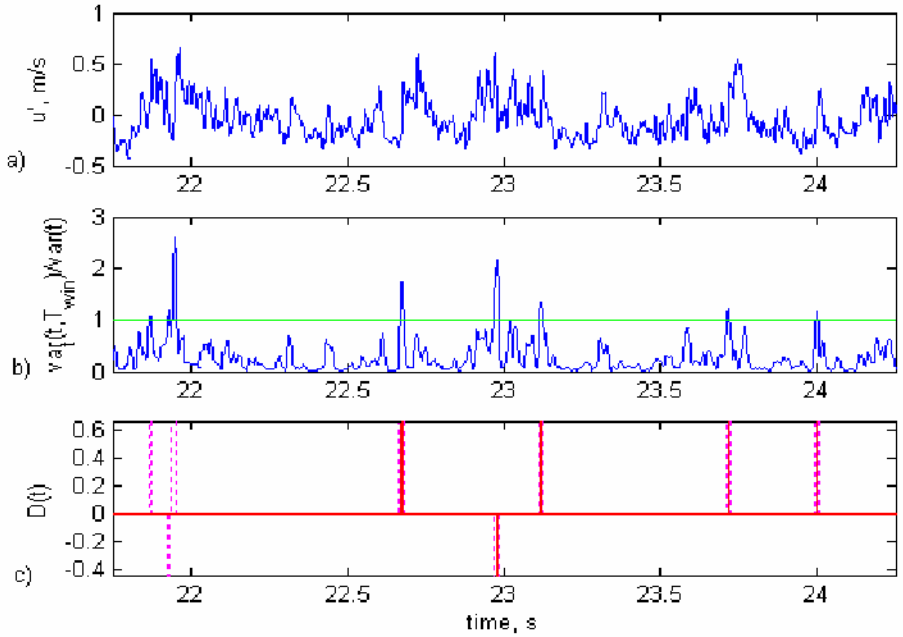

Figure 9.4.22. VITA detection scheme at y^+ = 30 with plasma. a) velocity fluctuation, *u'*. b) ratio of local variance to mean variance and threshold detection level (-). c) detector function, D(t), without discrimination against multiple events (--) and with discrimination (-).

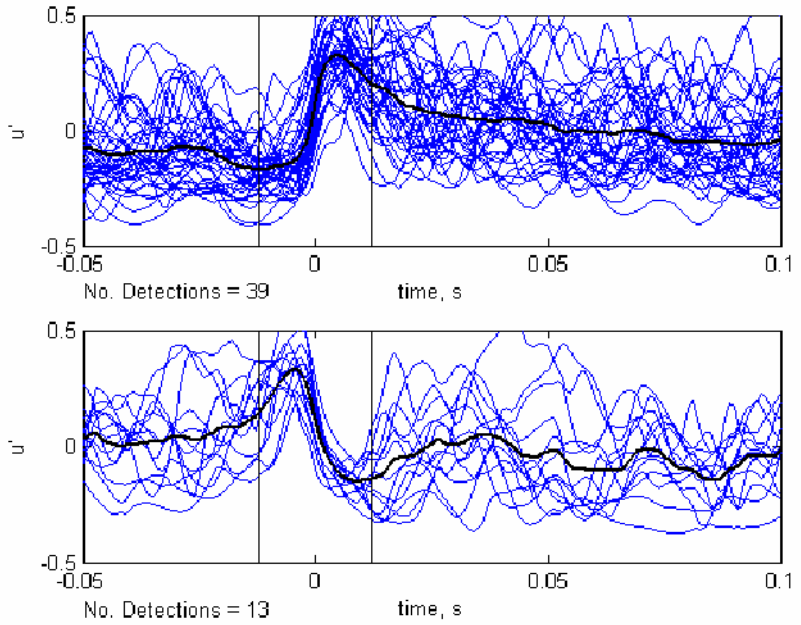

Figure 9.4.23. Ensemble averaged VITA events with plasma at y^+ = 30. a) du/dt > 0 events and b) du/dt < 0 events. Black lines indicate the window size, T_{win}.

9.4.5. VITA Events With and Without Plasma

The positive VITA signatures at y^+ = 5, 20, 30 and 60 are shown in Fig. 9.4.24. Figure 9.4.24a illustrates the way in which the sweep duration has been estimated. Here, the post-event signature has been extended to the intercept of the velocity axis (i.e. the expected time for the velocity fluctuation to return to zero after an event, had the signal not been contaminated by turbulent fluctuations nearby). The intensity of the near-wall sweep has been measured by taking the peak-to-peak magnitude of the VITA events. This should be treated with some caution since VITA detects on the signal variance. The canonical and plasma-on cases typically have different variances and the VITA detection scheme will consequently trigger on events of different magnitude. The comparison will, however, give a measure of the typical change in the velocity scale of sweep events at a given position in the boundary layer.

It is observed that at all positions shown in Fig. 9.4.24, the plasma causes a large reduction in sweep duration. For y^+ = 5, the duration of the event reduces from $t^+ \approx 23$ to $t^+ \approx 11$. This is a reduction of 50%. The intensity of the near wall sweeps has been decreased by around 15%. At y^+ = 20, the sweep duration has also been reduced by around 50%. Here, the event intensity has also been reduced by around 30%. At y^+ = 30, the sweep duration is reduced by nearly 80% and the intensity reduced by around 10%. Moving still further from the wall, at y^+ = 60, the duration is reduced by around 50% but the intensity is increased by 30%. This increase in sweep intensity corresponds to the increase in velocity fluctuation in the region $30 < y^+ < 200$.

Using mechanical spanwise-wall oscillation, Choi and Clayton (2001) found the sweep duration decreased by almost two-thirds for $y^+ < 5$. Also, Pang et al. (2004) found that the sweep duration was reduced by 50% and the intensity was reduced by 30-40% for $y^+ < 5$, using a spanwise-oscillating Lorentz force. The reduction in sweep duration and intensity by spanwise oscillating plasma forcing appears to be remarkably similar to these studies, suggesting that a similar mechanism is responsible for the drag reduction.

The VITA detection frequency, defined as the number of positive detections per unit time, is shown in Fig. 9.4.25. The amount of VITA detections is a function of the threshold, k. Note here that all positive detection events have been included in the count, (i.e. including multiple sweeps). The VITA detection frequency has roughly quadrupled for $y^+ = 5$ and tripled for $y^+ = 20$ and 30. For $y^+ = 60$, a 20-30% increase of event frequency was observed. Thus, in the near wall region there is a large increase in the quantity of sweep events, but their individual duration and strength is reduced. Again, this is similar behaviour to other drag reducing flows (Karniadakis and Choi, 2003). The induced motions caused by the plasma appear to be leading to premature sweep events, as also observed for riblets by Choi (1989). It is suggested that the plasma-induced streamwise vortices are disrupting or cancelling the quasi-streamwise vortices which naturally occur near the wall.

The positive VITA signatures at $y^+ = 5$ for the single hot-wire signal and the u-component signal from the two X-wires is shown in Fig. 9.4.26. It appears that the VITA event is in close agreement between all three signals, and this level of agreement is typical throughout the entire boundary layer. Thus, by triggering on the *u'*-component signal with the X-wire, the simultaneous *v'*,

w', *u'v'* and *u'w'* signals associated with the VITA event can be identified. These are presented at y^+ = 5, 20, 30 and 60 in Fig. 9.4.27. Single-wire velocity data is shown for the streamwise velocity events. The VITA events are normalised to the free stream velocity, U_∞, such that the comparison gives absolute change in velocity fluctuation and Reynolds stress at a given position in the boundary layer. These profiles must be treated again with some caution. The amount of events in the ensemble (around 60) is quite adequate for u since the event characteristics are already filtered depending on the sign of du/dt. The associated wall normal and spanwise velocities do not necessarily have a preferred sign (i.e. asymmetric structures) and the ensembles are unlikely to have converged in this limited data set. It is, however, possible to make a few tentative conclusions.

In the viscous sublayer (Fig. 9.4.27a), the *v'*-component sweep duration is reduced by a similar amount as the *u'*-component. Consequently, there appears to be less *u'v'*-component Reynolds stress produced per sweep event, consistent with the observed drag reduction. This is clearly seen in Fig. 9.4.27a, where it can be estimated that the *u'v'*-component Reynolds stress per event has roughly halved. Fig 9.4.27a does, however, show an increase in *u'w'*-component Reynolds stress. This is likely to be due to spatial resolution errors, since the X-wires are vertically separated by around 2.5 viscous units. At y^+ = 20 and 30 (Fig. 9.4.27b and c), the associated *v'*-component becomes increasingly negative. This again supports that there are increased motions towards the wall due to the pumping motion of streamwise vortices superimposed on the background turbulence, and due to downwash between electrodes because of the entrainment action of the plasma.

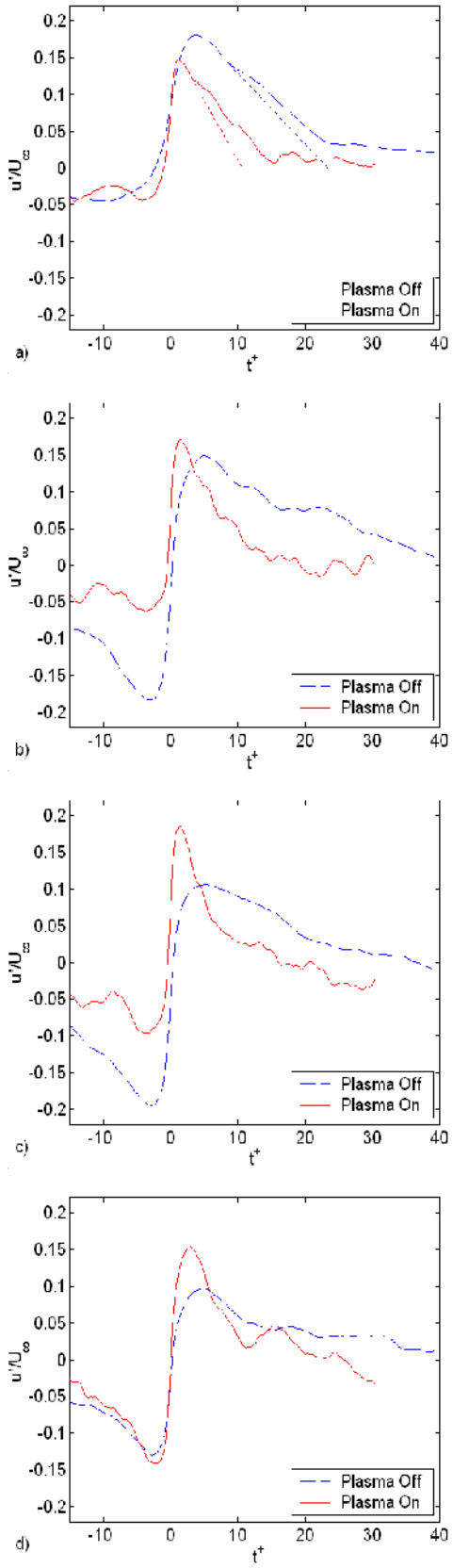

Figure 9.4.24. Ensemble averaged VITA events without (--) and with (-) plasma at: a) $y^+ = 5$; b) $y^+ = 20$; c) $y^+ = 30$; d) $y^+ = 60$.

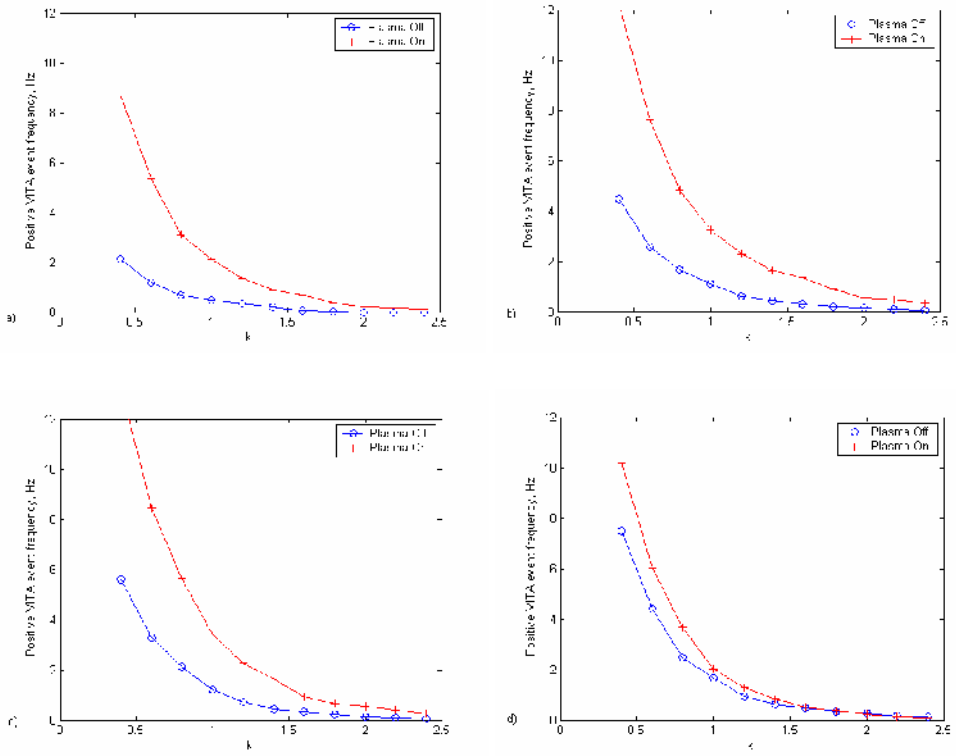

Figure 9.4.25. Frequency of positive VITA events as a function of the threshold, k, at: a) $y^+ = 5$; b) $y^+ = 20$; c) $y^+ = 30$; d) $y^+ = 60$.

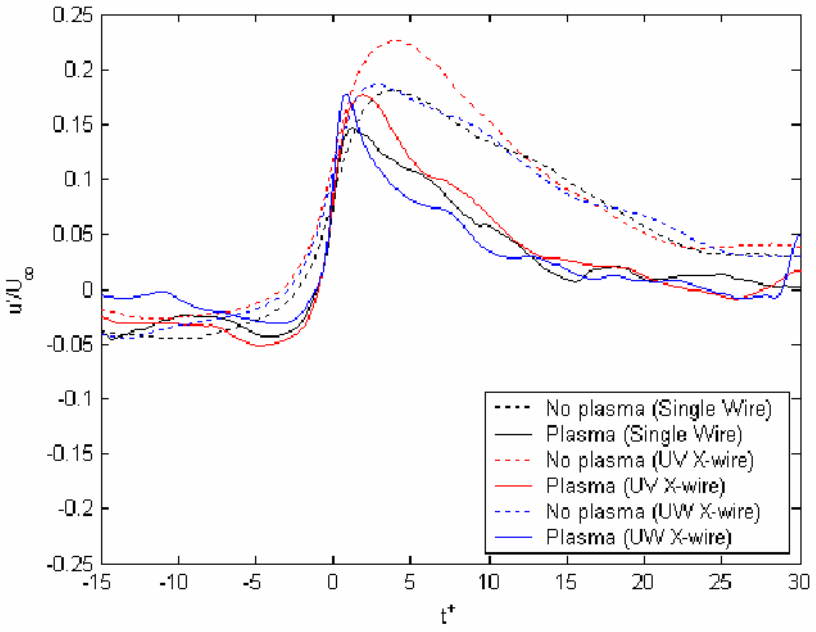

Figure 9.4.26. Ensemble averaged VITA events without (--) and with (-) plasma at $y^+ = 5$, showing good agreement between VITA events detected from a single hotwire and the u-component of UV and UW X-wires.

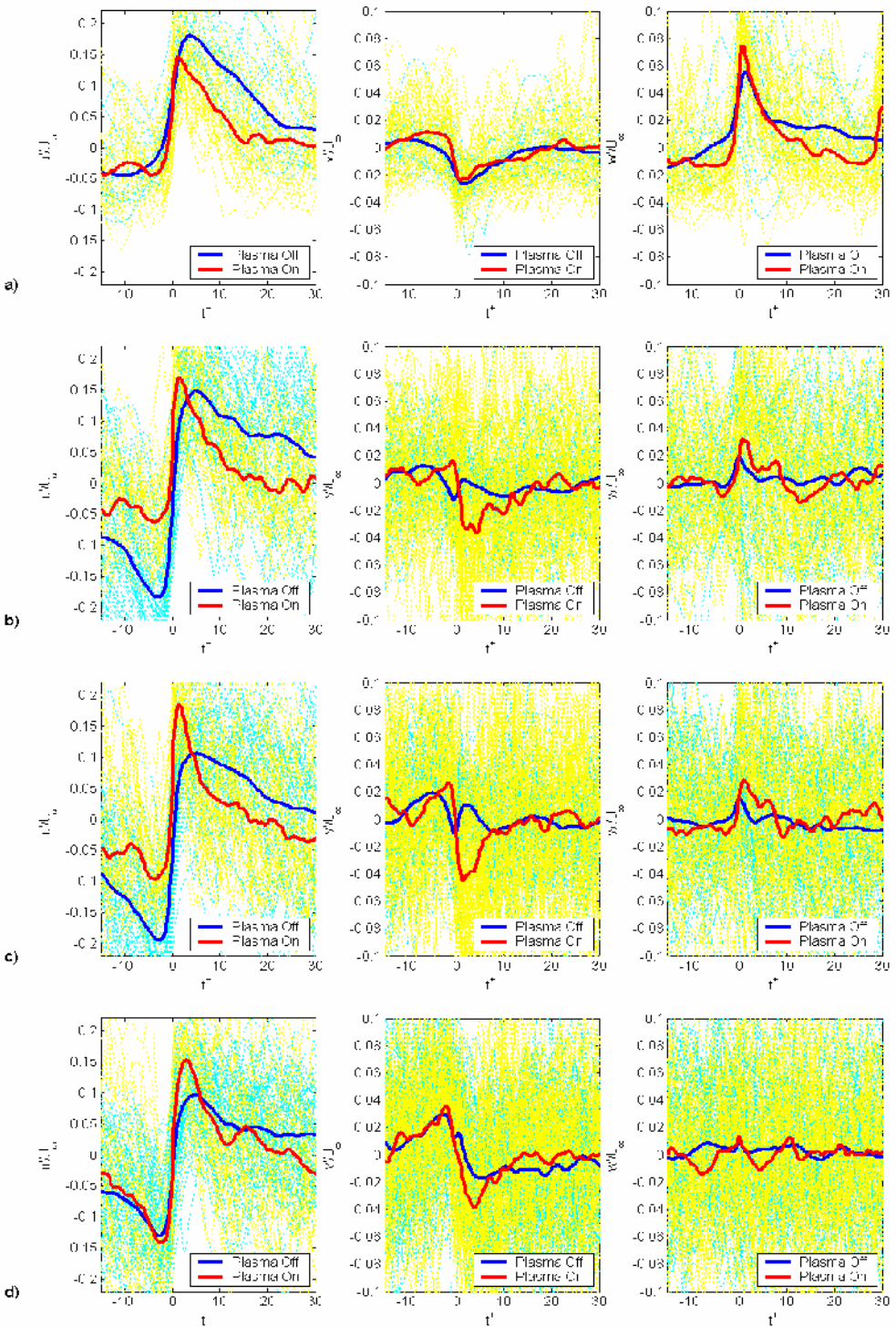

Figure 9.4.27 (continues overleaf). Ensemble averaged VITA events without (-, -) and with (-, -) plasma at: a) $y^+ = 5$; b) $y^+ = 20$; c) $y^+ = 30$; d) $y^+ = 60$. VITA event detected on positive du/dt and *v'* and *w'* are simultaneously ensembled during each detection. *u'* (left), *v'* (middle), and *w'* (right column).

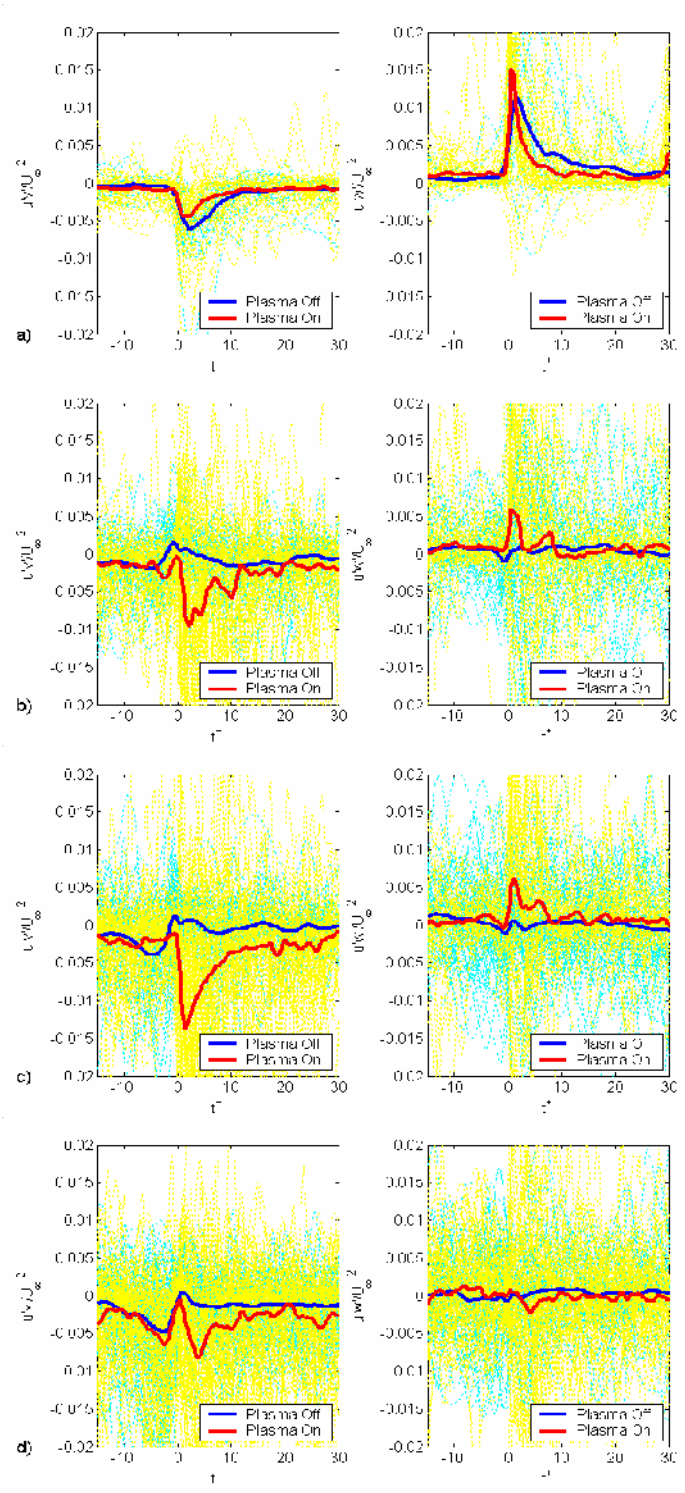

Figure 9.4.27 cont. Ensemble averaged VITA events without (-, -) and with (-, -) plasma at: a) $y^+ = 5$; b) $y^+ = 20$; c) $y^+ = 30$; d) $y^+ = 60$. VITA event detected on positive du/dt and *u'v'* and *u'w'* are simultaneously ensembled during each detection. *u'v'* (left), and *u'w'* (right column).

9.4.6. Phase-Averaged Spanwise Velocity

The UW X-wire probe was also used to study the phase-averaged spanwise velocity in order to check that the plasma is indeed inducing spanwise oscillations in the near-wall region. Figure 9.4.28a shows a typical extract of the spanwise velocity fluctuation, *w'*, with time at $y^+ = 20$. The timing of the plasma pulse train is also shown in the plot. The plasma was fired alternately on each electrode set, such that plasma forcing occurred in the positive z-direction for the 1^{st}, 3_{rd}, 5^{th} pulse envelopes, etc., whereas forcing was in the negative z-direction for the 2^{nd}, 4_{th}, 6^{th} pulse envelopes. It can be seen in the figure that there is a strong correlation between the plasma pulses and *w'*. In general, *w'* goes from negative to positive just after every odd-numbered pulse due to the plasma forcing in the positive z-direction, and vice versa. One can also make out that *w'* varies roughly sinusiodally, with turbulent fluctuations superimposed. Figure 9.4.28b illustrates the phase-averaging procedure, where *w'* was ensembled between every plasma oscillation cycle and then ensemble averaged over the entire 60s of plasma (roughly 1200 forcing cycles). One can clearly see that the phase-averaged spanwise velocity, $\langle w' \rangle$, does indeed vary periodically; thus indicating that the plasma induces a spanwise oscillatory flow near the wall.

Figure 9.4.29 shows $\langle w' \rangle$ with phase angle, $\phi = 2\pi t/T$, over the plasma oscillation cycle at various locations throughout the boundary layer. Recall that the hot wire was located at the centreline between two opposing plasma actuators (c.f. Fig. 8.3.2c). Fig. 9.4.29 thus shows that the magnitude of the forcing was roughly the same from each electrode set since $\langle w' \rangle$ has equal magnitude during both half-cycles. However, for $y^+ < 10$, a large positive

velocity was observed just after the start of the forcing cycle. This is expected to be caused by the physical separation of the two wires of the X-wire probe in the y-direction ($2.5l^+$), which biases measurement of *w'* near the wall due to the large shear.

It was observed that $\langle w' \rangle$ has an approximately sinusoidal variation to a wall normal distance of $y^+ \approx 60$. Above this height, there is little correlation between the timing of plasma pulses and *w'*, which again shows that the plasma only affects the near wall fluid. Figure 9.4.29 shows that the phase-averaged spanwise velocity also decreases with distance from the wall, such that the plasma effect decreases monotonically with y. It is also observed in Fig. 9.4.29 that $\langle w' \rangle$ has shifted phase by 180° at $y^+ = 62$. In Sec. 9.4.2 it was suggested that this location marked the edge of the plasma-induced streamwise vortices. This phase shift further supports this conclusion, so that the fluid above the vortex cores moves in a different z-direction relative to the near wall fluid throughout the plasma oscillation cycle.

The magnitude of spanwise velocity in Fig. 9.4.29 appears to be much lower than was expected ($\langle w' \rangle^+ < 1$, whereas $W^+_{opt} \approx 15$ from Choi et al., 1998). This is a direct consequence of the phase averaging procedure. As can be seen in Fig. 9.4.28, the phase average has magnitude of less than 25% of the velocity fluctuations, *w'*, thus indicating that the plasma-induced spanwise velocity is likely to be closer to $W^+ = 4$. This is still significantly less that the optimal wall speed of spanwise-wall oscillation. This could be the reason why only 22% drag reduction was observed here, as opposed to 45% in the study of Choi et al. (1998).

The phase-averaged spanwise velocity profile is shown throughout the oscillation cycle in Fig. 9.4.30. The maximum velocity magnitude occurred at $y^+ \approx 15$ throughout; similar to the optimum penetration depth from the spanwise-wall oscillation and Lorentz-forcing studies (Choi et al., 1998, Berger et al. 2000). The profiles suggest a shift in velocity intercept with the wall (i.e. $\langle w' \rangle \approx -0.15$ at $y^+ = 0$), but this is likely to be a result of spatial resolution errors of the X-wire probe in the near-wall region. The velocity profiles clearly show a spanwise-directed wall-jet-like flow which extends to around $y^+ = 60$. The jet reaches a maximum velocity just after each plasma pulse envelope ($\approx \pi/8$ and $9\pi/8$), then steadily diminishes in magnitude, until changing direction as soon as the next plasma pulse occurs.

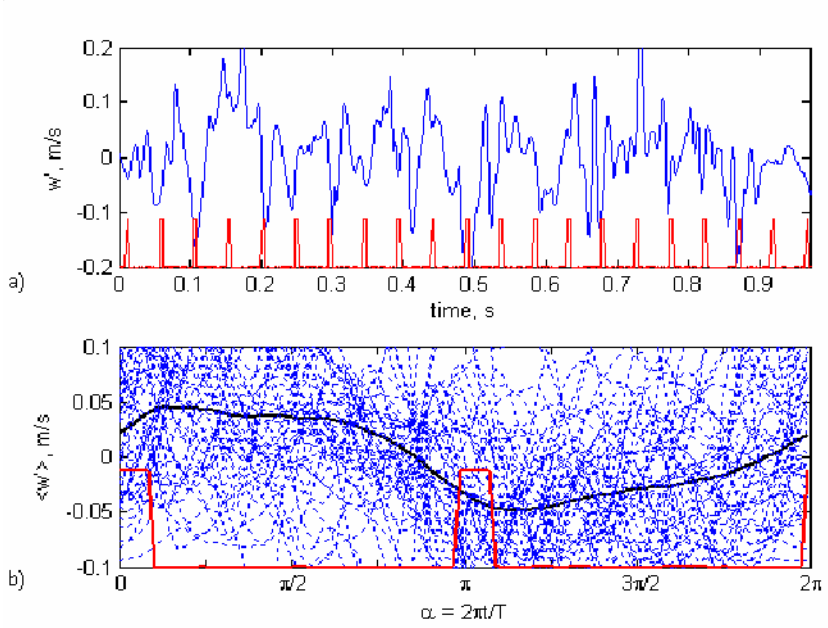

Figure 9.4.28. Spanwise velocity fluctuations at $y^+ = 20$ in the turbulent boundary layer with plasma forcing. a) *w'* (-) and timing of plasma pulses (-). Odd numbered pulses are delivered to the electrode set which induces plasma forcing in the positive z direction. Even pulses induce forcing in negative z direction. b) phased (--) and phase-averaged () spanwise velocity, $\langle w' \rangle$, with phase angle, α, throughout the plasma oscillation cycle.

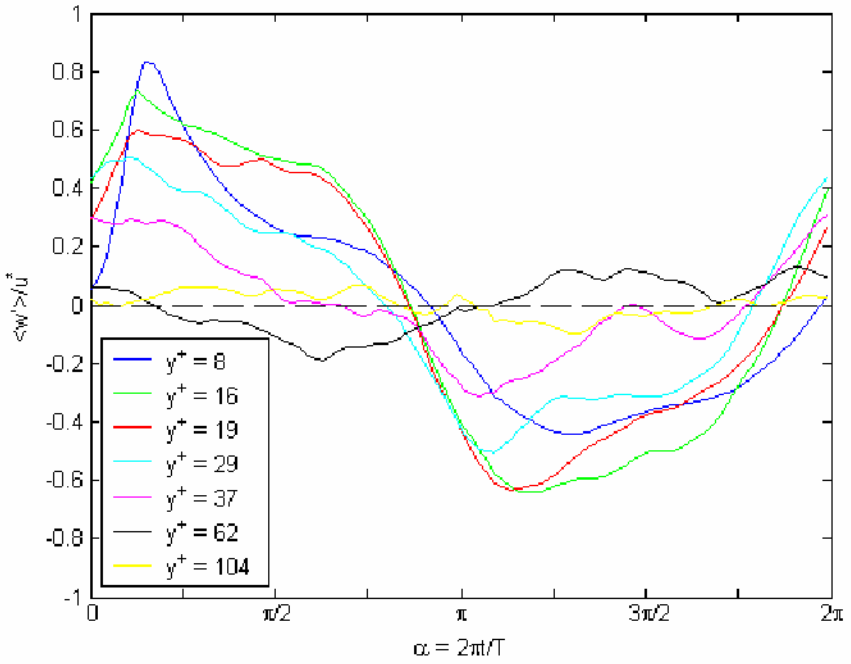

Figure 9.4.29. Non-dimensional phase-averaged spanwise velocity over the plasma oscillation cycle at various y^+.

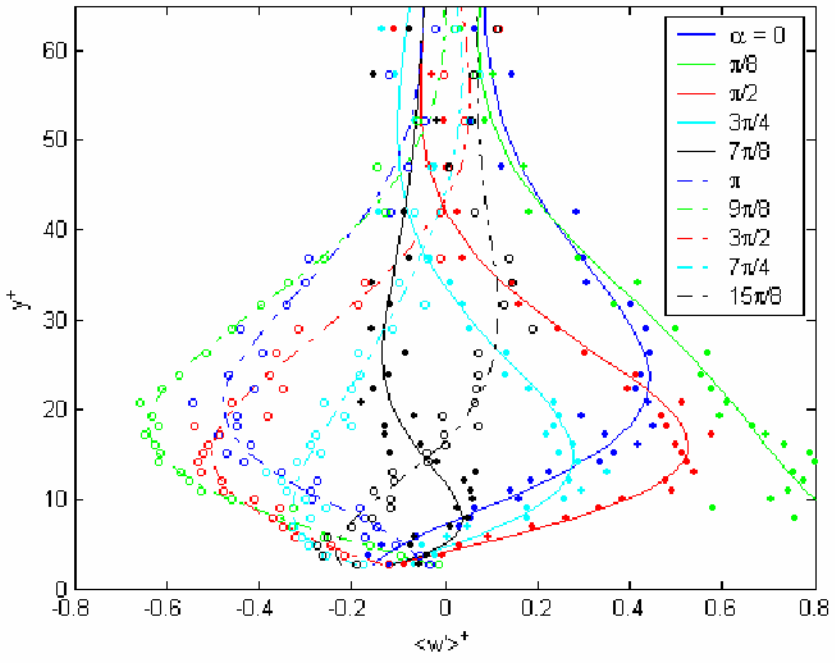

Figure 9.4.30. Phase-averaged spanwise velocity profile at various phase angle, $\alpha = 2\pi t/T$. Lines are polynomial fits to the data points.

9.4.7. Spanwise Variation

The measurements in the preceding sections were all taken at the midpoint between two opposing plasma actuators, as shown in Fig. 9.4.31 (z = 0). In order to investigate whether there is a spanwise variation of skin-friction, boundary layer traverses were taken with a single U-component hot-wire probe at five locations across the electrode sheet. Unfortunately, the sub-miniature X-wire probes were not available for this part of the study so that the spatial variation of V and W could not be investigated. Figure 9.4.31 illustrates the five spanwise measurement locations with reference to the electrode positions. Wall-normal hot-wire surveys were taken at a spanwise interval of 1mm that covered one-half a wavelength, , of the electrode spacing. This region should correspond to half the diameter of the oscillatory vortices created by the plasma. Data collection was identical to Sec. 9.4.1, although the hot-wire signals were not corrected for the thermal boundary layer associated with plasma. It was deemed too time consuming to perform a full spanwise cold-wire survey, and any variation in velocity will be apparent without this correction.

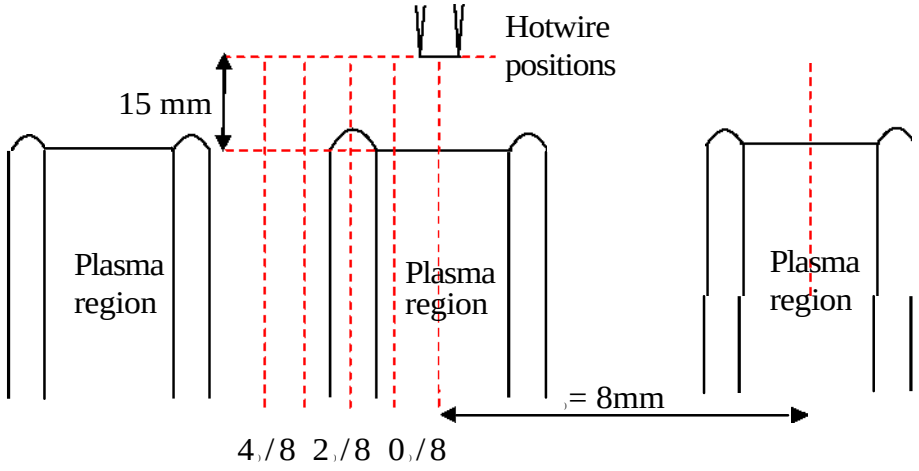

Figure 9.4.31. Measurement positions during spanwise traverse.

Figure 9.4.32 shows the spanwise variation in velocity deficit, $U/U_{\infty, \text{plasma}} - U/U_{\infty, \text{no plasma}}$. The differences between the profiles at the different locations are small, although there is a clear trend near the minimum position. The magnitude of the velocity deficit is greatest at z = 4/8, and reduces to a minimum at z = 0. This suggests that the core of the vortices have a preferential position at z = 4/8, which is the mid-way position between two electrode pairs (non-plasma sides). Thus, at z = 0 one would expect a preferential upwash or downwash associated with the vortex pumping; an observation confirmed by the negative Vin Fig. 9.4.11.

The measured skin-friction coefficient and level of drag reduction at the different spanwise locations, along with integral parameters, is given in Table 9.4.3. There is a small spanwise variation in u^*, c_f and the amount of drag reduction, with maximum at z = 0. This is at the centre of two opposing electrodes (plasma side) which is expected to be position of maximum induced spanwise velocity. However, the spanwise variation in the drag reduction is within the uncertainty of the results and the difference may merely be a result of experimental scatter. One must also bear in mind that the hot-wire sensor has a wire length of 1.25mm; just larger than the separation between measurements. It is plausible that any spatial variation in skin friction has been averaged out by the spatial resolution of the probe.

It is pleasing to see here that the spatial variations in velocity and drag reduction are small, yet the drag is reduced by more than 20% over the entire sheet.

	No Plasma					With Plasma					
z	0 mm	δ^* mm	H	u^* m/s	c_f 10^{-3}	0 mm	δ^* mm	H	u^* m/s	c_f 10^{-3}	DR %
4λ/8	7.64	11.11	1.45	0.0753	3.59	7.72	13.71	1.78	0.0673	2.87	20.1
3λ/8	8.04	11.79	1.47	0.0748	3.94	8.00	14.23	1.79	0.0664	3.10	21.2
2λ/8	7.98	11.67	1.46	0.0747	3.99	8.03	14.10	1.76	0.0658	3.09	22.4
λ/8	7.26	10.76	1.48	0.0755	3.65	7.54	13.29	1.76	0.0670	2.86	21.4
0	8.10	11.61	1.43	0.0766	4.00	8.18	13.84	1.69	0.0669	3.06	23.7

Table 9.4.3. Boundary layer integral quantities, friction coefficient and drag reduction (DR) at different spanwise locations between the plasma electrodes.

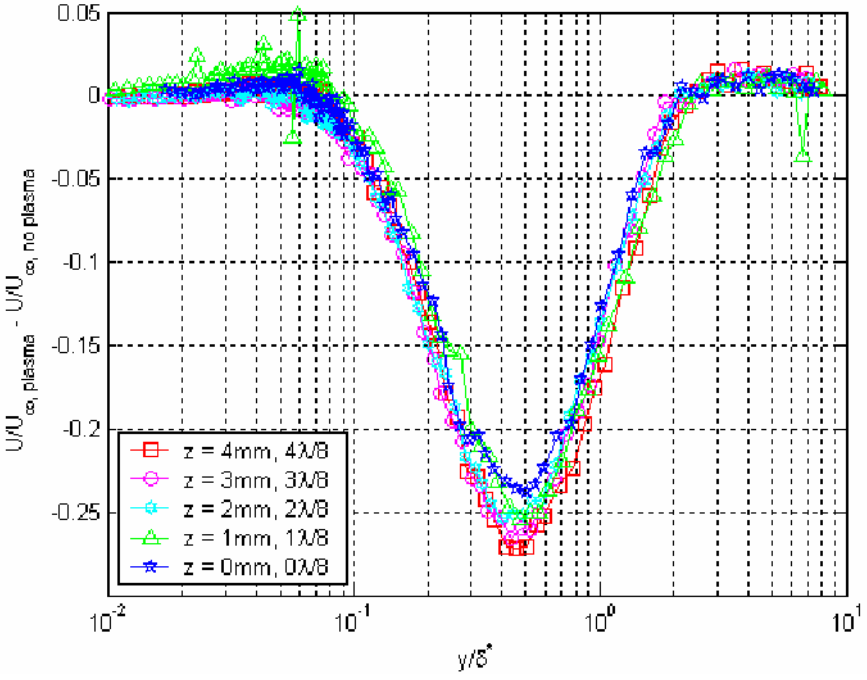

Figure 9.4.32. Mean velocity deficit across one half wavelength of the electrode gap. PRF = 38kHz, E_{max} = 3.3kV, PED = 5ms, PEF = 21Hz, U_∞ = 1.8m/s, Re_δ = 900, s = 4mm. Measurements taken 15mm downstream of electrodes.

9.5. Summary

By utilising two opposing sets of asymmetric plasma actuators, a viscous drag reduction of 22% was achieved in a turbulent boundary layer at Re_τ = 380. To achieve this level of drag reduction, the plasma was oscillated at T^+ = 38 with forcing such that $W^+ \approx 4$, and the plasma electrodes had a spacing of s^+ = 20 between opposing pairs. The effect of T^+, s^+, and PED on the skin-friction will be studied in Ch. 10, where it will be shown that an even greater drag reduction is possible with oscillatory surface plasma.

The evidence suggests that the plasma caused oscillating sets of streamwise vortices to be embedded in the logarithmic region of the boundary layer. These vortices are expected to move side to side in the spanwise direction and change rotation sense throughout the AC cycle. These caused a reduction in mean velocity throughout the logarithmic region and reduced velocity fluctuations near the wall. Similar behaviour was also reported by Sandborn (1981) for streamwise vortices induced by sub-boundary layer fins.

Although the vortex sizes and positions change with time, some average location of the lower, centre and upper extent can be observed in the data. The outer edge of the plasma-induced streamwise vortices corresponds to the position of maximum spanwise fluctuation, *w'*, due to induced vortex motions. This also corresponds to the position of maximum temperature fluctuations, *T'*, due to the intermittent (and cyclical) passage of the vortices past the probe, and occurs at $y/\delta^* \approx 1$, $y^+ \approx 60$. The average height of the vortex cores corresponds to the position of maximum wall-normal fluctuations, *v'*, due to induced vortex motions towards and away from the wall to either side of the core. The mean core location is also marked by the maximum temperature

difference, ΔT, and maximum reduction in streamwise velocity, ΔU, since the vortices originate at the plasma (i.e. very close to the wall), so that hot, low-momentum fluid is entrained within. This occurs at $y/\delta^* \approx 0.5$, $y^+ \approx 30$. The lower extent of the vortex cores is less well defined but can be identified as the location of the second peak in spanwise oscillations, *w'*, due to induced vortex motions below the core. This location also corresponds to the location of maximum reduction in streamwise velocity fluctuations, *u'*, and occurs at $y/\delta^* \approx 0.25$, $y^+ \approx 20$.

Though it is thought that the plasma actuators are creating streamwise vortices near the wall of the turbulent boundary layer, it has not been possible to directly 'see' them in this study. To provide further evidence that this may be the case, the results are compared in the following figures with a study which contained a single streamwise vortex embedded within the boundary layer. It will be seen that the results are very similar, supporting the existence of such structures with plasma.

Di Cicca and Iuso (2006) investigated the interaction between a flat plate turbulent boundary layer and a 2D yawed synthetic jet using PIV. The synthetic jet experiment was conducted in water at a Reynolds number nearly identical to the plasma experiment ($Re_{\theta,\ plasma} = 920$, $Re_{\theta,\ Di\ Cicca} = 1000$). Using a forcing frequency of 3.3Hz and an velocity ratio $U_0/U_\infty = 0.5$ (here U_0 is the time averaged velocity at the exit plane of the slit), Di Cicca and Iuso (2006) found that the synthetic jet caused a counter-rotating longitudinal vortex pair completely embedded within the boundary layer when the jet orifice was aligned with the mean flow (Fig. 9.5.1a, actuator slit length = 4.15). However, as the slit was rotated relative to the mean flow, only one of the two shear

layers producing the vortex pair was intensified while the other was diminished, thus causing a single streamwise vortex to be embedded in the boundary layer (Fig. 9.5.1b). This vortex caused a marked effect on the turbulence structure. In the up-flow and cross-flow regions (z = -5 and 0mm respectively, see Fig. 9.5.1b), the streamwise velocity became heavily reduced (up to 22% at $y^+ \leq 50$). In the down-flow region (z = 15mm), a reduction in velocity was evident for $y^+ > 60$, but below this position the streamwise velocity was slightly increased.

Figures 9.5.2 shown mean velocity profiles from the PIV data of Greco and Luo (2006) together with hot-wire measurements of the

oscillatory plasma experiment. Note that the figures are inner scaled with the canonical value of u^* in both cases. It can be seen that the behaviour of the mean velocities (Figs. 9.5.2 and 9.5.3), normal stresses (Figs 9.5.4 and 9.5.5), and Reynolds stress (Fig. 9.5.6) are qualitatively similar in the two studies, once it is recognised that the vortex locations are different. In the plasma experiment the vortex core is believed to be at around $y^+ = 30$. However, the vortex core in the synthetic jet experiment was at around $y^+ = 100$ (c.f. Fig 9.5.1). The locations of the cores have been marked on the figures.

In Fig. 9.5.2, it is observed that the synthetic jet vortex causes a large streamwise velocity deficit in the up-flow, cross-flow and down-flow regions. This deficit spans to either side of the vortex core; behaviour also observed for the velocity profile with plasma. The down-flow region shows a slight increase in velocity below the core, much like the slight increase in mean velocity within the viscous sublayer with plasma. It is suggested that the boundary layer measurements with plasma are in a down-flow-type region; an

observation also made in Sec. 9.4.2 (c.f. Fig. 9.4.11) and Sec. 9.4.7. To further support this, Fig. 9.5.3 shows a strong negative V-velocity close to the location of the vortex core in the down-flow region of the synthetic jet data. This is identical to that observed in the plasma data, where the data sets even agree in the magnitude of V^+.

Figure 9.5.4 shows that the synthetic jet vortex caused an increase in *u'* above the vortex core whilst a reduction below, again similar to the plasma data. Both data sets also show an increased in *v'* at the vortex core (Fig. 9.5.5), and an increase in Reynolds stress above the vortex (Fig. 9.5.6). Note that the synthetic jet data shows a reduction in Reynolds stress below the vortex cores (cross-flow and down-flow regions). This reduction was not observed for the plasma data for $y^+ < 30$.

The similarity in the changes in U, V, *u'*, *v'* and *u'v'* between the two studies gives very strong evidence that the plasma is indeed inducing streamwise vortices near the wall of the turbulent boundary layer.

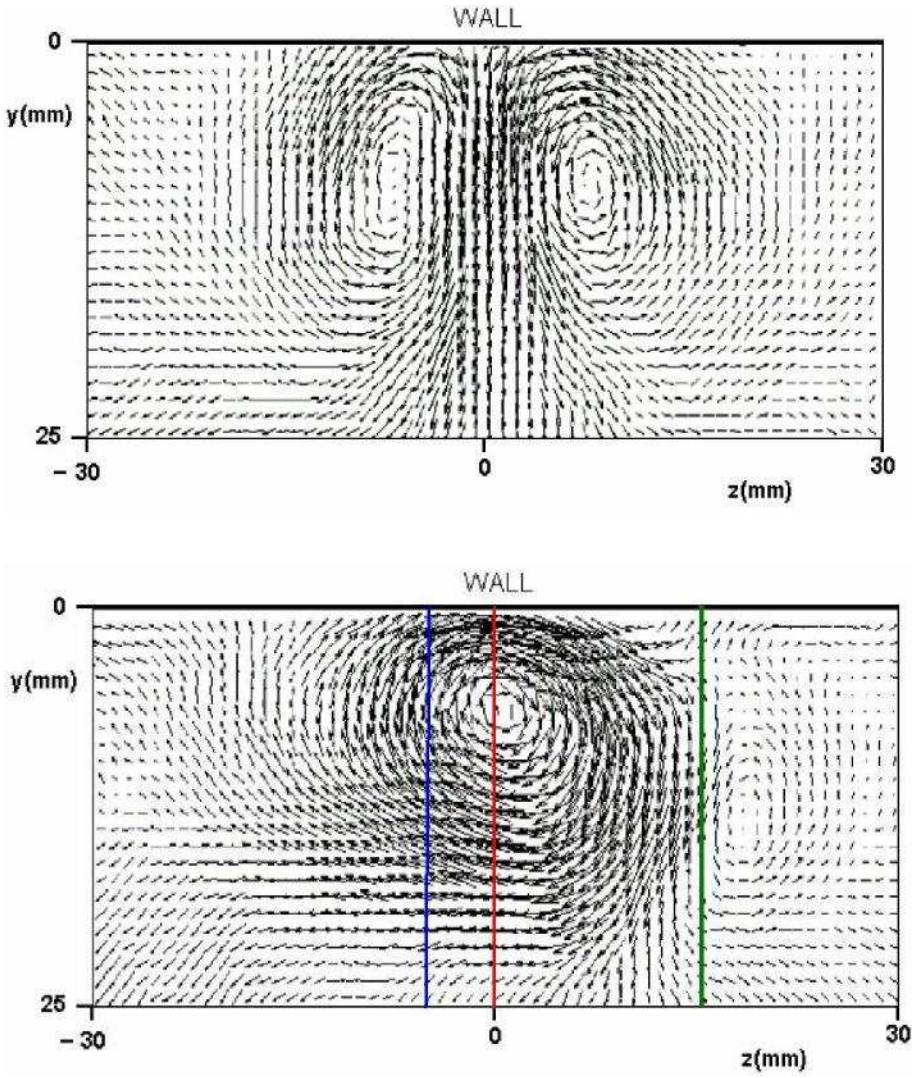

a)

b) Figure 9.5.1. Mean velocity vector field in the y-z plane of a turbulent boundary layer with a slit-type synthetic jet actuator at the wall (looking upstream). Measurements taken at $x/C5 = 3.7$ downstream of the actuator centre (note $C5_{canonical} = 30mm$). The wall is at $y = 0$ and $z = 0$ is the centre of the slit. a) major axis of the synthetic jet actuator aligned with the mean flow (i.e. yaw angle, $8 = 0°$). b) yaw angle, $8 = 16°$. Note that only one of the counter rotating vortex pairs is dominant in b). Coloured lines mark the position of z = -5, 0, 15mm; termed down-flow, cross-flow and up-flow regions respectively. From Di Cicca and Iuso (2006).

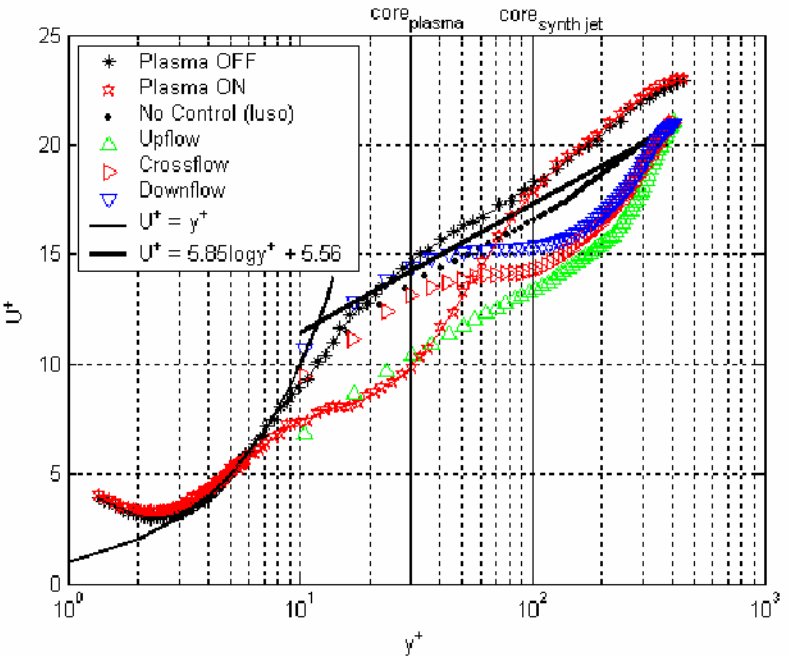

Figure 9.5.2. Inner scaled mean streamwise velocity profiles with and without surface plasma and at the upflow, crossflow and downflow regions of the vortex induced by a yawed synthetic jet at the wall (Di Cicca and Iuso, 2006).

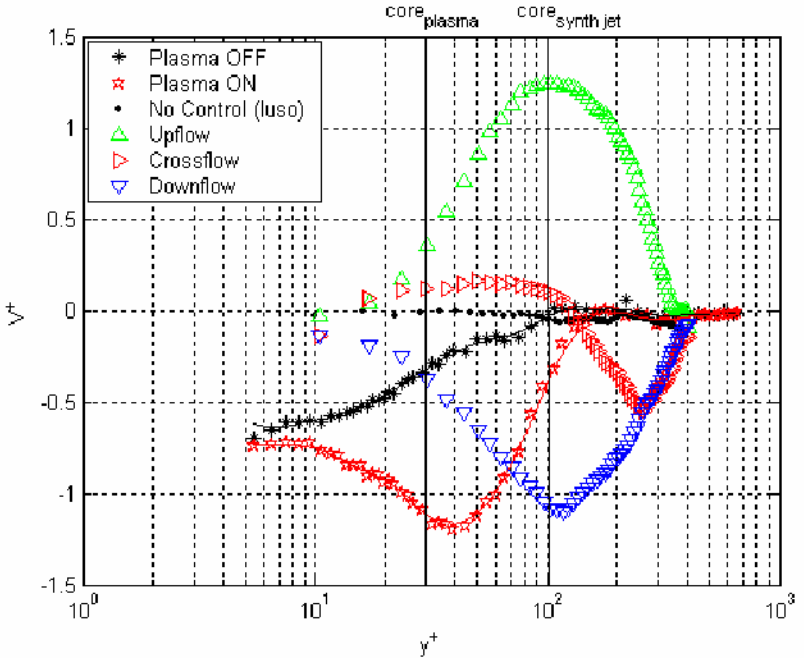

Figure 9.5.3. Inner scaled mean wall normal velocity profiles with and without surface plasma and at the upflow, crossflow and downflow regions of the vortex induced by a yawed synthetic jet at the wall (Di Cicca and Iuso, 2006).

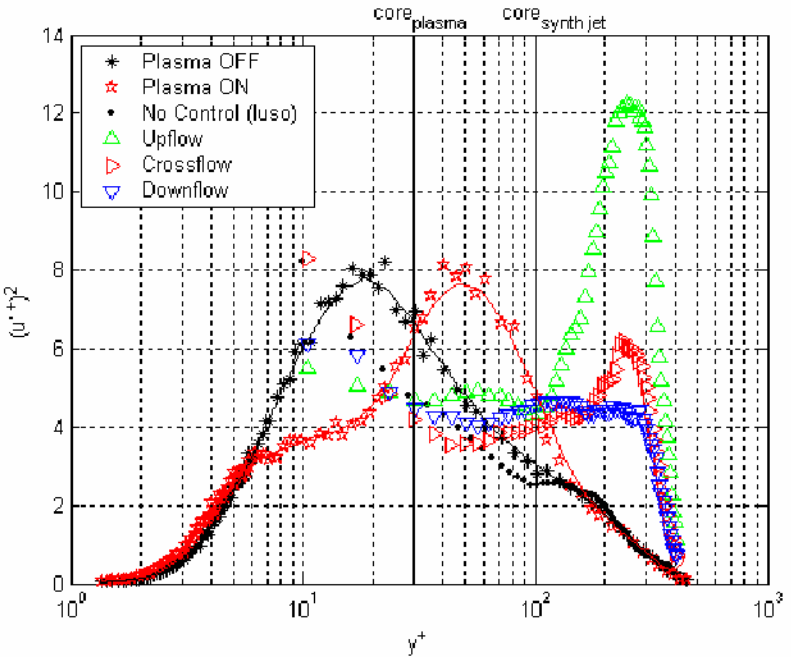

Figure 9.5.4. Inner scaled fluctuating streamwise velocity profiles with and without surface plasma and at the upflow, crossflow and downflow regions of the vortex induced by a yawed synthetic jet at the wall (Di Cicca and Iuso, 2006).

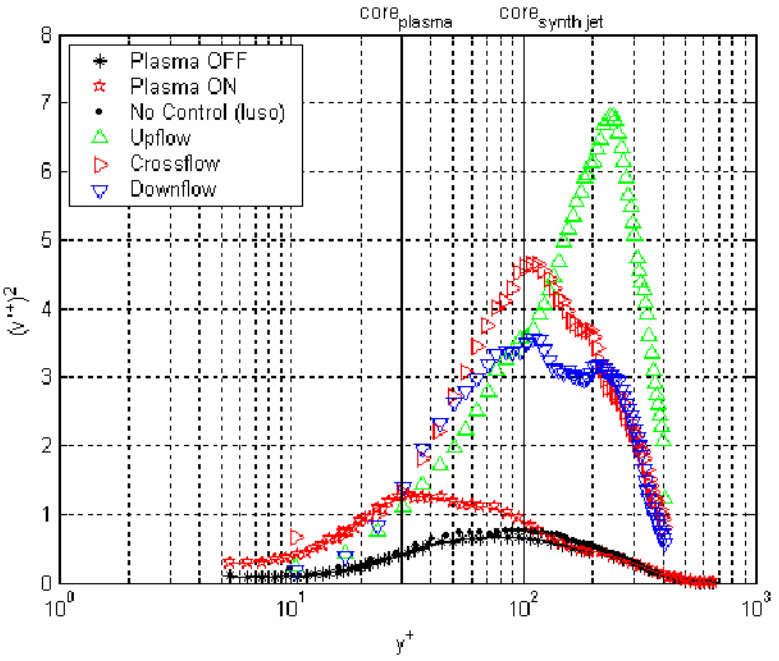

Figure 9.5.5. Inner scaled fluctuating wall normal velocity profiles with and without surface plasma and at the upflow, crossflow and downflow regions of the vortex induced by a yawed synthetic jet (From Di Cicca and Iuso, 2006).

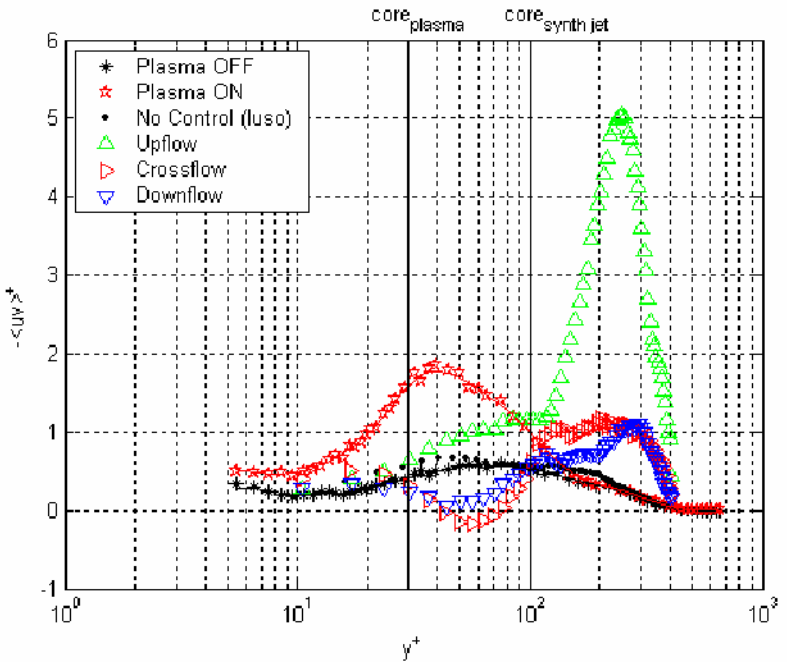

Figure 9.5.6. Inner scaled Reynolds shear stress profiles with and without surface plasma and at the upflow, crossflow and downflow regions of the vortex induced by a yawed synthetic jet at the wall (From Di Cicca and Iuso, 2006).

It is suggested here that the formation of streamwise vortices is disrupting the link between the outer and inner boundary layer structures. The streamwise vortices appear to act like a barrier to block large scale motions near the wall. It is postulated that they may be severing the link between the hairpin vortex legs and necks. This disconnection is expected to inhibit the growth of the hairpins, such that the sweep and ejection events will occur prematurely and at higher frequency; an observation confirmed by the VITA analysis and supported by the shift in the frequency spectrum. This will lead to the observed reduction in mean wall shear stress, since each shear stress producing event will be much weaker. This disconnection will also disrupt the whole turbulence production cycle. Also note that the streamwise vortices

produced by plasma are expected to be co-rotating because the plasma electrodes are activated in unison, with each producing its own vortex (c.f. Fig. 8.3.1). This is unlike the counter-rotating vortices that typically make up hairpin legs and cause near wall streaks due to vortex pumping. Thus, the induction motion from the co-rotating plasma vortices will be weaker which may be important for disrupting the ejection-sweep cycle. A conceptual model of the boundary layer with the plasma-induced streamwise vortices is provided in Fig. 9.5.7.

However, the creation of streamwise vortices may only be part of the reason for the observed drag reduction. Each vortex will induce low-speed fluid away from the wall on the upwash side (thus decreasing skin-friction), while simultaneously transporting high-speed fluid towards the wall on the downwash side (increasing skin-friction); as observed for a single vortex embedded in a turbulent boundary layer using vortex generators (Mehta et al., 1983, Westphal et al., 1985, Shabaka et al., 1985, Bradshaw, 1987). It is suggested that another vortex system is located below the streamwise vortices associated with the oscillatory spanwise motions in the viscous sublayer. Following Choi's (2001) model for drag reduction with spanwise-wall oscillation, it was shown that a spanwise vorticity, ω_z, was created as the periodic Stokes layer was tilted in the spanwise direction. This spanwise vorticity acted to reduce the streamwise velocity near the wall (thus reducing drag) and hampered the stretching of quasi-streamwise vortices. It is expected that a similar effect is occurring in the viscous sublayer with plasma. The plasma-induced streamwise vortices add to this effect. A schematic is provided in Fig. 9.5.8.

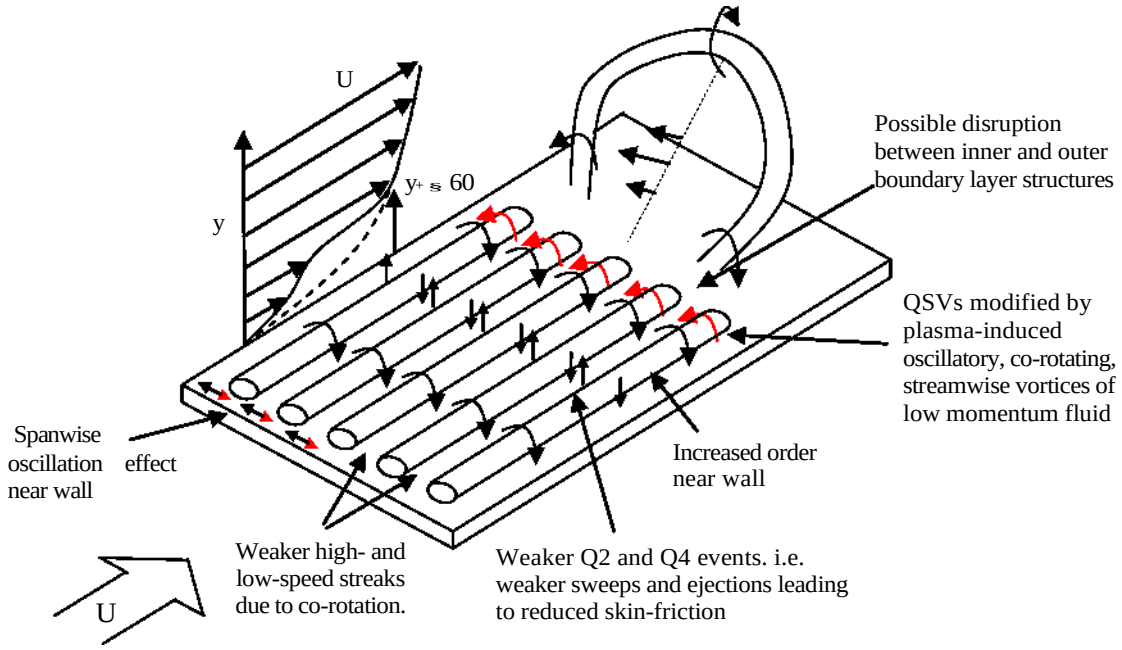

Figure 9.5.7. Conceptual model of the turbulent boundary layer with oscillatory plasma forcing.

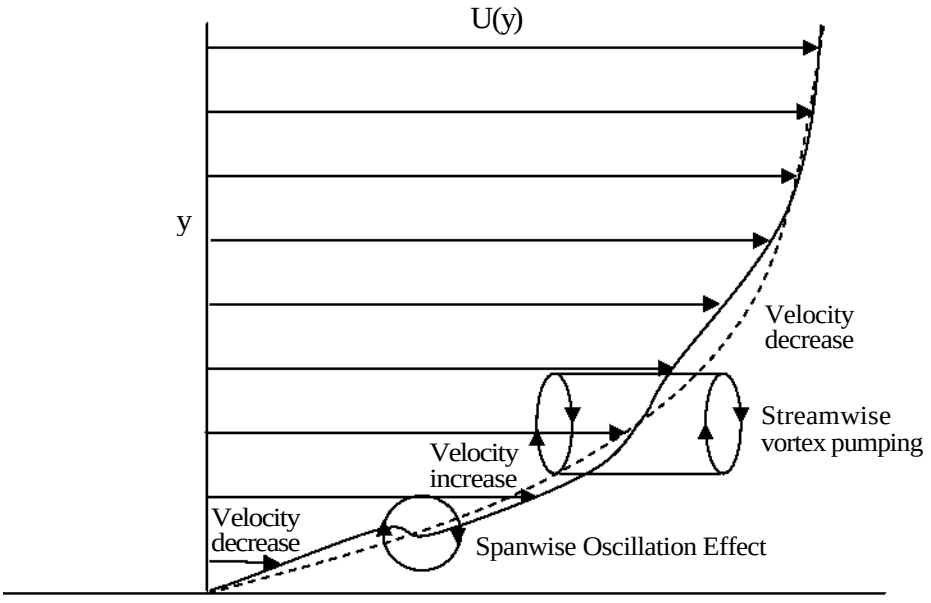

Figure 9.5.8. Schematic of the spanwise oscillation effect on the mean velocity profile with oscillatory plasma forcing.

Chapter 10

Parametric Effects

10.1. Effect of Oscillation Period, T^+

The effect of the oscillation frequencies on the skin-friction drag was studied by taking U-velocity measurements at the midpoint of opposing electrodes, as in Sec. 9.4.1. For the experiments in this section, no correction has been made for the thermal boundary layer due to the additional time necessary to perform traverses with the cold-wire probe. Note that the nature of the thermal boundary layer should have little effect on the measurement of skin-friction due to the absence of plasma directly below the measurement location (see Sec. 9.3).

The plasma was activated with fixed PRF = 38kHz, E_{max} = 3.4kV, PED = 5ms, over an electrode sheet with spacing, s = 4mm. The wind tunnel free-stream velocity was also fixed for all experiments (U_∞ = 1.8m/s). The plasma was activated with PEF = 1, 7, 21 and 50 Hz, such that the forcing oscillation frequency, f = 0.5, 3.5, 10.5 and 25Hz. Corresponding non-dimensional periods are, $T^+ \approx$ 800, 114, 38 and 16, respectively.

Extensive wear occurred on the electrode sheets during testing, especially when the oscillation frequency was high. For PEF = 50Hz (T^+ = 16), failure of the electrode sheet actually happened towards the end of the test, whereby an arc formed between the upper and lower electrodes. This arcing caused severe electromagnetic interference to the hot-wire signal, which caused the sudden dip in mean velocity at $y/\ell^* \approx 2$ in Fig. 10.1.3. The results for $y/\ell^* < 2$ are not

expected to have been effected since data collection proceeded in the positive y direction. This wear was most likely due to excessive heating of the sheet which weakened the dielectric. The material surface appeared brown after the test and was also pitted, probably due to ion bombardment within the plasma. The burnthrough and surface discoloration is shown in Figure 10.1.1 and 10.1.2. An oscillation period of PEF = 50Hz appears to be the upper frequency limit that can be maintained over these Mylar sheets (with PED = 5ms). It may be possible to maintain oscillation at still higher frequency by cooling the dielectric or using another material with better wear resistance (such as ceramic, see Sec. 5.4).

Figure 10.1.3 shows the outer-scaled mean velocity profile with and without plasma at the different oscillation periods. There is a clear decrease in the velocity in the logarithmic region as T^+ decreases. However, the position of maximum velocity change remains constant at $y/5^* = 0.5$. Also, the upper extent of the velocity deficit region remains constant at $y/5^* = 2$. This suggests that the size of the plasma-induced vortices do not change with T^+ (note that the PEF = 50Hz data is not to be trusted for $y/5^* > 2$ due to the sheet failure). Figure 10.1.4 shows the turbulence intensity profile. The velocity fluctuations in the logarithmic portion of the boundary layer increase through reducing T^+ ($y/5^* > 0.5$), along with the velocity fluctuations in the viscous sublayer. This corresponds to an increased number of plasma-induced vortices passing the probe position with time, as expected by the increased oscillation frequency. A trend is not so obvious in the region where the turbulence intensity is reduced ($0.1 < y/5^* < 0.5$).

There is a large effect on the mean velocity in the near wall region with oscillation period. In Fig. 10.1.5, one can clearly see that the near-wall velocity gradient reduces through reducing T^+ (i.e. increasing the oscillation frequency), indicating a greater drag reduction. Table 10.1.1 shows the measured skin-friction coefficient and level of drag reduction, and Fig. 10.1.6 shows the inner-scaled velocity profile. For PEF = 50Hz (T^+ = 16), it is astonishing to see that a drag reduction of 45% occurs. At this frequency, the velocity gradient and mean velocity are much lower than the canonical value, much like the spanwise oscillation studies of Choi et al. (1998). However, the increase in velocity fluctuation near the wall is inconsistent with their results. Also, the oscillation period used here (T^+ = 16) is much smaller than the optimum value for drag reduction using spanwise wall oscillation (T^+ = 100, Jung et al., 1992).

The reduction in skin-friction with T^+ is expected to be related to the plasma-induced spanwise velocity, W^+. Since the plasma forcing is pulsed, it is expected that the average spanwise velocity over the oscillation cycle is increased through reducing T^+ (for fixed PRF, PEF, E). In Sec. 9.4.6 it was shown that when T^+ = 38, $W^+ \approx 4$. Assuming that T^+ and W^+ are inversely proportional, T^+ = 16 should correspond to a spanwise velocity of around $W^+ \approx$ 10. This is close to the optimum for spanwise-wall oscillation, where Choi et al. (1998) showed that $W^+ \approx$ 10-15 gives a drag reduction of 45%. An identical level of drag reduction was also measured in these studies, so that it would seem that it is the spanwise induced velocity that is important for drag reduction, not the oscillation period. It is unfortunate that dielectric wear prevented experiments with $T^+ < 16$ ($W^+ > 10$).

	No Plasma					With Plasma					
PEF (Hz / T^+)	0 mm	δ^* mm	H	u^* m/s	c_f 10^{-3}	0 mm	δ^* mm	H	u^* m/s	c_f 10^{-3}	DR %
1 / 800	7.87	11.26	1.43	0.0763	3.85	7.85	11.28	1.44	0.0773	3.95	-2.5
7 / 114	8.46	11.71	1.38	0.0759	3.69	8.58	12.56	1.46	0.0730	3.41	7.6
21 / 38	8.10	11.61	1.43	0.0766	4.01	8.18	13.84	1.69	0.0669	3.06	23.7
50 / 16	8.63	12.56	1.46	0.0766	3.76	9.28	17.81	1.92	0.0568	2.07	45.0

Table 10.1.1. Boundary layer integral quantities, skin-friction coefficient and drag reduction / increase caused by different plasma oscillation frequency.

Figure 10.1.1. Detail of burnthrough of electrode sheet after the PEF = 50Hz experiment. Note discoloured regions and pitted areas of the Mylar material in plasma regions.

Figure 10.1.2. Discolouration of sheet after the PEF = 50Hz test caused by localised heating of the Mylar.

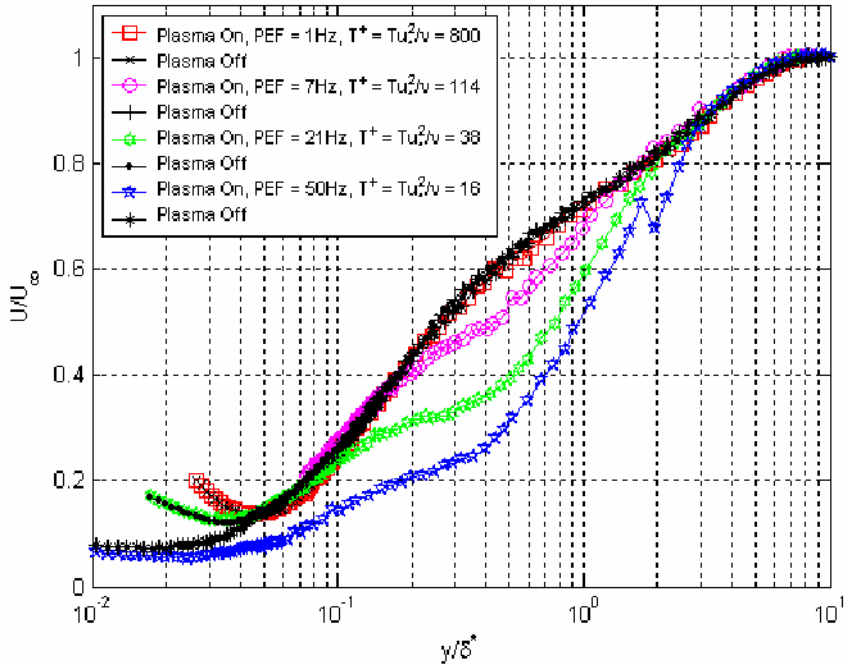

Figure 10.1.3. Mean velocity profile at various oscillation frequencies. PRF = 38kHz, E_{max} = 3.4kV, PED = 5ms, s = 4mm, U_∞ = 1.8m/s, Re_θ = 900. Measurements taken 15mm downstream of electrodes.

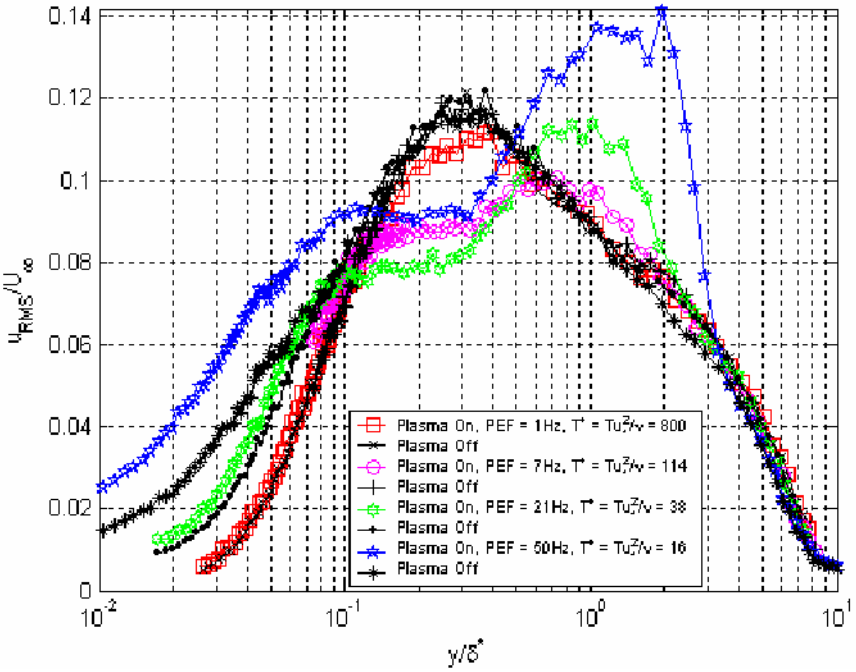

Figure 10.1.4. Turbulent intensity profile at various oscillation frequencies. Plasma conditions as Fig 10.1.3.

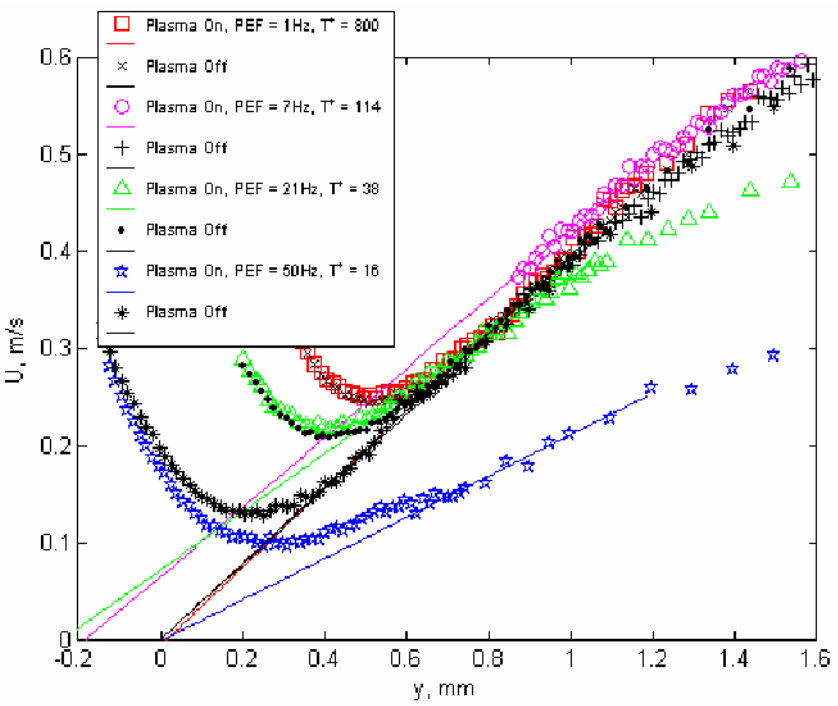

Figure 10.1.5. Near wall velocity profile at various oscillation frequencies. Plasma conditions as Fig. 10.1.3. Behaviour in near wall region (y < 0.5mm) is due to the wall effect. The difference in the wall effect between each sheet is due to different wall boundary conditions.

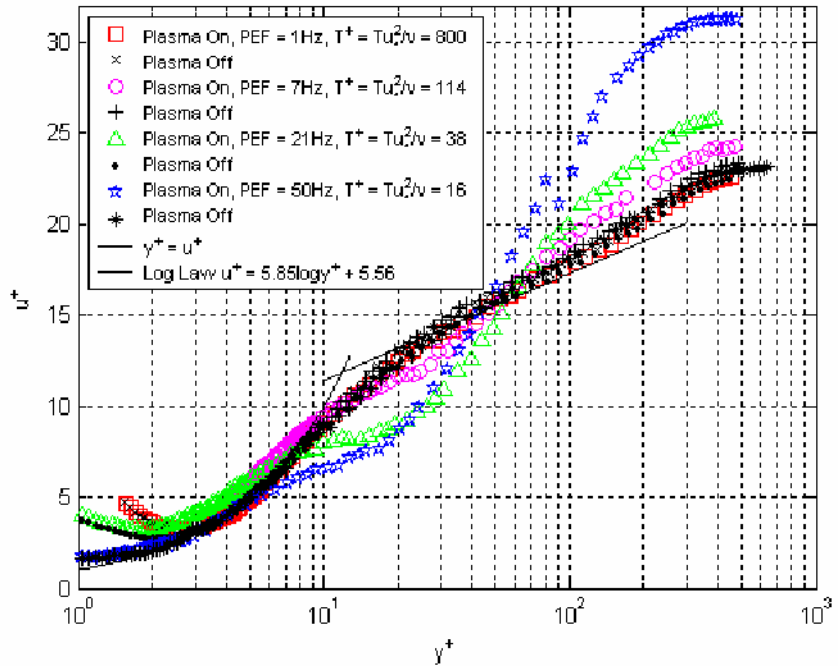

Figure 10.1.6. Inner scaled mean velocity profile without and with plasma at various oscillation frequencies. Plasma conditions as Fig 10.1.3.

10.2. Effect of Electrode Spacing, s

The effect of the electrode spacing, s, on the skin-friction drag was also studied using a single hot wire. Boundary layer traverses were taken over three different electrode sheets with plasma parameters fixed at PRF = 38kHz, E_{max} = 3.4kV, PED = 5ms, PEF = 21Hz (T^+_s 38, i.e. identical parameters as Ch. 9). The sheets had electrode spacing, s = 4, 6 and 10mm (s^+ = 20, 30, 50) between opposing electrodes and velocity measurements were taken at the centreline between opposing pairs (c.f. Fig. 8.3.2c). The 6mm and 10mm spacing sheet were of the 'busless' design, as described in Sec 9.2.2, and measurements were taken 10mm downstream of these electrodes, as opposed to 15mm downstream for the s = 4mm sheet. As in Sec. 10.1, no correction has been made for the thermal boundary layer.

Figures 10.2.1 and 10.2.2 show the outer-scaled mean and fluctuating velocity profiles over the three sheets, respectively. Figure 10.2.1 shows that the velocity deficit region has the same spatial extent irrespective of electrode spacing, suggesting that the height of the plasma-induced vortices do not scale with s. This means that the size of the plasma vortices are related to the lateral extent of the plasma and the plasma forcing parameters. This should come as no surprise since even single, isolated, plasma actuators produced these vortices in initially static air. Increasing s merely increases the spacing between the vortices.

Figure 10.2.1 shows that the mean streamwise velocity near the wall was higher than the canonical value when s > 4mm. Also, the magnitude of the velocity deficit in the logarithmic region was reduced through increasing s. Figure 10.2.2 shows that the velocity fluctuations within the viscous sublayer

were increased with electrode spacing. In addition, the plasma effect on the turbulence intensity in the logarithmic region diminished with s (0.1 U y/ℓ^* U 1).

Table 10.2.1 summarises the measured skin-friction coefficients and level of drag reduction. Figure 10.2.3 shows the near-wall region and Fig. 10.2.4 shows the inner scaled velocity profile. It appears that correct electrode spacing is crucial to achieving drag reduction using oscillatory surface plasma, since drag reduction was only measured for s = 4mm (s^+ = 20). If the spacing is too great, then the skin-friction drag can increase significantly (over 60% when s^+ = 50).

The cause of this drag increase is expected to be due to the increased spacing between plasma-induced streamwise vortices. If the spacing is too great, their spanwise separation will increase to such a degree that they are essentially independent. The induced pumping from each vortex will be increased (downwash / upwash) since the motion of the adjacent co-rotating vortex (upwash / downwash) will have no influence, and vice versa. This will lead to increased transport of high momentum fluid to the wall and an increase in drag. Also, the spanwise oscillatory motion may not be produced because the electrodes are too far apart. The viscous sublayer may only contain discrete section of, say, +w forcing and other section of –w forcing, instead of regions where the motion is oscillatory.

In addition, the induced spanwise velocity, W^+, is expected to be decreased through an increase in s. The plasma induces a tangential flow along the surface (wall-jet), such that spanwise-induced velocity decreases with distance from the electrode. By increasing the electrode spacing, the average induced

spanwise velocity decreases, so that the effect on the viscous sublayer is expected to be less. It may be that increasing s shifts the balance between the near-wall vortex system associated with the spanwise oscillation, and the vortex system associated with the plasma-induced streamwise vortices (c.f. Fig. 9.5.8), such that the induction of high-speed fluid towards the wall by the pumping dominates and thus increases the drag.

With the current electrode sheet design, s = 4mm was the closest electrode spacing that could be used at E_{max} = 3.4kV because the lateral extent of the plasma was nearly equal to the inter-electrode gap. With s < 4mm, the uniform glow will break down into concentrated arcs between electrodes and the plasma forcing will be lost. This may have major implications for industrial applications of the device, where the free stream velocity is much higher. One is likely to wish to increase the plasma forcing to counteract the increased inertial force (by increasing the PRF and $_{Emax)}$. This will inevitably require the electrode spacing to be increased so that arcing can be avoided. Though this study has not addressed the plasma effect with Reynolds number, it is likely that the desired electrode spacing will scale with inner variables. Thus, at higher velocity one requires closer electrode spacing – in direct conflict with the requirement of increased plasma force.

	No Plasma					With Plasma					
s mm/s^+	0 mm	δ^* mm	H	u^* m/s	c_f 10^{-3}	0 mm	δ^* mm	H	u^* m/s	c_f 10^{-3}	DR %
4/20	8.10	11.61	1.43	0.0766	4.01	8.18	13.84	1.69	0.0669	3.06	23.7
6/30	9.06	13.05	1.44	0.0720	3.24	9.22	15.09	1.64	0.0779	3.79	-16.9
10/50	9.21	13.07	1.42	0.0769	3.74	9.82	14.18	1.44	0.0980	6.06	-62.2

Table 10.2.1. Boundary layer quantities and drag change with s.

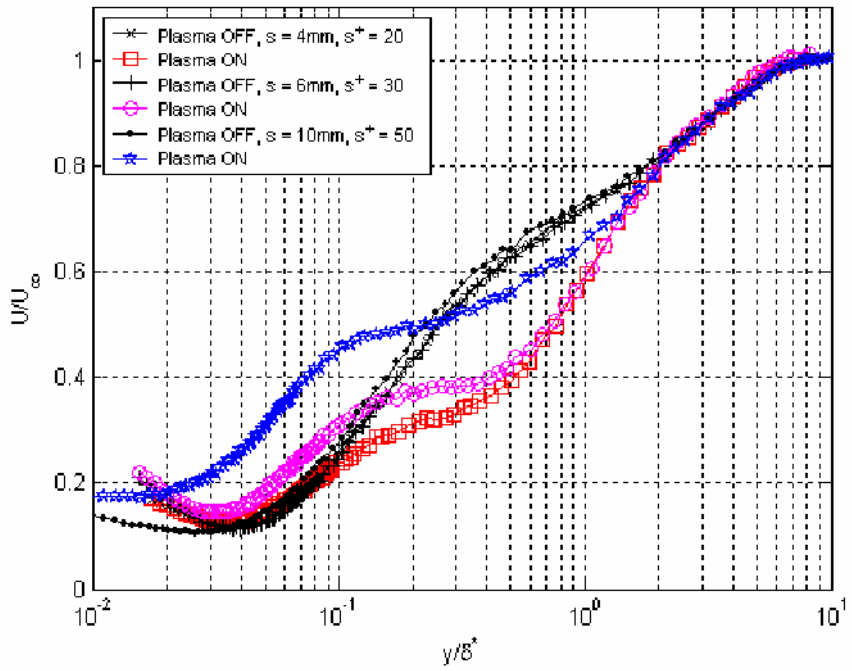

Figure 10.2.1. Mean velocity profile with various electrode spacing, s. PRF = 38kHz, E_{max} = 3.4kV, PED = 5ms, PEF = 21Hz, U_∞ = 1.8m/s, Re_θ = 900.

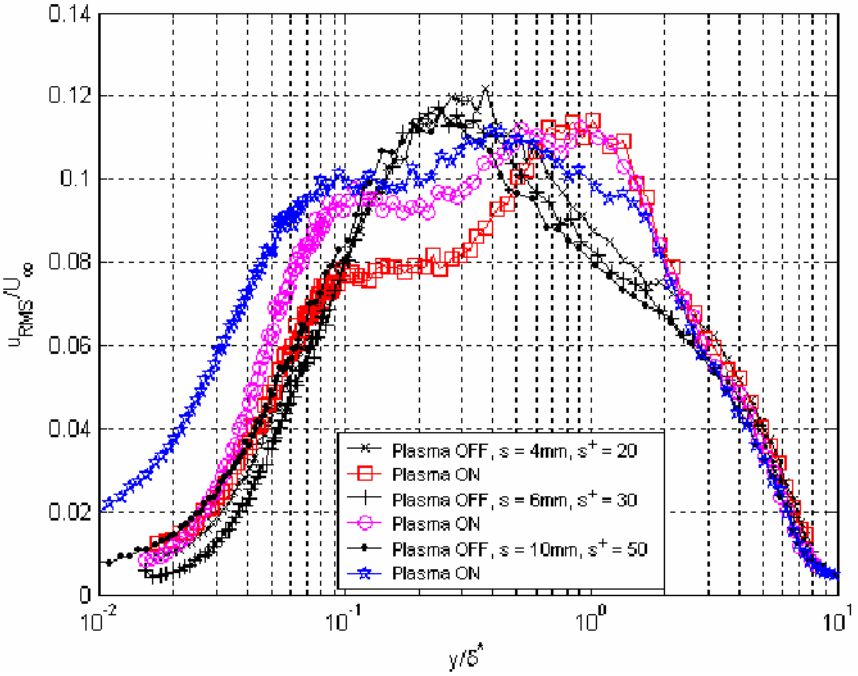

Figure 10.2.2. Turbulent intensity profile with various electrode spacing, s. Plasma conditions as Fig 10.2.1.

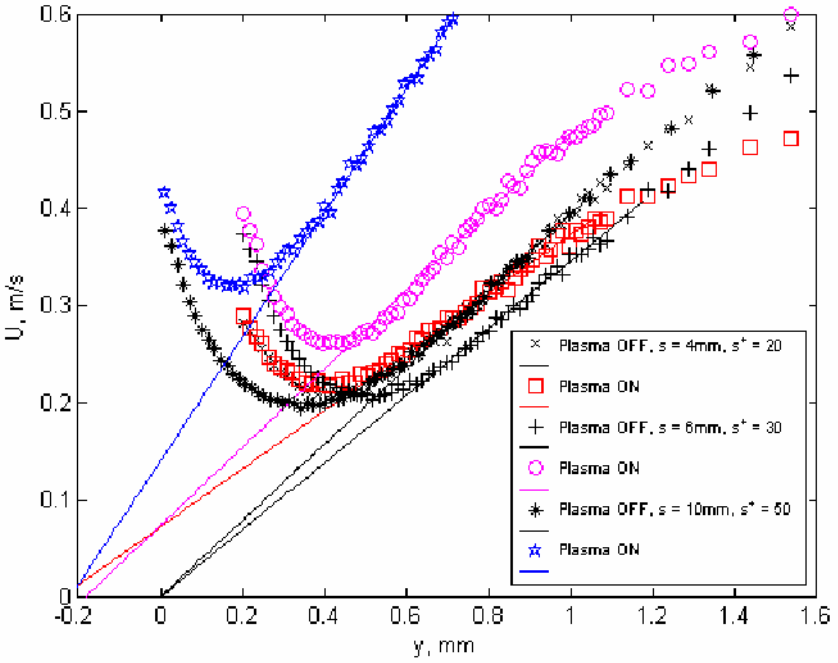

Figure 10.2.3. Inner region of the boundary layer with different electrode spacing. Plasma conditions as Fig 10.2.1. Lines are best fit to viscous sublayer region. Differences between each electrode sheet slightly alter the wall effect characteristics and result in the different behaviour for y < 0.4mm.

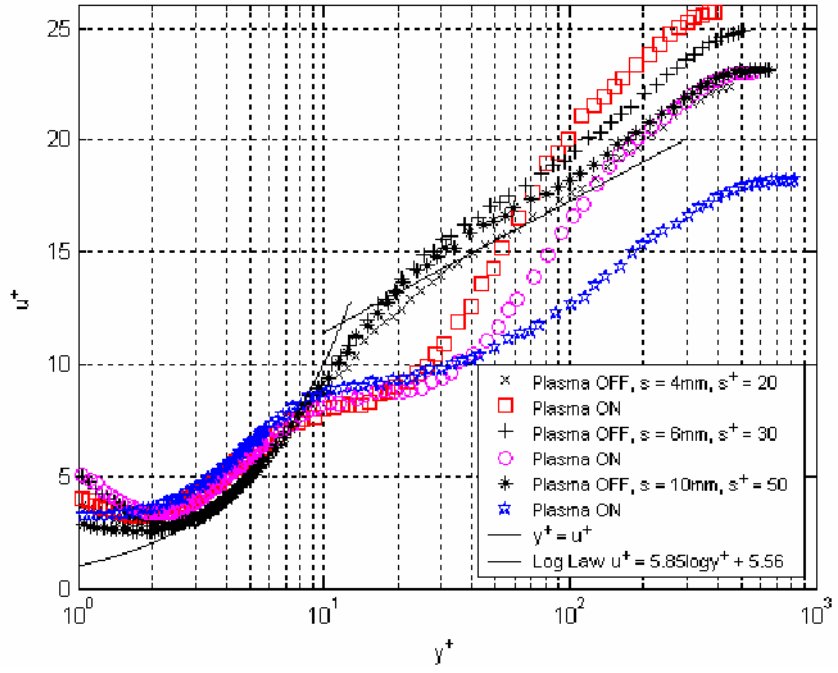

Figure 10.2.4. Inner scaled mean velocity profile with various electrode spacing. Plasma conditions as Fig 10.2.1.

10.3. Effect of Pulse Envelope Duration, PED

The effect of the Pulse Envelope Duration, PED, on the level of drag reduction has also been studied using a single hotwire probe. Due to excessive wear of the s = 4mm electrode sheets during the T^+ experiments in Sec. 10.1, none were available for these experiments. Subsequently, the variation of PED was studied using an electrode sheet with 6mm spacing, which was shown in Sec. 10.2 to cause an increase in drag. The plasma was activated with fixed PRF = 38kHz, E_{max} = 3.4kV, PEF = 21Hz ($T^+ \approx 38$), and boundary measurements were taken with PED = 1, 3 and 5ms (PED^+ = 0.4, 1.1, 1.9). Figure 10.3.1 shows the effect of PED on the outer-scaled mean velocity profile, and Fig 10.3.2 shows the turbulence intensity profiles. It is expected that increasing the PED will increase the near wall acceleration, leading to an increased spanwise-induced velocity and stronger plasma-induced streamwise vortices. Certainly U decreases with PED in the logarithmic region, which would be expected from plasma-induced vortices of increased strength (i.e. more low-momentum fluid is pumped away from the wall by the vortices). Also, the velocity fluctuations in the near wall region are increased with PED, which may be an indicator of increased *w'* motions.

Figure 10.3.3 shows the near wall region with different PED. The velocity gradient is above the canonical in all cases, together with an increase in near-wall velocity magnitude. Table 10.3.1 shows the level of drag increase for the three cases and Fig. 10.3.4 shows the inner-scaled mean velocity profile. The skin-friction has a slight tendency to reduce through increasing the PED. This would tentatively support the conclusion in Sec. 10.1 that it is the spanwise velocity that is important for drag reduction.

	No Plasma					With Plasma					
PED ms	0 mm	δ^* mm	H	u^* m/s	c_f 10^{-3}	0 mm	δ^* mm	H	u^* m/s	c_f 10^{-3}	DR %
1	8.94	12.73	1.42	0.0724	3.21	9.41	13.76	1.46	0.0826	4.18	-30.1
3	9.18	13.08	1.43	0.0727	3.24	9.78	14.81	1.51	0.0756	3.49	-7.9
5	9.06	13.05	1.44	0.0720	3.24	9.22	15.09	1.64	0.0779	3.79	-16.9

Table 10.3.1. Boundary layer integral quantities, friction coefficient based on near velocity gradient and drag reduction / increase caused by the plasma with various PED.

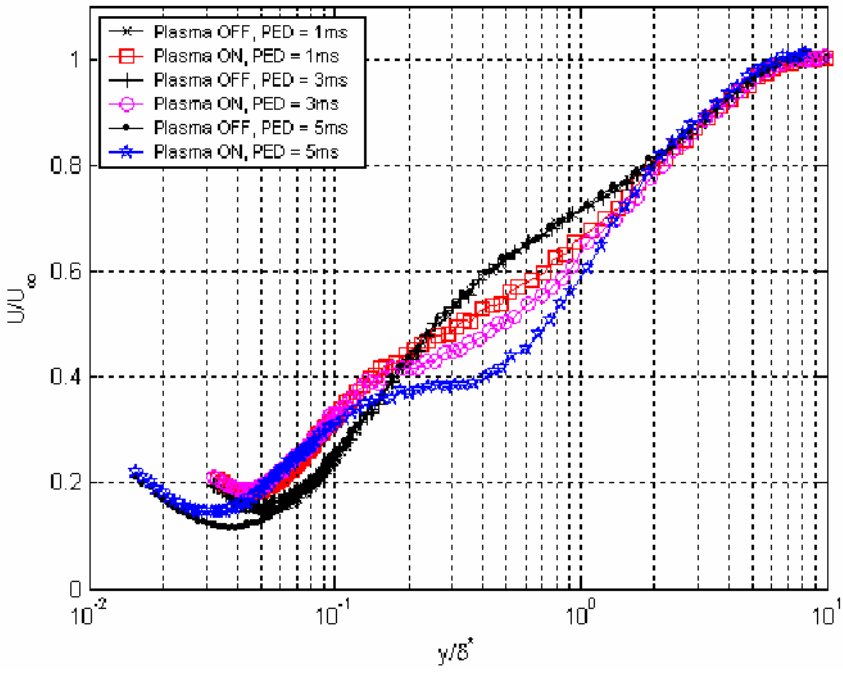

Figure 10.3.1. Mean velocity profile with different PED. PRF = 38kHz, E_{max} = 3.4kV, PEF = 21Hz, U_∞ = 1.8m/s, s = 6mm. Measurements taken 10mm downstream of electrodes.

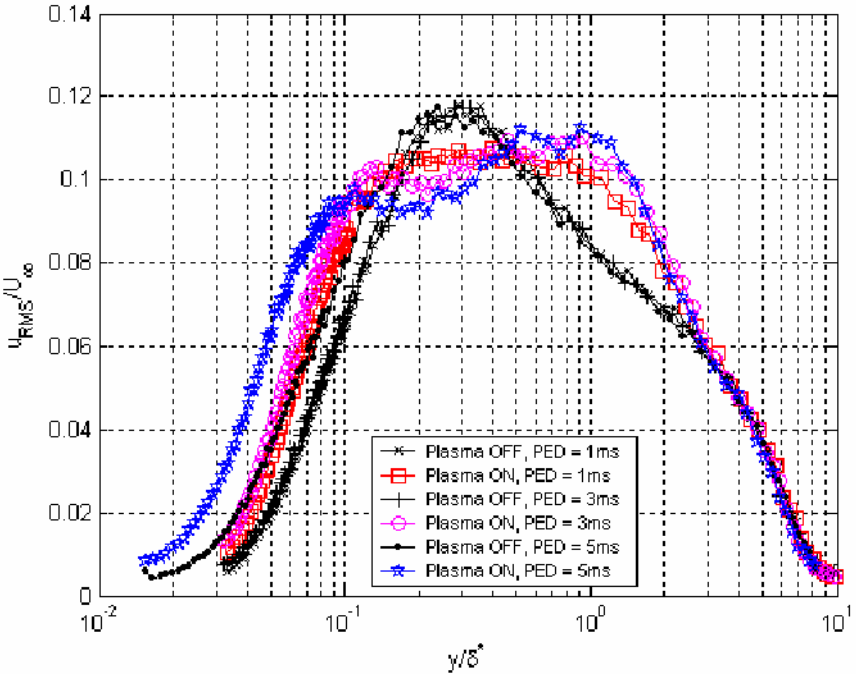

Figure 10.3.2. Turbulent intensity profile with different PED. Plasma conditions as Fig 10.3.1.

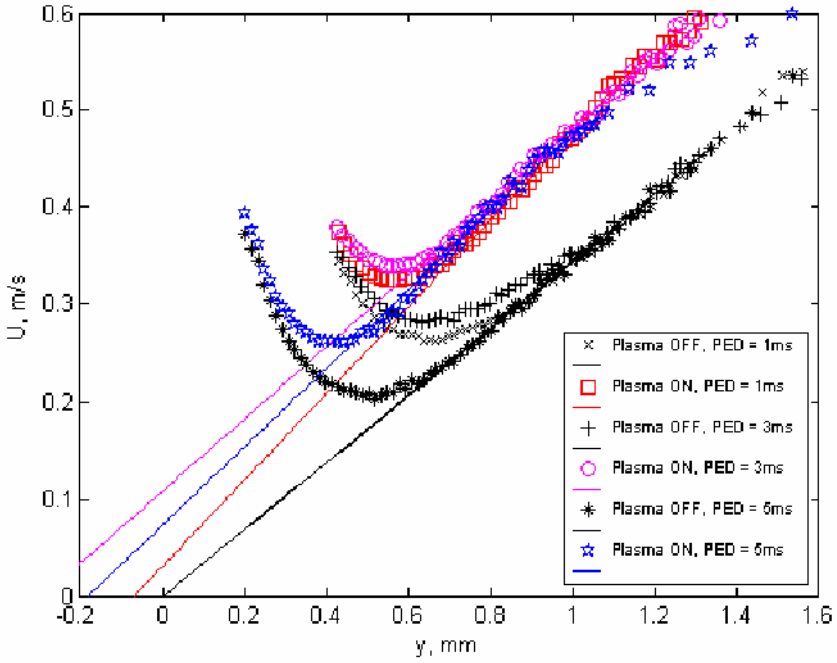

Figure 10.3.3. Inner region of the boundary layer with different PED. Plasma conditions as Fig 10.3.1. Lines are best fit to viscous sublayer region.

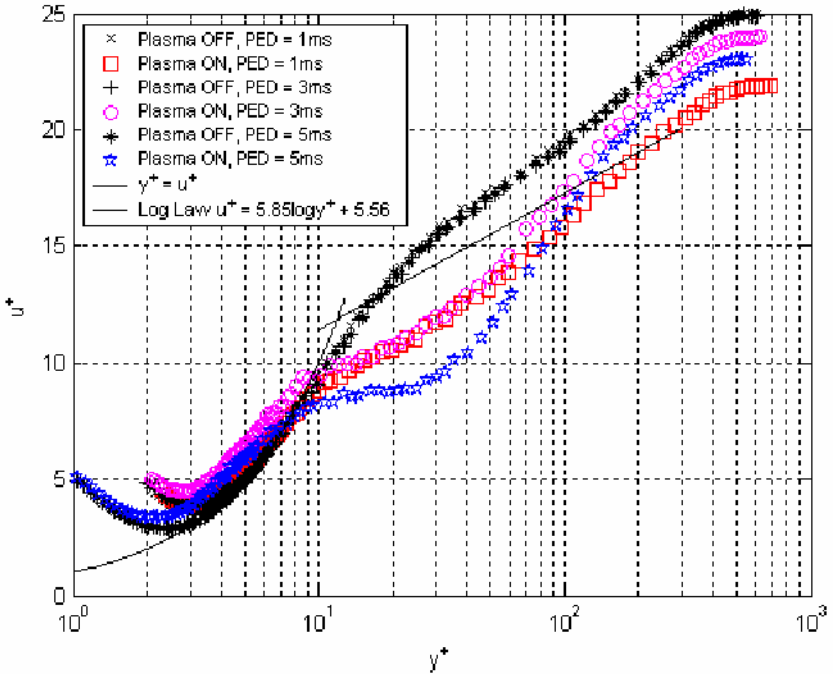

Figure 10.3.4. Inner scaled mean velocity profile with different PED. Plasma conditions as Fig 10.3.1.

Chapter 11

Conclusion and Future Recommendations

11.1. Introduction

Glow discharge surface plasma actuators have been studied in detail in this thesis. The plasma actuators were studied in initially static air in Chaps. 4 to 7, while plasma actuators for skin-friction drag reduction in a turbulent boundary layer were studied in Chaps 8-10. It was shown that the plasma directly transfers electrical energy into fluid momentum which can be used to create a flow of air, and significantly alter an existing flow. This is quite a remarkable development and has huge benefits for the aerospace industry since one could potentially drive and control atmospheric pressure air flow through purely electrical means. It is the author's opinion that we will see plasma actuators in many applications in the future.

11.2. Plasma Actuators in Initially Static Air

In Chaps 4 to 7, it was shown that single plasma actuators can be used to create a flow of gas from the exposed electrode in initially static air, with typical velocity of 2m/s. The plasma acted like a gaseous pump which transferred electrical energy into fluid momentum, such that a wall jet was produced along the electrode sheet surface, away from the electrode centreline. Fluid was entrained into the plasma from above the actuator in order to replace that ejected laterally. The plasma actuators used in this study were generally pulsed on a millisecond timescale such that heating of the

dielectric was minimised and the life of the actuator was prolonged. This produced a series of pulsed wall jets. A novel technique to create wall normal jets with surface plasma actuators was also described in Ch. 7.

The exact cause of the plasma induced flow is not well understood and an empirical approach had to be adopted here as it is extremely difficult to take measurements within the plasma region. Following the work of Enloe et al. (2004a), there are expected to be regions of net charge density within the plasma, particularly near the electrode edge and dielectric surface. These regions exist within a highly non-uniform electric field, so that a force is created within the plasma. This force is expected to be transferred to the ambient gas via the collision of charged plasma particles with molecules of the ambient air. Note that the direction of the force will be the same regardless of the sign of the applied voltage, since the charges at a given location change sign with the electric field.

Some of the previously undocumented behaviour found in this study concerns the formation of vortices when the plasma starts. These vortices appear to be inherent in the actuator design since fluid motion is created in the plasma region (very close to the wall) and then flows into a region without forcing. This junction between the ‘slip’ and ‘no-slip’ boundary conditions will inevitably create vorticity. However, once fluid is in motion, a quasi-steady pulsed wall jet could be maintained indefinitely, subject to wear of the dielectric material.

It was also found that the plasma produced a higher jet velocity during the first few milliseconds of plasma forcing. This was repeated every pulse envelope and was not a manifestation of the initiation vortices. It was suggested that the

plasma is more energetic during initiation due to the absence of pre-ionized air. This is a significant result which may help raise the plasma-induced jet velocity and warrants further investigation.

Symmetric and asymmetric actuator geometries were studied in Ch. 4. These configurations produced respectively bi- and uni-directional forcing, by controlling the plasma formation with the lower electrode. Both plasma actuator types were found to produce airflow with similar characteristics (i.e. wall-jets preceded by initiation vortices), except that the asymmetric actuators produced flow predominantly in one direction. The velocity of the induced flow from the asymmetric actuator was roughly double that of the symmetric actuator due to the enhancement of the electric field.

Parametric studies were undertaken in Chaps 4 and 5 to investigate the magnitude of the induced airflow with the applied voltage, E, pulse repetition frequency, PRF, pulse envelope duration, PED, and pulse envelope frequency, PEF. Figure 3.7.1 explained these parameters and is reproduced here for clarity. Parametric studies were performed for a range of geometries and for Mylar, Si_3N_4 and Al_2O_3 ceramic actuators.

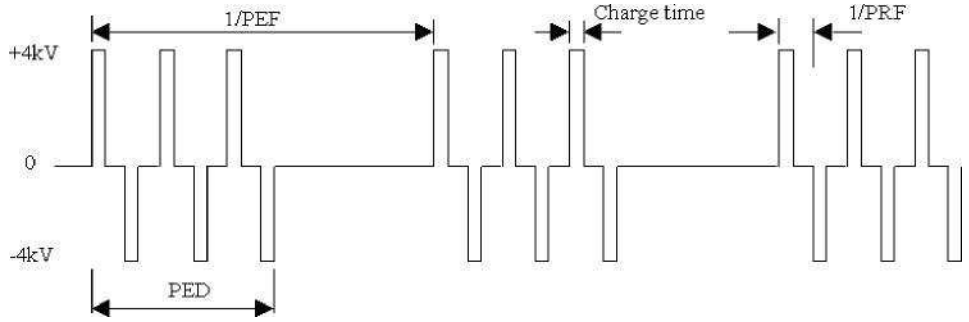

Figure. 3.7.1. Schematic of plasma excitation parameters. Typical excitation parameters were E_{max} = 3.6kV, PRF = 50kHz, Charge Time = 7μs, PEF = 50Hz, PED = 1ms.

For all the actuators studied, the induced jet velocity appeared to vary approximately linearly with the PRF. This showed that the PRF controls the amount of force produced per unit time and the momentum coupling is identical during each AC plasma cycle, except for the first few as described above.

The induced velocity also varied linearly with the PED up to a saturating limit of around PED $\leq$ 3ms under current experimental conditions. This is related to the creation of a higher jet velocity during the first few pulses of plasma formation. The PED alters the duration for which the flow 'sees' the force and should be set to make maximum use of the higher induced velocity during the plasma initiation.

The plasma-induced velocity was also observed to vary linearly with the PEF. This parameter controlled the minimum flow speed between plasma envelopes and thus dictated the gas velocity at the time of the next plasma pulse. However, only a small increase in jet velocity could be achieved by increasing this parameter.

The variation of induced velocity had slightly perplexing characteristics with applied voltage, where one would expect E to control the amount of force produced per AC cycle. When the plasma was continuously fired on a symmetric actuator (i.e. PEF =) and for pulsed plasma on an asymmetric actuator, the maximum induced velocity appeared to vary with $E_{max\ 2}$. However, for pulsed plasma on a symmetric Mylar actuator, the velocity appeared to vary as $E_{max7/2.}$ This 7/2 exponent was also reported by Enloe et al. (2004a) but for asymmetric actuators that were continuously fired. The velocity induced by the ceramic actuator appeared to vary as $E_{max\ 4.3}$. All types

of actuators also showed a saturation effect at high voltage, whereby further increase of the voltage did not increase the velocity further. This has limited the induced velocity to a meagre 2.5m/s in this study, which is probably too low for real aerospace applications.

It was found that the induced velocity could be increased by reducing the thickness of the dielectric sheet. This increases the electric field and enables more charge to be stored due to the increased capacitance of the device, thus leading to the production of a greater force. For Mylar sheets, a 30% increase in velocity was obtained by a 50% reduction in thickness. For $Si3N4$ sheets, the increase in velocity was inversely proportional to the actuator thickness. The efficiency of converting electrical energy into fluid velocity was also increased through decreasing the dielectric sheet thickness, but care should be taken not to decrease this so far that the dielectric will fail.

The induced velocity was also dramatically increased through increasing the dielectric constant of the material. A 200% increase was observed for a Si_3N_4 actuator of similar thickness to Mylar but with a dielectric constant 2.5 higher. Consequently, the induced flow velocity is thought to be proportional to the dielectric constant, at least for this rather limited range. It is therefore believed that the magnitude of the induced flow could be dramatically increased by using very thin samples of high r ceramics.

11.3. Spanwise Oscillation Plasma for Drag Reduction

In Chaps 8-10, the plasma actuators were used to modify the skin-friction of a fully developed turbulent boundary layer at Re_τ = 380. The plasma was used to create spanwise oscillatory forcing at the wall by utilising two sets of opposing asymmetric plasma actuators. An extensive study was presented in Ch. 9, where the electrode sheet had an electrode spacing, s, of 4mm between opposing pairs (s^+ = 20) and plasma excitation parameters were set with a PRF = 38kHz, E_{max} = 3.3kV, PED = 5ms, and PEF = 21Hz. Thus, the plasma produced periodic forcing with a non-dimensional period, T^+ = 38 and the non-dimensional spanwise velocity was estimated to be W^+ = 4. Measurements of U, V, W and T were taken throughout the boundary layer using hot- and cold-wire anemometry. Flow visualisation was also presented in initially static air in Ch. 8.

The mean velocity profile showed that the plasma caused skin-friction drag to be reduced by 22%. There was a small spanwise variation but drag was reduced significantly over the entire sheet, not just the small region between opposing electrodes where the plasma was present. A large streamwise velocity deficit occurred in the logarithmic region of the boundary layer, extending for $6 < y^+ < 110$, with a maximum of 40% reduction in U. Velocity fluctuations, *u'*, were reduced by as much as 30% for $6 < y^+ < 30$, whilst increased by up to 30% for $30 < y^+ < 140$. Cold-wire measurements showed that the plasma induces a thermal boundary layer of similar thickness to the velocity deficit region, with a maximum air temperature increase of 2.5°C occurring at $y^+ = 25$.

The energy spectra showed that, in the near-wall region, there was a shift of energy transfer from large scale eddies to small scale eddies. VITA analysis confirmed that the plasma caused a 70% reduction in the duration of sweep events and their intensity was reduced by around 20%. The frequency of near-wall events roughly tripled, indicating that the plasma-induced motions were leading to premature sweeps.

It was suggested that the plasma caused oscillating sets of co-rotating vortices to be embedded in the logarithmic region of the boundary layer. These vortices were expected to have a diameter of around 40 viscous units and be centred at around $y^+ = 30$; similar to the naturally existing quasi-streamwise vortices which have centres located at around $y^+ = 15\text{-}25$ (Kim et al., 1971). However, contrary to the 'natural' counter-rotating streamwise vortices, the plasma-induced vortices were co-rotating. These vortices will move in the spanwise direction and increase in size after each plasma forcing, and will change rotation sense and direction throughout the AC cycle.

The formation of these streamwise vortices was postulated to be disrupting the link between the outer and inner boundary layer structures and appeared to act like a 'barrier' to block large scale motions near the wall. It was thought that they may be severing the link between the hairpin vortex legs and necks, thus altering the whole turbulence production cycle. It was also suggested that another vortex system was located below the streamwise vortices associated with the oscillatory spanwise motions in the viscous sublayer (c.f. Fig. 9.5.8). This system is thought to reduce the near wall velocity gradient and cause the drag reduction.

Choi et al. (1998), found that for spanwise wall oscillation, the maximum local drag reduction actually occurred close to the midpoint of the oscillating plate (1800 viscous units upstream of the end of a plate). At $x^+ \approx 140$ downstream, the level of drag reduction was only one half of the maximum. If this were true for the plasma case, a maximum drag reduction of around 35% is expected since 22% drag reduction was recorded at $x^+ \approx 75$ downstream of the plasma. However no measurement of local skin-friction was possible due to the high voltages required to create the plasma and the sensitive nature of hot-wire probes.

The magnitude of viscous drag was reduced further through decreasing the oscillation period, T^+. A maximum drag reduction of 45% was recorded at the downstream edge of the electrode sheet when $T^+ = 16$. This is somewhat lower (higher frequency) than the optimum oscillation period for mechanical and Lorentz spanwise oscillations which occurs at $T^+ \approx 100$ (Jung et al. 1992). However, the spanwise induced velocity was estimated to be $W^+ \approx 10$, which is nearly identical to the optimum for spanwise wall-oscillation of Choi et al. (1998). This would suggest that it is the spanwise induced velocity that is important for drag reduction, not the oscillation period. It was also observed that the electrode spacing was critical to achieving drag reduction, with any benefit being lost for $s^+ > 30$.

Though it has been shown that skin-friction drag can be significantly reduced using surface plasma, one must address the issue of energy efficiency. In the experimental data, a maximum drag reduction of 45% has been observed at the downstream edge of the electrode sheet. The level of drag reduction within the plasma region is not known, but is expected to be at least this value.

Taking 50% drag reduction over the entire 366 x 304mm area, the net energy saved is:

$$P_{saved} = \text{åIJ}_w.A.U, \S\ 0.001W \qquad (11.3.1)$$

Figure 11.3.1 shows the voltage and current waveforms delivered to the electrodes sheet. On integrating and multiplying by the duty cycle, the electrical energy supplied to the electrode sheet is:

$$P_{elec} = PED.PEF.\frac{PRF}{2}\int_0^{t_{AC}} EI\,dt = 10W \qquad (11.3.2)$$

Note, that this is the total energy supplied to the sheet. Not all of this energy is directly consumed by the plasma, as was discussed in the AIAA J. paper in Sec. 4.3. Nevertheless, the efficiency of the plasma actuators is at most 10^{-2} %. Improvements to the material properties and driving circuit may improve this but it is expected that the efficiency, at least in these low-speed tests with the present electrode design, will be no better than 10^{-1} %.

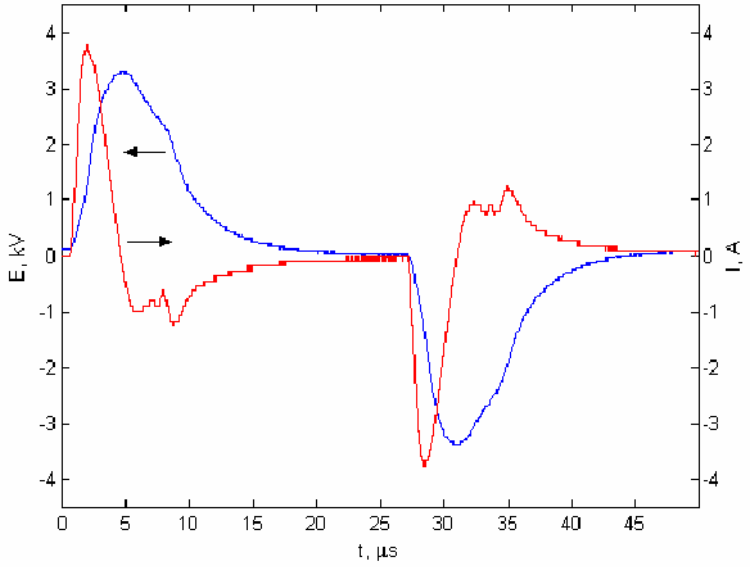

Figure 11.3.1. Voltage (-) and current (-) waveforms delivered to the spanwise oscillation electrode sheet during one AC cycle of plasma formation. Waveforms averaged over 128 cycles to eliminate random noise.

Though the efficiency is discouraging, little is known about the viability of using this approach at higher Reynolds number. Power lost to skin-friction drag varies as U_∞^3, yet Chaps. 4 and 5 showed that the plasma-induced velocity varies linearly with power. This means that there must be some value of U_∞ whereby the power lost to skin-friction is greater than the power required to create plasma with $W^+ \leq 10$, so that the device becomes efficient. This is estimated to be at around U_∞ = 200m/s. In addition, a commercial airliner at typical cruising speed expends about 5000W/m^2 to overcome skin-friction (Roth et al. 1998), whereas the plasma actuator sheets used here consumed around 80W/m^2 at the present experimental conditions. Thus a drag reduction of only a few percent would make the device economically viable. However, as mentioned in Sec. 10.2, there will be problems with scaling W^+ and s^+ to the optimal conditions in this thesis. As U_∞ increases, one has to increase W which requires an increase in the applied voltage, thus increasing the lateral extent of the plasma. However, it is also expected that the electrode spacing, s, will need to be reduced. This is not possible since the plasma will arc between adjacent electrodes and the spanwise oscillation will be lost. In addition, the induced velocity was not able to be increased above 3m/s in the present study. This induced flow must be increased at least ten-fold before the technology really looks feasible on actual aerodynamic applications. Nevertheless, the occurrence of 45% drag reduction certainly warrants further investigation.

11.4. Summary

- Plasma actuators act as gaseous pumps which directly convert electrical energy to fluid momentum.
- Skin-friction drag was reduced by up to 45% by using plasma to create a spanwise oscillating force near the wall of a turbulent boundary layer ($Re_\tau = 380$).
- Maximum drag reduction occurred when $T^+ = 16$, $s^+ = 20$, $W^+ \approx 10$.
- Such forcing produces a spanwise oscillation effect, similar to mechanical-wall oscillation, and the creation of oscillatory sets of co-rotating vortices near the wall ($y^+ < 60$) which add to the spanwise oscillation effect.
- Plasma causes 'premature' sweeps of reduced duration and intensity but increased frequency, thus reducing drag.
- In stationary air, the actuators initially create start-up vortices then produce a laminar wall-jet along the electrode sheet surface with velocity magnitude of the order of 1m/s and jet thickness of the order of 1mm.
- Higher jet velocity can be produced by increasing the voltage or frequency, increasing the dielectric constant of the material, or reducing the actuator thickness.
- Wall-normal jets can also be created by placing actuators side by side or in annular rings.

11.5. Future Recommendations

Thermal anemometry was used in this study to invoke the 2D flow profile around surface plasma actuators. It is recommended that the structure of starting vortices and laminar wall jets be further investigated with a global velocity measurement system, such as PIV. However, care should be taken since the electric field may directly influence seeding particles.

In all of the static air testing, the induced wall jet velocity could not be raised above 3m/s, which is not very attractive for the use of plasma actuators in real aerospace applications. The actuator efficiency and induced flow was, however, substantially improved by using ceramics with higher dielectric constant. The induced flow seemed directly proportional to ε, at least over the limited range used here. The question remains as to what will happen if materials with considerably larger dielectric constant are used, for example lead zirconium titanate (PZT) which has a dielectric constant of 820. This should significantly increase the velocity of the induced jet. It is also recommended that the actuators be activated with a much higher voltage (many tens of kV) on ceramic actuators with high dielectric strength. This too will dramatically increase the induced flow velocity which may make the actuators more appropriate for large-scale use.

It is apparent that understanding of the complete plasma physics (including momentum coupling to the ambient gas) is required to fully appreciate the plasma actuator, and it is suggested that numerical simulation should be used. This would help explain some of the effects here (e.g. the induced velocity variation with $E^{7/2}$ and E^2 for symmetric and asymmetric actuators respectively and the saturation of induced flow at the highest available

voltages). Such modelling will require solution of Maxwell's equations coupled to the Navier Stokes equations, with special attention to the changes in dielectric properties due to heating and the electric field. Such a task would be quite formidable, although this may help gain insights as to how to raise the induced airflow and increase the efficiency.

During the boundary layer tests, it was observed that the plasma caused an increase in mean velocity in the viscous sublayer whilst the velocity gradient is reduced. This phenomenon was explained due to error in the hot wire caused by non-streamwise velocity components induced by the plasma. The reduction in skin-friction should, however, be verified by another method of measuring drag. Ideally this should be a direct measuring device, such as using a Fibre-Bragg grating system, as used by Segawa et al. (2005). PIV measurements should also be taken in order to directly verify the spatial locations of the plasma-induced co-rotating streamwise vortices, and to observe the modifications to the boundary layer structure.

The maximum drag reduction in this study was 45% at Re_{τ} = 380. Although this is a very low Reynolds number the drag reduction is considerable, which certainly warrants further investigation. It is recommended that further tests be performed to see how the plasma-induced vortices, level of drag reduction and efficiency varies at higher Reynolds numbers.

References

Adrian, R. J., Meinhart, C. D. and Tomkins, C. D., 2000, "Vortex Organization in the Outer Region of the Turbulent Boundary Layer", J. Fluid Mech., **422**, pp. 1-54.

Allen, J. J., and Naitoh, T., 2005, "Instability of a Vortex Junction", Under consideration for publication in J. Fluid Mech.

Almquist, P. and Legath, E., 1965, "The Hot-Wire Anemometer at Low Velocities", DISA Info., No. 2, pp. 3-4.

Andreopoulos, J., Durst, F., Zaric, Z., and Jovanovic, J., 1984, "Influence of Reynolds Number on Characteristics of Turbulent Wall Boundary Layers", Exp. in Fluids, **2**, pp. 7-16.

Antonia, R. A., 1981, "Conditional Sampling in Turbulence Measurement", Ann. Rev. Fluid Mech., **13**, pp. 131-156.

Antonia, R. A., Zhu, Y., and Sokolov, M., 1995, "Effect of Concentrated Wall Suction on a Turbulent Boundary Layer", Phys. Fluids, **7**, No. 10, pp. 2465-2474.

Artana, G., DiPrimion, G., Moreau, E., and Touchard, G., 2001, "Electrohydrodynamic Actuators on a Subsonic Airflow Around a Circular Cylinder", 32nd Plasmadynamics and Lasers Conference and 4th Weakly Ionised Gases Workshop, 11-14 June, Anaheim, CA, AIAA 2001-3056.

Artana, G., Sosa, R., Moreau, E., and Touchard, G., 2003, "Control of the Near-Wake Flow around a Circular Cylinder with Electrohydrodynamic Actuators", Exp. in Fluids, **35**, pp. 560-588.

Asghar, A, and Jumper, E. J., 2003, "Phase Synchronization of Vortex Shedding from Multiple Cylinders Using Plasma Actuators", 41st Aerospace Sciences Meeting and Exhibit, 6-9 Jan, Reno, NV, AIAA 2003-1028.

Aydin, M. and Leutheusser, H. J., 1980, "Very Low velocity Calibration and Application of Hot-Wire Probes", DISA Info., No. 25, pp. 17-18.

Bandyopadhyay, P. R., 1986, "Mean Flow in Turbulent Boundary Layers Disturbed to Alter Skin Friction", J. Fluids Eng. Trans. ASME, **108**, No. 2, pp. 127-140.

Bahder, T. B., and Fazi, C., 2003, "Force on an Asymmetric Capacitor", Army Research Laboratory Tech. Report, Adelphi, MD, No. ARL-TR-3005. Available at http://jlnlabs.imars.com/lifters/arl_fac/0211001.pdf

Baron, A., and Quadrio, M., 1996, "Turbulent Drag Reduction by Spanwise Wall Oscillations", App. Sci. Res., **55**, pp. 311-326.

Berger, T. W., Kim, J., Lee, C., Lim., J., 2000, "Turbulent Boundary Layer Control Utilizing the Lorentz Force", Phys. Fluids, **12**, No. 3, pp. 631-649.

Berman, N. S., 1978, "Drag Reduction by Polymers", Ann. Rev. Fluid Mech., **10**, pp. 47-64.

Blackwelder, R. F., and Kaplan, R. E., 1976, "On the Wall Structure of the Turbulent Boundary Layer", J. Fluid Mech., **76**, pp. 89-112.

Bradshaw, P., 1971, An Introduction to Turbulence and its Measurement, Pergamon Press, UK.

Bradshaw, P., 1987, "Turbulent Secondary Flows", Ann. Rev. Fluid Mech., **19**, pp. 53-74.

Bradshaw, P., and Pontikos, N., 1985, "Measurements in a Turbulent Boundary Layer on an Infinite Swept Wing", J. Fluid Mech., **159**, pp. 105-130.

Breuer, K. S., Park. J., and Henoch, C., 2004, "Actuation and Control of a Turbulent Channel Flow Using Lorentz Forces", Phys. Fluids, **16**, No. 4, pp. 897-907.

Bruun, H., H., 1995, Hot-wire Anemometry: Principles and Signal Analysis, Oxford University Press, New York, ISBN 0198563426.

Champagne, F. H., Sleicher, C. A., and Wehrmann, O. H., 1967, "Turbulence Measurements with Inclined Hot-wires Part 1. Heat Transfer Experiments with Inclined Hot-wire", J. Fluid Mech., **28**, pp. 153-175.

Choi, J-I., Xu, C-X., and Sung, H. J., 2002, "Drag Reduction by Spanwise Wall Oscillation in Wall-Bounded Turbulent Flows", AIAA J., **40**, No. 5, pp. 842-850.

Choi, K.-S., 1987, "On Physical Mechanisms of Turbulent Drag Reduction using Riblets", In Hirata, M., and Kasagi, N., eds., Transport Phenomena in Turbulent Flows. New York: Hemisphere, pp. 185-198.

Choi, K.-S., 1989, "Near-wall Structure of Turbulent Boundary Layer with Riblets", J. Fluid Mech., **208**, pp. 417-458.

Choi, K.-S., 2001, "Turbulent Drag-Reduction Mechanisms: Strategies for Turbulence Management", In Turbulence Structure and Modulation, CISM Courses and Lectures No. 415, eds. Soldati, A., and Monti, R., Springer-Verlag.

Choi, K.-S., 2002, "Near-wall Structure of Turbulent Boundary Layer with Spanwise–Wall Oscillation," Phys. Fluids, **14**, No. 7, pp. 2530-2542.

Choi, K.-S., 2005, "Drag Reduction by Spanwise Flow Control of Near-Wall Turbulence", 2nd Int. Symp. Seawater Drag Reduction, 23-26 May, Busan, Korea.

Choi, K.-S., and Clayton, B. R., 2001, "The Mechanism of Turbulent Drag Reduction with Wall Oscillation", Int. J. Heat and Fluid Flow, **22**, pp. 1-9.

Choi, K-S., and Graham, M., 1998, "Drag Reduction of Turbulent Pipe Flow by Circular-Wall Oscillation", Phys. Fluids, **10**. No. 1, pp. 7-9.

Choi, K.-S., Yang, X., Clayton, B. R., Glover, E. J., Atlar, M., Semenov, B. N., and Kulik, V. M., 1997, "Turbulent Drag Reduction using Compliant Surfaces", Proc. Royal Society. A453, pp. 2229-2240.

Choi, K.-S., DeBisschop, J.-R., and Clayton, B. R., 1998, "Turbulent Boundary-Layer Control by Means of Spanwise-Wall Oscillation", AIAA J., **36**, No. 7, pp. 1157-1163.

Chun, D. H., and Schwarz, W. H., 1967, "Stability of the Plane Incompressible Viscous Wall Jet Subjected to Small Disturbances," Phys. Fluids, **10**, 911-915.

Clauser, F., 1954, "Turbulent boundary layers in adverse pressure gradients", J. Aero. Sci., **21**, 91–108.

Clauser, F. H., 1956, "The Turbulent Boundary Layer", Adv. Appl. Mech., **4**, pp. 1-54.

Collis, D. C. and Williams, M. J., 1959, "Two-Dimensional Convection from Heated Wires at Low Reynolds Numbers", J. Fluid Mech., **6**, pp. 357-384.

Corino, E. R. and Brodkey, R. S., 1969, "A Visual Investigation of the Wall Region in a Turbulent Flow", J. Fluid Mech., **37**, 1, pp. 1-30.

Corke, T. C., and Matlis, E., 2000, "Phased Plasma Arrays for Unsteady Flow Control", Fluids 2000 Conference and Exhibit, 19-22 June, Denver, CO, AIAA 2000-2323.

Corke, T. C., and Post, M. L., 2005, "Overview of Plasma Flow Control: Concepts, Optimization, and Applications", 43rd Aerospace Sciences Meeting, 10-14 Jan, Reno, NV, AIAA 2005-0563.

Corke, T. C., Jumper, E. J., Post, M. L., Orlov, D., McLaughlin, T. E., 2002, "Application of Weakly-ionized Plasmas as Wing Flow-Control Devices", 40th Aerospace Sciences Meeting and Exhibit, 14-17 Jan, Reno, NV, AIAA 2002-0350.

Corke, T. C., He, C., and Patel, M., 2004, "Plasma Flaps and Slats: An Application of Weakly-Ionized Plasma Actuators", 2nd Flow Control Conference, 28 Jun – 1 July, Portland, OR, AIAA 2004-2127.

Corrsin, S., 1943, "Investigation of Flow in an Axially Symmetric Heated Jet of Air", NACA Adv. Conf. Rep. 3123.

Corrsin, S., Kistler, A. L., 1954, "The Free-Stream Boundaries of Turbulent Flows", NACA TN-3133.

Crawford, C. H., and Karniadakis, G. E., 1997, "Reynolds Stress Analysis of EMHD-controlled Wall Turbulence. Part I. Streamwise Forcing", Phys. Fluids, **9**, No. 3, pp. 788-806.

D'Adamo, J, Artana, G., Moreau, E., and Touchard, G., 2002, "Control of the Airflow Close to a Flat Plate with Electrohydrodynamic Actuators", ASME 2002 Fluids Engineering Division Summer Meeting, 14-18 July, Montreal, FEDSM2002-31041.

Dhanak, M. R., and Si, C., 1999, "On Reduction of Turbulent Wall Skin Friction through Spanwise Wall Oscillations", J. Fluid Mech., **383**, pp. 175-195.

Di Cicca, G. M., and Iuso, G., 2006, "On Large-Scale Vortical Structures Produced by a Yawed Synthetic Jet – Turbulent Boundary Layer Interaction", 3rd AIAA Flow Control Conference, 5-8 June, San Francisco, CA, AIAA 2006-2861.

Dring, R. P. and Gebhart, B., 1969, "Hot-Wire Anemometer Calibration for Measurements at Very Low Velocity", ASME J. Heat Transfer, **91**, pp. 241-244.

El-Khabiry, S., and Colver, G. M., 1997, "Drag Reduction by DC Corona Discharge Along an Electrically Conductive Flat Plate for Small Reynolds Number Flow", Phys. Fluids, **9**, No. 3, pp. 587-599.

Enloe, C. L., McLaughlin, T. E., VanDyken, R. D., Kachner, K. D., Jumper, E. J., Corke, T. C., Post. M., Haddad, O., 2004a, "Mechanisms and Responses of a Single Dielectric Barrier Plasma Actuator: Geometric Effects", AIAA J., **42**, No.3, pp. 595-604.

Enloe, C. L., McLaughlin, T. E., VanDyken, R. D., Kachner, K. D., Jumper, E. J., Corke, T. C., 2004b, "Mechanisms and Responses of a Single Dielectric Barrier Plasma Actuator: Plasma Morphology", AIAA J., **42**, No.3, pp. 589-594., also AIAA 2003-1021.

Enloe, C. L., McLaughlin, T. E., Font, G. I., and Baughn, J. W., 2005, "Parameterization of Temporal Structure in the Single Dielectric Barrier Aerodynamic Plasma Actuator", 43rd Aerospace Sciences Meeting, 10-13 Jan, Reno, NV, AIAA 2005-0564.

Falco, R. E., 1977, "Coherent Motions in the Outer Region of Turbulent Boundary Layers", Phys. Fluids, **20**, pp. S124-S132.

Favre, A. J., Gaviglio, J. J., and Dumas, R., 1957, "Space-time Double Correlations and Spectra in a Turbulent Boundary Layer", J. Fluid Mech., **2**, pp. 313-341.

Fomin, V. M., Tretyakov, P. K., and Taran, J.-P., 2004, "Flow Control Using Various Plasma and Aerodynamic Approaches (Short Review)", Aero. Sci. and Tech., **8**, pp. 411-421.

Frolich, H., 1958, Theory of Dielectrics – Dielectric Constant and Dielectric Loss, Oxford University Press.

Gad-el-Hak, 2000, Flow Control: Passive, Active and Reactive Flow, Cambridge University Press.

Gibalov, V. I., and Pietsch, G. J., 2000, "The Development of Dielectric Barrier Discharges in Gas Gaps and on Surfaces", J. Phys, D: Appl. Phys., **33**, pp. 2618-2636.

Glauert, M. B., 1956, "The Wall Jet," J. Fluid Mech., **1**, pp. 625-643.

Glezer, A., and Amitay, M., 2002, "Synthetic Jets", Ann. Rev. Fluid Mech., **34**, pp. 503-529.

Head, M. R. and Bandyopadhyay, P, 1981, "New Aspects of Turbulent Boundary-Layer Structure", J. Fluid Mech., **107**, pp. 297-338.

Huang, J., Corke, T. C., Thomas, F. O., 2003, "Plasma Actuators for Separation Control of Low Pressure Turbine Blades", 41st Aerospace Sciences Meeting and Exhibit, 6-9 Jan, Reno, NV, AIAA 2003-1027.

Hultgren, L., S., and Ashpis, D. E., 2003, "Demonstration of Separation Delay with Glow-Discharge Plasma Actuators", 41st Aerospace Sciences Meeting and Exhibit, 6-9 Jan, Reno, NV, AIAA 2003-1025.

Hussain, A. K. M. F., 1986, "Coherent Structures and Turbulence", J. Fluid Mech., **173**, pp. 303-356.

Hutchins, N. and Choi, K.-S., 2002, "Accurate Measurements of Local Skin Friction Coefficient using Hot-wire Anemometry," Prog. Aero. Sci., **38**, pp. 421-446.

Hutchins, N., 2003, An Investigation of Larger-Scale Coherent Structures in Fully Developed Turbulent Boundary Layers, PhD Thesis, University of Nottingham.

Johnson, G. A., and Scott, S. J., 2001, "Plasma-Aerodynamic Boundary Layer Interaction Studies", 32nd Plasmadynamics and Lasers Conference and 4th Weakly Ionised Gases Workshop, 11-14 June, Anaheim, CA, AIAA 2001-3052.

Jung, W. J., Mangiavacchi, N., and Akhavan, R., 1992, "Suppression of Turbulence in Wall-Bounded Flows by High Frequency Spanwise Oscillation", Phys. Fluids A, **4**, pp. 1605-1607.

Karniadakis, G. E., and Choi, K.-S., 2003, "Mechanisms on Transverse Motions in Turbulent Wall Flows," Ann. Rev. Fluid Mech., **35**, pp. 45-62.

Kim, H. T., Kline, S. J. and Reynolds, W. C., 1971, "The Production of Turbulence Near a Smooth Wall in a Turbulent Boundary Layer", J. Fluid Mech., **50**, No. 1, pp. 133-160.

Kim, J., 2005, "Physics of Wall Turbulence: A Perspective on Boundary-Layer Control", 2nd Int. Symp. on Seawater Drag Reduction, 23-26 May, Busan, Korea.

King, L. V., 1914, "On the Convection of Heat from Small Cylinders in a Stream of Fluid: Determination of Convection Constants of Small Platinum Wire with Applications to Hot-Wire Anemometry", Phil. Trans. Roy. Soc., **A214**, pp. 373-432.

Klebanoff, P. S., 1954, "Characteristics of Turbulence in a boundary Layer with Zero pressure Gradient", NACA TN 3178.

Kline, S. J., and McClintock, F. A., 1953, "Describing Uncertainties in Single-Sample Experiments", Mech. Eng., **75**, pp. 3-8.

Kline, S. J., Reynolds, W. C., Schraub, F. A. and Runstadler, P. W., 1967, "The Structure of Turbulent Boundary Layers", J. Fluid Mech., **30**, 4, pp. 741-773.

Kline, S. J., and Robinson, S. K., 1989a, "Quasi-Coherent Structures in the Turbulent Boundary Layer. Part I: Status Report on a Community-Wide Summary of the Data", In Near Wall Turbulence. Proc. Zaric Meml. Conf. 1988, eds. Kline, S. J. and Afgan, N. H., pp. 200-217.

Kline, S. J., and Robinson, S. K., 1989b, "Turbulent Boundary Layer Structure: Progress, Status, and Challenges", Proc. 2nd IUTAM Symp. Struct. of Turbul. and Drag Reduct., Zurich, 1989.

Kogelschatz, U., Eliasson, B., Egli, W., 1997, "Dielectric-Barrier Discharges. Principles and Applications", J. Phys. IV France, **7**, C4, pp. 47-66.

Kovasznay, L. S. G., 1970, "The Turbulent Boundary Layer", Ann. Rev. Fluid. Mech, **2**, pp. 95-112.

Kovasznay, L. S. G., Kibens, V., and Blackwelder, R. F., 1970, "Large-scale Motion in the Intermittent Region of a Turbulent Boundary Layer", J. Fluid Mech., **41**, pp. 283-325.

Kramer, M. O., 1961, "The Dolphin's Secret", J. Am. Soc. Nav. Engr., **73**, pp. 103-107.

Kreith, F. and Bohn, M. S. 1993, Principle of Heat Transfer, Fifth edition, West Publishing Company, pp. 133-137.

Kroschwitz, J. I., (ed. in chief), Mark, H., Bikales, N. M., Overberger, C. G., Menges, G, (eds.), 1986, Encyclopaedia of Polymer and Science Engineering, Vol. 5, 2nd ed. J. Wiley & Sons, New York.

Kundardt, E. E., 2000, "Generation of Large-Volume, Atmospheric-Pressure, Nonequilibrium Plasma", IEEE Transactions on Plasma Science, **28**, No. 1, pp. 189-200.

Laadhari, F., Skandaji, L., and Morel, R. 1994, "Turbulence Reduction in a Boundary Layer by a Local Spanwise Oscillating Surface", Phys. Fluids, **6**, No. 10, pp. 3218-3220.

Liu, S., and Nieger, M., 2001, "Excitation of Dielectric Barrier Discharges by Unipolar Submicrosecond Square Pulses", J. Phys. D: Appl. Phys., **34**, pp. 1632-1638.

Liu, Z.-C., Landreth, R. J., Adrian, T. J., and Hanratty, T. J., 1991, "High Resolution Measurement of Turbulent Structure in a Channel with Particle Image Velocimetry", Exp. In Fluids, **10**, pp. 301-312.

Lorber, p. McCormick, D., Anderson, T., Wake, B., MacMartin, D., Pollack, M., Corke, T., and Breuer, K., 2000, "Rotorcraft Retreating Blade Stall Control", Fluids 2000 Conference and Exhibit, 19-22 June, Denver, CO, AIAA 2000-2475.

Lu, S. S. and Willmarth, W. W., 1973, "Measurements of the Structure of the Reynolds Stress in a Turbulent Boundary Layer", J. Fluid Mech., **60**, 3, pp. 481-511.

Malik, M. R., Weinstein, L. M., and Hussaini, M. Y., 1983, "Ion Wind Drag Reduction", 22nd Aerospace Sciences Meeting, Reno, NV, AIAA 83-0231.

Manca, O., Mastrullo R., and Mazzei, P., 1988, "Calibration of Hot-Wire Probes at Low Velocities in Air with Variable temperature", DANTEC Info., No. 6, pp. 6-8.

Massines, F., Rabehi, A., Decomps, P., Gadri, R. B., Segur, P., Mayoux, C, 1998, "Experimental and Theoretical Study of a Flow Discharge at Atmospheric Pressure Controlled by Dielectric Barrier", J. App. Phys., **83**, No. 6., pp. 2950-2957.

Mehta, R. D., Shabaka, I. M. M., Shibl, A., and Bradshaw, P., 1983, "Longitudinal Vortices Imbedded in Turbulent Boundary Layers", 21st Aerospace Science Meeting, Reno, NV, AIAA 83-0378.

Mei, C. C., MIT, Lecture Notes on Fluid Dynamics (1.63J/2.21J). Last accessed 07/12/05. web.mit.edu/1.63/www/Lec-notes/ chap3_fast/3-3-lamjet.pdf.

Merkle, C. L., and Deutsch, S., 1989, "Drag Reduction in Liquid Boundary Layers by Gas Injection", In Bushnell, C. M., and Hefner, J. N., eds., Viscous Drag Reduction in Boundary Layers. Washington, DC: AIAA 203-261.

Moin, P. and Kim, J., 1985, "The Structure of the Vorticity Field in Turbulent Channel Flow. Part I: Analysis of Instantaneous Fields and Statistical Correlations", J. Fluid Mech., **155**, pp. 441-464.

Moser, R. D., Kim, J., and Mansour, N. N., 1999, "Direct Numerical Simulation of Turbulent Channel Flow up to Re_{τ} = 590", Phys. Fluids., **11**, No.4, pp. 943 945.

Murlis, J., Tsai, H. M., and Bradshaw, P., 1982, "The Structure of Turbulent Boundary Layers at Low Reynolds Numbers", J. Fluid Mech., **122**, pp. 13-56.

Mylar polyester film product information, DuPont Teijin Films, www.dupontteijinfilms.com/datasheets/mylar/productinfo/properties/h32192-1.pdf. last accessed 01/12/2005.

O'Dwyer, J. J., 1964, The Theory of Dielectric Breakdown of Solids, Oxford University Press.

O'Sullivan, P. L., 1998, "Direct Numerical Simulation of Low Reynolds Number Turbulent Channel Flow with EMHD Control", Phys. Fluids, **10**, No. 5, pp. 1169-1181.

Offen, G. R. and Kline, S. J., 1975, "A Proposed Model of the Bursting Process in Turbulent Boundary Layers", J. Fluid Mech., **70**, 2, pp. 209-228.

Orlandi, P. and Jiménez, J., 1994, "On the Generation of Turbulent Wall Friction", Phys. Fluids., **6**, pp. 634-641.

Orlov, D. M., and Corke, T. C., 2005, "Numerical Simulation of Aerodynamic Plasma Actuator Effects", 43rd Aerospace Sciences Meeting, 10-13 Jan, Reno, NV, AIAA 2005-1083.

Pang, J., and Choi, K.-S., 2004, "Turbulent Drag Reduction by Lorentz Force Oscillation", Phys. Fluids, **16**, No. 5, pp. L35-L38.

Pang, J., Choi, K.-S., Aessopos, A., and Yoshida, H., 2004, "Control of Near-wall Turbulence for Drag Reduction by Spanwise Oscillating Lorentz Force", 2nd Flow Control Conference, 28 June 1 July, Portland, OR, AIAA-2004-2117.

Panton, R. L., 2001, "Overview of the Self-Sustaining Mechanisms of Wall Turbulence", Progress in Aerospace Sciences, **37**, pp.341-383.

Pashaie, B., Dhali, S. K., and Honea, F. I., 1994, "Electrical Characteristics of a Coaxial Dielectric Barrier Discharge", J. Phys. D: Appl. Phys., **27**, pp. 2107-2210.

Patel, V. C., 1965, "Calibration of the Preston Tube and Limitations on its use in Pressure Gradients", J. Fluid Mech., **23**, pp. 185-208.

Perry, A. E., Hot-wire Anemometry, Oxford University Press, New York, 1982.

Post, M. L., 2001, Phased Plasma Actuators for Unsteady Flow Control, MS Thesis, University of Notre Dame, IN.

Post, M. L., and Corke, T. C., 2003, "Separation Control on High Angle of Attack Airfoil Using Plasma Actuators", 41st Aerospace Sciences Meeting and Exhibit, 6-9 Jan, Reno, NV, AIAA 2003-1024.

Post, M. L., and Corke, T. C., 2004, "Separation Control Using Plasma Actuators – Dynamic Stall Control on an Oscillating Airfoil", 2nd Flow Control Conference, 28 Jun – 1 July, Portland, OR, AIAA 2004-2517.

Prantdl, L., 1905, "On the Motion of a Fluid with Very Small Viscosity", Verh. Int. Math. Kongr., 3rd, Heidelberg, 1904, pp. 484-91. Transl. 1928, NACA Memo No. 452.

Quadrio, M., and Ricco, P., 2004, "Critical Assessment of Turbulent Drag Reduction through Spanwise Wall Oscillation", J. Fluid Mech., **521**, pp. 251-271.

Rathnasingham, R., and Breuer, K. S., 2003, "Active Control of Turbulent Boundary Layers", J. Fluid Mech., **495**, pp. 209-233.

Reid, A. M., 1962, "Turbulence Measurements Using a Glow Discharge as an Anemometer", R&D, **6**, pp. 69-71.

Robinson, M., 1962, "A History of the Electric Wind", Am. J. Phys., **30**. pp. 366-372.

Robinson, S. K, 1991a, "Coherent Motions in the Turbulent Boundary Layer", Ann. Rev. Fluid. Mech, **23**, pp. 601-639.

Robinson, S. K., 1991b, "Kinematics of Turbulent Boundary Layer Structure", NASA TM 103859.

Rossi, L., and Thibault, J.-P., 2002, "Investigation of wall normal electromagnetic actuator for seawater flow control", J. Turbulence, **3**, 005.

Roth, J. R., 1995, Industrial Plasma Engineering. Volume 1: Principles, Institute of Physics Publishing, Bristol, UK.

Roth, J. R., 2001a, Industrial Plasma Engineering. Volume 2: Applications to Nonthermal Plasma Processing, Institute of Physics Publishing, Bristol, UK.

Roth, J. R. 2001b. "Neutral Gas Flow Induced by Lorentzian Collisions at Plasma Boundaries and the Possibility of Operating Fusion Reactors at One Atmosphere", Proc. 3rd Symp. Current Trends in International Fusion Research, Ottawa, Ontario, Canada.

Roth, J. R. and Sherman, D. M., 2000, "Electrohydrodynamic Flow Control with a Glow-Discharge Surface Plasma", AIAA J., **38**, No. 7, pp. 1166-1172.

Roth, J. R., Tsai, P., P., Liu, C., Laroussi, M., Spence, P., 1995, "One Atmosphere Uniform Glow Discharge Plasma", US Patent No. 5,414,324.

Roth, J. R., Sherman, D. M. and Wilkinson, S. P., 1998, "Boundary Layer Flow Control with a One Atmosphere Uniform Glow Discharge Plasma", 36th Aerospace Sciences Meeting and Exhibit, 12-15 Jan, Reno, NV, AIAA 98-0328.

Roth, J. R., Sherman, D. M. and Wilkinson, S. P. 2001. "Paraelectric Gas Flow Accelerator", US Patent No. 6,200,539.

Roth, J. R., Madhan, R. C. M., Yadav, M., Rahel, J., and Wilkinson, S. P., 2004, "Flow Field Measurements of Paraelectric, Peristaltic, and Combined Plasma Actuators Based on the One Atmosphere Uniform Glow Discharge Plasma (OAUGDP)", 42nd Aerospace Sciences Meeting and Exhibit, 5-8 Jan, Reno, NV, AIAA 2004-845.

Roth, J. R., Dai, X., Rahel, J., and Sherman, D. M., 2005, "The Physics and Phenomenology of Paraelectric One Atmosphere Uniform Glow Discharge Plasma (OAUGDP) Actuators for Aerodynamic Flow Control", 43rd Aerospace Sciences Meeting and Exhibit, 10-13 Jan, Reno, NV, AIAA 2005-0781.

Sandborn, V. A., 1981, "Control of Surface Shear Stress Fluctuations in Turbulent Boundary Layers", Colorado State Uni. No. CSU-CER80-81-VAS-46.

Schlichting, H., 1979, Boundary Layer Theory, Mc-Graw Hill, 7th Ed., First published 1951.

Schoppa, W., and Hussain, F., 1998, "A Large-Scale Control Strategy for Drag Reduction in Turbulent Boundary Layers", Phys. Fluids, **10**, No. 5, pp. 1049-1051.

Schoppa, W., and Hussain, F., 2002, "Coherent Structure Generation in Near-Wall Turbulence", J. Fluid Mech., **453**, pp. 57-108.

Schwaiger, A., 1932, Theory of Dielectrics, tr. by Soreonson, R., John Wiley & Sons, Inc., New York. pp. 189-207.

Scott, S. J., Johnson, G. A., and Thornton, E., 2002a, BAE SYSTEMS plc, GB Patent Application for "Turbulent Flow Drag Reduction," International Publication No. WO 0/2081303, filed 26 March 2002.

Scott, S. J., Johnson, G. A., and Thornton, E., 2002b, BAE SYSTEMS plc, GB Patent Application for "Turbulent Flow Drag Reduction," International Publication No. WO 0/2081304, filed 26 March 2002.

Segawa, T., Murakami, K., Mizunuma, H., and Yoshida, H., 2005, "Measurement of Skin-Friction Drag Reduction by Means of Alternative Suction and Blowing Jets Using Fiber Bragg Grating System", Under consideration for publication with J. Turbulence.

Sellin, R. H. J., and Moses, R. T., 1989, Drag Reduction in Fluid Flows: Techniques for Friction Control, Ellis Horwood, ISBN 0132191970.

Spalding, D. D., 1961, "A Single Formula for the 'Law of the Wall'", J. Appl. Mech., **28**. pp. 455-458.

Shabaka, I. M. M. A., Mehta, R. D., and Bradshaw, P., 1985, "Longitudinal Vortices Imbedded in Turbulent Boundary Layers. Part 1. Single Vortex", J. Fluid Mech., **155**, pp. 37-57.

Sherman, D. M., 1998, Manipulating Aerodynamic Boundary Layers Using an Electrohydrodynamic Effect Generated by a One Atmosphere Uniform Glow Discharge Plasma, MS Thesis, University of Knoxville, TN.

Sherman, F. S., 1990, Viscous Flow, Int. Edition, McGraw Hill, Singapore.

Shyy, W., Jayaraman, B., and Anderson, A., 2002, "Modelling of Glow Discharge-Induced Fluid Dynamics", J. App. Phys., **92**, No. 11, pp. 6434-6443.

Suzen, Y. B., Huang, p. G., Jacob, J. D., and Ashpis, D. E., 2005, "Numerical Simulation of Plasma Based Flow Control Applications", 35th Fluid Dynamics Conference and Exhibit, 6-9 June, Toronto, AIAA 2005-4633.

Tani, I, 1977, "History of Boundary-Layer Theory", Ann. Rev. Fluid Mech., **9**, pp. 87-111.

Taylor, G. I., 1916, "Conditions at the Surface of a Hot Body Exposed of the Wind", Brit. Aero. Res. Comm. R&M No. 272, p. 423.

Tetervin, N., 1948, "Laminar Flow of a Slightly Viscous Incompressible Fluid that Issues from a Slit and Passes Over and Flat Plate", NACA TN 1644.

Tewari, S. S. and Jaluria Y., 1990, "Calibration of Constant-Temperature Hot-Wire Anemometers for Very Low Velocities in Air", Rev. Sci. Instrum., **61**, No. 12, pp. 3834-3845.

Theodorsen, T., 1952, "Mechanism of Turbulence", Proc. 2nd Midwestern Conf. Fluid Mech., 17-19 March, Ohio State University, Columbus, Ohio.

Tsanis, I. K., 1987, "Calibration of Hot-Wire Anemometers at Very Low Velocities", DANTEC Info., No. 4, pp. 13-14.

Virk, P., 1975, "Drag Reduction Fundamentals", AIChE J., **21**, pp.625-656.

Wallace, J. M., Eckelmann, H. and Brodkey, R. S., 1972, "The Wall Region in Turbulent Shear Flow", J. Fluid Mech., **54**, No. 1, pp. 39-48.

Walsh, M. J., 1990, "Riblets", In Bushnell, C. M., and Hefner, J. N., eds., Viscous Drag Reduction in Boundary Layers. Washington, DC: AIAA 203-261.

Warsop, C., 2004, "AEROMEMS-II: A European Research Effort to Develop MEMS Based Flow Control Technologies", 2nd Flow Control Conference, 28 June – 1 July, Portland, OR, AIAA 2004-2209.

Westphal, R. V., Eaton, J. K., and Pauley, W. R., 1985, "Interaction between Vortex and a Turbulent Boundary Layer in a Streamwise Pressure Gradient", 5th Symp. Turbulent Shear Flows, ITHACA, N.Y.

Willmarth W. W., and Lu, S. S., 1972, "Structure of the Reynolds Stress near the Wall", J. Fluid Mech., **55**, No. 1, pp. 65-92.

Wilkinson, S. P., 2003, "Investigation of an Oscillating Surface Plasma for Turbulent Drag Reduction", 41st Aerospace Sciences Meeting and Exhibit, Reno, NV, AIAA 2003-1023.

Wills, J. A. B., 1962, "The Correction of Hot-wire Readings for Proximity to a Solid Boundary", J. Fluid Mech., **12**, pp. 388-396.

Winter, K. G., 1977, "An Outline of Techniques Available for the Measurement of Skin Friction in Turbulent Boundary Layers", Prog. Aero. Sci., **18**, pp. 1-57.

White, F. M., 1999, Fluid Mechanics, Mc-Graw Hill.

Yokoyama, T., Kogoma, M., Moriwaki, T., and Okazaki, S., 1990, "The Mechanism of the Stabilisation of Glow Plasma at Atmospheric Pressure", J. Phys. D: Appl. Phys., **23**, pp. 1125-1128.

Zhou, J., Adrian, R. J., Balachandar, S. and Kendall, T. M., 1999, "Mechanisms for Generating Coherent Packets of Hairpin Vortices in Channel Flow", J. Fluid Mech., **387**, pp. 353-396.

Appendix

Omitted
due to 3rd
party
copyright